ORBITAL ELECTRON DENSITY FROM ELECTRON MOMENTUM SPECTROSCOPY: COMPARISON WITH AB INITIO CALCULATIONS

By

James M. Rolke

B. Sc. (Hons.), University of British Columbia, 1992

A THESIS SUBMITTED IN PARTIAL FULFILLMENT OF

THE REQUIREMENTS FOR THE DEGREE OF

DOCTOR OF PHILOSOPHY

in

THE FACULTY OF GRADUATE STUDIES

DEPARTMENT OF CHEMISTRY

We accept this thesis as conforming

to the required standard

THE UNIVERSITY OF BRITISH COLUMBIA

May 1997

In presenting this thesis in partial fulfilment of the requirements for an advanced degree at the University of British Columbia, I agree that the Library shall make it freely available for reference and study. I further agree that permission for extensive copying of this thesis for scholarly purposes may be granted by the head of my department or by his or her representatives. It is understood that copying or publication of this thesis for financial gain shall not be allowed without my written permission.

Department of Chemistry

The University of British Columbia
Vancouver, Canada

Date July 2, 1997

DE-6 (2/88)

Abstract

Orbital electron momentum profiles measured by electron momentum spectroscopy (EMS) at a total energy of 1200 eV are presented in this work for the HOMOs of open-shell molecules (NO and NO_2), phosphorus compounds (PH_3, PF_3 and $P(CH_3)_3$) and transition metal hexacarbonyls ($Cr(CO)_6$, $Mo(CO)_6$ and $W(CO)_6$). In addition, the complete valence shell binding energy spectra and all valence momentum profiles have been obtained for molecular oxygen (O_2) and methanol (CH_3OH) in the 9-59 eV and 6-47 eV binding energy ranges, respectively. A highly sensitive energy-dispersive multichannel EMS spectrometer has been used to obtain most of the measurements in the present work. The experimental momentum profiles for NO, O_2 and CH_3OH are a significant improvement over previously published single-channel EMS results.

The measured momentum profiles are compared with calculated cross-sections using a range of Hartree-Fock (HF) wavefunctions from minimal basis set to near-Hartree-Fock limit in quality. The effects of correlation and relaxation on the calculated momentum profiles of NO, NO_2, O_2, PH_3 and CH_3OH are investigated using multi-reference singles and doubles configuration interaction (MRSD-CI) calculations of the full ion-neutral overlap distributions. The experimental measurements have also been compared with calculated density functional theory (DFT) momentum profiles using the target Kohn-Sham approximation. The measured valence experimental shell binding energy spectra for O_2 and CH_3OH have been compared with spectra calculated using MRSD-CI and many-body Green's function methods.

Generally good agreement has been obtained between either high-level HF, MRSD-CI or DFT calculated momentum profiles and the experimental momentum profiles for NO, NO_2, O_2, PH_3, PF_3, $P(CH_3)_3$ and CH_3OH. However, there are still some small but significant discrepancies at low momentum for the outermost orbitals of NO and O_2 as well as the 2a″ (HOMO), 7a′ and 5a′ orbitals of CH_3OH. Post-Hartree-Fock calculations have little effect on the shapes of the calculated momentum profiles for NO, NO_2 and PH_3. In contrast, the 7a′,

(6a′+1a″) and 5a′ orbital experimental momentum profiles for methanol display shapes and intensities that can only be predicted by the MRSD-CI and/or DFT calculations and it is clear that in these cases electron correlation is important. The presently reported MRSD-CI calculated pole strengths and energies for O_2 and the measured momentum profiles have been used to assign the significant satellite splitting observed in the $2\sigma_u$ and $2\sigma_g$ ionization strength. Experimental determinations of the pole strengths for the inner valence $(4a')^{-1}$ and $(3a')^{-1}$ satellite ionization processes of CH_3OH have also been achieved in the present work.

The observed increase in s-type character for the outermost orbitals of PF_3 and $P(CH_3)_3$ relative to the HOMO of PH_3 is explained by molecular orbital calculations. This increased s-type character has been interpreted in terms of a delocalization of the charge density in the HOMO orbitals when H is replaced by F or CH_3. The present experimental results for the HOMO of $Cr(CO)_6$ verify earlier measurements in that they display large intensity at low momentum which is not predicted by either symmetry considerations or calculations within the plane wave impulse approximation (PWIA). High intensity at low momentum is also observed for the HOMOs of $Mo(CO)_6$ and $W(CO)_6$ and it is suggested that this is due either to ground state vibrational effects or distortion of the incoming and outgoing electrons waves. The latter suggestion is supported by distorted wave impulse approximation (DWIA) calculations for Cr 3d and Mo 4d atomic orbitals.

Table of Contents

List of Tables

List of Figures

List of Abbreviations

au	atomic units
ACPF	average coupled-pair functional
ADC	analog to digital converter
BES	binding energy spectrum
BW	background window
CFD	constant fraction discriminator
CGTO	contracted Gaussian type orbital
CI	configuration interaction
CW	coincidence window
D	Debye
DAC	digital to analog converter
DFT	density functional theory
DWIA	distorted wave impulse approximation
DZ	double zeta
ECP	effective core potential
EMS	electron momentum spectroscopy
eV	electron volt
FWHM	full width at half-maximum
G(CI)	a configuration interaction calculation based on a Gaussian type orbital basis set
GF	Green's function (calculation)
GTO	Gaussian type orbital
GW-PG	Gaussian weighted planar grid
HF	Hartree-Fock
HOMO	highest occupied molecular orbital
IP	ionization potential
LCAO	linear combination of atomic orbitals
LDA	local density approximation
KS	Kohn-Sham
MBPT	many-body perturbation theory
MBS	minimal basis set
MC	multichannel
MCP	microchannel plate

MD	momentum distribution
MO	molecular orbital
MP	Møller-Plesset
MR-CI	multireference configuration interaction
MRSD-CI	multireference singly and doubly excited configuration interaction
NHOMO	next highest occupied molecular orbital
OVD	overlap distribution
PES	photoelectron spectroscopy
PSDA	position sensitive detector analyzer
PWIA	plane wave impulse approximation
QDVPT	quasi-degenerate variational perturbation theory
RA	resistive anode encoder
RHF	restricted Hartree-Fock
ROHF	restricted open-shell Hartree-Fock
SC	single-channel
SCA	single channel analyzer
SCF	self consistent field
STO	Slater type orbital
TAC	time to amplitude converter
THFA	target Hartree-Fock approximation
TKSA	target Kohn-Sham approximation
TMP	theoretical momentum profile
VWN	Vosko, Wilk and Nusair
UHF	unrestricted Hartree-Fock
XMP	experimental momentum profile
XPS	X-ray photoelectron spectroscopy

Units

Atomic units are a system of reduced units that are useful for discussing quantities on the atomic scale. In this system, the Bohr radius a_0 Planck's constant $\hbar$, the charge on an electron e and the permittivity of free space $4\pi\varepsilon_0$ are all considered to be dimensionless quantities of magnitude 1.

Quantity	Atomic units (1 au)	1 au converted to other units
Distance	a_0 Bohr radius	0.52918 Å 5.2918×10^{-11} m
Momentum	$\frac{\hbar}{a_0}$	1.9929×10^{-24} kg m s^{-1}
Energy	$\frac{e^2}{4\pi\varepsilon_0 a_0}$ 1 hartree = 2 Rydberg	4.2398×10^{-18} J 27.2114 eV
Charge	e Elementary charge	1.6022×10^{-19} C
Dipole Moment	$a_0 e$ charge×distance	8.4785×10^{-11} C·m 2.5418 Debye (D)
Quadrupole Moment	$a_0^2 e$ charge×distance^2	4.4867×10^{-21} C·m 1.3451×10^{-26} esu·cm^2

1 Debye is defined to be 10^{-18} esu cm which is approximately 3.3×10^{-30} C·m or 0.393427 au.

1 torr is equivalent to 1 mm Hg or 0.1333 kPa

Acknowledgements

First of all, I would like to thank my research supervisor, Prof. C.E. Brion. It has been a great privilege to work for Chris and to learn from our discussions. His academic and personal support as well as his enthusiasm for scientific research have enabled me to complete this work.

I also owe special gratitude to the many past and present members of the research group over the last few years: Jennifer Au, Gordon Burton, Natalie Cann, Glyn Cooper, Monica Dyck, Bruce Hollebone, Noah Lermer, John Neville, Terry Olney, and Yenyou Zheng. I especially thank Bruce, John and Yenyou for showing me how to run the spectrometers and for assistance with my experiments and the various technical difficulties along the way. In addition to all of their help with my research, I must also thank all of the members of the group for the many enjoyable discussions and cups of coffee together.

I would also like to acknowledge the staff members of the Chemistry Department for their technical support. In particular, I would like to thank Ed Gomm, Ron Marwick, Bill Henderson and Brian Snapkauskas of the Mechanical Shop as well as Brian Greene of the Electronics Shop for their assistance in keeping the spectrometers running.

I would also like to thank Prof. Ernest R. Davidson, Yan Wang and S.J. Chakravorty of Indiana University for their invaluable contributions to the theory involved in this work. In addition, I thank Prof. I.E. McCarthy for his theoretical contributions to the work on the metal carbonyls.

I gratefully acknowledge the financial assistance of the Natural Sciences and Engineering Research Council of Canada (NSERC) for a postgraduate scholarship.

I thank my family for their support throughout this degree in addition to all their contributions throughout my education. The support and encouragement of Dad, Richie and Jodi has helped me reach this point. In addition, the contributions of my step-mother Barb to my life during this work cannot be forgotten.

Although a complete list of all the friends who have influenced my life during the course of this work would be impossible, some of them deserve special mention for their contributions. In particular, I thank Kyle Marling, Anne Spademan and Raphael Chan for their invaluable support and advice. I would also like to thank Beth Gatehouse, Kaley Walker and Almira Blazek for their help and for adding some fun to the program. Other friends who deserve credit for their interest, support and advice during this work are Kelle Pegg, Lisa Wall, Dave Ham, Maura Bushell, Jennifer Jamieson, Chris Nichols, Mike Wong, Deanna Tan, Laurie Garret and Kim Yee.

Chapter 1

Introduction

It has long been known that chemical phenomena are largely determined by the behaviour of electrons in the outermost valence orbitals with the remaining electrons having relatively little effect. In particular, the frontier molecular orbital theory of Fukui [1], Woodward and Hoffman [2] has emphasized the importance of the electron density distribution in the highest-occupied molecular orbital (HOMO) in determining chemical reactivity. Thus, experimental techniques which provide measurements of the electron density in individual outer valence orbitals are highly desirable so that a wide range of chemical and physical phenomena can be better understood. In addition, ab initio quantum chemistry procedures can be used to provide theoretical electronic wavefunctions and charge distributions, but the quality of the results is highly dependent upon the choice of basis set and the various approximations that are required in the chosen quantum mechanical procedure. Experimental electron density distributions for individual orbitals therefore play an important role because, in addition to providing fundamental information regarding the potential for chemical reactivity and behaviour, they can also be used in the direct evaluation of the quality of theoretical methods. It should be noted that measurements of electron density distributions have long been provided by X-ray and γ-ray Compton scattering profile studies [3-6], by high energy electron impact ionization [7,8] and by positron annihilation [9,10] techniques, but these various methods all measure the total electron density due to all electrons in the target and do not provide specific electron density information for the individual atomic and molecular orbitals. A unique experimental technique that can investigate individual orbital electron densities (momentum

distributions) is electron momentum spectroscopy (EMS). The EMS experiment and the information provided by the technique are discussed in Section 1.1 below.

1.1 Electron Momentum Spectroscopy

1.1.1 The EMS Experiment

The EMS experiment involves the complete kinematic determination of a high impact energy, high momentum transfer electron impact ionization (e, 2e) reaction:

$$e_0^- + M \rightarrow M^+ + e_1^- + e_2^- \tag{1.1}$$

A schematic of the EMS (or binary (e, 2e)) collision process in the commonly used symmetric non-coplanar geometry [11,12] is shown in Fig. 1.1. The reaction involves the ionization of a target (M) by an energetic electron followed by the coincidence detection of the scattered and ejected electrons. The energies and directions (and thus the momenta) of the incoming and outgoing electrons are determined experimentally by the geometric arrangement and electrostatic potentials of the electron optics and energy analyzers. The incident electron e_0 has an impact energy of E_0 with corresponding momentum $\boldsymbol{p}_0$ while the two outgoing electrons e_1 and e_2 have energies E_1 and E_2 and momenta $\boldsymbol{p}_1$ and $\boldsymbol{p}_2$, respectively. The collision results in an ion M^+ in a final state f with recoil energy and momentum E_{recoil} and $\boldsymbol{q}$, respectively. In addition, θ_1 and θ_2 are the polar angles between the incident electron and the directions of the two outgoing electrons. As can be seen from Fig. 1.1, the angle ϕ is the relative azimuthal angle between the two planes $(\boldsymbol{p}_0,\boldsymbol{p}_1)$ and $(\boldsymbol{p}_0,\boldsymbol{p}_2)$. The EMS experiment operates in two modes [11,12]. Variation of the impact energy at fixed E_1, E_2, θ_1, θ_2 and ϕ results in a binding energy spectrum (BES). Alternatively, as will be shown in Chapter 2, an orbital electron momentum distribution for a binding (i.e. ionization) energy selected electron can be obtained by variation of the azimuthal angle ϕ. An electron momentum distribution measured in EMS is often referred to as an experimental momentum profile (XMP).

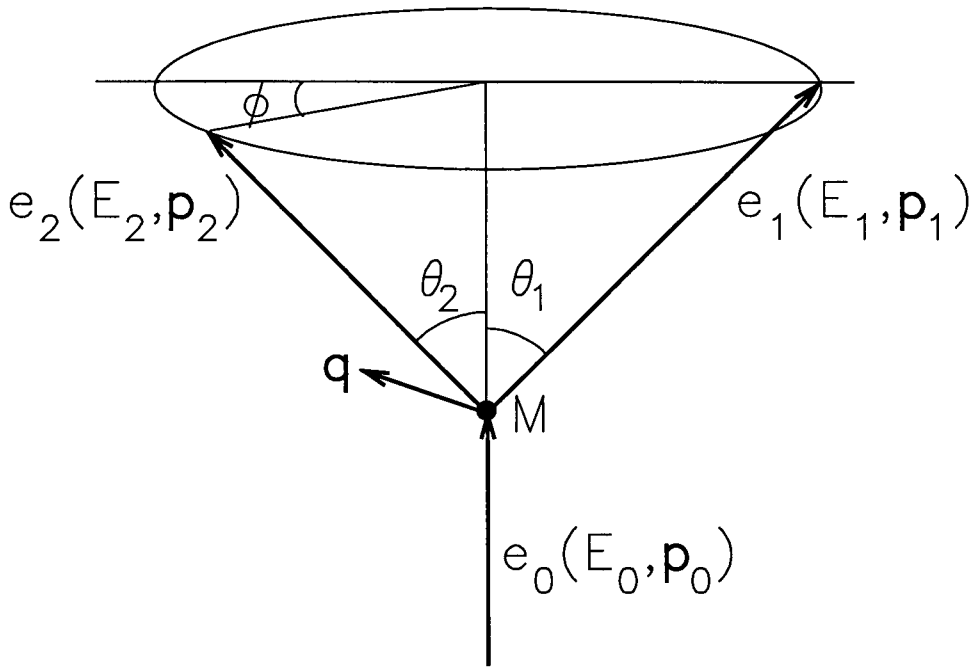

Fig. 1.1: A schematic of the symmetric non-coplanar (e, 2e) scattering geometry.

The possibility of using the (e, 2e) reaction in Eq. (1.1) as an experimental technique to investigate individual orbital electron densities was first suggested in 1960 by Baker, McCarthy and Porter [13] in the concluding paragraph of a paper dealing with the theory of the (p, 2p) reaction as a probe of proton momenta in nuclei. Because of these origins involving the (p, 2p) reaction in nuclear physics, EMS was known as binary (e, 2e) spectroscopy for much of its early history. The possibility of such (e, 2e) experiments was investigated theoretically in the late 1960s by Neudatchin and co-workers [14,15] and by Glassgold and Ialongo [16].

The first instrument developed to study (e, 2e) scattering was reported in 1969 by Ehrhardt et al. [17]. However, this instrument was specifically designed to observe the scattering of slow (~ 100 eV) electrons from a gas in a coplanar geometry to provide a test for theories of low energy impact ionization rather than for studies of electron momentum distributions. In the same year, Amaldi et al. [18] developed a symmetric coplanar (e, 2e) instrument with high impact energy (14.6 keV) and measured the binding energy spectrum with an energy resolution sufficient to separate the carbon K and L shell electrons in a transmission experiment through a thin film graphite target. This study [18] indicated that important information concerning the electronic structure of the target could be obtained using the (e, 2e) technique.

In 1972, Camilloni et al. [19] reported the first experimental orbital momentum distributions in a high energy transmission (e, 2e) study of the carbon K (1s orbital) shell for a thin graphite film target. However, due to the very low energy resolution of the instrument, the momentum distributions of the individual C 2s and 2p valence orbitals could not be obtained [19]. In 1973 the first gas phase binary (e, 2e) experiment was carried out by Weigold and co-workers who reported valence shell orbital momentum distributions for the individual 3p and 3s atomic orbitals of argon [20,21]. These atomic measurements were soon followed by the first molecular results which were for the valence electrons of methane [22]. In 1974 molecular EMS studies were started at the University of British Columbia and results were soon reported for the individual valence orbitals of NH_3 [23] and H_2O [24]. In parallel with

these early experimental advances, the theoretical interpretation of the binary (e, 2e) scattering cross-section was further developed [25-27]. EMS studies were subsequently reported by groups at the University of Maryland [28] and the University of Waterloo [29]. More recently, EMS experiments have also been carried out at Carleton University [30], Tsinghua University (Beijing, China) [31] and Tohoku University (Sendai, Japan) [32].

The EMS technique has been further developed over the past two decades and applied to a growing range of studies of chemical interest. These developments are summarized in a number of EMS review articles [11,12,33-40] and bibliographies [38,41]. The advent of multichannel energy-dispersive [42-46] and momentum-dispersive [47] EMS spectrometers which provide greatly improved count rates (one or two orders of magnitude) compared to earlier single-channel spectrometers has greatly increased the range of studies possible. For example, Zheng et al. [48] used an energy-dispersive multichannel spectrometer to provide the first EMS results for an excited and oriented target (sodium atoms in the $3^2P_{3/2}$, $m_l = +1$ state). Lermer et al. [49-51] have reported improved measurements of the low cross-section XMPs corresponding to the excited $n = 2$ and $n = 3$ ion states of helium as well as the $2p\sigma_u$ and $2p\sigma_g$ orbitals of H_2 and D_2, obtained with a momentum dispersive EMS spectrometer. Recently, Storer et al. [52] have reported an EMS spectrometer that is multichannel in both energy and momentum which has been used to study thin solid films and thus have extended EMS studies to condensed matter targets. In particular, this spectrometer [52] has been used to obtain EMS measurements for the valence shell of graphite as well as amorphous forms of carbon. Multichannel EMS spectrometers have also made feasible the study of larger molecules such as SF_6 [42] and acetone [45]. Results obtained very recently at the University of British Columbia for glycine [53-55] have extended the EMS technique to prototype biomolecules.

In parallel with these experimental developments, the theoretical treatments involved in the interpretation of EMS studies (and quantum chemistry in general) have advanced considerably [56,57]. As will be discussed in more detail in Chapter 2, the XMPs obtained from EMS are directly comparable to theoretical momentum profiles (TMPs) calculated from

quantum chemistry wavefunctions. Much larger basis sets are now employed in the calculation of TMPs from Hartree-Fock (HF) wavefunctions than in earlier EMS studies. Substantial advancement has also been made in the theory of post-Hartree-Fock methods such as configuration interaction (CI) as well as the capability to compute large CI wavefunctions [56,57] for calculation of TMPs. In other work, the incorporation of instrumental momentum resolution effects in TMPs has been found to be an extremely important consideration in the interpretation of the EMS experiment [58,59]. Lastly, the development of the target Kohn-Sham approximation (TKSA) for the calculation of theoretical momentum profiles using density functional theory (DFT) [60] has permitted high-level calculations which include some accounting of electron correlation effects through the exchange-correlation potential. The DFT calculations are particularly important for larger molecules where large CI calculations are not feasible. In the last few years, the application of Kohn-Sham orbital momentum profiles has been extended to other larger molecules and, while the method is still relatively new, it has thus far provided very good descriptions of the momentum profiles of several molecules if sufficiently large basis sets are used [45,53-55,60-62].

1.1.2 Binding Energy Spectrum

The binding energy mode is principally used to select the various orbitals for the study of momentum profiles. The energy resolution in existing EMS studies is typically limited to ~ 1.3 eV FWHM due to the Maxwell-Boltzmann distribution of electron energies from the heated electron gun cathode (~ 0.7 eV FWHM) and the contributions from the energy resolutions of the two electron energy analyzers. Even with present multichannel instrumentation, monochromation of the incident electron beam is not a realistic possibility in the EMS experiment because of the very low (e, 2e) coincidence cross-section and the resulting low count rates. Further improved multichannel EMS spectrometers are currently being developed with much increased count rates and thus incident electron beam monochromation may soon be employed.

Despite the present limitations in energy resolution for the EMS experiment, BES have some distinct advantages compared with high resolution photoelectron spectroscopy (PES) studies which can provide very accurate ionization potentials. Before the advent of monochromated synchrotron radiation, discrete atomic emission resonance lamp sources were routinely used for PES due to their high intensity and very narrow natural line widths. The most commonly used resonance lines are He I and He II with energies of 21.2 eV and 40.8 eV, respectively. However, higher binding energy studies above ~ 20 eV are not possible with He I PES sources. In addition, studies with He II sources are normally contaminated above ~ 20 eV by a He I "shadow" and by self-ionization of He at 24.6 eV. Thus, the inner valence region of molecules (usually in the 20-40 eV binding energy range) has not been studied with these low energy photon line sources [63,64]. In contrast, the EMS experiment does not suffer from such spectral contamination effects and there are no restrictions on the incident energy since higher binding energies are readily accessible by simply increasing the electron beam impact energy. While X-ray line light sources involving the decay of atomic inner-shell hole states (e.g. the Al and Mg $K\alpha$ lines at 1486.6 eV and 1253.6 eV, respectively) can provide higher energy PES studies, the resolution is significantly poorer (0.7-1.0 eV FWHM) than for the He I and He II sources. A wide range of tunable photon energies is now available for PES studies using monochromated synchrotron radiation sources, but such facilities are remotely located and beam time must be obtained. In addition, the energy resolutions of monochromated synchrotron radiation sources are typically wider than that of emission line sources such as He I and II resonance lamps and are often only of the same order of magnitude as the best overall EMS energy resolution, particularly at higher photon energies. It should also be noted that PES spectra usually have large sloping non-spectral backgrounds (particularly at lower kinetic energies) while the EMS experiment results in a constant background (due to random coincidences - see Chapter 3) which is easily and unambiguously removed during the collection of the data.

Within the Hartree-Fock independent particle model, one peak occurs in the binding energy spectrum corresponding to each occupied orbital (neglecting effects such as spin-orbit interaction and nuclear motion). This behaviour is normally observed for ionization from the outer valence orbitals. However, electron correlation (many body effects) and electronic relaxation can distort this simple picture and ionization from a more tightly bound valence orbital may occur at several ionization energies and produce a manifold of final ion states for a given orbital ionization [63-65]. This results in "satellite peaks" in the binding energy spectra. In terms of the CI model, these peaks can be modelled by linear combinations of ionizations and simultaneous excitations of other electrons which occur in addition to the primary (single-hole) ionization process. Alternatively, many body Green's function methods can be used to predict the spectra [65]. The presence of satellite peaks is most common in the higher energy inner valence region with binding energies typically in the range 20-60 eV [65]. Although these satellite peaks are generally of lower intensity than that due to the main ionization peak, they are frequently very numerous and can account for a significant portion of the total orbital ionization intensity (ionization strength). The sum of the intensities of all of the ionization peaks having the same parentage must also be equal to the number of electrons removed (the spectroscopic sum rule - see Chapter 2). The capability of EMS to detect such electron correlation effects has been known since the early measurements on argon [20,21] in which $(3s)^{-1}$ satellite processes were observed at energies above that of the main $(3s)^{-1}$ peak.

It is difficult to assign the final ion state and overall symmetry of parent and satellite ionization processes with PES [66] and, although some information on the character and parentage of ionization processes can be obtained using angular resolved PES measurements [63,64] and/or the dependence of intensity on photon energy, the results are not always conclusive. In contrast, the EMS cross-section provides more direct information concerning the origin of satellite peaks in binding energy spectra. Since the EMS binding energy spectra can be obtained as a function of electron momentum (i.e. angle ϕ) consideration of the relative intensities in BES at two different angles can provide some symmetry

information. Furthermore, the shapes of the electron momentum profiles often allow assignment of the orbital parentage of the given ionization process by comparison with ab initio calculations. Different ionization processes sharing the same initial orbital parentage would be expected to have the same shape momentum profile if initial state correlation is negligible. For example, the disputed energy ordering of the $(5a_1)^{-1}$ and $(1b_2)^{-1}$ orbital ionizations of formaldehyde (H_2CO) has been clarified by EMS measurements and momentum profile calculations [67,68].

1.1.3 Momentum Profile

The unique feature of EMS is the measured electron momentum profiles obtained using the technique. The spherically averaged square of the momentum space molecular orbital, $\psi(\boldsymbol{p})$, generally provides good descriptions of the measured XMP (see Section 2.2.5) and thus EMS permits the "imaging" of electron density in momentum space for individual orbitals. This imaging ability is useful not only for the fundamental electronic structure information it provides but also because the experimental momentum profiles provide a stringent quantitative test of the basis sets and quantum chemistry procedures (e.g. HF, CI and DFT) used to obtain theoretical wavefunctions. The XMP is particularly sensitive to the low momentum region of a wavefunction. It should be noted that position (r) and momentum (p) space are inversely weighted according to the Fourier transform (see Section 2.2.7) so that large r generally corresponds to low p and vice versa. Therefore, EMS is particularly sensitive to the outermost (large r) spatial regions of electron density. Although a good description of the large r regions of electron density is vitally important in understanding chemical reactivity, this region is often poorly represented by theoretical wavefunctions commonly calculated with the variational method because of the insensitivity of the total energy to the larger r regions. The energy minimization constraints of the variational method tend to emphasize the opposite regions (i.e. small r, large p) of the wavefunction [69]. The momentum profiles from EMS therefore provide an additional criterion to variationally determined total energies and other properties

emphasizing medium r and p such as dipole and quadrupole moments. Consideration of a range of properties is necessary for the calculation of "universal" wavefunctions that provide reliable modelling in all regions of phase space. For example, even near-Hartree-Fock limit TMPs for H_2O and NH_3 were initially found to underestimate the low momentum regions of the HOMO experimental momentum profiles for these molecules [39,69,70]. As a result, the EMS studies on these molecules led to the development of more highly saturated basis sets with polarization and extremely diffuse functions that resulted in a significant improvement in the agreement between theory and experiment in the low momentum regions of these orbitals and also very accurate prediction of a wide range of properties [56,69]. However, because of the almost negligible effects of such diffuse and polarization functions on the small r region heavily emphasized by the variational method, the calculated total energies differed only very slightly when these diffuse and polarization functions were added to the basis set.

The development of wavefunctions that provide good calculated results for a range of properties emphasizing different regions of phase space has been of particular interest in many EMS studies. High-level multi-reference single and double excitation configuration interaction (MRSD-CI) wavefunctions have been developed in ongoing collaborative work between this laboratory and co-workers at Indiana University and the corresponding theoretical momentum profiles have been compared with the experimental momentum profiles [37,39,71]. For example, one factor contributing to the initial disagreement between the theoretical and experimental momentum profiles for the HOMOs of H_2O and NH_3 mentioned above was found to be the absence of a treatment of electron correlation effects in the theoretical calculations [39,69,70]. When electron correlation effects were accounted for by using large basis set MRSD-CI calculations (and also including the GW-PG resolution folding method [59] to account for the instrumental angular resolution) excellent agreement between theory and experiment was obtained for these hydrides [39,69,70]. The inclusion of electron correlation effects was also necessary to obtain reasonable agreement between theory and the experimental momentum profile for the HOMO of hydrogen fluoride [72]. However, the

momentum profiles of the third row hydrides SiH_4 [73], PH_3 [74], H_2S [75] and HCl [76] as well as CH_4 [77] showed good agreement with near Hartree-Fock limit TMPs. The effects of correlation and relaxation on the momentum profiles were found to be negligible for these molecules [73-77]. Further investigations of the effects of electron correlation have been provided by the recent comparison of theoretical momentum profiles obtained using DFT with measured XMPs [45,53-55,60-62].

The "orbital imaging" provided by the measured momentum profile facilitates the study of bonding and chemical behaviour of a series of compounds by measurement of the momentum profiles of similar orbitals. The sensitivity of the EMS cross-section to the low p (large r) region is particularly useful for the study of such effects. For example, Leung and Brion [78,79] have used this technique to study the changes in electron density distribution occurring on forming the chemical bond in molecular hydrogen. In other work, the methyl inductive effect has been studied by comparison of experimental and theoretical momentum profiles for the HOMOs of ammonia and the various methylamines together with a consideration of calculated momentum and position space density difference maps [70,80-82]. Methyl substitution effects have also been investigated in the calculated and experimental orbital momentum profiles for the HOMOs of the series formaldehyde, acetaldehyde and acetone [83] and for the series H_2O [69], CH_3OH [84] and CH_3OCH_3 [85,86].

Electronic structure information is more commonly studied and understood in terms of the position space representation. The experimental results from EMS studies therefore provide a complementary picture of chemical phenomena in the momentum space description. Although the Schrödinger equation is most commonly solved in the position space representation for the total r-space wavefunction, it has long been known that there is an analogous p-space equation that may be solved for the momentum space wavefunction. The p-space representation depends upon the momenta rather than the positions of the electrons. The two wavefunctions are related by the Fourier Transform (see Section 2.2.7). This alternative momentum space representation was investigated by Coulson and Duncanson in a

series of theoretical papers on the electron density for H_2 and simple hydrocarbons [87-89]. It was shown [87-89] that chemical bonding concepts could be discussed in terms of the *p*-space electron density and that the momentum space representation provided complementary information that was not readily obtained from the position space viewpoint. Although momentum space theoretical studies are not widely found in the literature, the effectiveness of such approaches is well illustrated by the recent theoretical work of Cooper, Allan and co-workers [90-92]. These calculations [90-92] have demonstrated the usefulness of the momentum space representation and have shown that molecular similarity and dissimilarity indices calculated using momentum space electron densities are capable of rationalizing chemical properties and reactivity. In particular, the momentum space approach gave satisfactory predictions of the biomedical activity of molecules such as anti-HIV phospholipids [90-92] where *r*-space calculations were inconclusive. The experimental and theoretical results from EMS studies over the last quarter century have been used to illustrate chemical behaviour such as bonding and reactivity in the momentum space representation and to provide a pedagogical approach to this complementary viewpoint. The studies of the bonding in H_2 [78,79] and methyl substitution [70,81-83,85,86] mentioned above as well as studies of many other molecules have been aided by calculated momentum and position density contour maps. Brion [11], McCarthy and Weigold [35] and Leung [93] have discussed momentum and position space properties in various review articles. Zheng, Neville and Brion [53,54] have studied the distribution of "lone pair" density on the nitrogen and oxygen atoms of glycine and the role of correlation using EMS measurements and position density maps for the HOMOs generated with the best fitting DFT calculations for the three lowest energy conformers.

1.2 Overview of the thesis

In the present work, the technique of EMS has been extended to the investigation of several types of molecules of particular experimental and theoretical interest. The remaining chapters of the thesis are organized as outlined below.

The theoretical aspects of quantum chemistry related to EMS studies are discussed in Chapter 2. In addition, the methods for the interpretation and calculation of the EMS cross-section are also introduced.

Chapter 3 gives details of the construction and operation of the multichannel electron momentum spectrometer used in the present work. The data processing procedures profiles are also explained in this chapter.

Experimental and theoretical investigations of the electron momentum distributions for the outermost (HOMO) orbitals of the open-shell molecules NO and NO_2 are described in Chapter 4. Systematic comparisons of the experimental results with Unrestricted Hartree-Fock (UHF), Restricted Open-shell Hartree-Fock (ROHF), MRSD-CI and DFT calculations. An averaged coupled-pair functional (ACPF) calculation is also reported for NO while a quasi-degenerate variational perturbation theory (QDVPT) calculation is presented for NO_2. This work has been published as J. Rolke, N. Cann, Y. Zheng, B.P. Hollebone, C.E. Brion, Y.A. Wang and E.R. Davidson, in *Chem. Phys.* **201** (1995) 1 [94].

EMS measurements of the complete valence shell of molecular oxygen are presented in Chapter 5. The experimental EMS binding energy spectra are compared to theoretical predicted binding energies and pole strengths from a new MRSD-CI calculation. In addition, the EMS valence momentum profiles are compared with calculations using both the UHF and ROHF methods, with MRSD-CI momentum profiles and also with density functional methods employing a range of exchange-correlation functionals. In the case of the outermost $1\pi_g$ orbital ($^2\Pi_g$ final ion state) an ACPF calculation is also reported. An assignment of binding energy peaks of disputed origin is provided by a comparison of the measured EMS binding energy spectra and momentum profiles with MRSD-CI calculations.

EMS studies of phosphorus compounds and the investigation of inductive effects is discussed in Chapter 6, where results for the HOMOs of PH_3, PF_3, and $P(CH_3)_3$ are presented. The experimental momentum profiles for the HOMOs of PF_3 and $P(CH_3)_3$ are the first to be reported and are used to investigate substituent effects of the methyl group relative to hydrogen

and fluorine. The present experimental results for PF_3 and $P(CH_3)_3$ are compared with previous EMS results for PH_3 [74]. In addition, the experimental momentum profiles for PH_3 [74], PF_3 and $P(CH_3)_3$ are compared to HF, MRSD-CI and DFT theoretical momentum profiles. This work has appeared in the literature as J. Rolke and C.E. Brion, in *Chem. Phys.* **207** (1996) 173 [95].

The application of EMS to larger inorganic molecules is investigated in Chapter 7, where results for the HOMOs of the transition metal hexacarbonyls $Cr(CO)_6$, $Mo(CO)_6$ and $W(CO)_6$ are presented. EMS measurements for the t_{2g} HOMOs of these molecules are of particular interest because these orbitals are primarily metal valence d in character. The experimental momentum profiles are compared with Hartree-Fock and DFT theoretical momentum profiles within the plane wave impulse approximation (PWIA) of the EMS cross-section. Distorted wave impulse approximation (DWIA) calculations for atomic Cr 3d and Mo 4d orbitals have also been carried out to investigate the role of distorted wave effects in the EMS cross-section in systems involving these atoms (see Chapter 2 for descriptions of the PWIA and DWIA methods for calculation of the EMS cross-section). This work has been published as J. Rolke, Y. Zheng, C.E. Brion, S.J. Chakravorty, E.R. Davidson and I.E. McCarthy, in *Chem. Phys.* **215** (1997) 191 [96].

EMS measurements of the full valence shell of methanol (CH_3OH), including the satellite structure up to 47 eV, are presented in Chapter 8. Calculated binding energy spectra obtained by combining large basis set Hartree-Fock calculations of the momentum profiles with Green's function pole strengths are compared to the experimental BES. In addition, a range of Hartree-Fock, MRSD-CI and DFT calculations are investigated and compared to experimental momentum profiles.

Chapter 9 summarizes the general conclusions arising from the present work. The major results are summarized and some suggestions for future experimental and theoretical studies are presented.

Chapter 2

Theory

2.1 The Calculation of Wavefunctions

The focus of this section is the description of the theoretical methods which are commonly used to calculate the EMS cross-section for comparison to experiment. Over the past seventy years, theoretical models used to aid in the interpretation of experiment have advanced greatly. This chapter will be concerned with the following methods:

(a) Hartree-Fock (for both closed- and open-shells)

(b) Configuration interaction (CI)

(c) Density functional theory (DFT)

Since these methods are well-known and can be found in detail in standard quantum chemistry texts [57,97,98] only brief descriptions will be given here. Both Hartree-Fock and configuration interaction methods have been used in the interpretation of EMS studies for many years. However, the application of DFT to EMS is much more recent and it provides a useful alternative to the more established methods. Before the individual methods are described in Sections 2.1-2.4, it will be useful to review some basic concepts of quantum chemistry such as the *Schrödinger equation*, the *variational principle*, the *molecular Hamiltonian* and the *Born-Oppenheimer approximation.*

According to quantum mechanics, the energy and properties of a stationary state of a molecule can be obtained by solution of the *Schrödinger equation*:

$$\hat{H}\Psi = E\Psi \tag{2.1}$$

In Eq. (2.1) $\hat{H}$ is the *Hamiltonian*, an operator representing the total energy E for the stationary state of the system described by the total wavefunction Ψ. The Schrödinger equation for a molecule will have many solutions, corresponding to different stationary states. The state with the lowest energy is the *ground state*.

The most common techniques for the calculation of wavefunctions (e.g. Hartree-Fock and CI) are based on the *variational principle* [98]. If Ψ_0 is the exact ground state wavefunction for a system, then it satisfies the Schrödinger equation (Eq. (2.1)) such that:

$$\hat{H}\Psi_0 = E_0\Psi_0 \tag{2.2}$$

where $\hat{H}$ is again the Hamiltonian and E_0 is the exact ground state energy. The expectation value of the energy (E) of *any* normalized wavefunction Φ is given by:

$$E = \int \Phi^* \hat{H} \Phi d\tau \geq E_0 \tag{2.3}$$

where integration is over the coordinates of all electrons. Thus, E is greater than or equal to E_0 (equality results only if the trial wavefunction Φ is identical to the ground state wavefunction Ψ_0). E is therefore an upper bound to the exact ground state energy and, in the variational method, the lowest energy wavefunction is assumed to be the best approximation to the exact wavefunction. However, the degree to which such a wavefunction can provide accurate electronic properties (e.g. dipole moment, quadrupole moment, momentum profile) depends on the computational method (e.g. Hartree-Fock, CI, etc.) and also on the basis set chosen in the calculation.

If we assume the nuclei and electrons to be point masses and neglect spin-orbit and other relativistic effects, then the *molecular Hamiltonian* is

$$\hat{H} = -\frac{\hbar^2}{2}\sum_A \frac{1}{m_A}\nabla_A^2 - \frac{\hbar^2}{2m_e}\sum_i \nabla_i^2 + \sum_A \sum_{B>A} \frac{Z_A Z_B e^2}{r_{AB}} - \sum_A \sum_i \frac{Z_A e^2}{r_{iA}} + \sum_j \sum_{i>j} \frac{e^2}{r_{ij}} \tag{2.4}$$

where A and B refer to nuclei and i and j refer to electrons. The first term in Eq. (2.4) is the operator for the kinetic energy of the nuclei and the second term is the operator for the kinetic

energy of the electrons. The third term is the potential energy of the repulsions between nuclei with atomic numbers Z_A and Z_B which are separated by a distance of r_{AB}. The fourth term is the potential energy of the attractions between the electrons and the nuclei, with a distance of r_{iA} between electron i and nucleus A. The last term is the potential energy of the repulsions between the electrons, with r_{ij} being the distance between electrons i and j.

The full molecular Hamiltonian given by Eq. (2.4) is formidable and thus the *Born-Oppenheimer approximation* is used as a simplification. Since the electrons are much lighter than the nuclei, they move much faster than the nuclei. Thus, to a good approximation, we can regard the nuclei as fixed while the electrons carry out their motions (i.e. in a classical sense, the change in nuclear positions is negligible during time that the electrons carry out a "cycle" of their motions). Therefore, the terms involving the kinetic energy of the nuclei in Eq. (2.4) can be omitted to give a new molecular Hamiltonian:

$$\hat{H} = \hat{H}_{\text{el}} + V_{NN} \tag{2.5}$$

where the *purely electronic Hamiltonian* $\hat{H}_{\text{el}}$ contains terms involving only the electrons:

$$\hat{H}_{\text{el}} = -\frac{\hbar^2}{2m_e}\sum_i \nabla_i^2 - \sum_A \sum_i \frac{Z_A e^2}{r_{iA}} + \sum_j \sum_{i>j} \frac{e^2}{r_{ij}} \tag{2.6}$$

and the *nuclear repulsion term* V_{NN} is the only remaining term involving the nuclei:

$$V_{NN} = \sum_A \sum_{B>A} \frac{Z_A Z_B e^2}{r_{AB}} \tag{2.7}$$

The V_{NN} term is constant for a given choice of the r_{AB} distances and therefore does not affect the electronic wavefunction of the system. The variables in Eq. (2.5) are the electronic coordinates and the electronic Hamiltonian $\hat{H}_{\text{el}}$ can be used to solve the *purely electronic Schrödinger equation*:

$$\hat{H}_{\text{el}}\Psi_{\text{el}} = E_{\text{el}}\Psi_{\text{el}} \tag{2.8}$$

and the resulting electronic energy E_{el} can then be added to the nuclear repulsion to give the total energy E:

$$E = E_{el} + V_{NN} \tag{2.9}$$

While the Born-Oppenheimer approximation simplifies the procedure, the determination of the electronic wavefunctions for a many-electron system is still a challenging problem mainly due to the inter-electron $1/r_{ij}$ terms of the Hamiltonian. Hartree-Fock theory (see Section 2.1.1 below) provides the simplest and most common method for handling these problems and calculating the electronic wavefunctions.

2.1.1 Hartree-Fock Theory for Closed-Shell Molecules

The Hartree-Fock method was developed in the late 1920s and early 1930s from intuitive, physical arguments as a model of electronic structure. The electrons in a molecule are assumed to be independent of one another in Hartree-Fock theory and thus they may be described by a series of one-electron functions called *orbitals*. In particular, the total n-electron Hartree-Fock wavefunction Ψ_{HF} is expressed as a single antisymmetrized Slater determinant composed of one-electron functions called spin orbitals. This antisymmetric determinant restriction is chosen so that the wavefunctions obey the Pauli principle and thus are physically acceptable. Each spin orbital is composed of the product of a spatial orbital ψ_i and a spin function (α or β). The one-electron spatial part of a molecular spin-orbital is called a *molecular orbital* (MO). Using the variational method (Eq. (2.3)), the Hartree-Fock total molecular electronic energy E_{HF} is given by:

$$E_{HF} = \langle \Psi_{HF} | \hat{H}_{el} + V_{NN} | \Psi_{HF} \rangle \tag{2.10}$$

where $\hat{H}_{el}$ and V_{NN} have the forms given in Eqs. (2.6) and (2.7). Substituting in the forms for the operators, converting to atomic units and expanding Ψ_{HF} in terms of its constituent orbitals ψ_i, it can be shown that:

$$E_{\mathrm{HF}} = 2\sum_{i=1}^{n/2} H_{ii}^{\mathrm{core}} + \sum_{i=1}^{n/2}\sum_{j=1}^{n/2}(2J_{ij} - K_{ij}) + V_{NN} \tag{2.11}$$

where

$$\begin{aligned} H_{ii}^{\mathrm{core}} &= \left\langle \psi_i(1) \middle| \hat{H}_{(1)}^{\mathrm{core}} \middle| \psi_i(1) \right\rangle \\ &= \left\langle \psi_i(1) \middle| -\frac{1}{2}\nabla_1^2 - \sum_A \frac{Z_A}{r_{1A}} \middle| \psi_i(1) \right\rangle \end{aligned} \tag{2.12}$$

$$J_{ij} = \left\langle \psi_i(1)\psi_j(2) \middle| \frac{1}{r_{12}} \middle| \psi_i(1)\psi_j(2) \right\rangle \tag{2.13}$$

$$K_{ij} = \left\langle \psi_i(1)\psi_j(2) \middle| \frac{1}{r_{12}} \middle| \psi_j(1)\psi_i(2) \right\rangle \tag{2.14}$$

The *one-electron core Hamiltonian* $\hat{H}_{(i)}^{\mathrm{core}}$ omits the interactions of electron i with the other electrons. The sums involving i and j are over the $n/2$ occupied spatial orbitals ψ_i of the n-electron molecule (hence the factor of 2 in some terms). The quantities J_{ij} and K_{ij} are known as the *Coulomb* and *Exchange integrals*, respectively and the integration is over the spatial coordinates of electrons 1 and 2.

The next step in the Hartree-Fock method is to find the orbitals ψ_i that minimize the variational integral in Eq. (2.10) such that the Hartree-Fock energy E_{HF} is as close as possible to the energy E_{HF} from the exact wavefunction. As a computational simplification, the orbitals are taken to be orthonormal. Minimization of E_{HF} with respect to ψ_i results in $n/2$ one-electron *Hartree-Fock equations* [57] each of which satisfy:

$$\hat{F}(1)\psi_i = \varepsilon_i \psi_i \tag{2.15}$$

$\hat{F}(1)$ is the one-electron *Fock operator* and ε_i is the energy of orbital ψ_i. The Fock operator is given (in atomic units) by:

$$\begin{aligned} \hat{F}(1) &= \hat{H}_{(1)}^{\mathrm{core}} + \sum_{j=1}^{n/2}[2\hat{J}_j(1) - \hat{K}_j(1)] \\ &= -\frac{1}{2}\nabla_1^2 - \sum_A \frac{Z_A}{r_{1A}} + \sum_{j=1}^{n/2}[2\hat{J}_j(1) - \hat{K}_j(1)] \end{aligned} \tag{2.16}$$

The *Coulomb* operator $\hat{J}_j$ and the *exchange* operator $\hat{K}_j$ for interactions of electron (1) with

electron (2) are defined by their operation on any arbitrary function $f(1)$:

$$\hat{J}_j(1)f(1)=f(1)\int\left|\psi_j(2)\right|^2\frac{1}{r_{12}}d\tau_2 \tag{2.17}$$

$$\hat{K}_j(1)f(1)=\psi_j(1)\int\frac{\psi_j^*(2)f(2)}{r_{12}}d\tau_2 \tag{2.18}$$

It should be noted that these last two operators depend on the coordinates of one electron only. The Coulomb operator $\hat{J}_j(1)$ describes the potential energy of the interaction between electron (1) and a smeared-out electron density $\left|\psi_j(2)\right|^2$ for electron (2). Thus, instantaneous interactions between electrons are neglected in favor of an "average field" of electrons and this form for the Coulomb operator is required for the total electronic wavefunction to be separated into products of one-electron wavefunctions. The exchange operator arises from the antisymmetry requirement on the total wavefunction and has no obvious physical meaning. From the forms of the Coulomb and exchange operators, it can be seen that the Fock operator $\hat{F}$ depends on its own eigenfunctions ψ_i. However, the ψ_i are not known initially and thus the n Hartree-Fock equations (Eq. (2.15)) must be solved by an iterative process by which the calculations are repeated until the results are self-consistent (i.e. until the no change results with further iteration). Because the (average) electric field of the molecular orbitals is used to iteratively determine the orbitals themselves, the Hartree-Fock method is considered to be a *self-consistent field* (SCF) method.

Until the 1950s, the Hartree-Fock MOs were evaluated numerically and were generally limited to atoms and small linear molecules because of computational difficulties. However, great advances were made in 1951 when Roothaan proposed [99] that the spatial orbitals ψ_i could be expanded as linear combinations of a set of N well behaved functions basis functions χ_s:

$$\psi_i=\sum_{s=1}^{N}c_{si}\chi_s \tag{2.19}$$

Substituting Eq. (2.19) into the Hartree-Fock equation (2.15) gives:

$$\sum_s c_{si}\hat{F}\chi_s = \varepsilon_i \sum_s c_{si}\chi_s \tag{2.20}$$

Multiplication by χ_r^* and integration gives a set of N equations (the *Hartree-Fock-Roothaan equations*) with unknowns c_{si}:

$$\sum_s c_{si}(F_{rs} - \varepsilon_i S_{rs}) = 0, \quad r = 1, \ldots, N \tag{2.21}$$

$$F_{rs} = \langle \chi_r | \hat{F} | \chi_s \rangle, \quad S_{rs} = \langle \chi_r | \chi_s \rangle \tag{2.22}$$

The non-trivial solution for the set of coefficients c_{si} requires that

$$\det | F_{rs} - \varepsilon_i S_{rs} | = 0 \tag{2.23}$$

This is known as the *Hartree-Fock secular equation.* Thus, Roothaan's procedure is very amenable to computer-based calculation because of it can be reduced to a common matrix algebra determinant problem.

The iterative procedure is started by an initial guess of the individual one-electron orbitals ψ_i and then the Fock operator is constructed according to Eqs. (2.16)-(2.18). The matrix elements, F_{rs} and S_{rs}, are then computed and used to find the set of orbital energies ε_i from the secular equation (Eq. (2.23)). The values of ε_i are used in turn to find the coefficients c_{si} from Eq. (2.21) which gives an improved approximation of the orbitals ψ_i. The procedure is then repeated using the improved orbitals until the improvement in total energy from one cycle to the next is smaller than a preset value, typically less than 10^{-5} hartrees.

The quality of the final Hartree-Fock result is very sensitive to the choice of basis functions χ_s. For molecules, the basis set commonly consists of functions resembling atomic orbitals centered on each of the nuclei of the molecule. This is known as the linear combination of atomic orbitals or *LCAO approximation.* The two main types of basis

functions used are *Slater-type orbitals* (STOs) and *Gaussian-type orbitals* (GTOs). In spherical polar coordinates, STOs are defined as

$$\chi_s \propto r^{n-1} e^{-\zeta r} Y_{lm}(\theta, \phi) \tag{2.24}$$

where n is a positive integer, l and m are angular momentum quantum numbers, $Y_{lm}(\theta, \phi)$ are the spherical harmonics, and ζ is the orbital exponent (ζ determines the diffuseness of the basis function). The main advantage of using Slater-type orbitals is that they have the proper short range (i.e. cusp at the nucleus) and long range (tail) behavior for calculation on atoms. This advantage is offset, however, by the fact that integrals involving STOs are often difficult to evaluate (particularly for the two-electron $r \neq s$ terms of the matrix elements F_{rs} and S_{rs}) and require more computing time than integrals involving GTOs.

Cartesian Gaussian-type orbitals are very popular for molecular calculations because of the ease of computing the integrals required. The Cartesian GTOs are defined by

$$\chi_s \propto x^k y^m z^n e^{-\zeta r^2} \tag{2.25}$$

where ζ is as above, and k,m,n are non-negative integers. Gaussian-type orbitals do not model wavefunction tails and cusps as well as STOs and thus, to make up for this deficiency, more Gaussian primitive functions are needed than STOs to model a wavefunction to the same level of accuracy. Like STOs, the exponents ζ for GTOs are chosen to minimize the Hartree-Fock energy of the atom. LCAOs of these basis functions are used to describe the molecular orbital wavefunctions with the coefficients optimized variationally. Because of the relatively large number of basis functions in a Gaussian-type calculation, it is usual to constrain groups of functions to have a fixed ratio of coefficients. The individual functions are called *primitives*, and the resultant linear combination is called a *contracted* Gaussian. An overview of basis sets and techniques has been given by Davidson and Feller [100].

It should also be noted that if the basis set were complete (i.e. $N=\infty$ in Eq. (2.19)), then it would be possible to express exactly any well-behaved function as an expansion of the basis

set. The resulting wavefunction and total energy from such a complete basis set would then be the best possible from the Hartree-Fock method and thus these are referred to as the *Hartree-Fock limit* wavefunction and total energy. In practical calculations, however, the number of basis functions used must be finite and the resulting Hartree-Fock energy is greater than the Hartree-Fock limit energy. Therefore, successive calculations with increasing basis set size and flexibility give energies that come increasingly closer to the Hartree-Fock limit energy. If the number of basis functions is very large, the basis set offers great flexibility and there is only a small change in the Hartree-Fock total energy upon the addition of further basis functions to the set. The resulting wavefunction and total energy (and other calculated properties) from such a large and flexible basis set are referred to as being *near-Hartree-Fock limit* quantities because they closely approach the Hartree-Fock limit quantities.

A brief description of the varying classes and features of basis sets is now considered. A *minimal basis set* (MBS) is one in which one basis function is included for each atomic orbital. If the calculation is Slater-type, each basis function consists of one Slater-type orbital. Thus, minimal basis sets are often described as *single zeta* basis sets because they are equivalent to using a single Slater function for each atomic orbital (i.e. a single ζ exponent - see Eq. (2.24)). For Gaussian-type calculations, however, the basis function may be a single primitive Gaussian or a linear combination (i.e. contraction) of primitives. For example, the STO-3G basis set [101] used in this thesis is a minimal basis set in which each basis function is a linear combination of three Gaussian functions. Because it is the smallest calculation possible, the minimal basis set is very limited in its flexibility and typically leads to an inaccurate quantitative description of molecular structure and properties.

The flexibility of the basis set can be increased by including more than one function per atomic orbital. A *double zeta* basis has two Slater functions with different exponents. An equivalent Gaussian basis would have to contain two contracted Gaussians per atomic orbital. A *split valence* basis set has different handling of the core and valence atomic orbitals. For example, the 4-31G basis [102] used in this thesis has one basis function or contracted

Gaussian representing each core atomic orbital and two for each valence orbital (the 4-31G basis set is thus said to be *single zeta* with respect to the core orbitals and *double zeta* with respect to the valence orbitals). Core orbitals contribute to the total energy but not very much to bonding, and thus split valence basis sets give results comparable to handling both core and valence in the same way. However, the main advantage of split-valence basis sets is decreased computation time. It should also be noted that the 4-31G basis set notation indicates that the single core contracted Gaussian function consists of four Gaussian primitive functions while the two valence contracted Gaussians consist of three and one primitives. In this thesis, the split-valence 6-311G basis set [103] of Pople and co-workers is used and it consists of a single zeta for the core (consisting of six primitives) and triple zeta modelling of the valence (three contracted Gaussians consisting of three, one and one primitives).

Polarization functions are often added to basis sets to provide a good description of polar charge distributions [98]. For example, a spherical charge distribution is given for the H atom by minimal basis and double zeta basis sets (i.e. only s-orbitals in these basis sets), but such a description is not realistic when hydrogen is bonded to an electronegative atom, such as in HF. The charge distribution can be polarized to one side of the H atom by the addition of a p-type function to the H basis set. Augmentation of the basis set with d and f functions can also be done to allow for polarization of charge. Basis sets augmented by the minimal set of polarization functions on all non-hydrogen (*heavy*) atoms are commonly identified by an asterisk (*) following the "G" in the basis set name. If p-type polarization functions are also added to the hydrogen atom basis, two asterisks are used (**). For example, the 6-311G* and 6-311G** basis sets [104] are formed by augmentation of the 6-311G basis set [103] with spherical d-type polarization functions on the heavy atoms (6-311G*) and a p-type polarization function on all H atoms (6-311G**).

In addition to polarization functions, *diffuse functions* (i.e. having small ζ exponents) are often added to basis sets [98]. The inclusion of such functions often allows a better modelling of the large-r (long range) charge density that is generally not described well by

GTOs. If the energy minimization criterion is used for convergence, these diffuse orbitals make very little contribution to the total energy. However, diffuse functions have been shown to be important in the calculation of properties such as electron affinities, proton affinities and valence orbital momentum profiles that are highly dependent upon the outermost regions of electron density and well as medium r and p properties such as dipole and quadrupole moments. The addition of diffuse functions to all heavy (i.e. non-hydrogen) atoms is designated by a single "+" preceding the "G" in the basis set name. The addition of diffuse functions to all atoms, including H, is designated by a double plus "++". For example, the commonly used 6-311+G and 6-311++G basis sets [105] include augmentation of the 6-311G basis set [103] with diffuse s- and p-type functions on the non-hydrogen atoms (6-311+G) and addition of a diffuse sp-shell on all hydrogen atoms (6-311++G).

Polarization and diffuse functions are often combined when added to the basis set. For example, the 6-311+G* and 6-311++G** basis sets are commonly used in calculations to include descriptions of both the diffuse and polarized charge density.

2.1.2 Hartree-Fock Theory for Open-Shell Molecules

For open-shell molecules, free radicals and triplet states there are unpaired electrons and the Hartree-Fock-Roothaan equations need modification. For doublet states, there will be one extra α electron, for triplet states, two extra α electrons, and so forth.

Simple molecular orbital theory can be extended to open-shell systems in two ways. The first is described as *restricted open-shell Hartree-Fock (ROHF) theory* [57,97,98,107]. In this approach, a single set of molecular orbitals is used, some being doubly occupied and some being singly occupied with an electron of α spin. This is the case illustrated for a five-electron doublet state in Fig. 2.1. The spin orbitals used in the single determinant are then $(\psi_1\alpha)(\psi_1\beta)(\psi_2\alpha)(\psi_2\beta)(\psi_3\alpha)$. The coefficients c_{si} are still defined by the expansion (2.19) and their optimum values are still obtained from the secular equation (2.23). However, details are more complicated since different conditions apply to singly- and doubly-

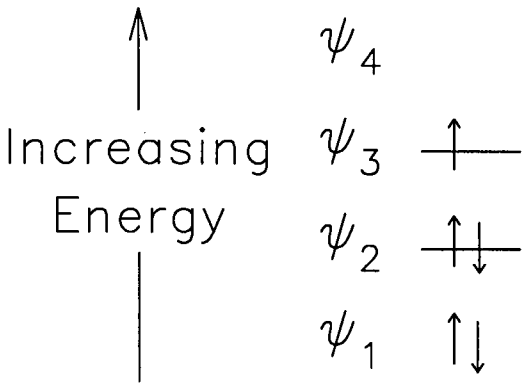

Fig. 2.1: Electron configuration diagram for $(\psi_1\alpha)(\psi_1\beta)(\psi_2\alpha)(\psi_2\beta)(\psi_3\alpha)$.

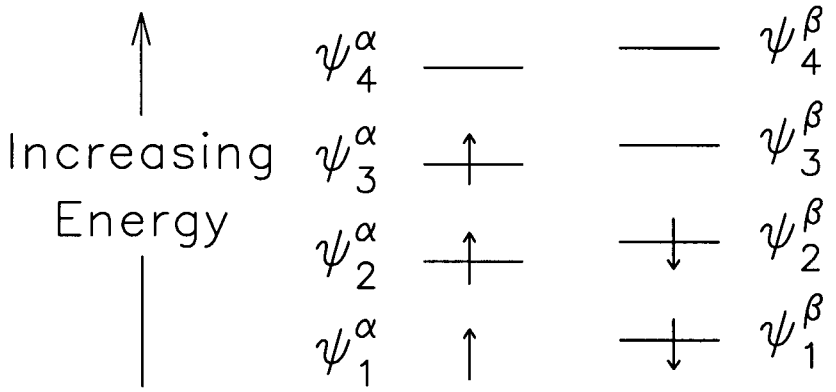

Fig. 2.2: Electron configuration diagram for $(\psi_1^\alpha\alpha)(\psi_1^\beta\beta)(\psi_2^\alpha\alpha)(\psi_2^\beta\beta)(\psi_3^\alpha\alpha)$.

occupied orbitals [57,97,98,106,107].

The second type of molecular orbital theory in common use for open-shell systems is *spin-unrestricted Hartree-Fock (UHF) theory* [57,97,98,108]. In this approach, different spatial orbitals are assigned to α and β electrons. Thus, there are two distinct sets of molecular orbitals ψ_i^α and ψ_i^β (i = 1, ..., N). The electron configuration for a five-electron doublet may be written as $(\psi_1^\alpha\alpha)(\psi_1^\beta\beta)(\psi_2^\alpha\alpha)(\psi_2^\beta\beta)(\psi_3^\alpha\alpha)$ and is illustrated in Fig. 2.2. It is important to note that the previously doubly-occupied orbital ψ_1 is now replaced by two distinct orbitals, ψ_1^α and ψ_1^β. Since the ROHF function is a special case of the UHF function, it follows from the variational principle that the optimized UHF energy must be below the optimized ROHF value. On the other hand, UHF functions have the disadvantage that they are not true eigenfunctions of the total spin operator $\hat{S}^2$ [57,97,98,108], unlike exact wavefunctions which are necessarily spin-pure. Thus, UHF wavefunctions which are designed for doublet states (as in the example shown in Fig. 2.2) are contaminated by functions corresponding to states of higher spin multiplicity, such as quartets.

In UHF theory, the two sets of molecular orbitals are defined by two sets of coefficients:

$$\psi_i^\alpha = \sum_{s=1}^{N} c_{si}^\alpha \chi_s \tag{2.26}$$

$$\psi_i^\beta = \sum_{s=1}^{N} c_{si}^\beta \chi_s \tag{2.27}$$

These coefficients are varied independently, leading to the following UHF generalizations of the Hartree-Fock-Roothaan equations [98,108]:

$$\sum_s c_{si}^\alpha (F_{rs}^\alpha - \varepsilon_i^\alpha S_{rs}) = 0, \quad r = 1, \ldots, N \tag{2.28}$$

$$\sum_s c_{si}^\beta (F_{rs}^\beta - \varepsilon_i^\beta S_{rs}) = 0, \quad r = 1, \ldots, N \tag{2.29}$$

For non-trivial solutions of the two sets of coefficients c_{si}^{α}, and c_{si}^{β}, the following secular equations for the α and β orbitals must be independently solved:

$$\det\left|F_{rs}^{\alpha}-\varepsilon_i^{\alpha}S_{rs}\right|=0 \tag{2.30}$$

$$\det\left|F_{rs}^{\beta}-\varepsilon_i^{\beta}S_{rs}\right|=0 \tag{2.31}$$

2.1.3 Configuration Interaction (CI)

A Hartree-Fock wavefunction takes into account the interactions between electrons only in an average way. For a more accurate model of electronic structure the instantaneous electron interactions must be included. Since electrons repel each other, they tend to keep out of each other's way. For example, if one electron in helium is close to the nucleus at one instant, then it is energetically favorable for the other be far away because of the repulsive electron-electron force. The motions of electrons are therefore correlated with each other. To fully describe this *electron correlation*, methods other than the Hartree-Fock treatment must be used. It should also be noted that the *correlation energy* is the difference between the exact non-relativistic energy E_{exact} and the Hartree-Fock limit energy E_{HF}:

$$E_{\text{corr}}=E_{\text{exact}}-E_{\text{HF}} \tag{2.32}$$

Although the Hartree-Fock limit energy differs from the exact energy usually by only a few percent [98], neglect of correlation often precludes the detailed and accurate description of many molecular properties. Therefore, the role of electron correlation is an important consideration since it may be a determining factor in predicting chemical phenomena [71].

One method that is used extensively to incorporate instantaneous electron correlation into the wavefunction is the *configuration interaction* (CI) approach. The CI calculation for an atom or molecule first involves choosing a basis set of one electron functions χ_s. The Hartree-Fock orbitals ψ_i are written as LCAOs of the basis set functions and the Hartree-Fock equations (2.23) are then solved for the linear combination coefficients c_{si}. The number of

resulting atomic or molecular orbitals equals N, the number of basis functions used. If the molecule has n electrons, $n/2$ of these orbitals will be *occupied orbitals* while the remaining N-$n/2$ orbitals will be unoccupied *virtual orbitals*. The Hartree-Fock wavefunction will be a determinant composed of spin orbitals formed from the occupied MOs. This Hartree-Fock ground state electron configuration is called the *reference function* or *reference state*. Using the set of occupied and virtual spin-orbitals, other electron configurations can be created that have different orbital occupancies. Some of the occupied orbitals are replaced with virtual orbitals corresponding to the excitation of one or more electrons to virtual orbitals. Each configuration has an associated many-electron function Ψ_i^{config} (a Slater determinant) called a *configuration function* or *configuration state function*. The configuration functions in a CI calculation are classified as *singly excited, doubly excited, triply excited, ...* , according to whether 1,2,3, ... , electrons are excited from occupied to unoccupied (virtual) orbitals. The total electronic CI wavefunction Ψ_{CI} is then written as a linear combination of the electron configurations:

$$\Psi_{\text{CI}} = \sum_{i=0} a_i \Psi_i^{\text{config}} \tag{2.33}$$

where $\Psi_0^{\text{config}} = \Psi_{\text{HF}}$ is the reference state function corresponding to the ground state HF configuration. In a very similar manner to that outlined for the Hartree-Fock method above, the matrix elements H_{ij} and S_{ij} are constructed from the n-electron Hamiltonian for the configurations i and j. The CI expansion coefficients a_i are then solved variationally to minimize the total energy using the following secular equation:

$$\det\left|H_{ij} - E_i S_{ij}\right| = 0 \tag{2.34}$$

The coefficient of the ground state configuration is usually much larger than any of the excited configurations.

It should be noted that the type and size of the basis set affects the final CI results greatly since the "quality" of the reference state HF wavefunction is determined by the basis

set. Therefore, it is useful to perform the CI calculations with a basis set which gives initial near-Hartree-Fock limit results for several properties (if the CI calculation for such as a large basis set is computationally viable).

The configuration coefficients a_i need not be the only variables in Eq. (2.33) and the molecular orbital coefficients c_{si} can be varied simultaneously with the a_i after the initial Hartree-Fock reference state is constructed. Such a procedure is obviously more computationally demanding.

A CI calculation which includes all the possible electron configurations possible for a given basis set in the CI expansion (Eq. (2.33)) is referred to as a *full CI* calculation. However, full CI calculations are only possible for small molecules and small basis sets because of the large number of configurations involved. Even with a modest-size basis set, the number of possible configurations for most molecules is extremely large and therefore it is not computationally feasible to include them all. Thus, a *limited CI* procedure is usually chosen in which only selected configurations from the total possible configurations are used. In addition, it is not generally necessary to include all of the possible configurations to obtain "good" total energies and other properties. Selecting the important configurations (i.e. those which have the largest coefficients and contributions to the total energy) is a difficult procedure that requires considerable experience. Because of these considerations, sufficiently accurate CI calculations even for systems with only more than a few electrons are extremely challenging and are not feasible for larger molecules. It should also be noted that in the CI expansion given by Eq. (2.33) one includes only configuration functions that have the same symmetry properties as the state being approximated (usually the molecular ground state). For example, the ground state of H_2 is a $^1\Sigma_g^+$ state, and thus a CI calculation of the H_2 ground state would include only configurations with this symmetry.

One common way to decrease the size of CI calculations is to use the *frozen-core approximation* in which only excitations out of the valence orbitals are used. Excitations out of the inner-shell core MOs are not included in Eq. (2.33). The contributions to the total

correlation energy due to inner-shell electrons are not particularly small, but appear to be relatively constant from one molecular environment to another.

The procedure outlined above is referred to as *single reference CI*, since only the Hartree-Fock ground reference state is used to derive the configurations. However, if several configurations contribute strongly to the total wavefunction then the single reference technique is not very efficient and a *multireference configuration interaction* (MR-CI) calculation provides better results. An MR-CI calculation is usually performed in two (or more) stages. First, a CI calculation is performed as described above. The most important configurations are then each used as reference states (i.e. multiple reference states are used) to generate further configurations and the coefficients computed again. The choice of which configurations to include in the second stage (or any further stages) is generally made depending on the coefficient of the configuration in the expansion and its contribution to the total energy. The CI calculations presented in this thesis (performed by Prof. E.R. Davidson and co-workers at Indiana University) involve multiple reference states as described above. In particular, an initial singles and doubles excitation CI calculation was done to produce reference configurations. A second CI calculation was then performed in which all singles and doubles excitations from the multiple reference configurations were included. This type of MR-CI calculation is therefore known as *multireference singly and doubly excited configuration interaction* (MRSD-CI) because of its use of one- and two-electron excitations. Because of the two steps in the calculation, the final MRSD-CI wavefunction will include some triple and quadruple excitations.

2.1.4 Density Functional Theory

The DFT method, its underlying assumptions and its computational implementation are introduced in this section. In addition, it will be shown that implementation of density functional theory is very similar to that of the conventional Hartree-Fock method.

In 1964, Hohenberg and Kohn [109] showed that the total energy (and other properties) of a system of n interacting electrons can be expressed as a *functional* of the electron density $\rho(\boldsymbol{r})$. While the Hohenberg-Kohn theorem proved that it was possible in principle to calculate the ground state molecular properties from $\rho(\boldsymbol{r})$, it did not provide explain *how* such calculations could be done. Kohn and Sham [110] gave the first steps to making DFT computationally viable when they considered a fictitious system of n non-interacting electrons having a total density equal to the true electron density of the system of interest. Kohn and Sham showed that the total ground state electronic energy of such a system with ground state electron probability density $\rho(\boldsymbol{r})$ is given by:

$$E[\rho]=T_s[\rho]+J[\rho]+\int \rho(\boldsymbol{r})v(\boldsymbol{r})d(\boldsymbol{r})+E_{xc}[\rho] \tag{2.35}$$

where $T_s[\rho]$ is the kinetic energy, $J[\rho]$ is the classical Coulomb repulsion energy and $\int \rho(\boldsymbol{r})v(\boldsymbol{r})d(\boldsymbol{r})$ is the potential energy from any external fields $v(\boldsymbol{r})$ present (usually just the field of the nuclei in the electron-nuclear attraction). The first three terms in Eq. (2.35) have similar terms in Eq. (2.11) for the Hartree-Fock total energy. The term $E_{xc}[\rho]$ is known as the exchange-correlation functional and it includes the exchange energy and all contributions to $E[\rho]$ due to correlated electronic motion. The principal difference between the density functional energy and the Hartree-Fock energy arises from this term. Eq. (2.35) would simply be an alternative expression for the Hartree-Fock energy if $E_{xc}[\rho]$ is replaced by the Hartree-Fock exchange energy K_{ij} in Eq. (2.14). Kohn and Sham also imposed the constraint that the density must integrate to the number of electrons in the system:

$$\rho(\boldsymbol{r})=\sum_{i=1}^{n}\left|\psi_i^{KS}(\boldsymbol{r})\right|^2 \tag{2.36}$$

The *Kohn-Sham orbitals* ψ_i^{KS} are found from the following *Kohn-Sham equations*, which are derived by minimization of the energy $E[\rho]$ in Eq. (2.35) subject to the constraint in Eq. (2.36):

$$\hat{F}_{KS}(1)\psi_i^{KS}=\varepsilon_i\psi_i^{KS} \tag{2.37}$$

It should be noted that Eq. (2.37) is very similar to the Hartree-Fock equations in Eq. (2.15). The Kohn-Sham operator $\hat{F}_{KS}$ is also similar to the Fock operator in Eq. (2.16) and is given by:

$$\hat{F}_{KS}(1) = -\frac{1}{2}\nabla_1^2 - \sum_A \frac{Z_A}{r_{1A}} + \sum_{j=1}^{n} 2\hat{J}_j(1) + V_{xc}(1) \tag{2.38}$$

The Coulomb repulsion operator $\hat{J}_j(1)$ has exactly the same form as the corresponding Hartree-Fock operator in Eq. (2.17), except that $\psi_j(2)$ is the Kohn-Sham orbital $\psi_j^{KS}(2)$. The only difference between the KS equations and the HF equations is that the HF exchange operator $\hat{K}_j(1)$ is replaced by the *exchange-correlation potential* $V_{xc}(1)$. The name of $V_{xc}(1)$ is therefore derived from the fact that it handles the effects of both exchange (antisymmetry) and electron correlation similar to the HF exchange operator. $V_{xc}(1)$ is formally defined as the functional derivative of the exchange-correlation energy:

$$V_{xc} = \frac{\delta E_{xc}[\rho]}{\delta \rho} \tag{2.39}$$

How a functional derivative is computed is described in [111] but such detail it is not necessary in this thesis. The solution of the KS equations is also similar to that for the HF equations. The KS operator is first constructed and the equations solved for the ψ_i^{KS}, then a new KS operator is constructed and the process repeated (an iterative solution is necessary because the KS operator depends on its solutions) until the results are self-consistent. In a manner similar to Eqs. (2.19)-(2.23), the Kohn-Sham orbitals may be expressed as a linear combination of a basis set and the coefficients solved for variationally.

The important fact that should be noted from (2.39) is that V_{xc} is known exactly only if the form of E_{xc} is known exactly. If V_{xc} is known, then the Kohn-Sham equations can be solved for the KS orbitals ψ_i^{KS} and therefore for the density ρ and energy $E[\rho]$. The major complication of Kohn-Sham DFT therefore arises from the fact that the exact functional E_{xc} is not known for molecules. In practical calculations, approximations must be made and a functional form for E_{xc} (and hence V_{xc}) must be chosen before any calculations may be

performed. Many approximate functionals have been devised in DFT. These are usually constructed by choosing an analytical form for E_{xc} and then comparing the properties from DFT calculations with this approximate functional to experimental values. Unfortunately, such a procedure is not systematic and a suitable form for E_{xc} is not always clear. Some of the common choices for the exchange-correlation potential are described below. These may generally be divided into two classes: *local* and *non-local functionals*.

Local functionals employ the *local density approximation* (LDA) in which the exchange-correlation energy is approximated as [109,110]:

$$E_{xc}^{LDA}[\rho]=\int \rho(\mathbf{r})\varepsilon_{xc}[\rho(\mathbf{r})]\mathbf{dr} \tag{2.40}$$

where $\varepsilon_{xc}[\rho(\mathbf{r})]$ is the exchange-correlation energy per electron in a homogeneous electron gas with electron density ρ. The LDA therefore assumes that ρ varies slowly with position and is often very accurate for metallic and strongly delocalized systems with fairly constant electron density. However, the electron density in a molecule varies rapidly in a molecule (because the positive charge is located only at the nuclei instead of being uniformly distributed) and therefore this approximation can be expected to be less accurate for such a system. Despite these shortcomings for molecules, LDAs are commonly used in the DFT literature because of their ease of computation. For example, in the LDA a single point in space is used to calculate the exchange-correlation energy and potential whereas non-local density approximations (described below) are more complex because they use a region of space instead of just a single point in the calculation. In addition, for computational purposes it is often convenient to represent the results for ε_{xc} and V_{xc} in an analytic form. The LDA used in this thesis is that of Vosko, Wilk and Nusair (VWN) [112] which is commonly found in the DFT literature. The VWN functional [112] was obtained by combining the homogeneous electron gas correlation energy from Ceperly and Alder [113] with the exchange energy for such an electron gas from Dirac [114]. Vosko et al. [112] chose their analytical form for the correlation energy functional by performing a Padé fit on the results of Ceperly and Alder [113]. This form was chosen

because the derivative is easily obtained and thus the correlation potential is easily determined (similar to Eq. (2.39), the correlation potential is the functional derivative of the correlation energy). This method is of separating the exchange-correlation energy into two separate terms is commonly used and the resulting total potential is therefore also the sum of two parts:

$$V_{xc} = V_x + V_c \tag{2.41}$$

The VWN functional includes some accounting for correlation and thus is an improvement over older DFT methods that neglected correlation (e.g. the *Xα method* [110] uses the same V_x as the VWN method, but V_c is neglected). However, the correlation energies in such LDA approximations are still often overestimated by as much as 100% [115] while the exchange energy is sometimes underestimated by 10% [116]. Because the molecular geometries are unaffected by these errors, many molecular properties are still well described by LDA functionals. However, these errors in the correlation and exchange energies produce dissociation energies that are almost always too high (often by a few eV). This overbinding of molecules is due to the incorrect asymptotic form of the VWN exchange potential. The exchange potential V_x falls off too rapidly at large r so that an electron in the large r region feels the full Coulomb potential. The outermost regions of the electron density distribution are therefore too diffuse.

Non-local functionals have been developed as a solution to the problems of overbinding and incorrect asymptotic exchange from LDA functionals. The usual results involve the addition of gradient corrections to the potential (i.e. derivatives of the charge density are added to the potential similar to a Taylor series expansion). The potential is referred to as non-local because it reflects the charge density about a region of space (due to the derivative terms) instead of just the charge density at one point in space. The non-local exchange potential used in this thesis is the gradient-corrected exchange functional of Becke [116]. Becke ensured that the exchange energy E_x showed the correct asymptotic behaviour at large r by adding gradient corrections. However, it should be noted that the exchange *potential* which arises from the

functional derivative of Becke's exchange energy does not necessarily have such correct behaviour at large r. The two non-local correlation potentials used in this thesis are those of Perdew and Wang [115,117,118] and Lee, Yang and Parr [119]. Similar to the work of Becke, Perdew's correlation potential [115,117,118] uses coefficients for the gradient expression that are derived from least square fits.

Hybrid non-local functionals have recently been proposed which include a mixture of Hartree-Fock exchange with DFT exchange-correlation. One hybrid method (B3LYP) employed in this thesis is Becke's three parameter functional [120] using the correlation functional of Lee, Yang and Parr [119]. This is generally the most commonly used hybrid functional in the DFT literature. Another hybrid functional used in this thesis (B3PW91) also consists of Becke's three parameter functional [120], but the correlation functional of Lee, Yang and Parr [119] is replaced by that of Perdew and Wang [118].

Even after a choice is made for the exchange and correlation potentials, there are still some approximations that often arise in the computational evaluation of the potentials. In particular, the evaluation of the functional forms of the exchange and correlation potentials involves integrals with fractional powers of the electron density [121]. One density functional program used to obtain the results presented in this thesis (the deMon [122,123] program) uses numerical approximations to facilitate the evaluation of such integrals. First, the deMon program evaluates the exchange and correlation potential at a series of points about the molecule called a *grid*. A secondary basis set called an *auxiliary basis set* is then used to fit the calculated potential via a least squares fit. The deMon program auxiliary basis sets used consist of Gaussian primitives and are described by the $(j,k;m,n)$ notation, where j and k are the number of s-type and sets of s-, p-, d-type GTOs for the charge density fit, and m and n are the sizes of similar basis sets for the fit of the exchange-correlation potential. Each set of s-, p-, and d-type GTOs in the auxiliary deMon basis set has a common exponent for all l values. The fit to the potential converts the exchange and correlation potential to a simple sum of Gaussian functions that can be integrated more easily. Because the calculation of the Coulomb potential

can also be difficult, the charge density is also fitted with the set of auxiliary functions to hasten integral evaluation. However, it should be stressed that the fit quality and precision of calculated properties (e.g. total energy) are highly dependent upon the choices of the grid and auxiliary basis sets. As a general guide, larger auxiliary or orbital basis sets and finer grids will provide more accurate results [121]. It should be noted that for the other programs employed to obtain density functional results in this thesis (the Gaussian 92 [124] and Gaussian 94 [125] programs) the least squares fit to the calculated potential is simply replaced by calculating a much finer grid.

2.2 The Interpretation and Calculation of the EMS Cross-Section

2.2.1 The Binary Encounter and Impulse Approximations

The (e, 2e) reaction has been described in Section 1.1.1 and a schematic of the symmetric non-coplanar (e, 2e) geometry most commonly used in EMS experiments is shown in Fig. 1.1. If conservation of energy is applied to the reaction, then the following equation results:

$$E_0 = E_1 + E_2 + \varepsilon \tag{2.42}$$

where ε is the energy transferred to the target molecule. It should be noted that the ion recoil energy E_{recoil} (the kinetic energy transfer to the molecule) is extremely small and therefore it has been neglected in Eq. (2.42). The quantity ε is the binding (ionization) energy corresponding to formation of the final ion state *f*. However, the ion recoil momentum $\boldsymbol{q}$ cannot be neglected and it is related (by conservation of momentum) to the momenta of the electrons by:

$$\boldsymbol{q} = \boldsymbol{p}_0 - \boldsymbol{p}_1 - \boldsymbol{p}_2 \tag{2.43}$$

The *binary encounter* [12,126] and *impulse approximations* [12,127] are used to simplify the interpretation of the (e, 2e) reaction. Under these conditions, the ionization event is well described by a two-body electron collision (i.e. the ion resulting from the collision can

be considered to be a spectator to the (e, 2e) collision) and the incident electron can be said to knock out the target electron in an essentially clean manner. In order to provide the necessary conditions for the binary encounter approximation and impulse approximations to be valid, the momentum transfer $\boldsymbol{K}=\boldsymbol{p}_0-\boldsymbol{p}_1$ from the incident electron to the target M is maximized in EMS by the choice of high impact energy E_0 and the symmetric non-coplanar scattering geometry [12,33] (Fig. 1.1). The value of E_0 is chosen to be very large in comparison with the ionization energy of the orbital being studied (E_0 is typically 1200 eV + ε and ε is usually in the range 5-60 eV). In addition, the energies of the outgoing electrons and their corresponding polar angles are selected to be equal (i.e. $E_1 = E_2 = 600$ eV and $\theta_1 = \theta_2 = \theta = 45°$ so that the kinematics are "symmetric"). The kinematics are referred to as non-coplanar because the out-of-plane azimuthal angle ϕ is allowed to vary (in most EMS experiments, ϕ is typically varied over the range of ±30°). It should also be noted that the symmetric non-coplanar kinematics is chosen because experimental results obtained with this geometry is essentially independent of kinematic factors (see Section 2.2.3).

Within the binary encounter and impulse approximations, the ion recoil momentum is equal in magnitude and opposite in sign to the momentum $\boldsymbol{p}$ of the struck electron immediately prior to the collision (i.e. its momentum while still bound to the target M):

$$\begin{aligned}\boldsymbol{p} &= -\boldsymbol{q} \\ &= \boldsymbol{p}_1 + \boldsymbol{p}_2 - \boldsymbol{p}_0\end{aligned} \tag{2.44}$$

In this type of collision (binary encounter, high momentum transfer, symmetric non-coplanar), the momentum p of the ejected electron prior to knock-out is related to the out-of-plane azimuthal angle ϕ as follows [12,33]:

$$p = \left[(2p_1\cos\theta - p_0)^2 + (2p_1\sin\theta\sin(\phi/2))^2\right]^{1/2} \tag{2.45}$$

where $p_1 = \sqrt{2E_1}$ and $p_0 = \sqrt{2E_0}$ in atomic units. It can be seen from Eq. (2.45) that two general types of information can be measured for electrons by EMS. First, scanning the impact energy of the incoming electron (and hence p_0 in Eq. (2.45)) allows the binding energy

spectrum (BES) of the target molecule to be obtained. Second, scanning the azimuthal angle ϕ over a range while keeping the impact energy at a constant value corresponding to the binding energy of interest allows a measurement of the EMS cross-section as a function of momentum (ϕ is easily transformed to p by use of Eq. (2.45)). The measured distribution of cross-section as a function of momentum is known as the experimental momentum profile (XMP).

2.2.2 The EMS Scattering Cross-Section

The (e, 2e) cross-section, σ_{EMS}, is given in atomic units by [12]:

$$\sigma_{\mathrm{EMS}} = (2\pi)^4 \frac{p_1 p_2}{p_0} \sum_{\mathrm{ave}} |T_f|^2 \tag{2.46}$$

where T_f is called the scattering amplitude (i.e. the reaction amplitude for ionization to final ion state *f*) and is given by:

$$T_f = \left\langle \chi^{(-)}(\boldsymbol{p}_1)\chi^{(-)}(\boldsymbol{p}_2)\Psi_f^{N-1} \middle| T(E) \middle| \Psi_i^N \chi^{(+)}(\boldsymbol{p}_0) \right\rangle \tag{2.47}$$

where $\chi^{(-)}(\boldsymbol{p}_1)$, $\chi^{(-)}(\boldsymbol{p}_2)$ and $\chi^{(+)}(\boldsymbol{p}_0)$ represent the wavefunctions for the outgoing (-) and incoming (+) electrons, $T(E)$ is the transition operator for the (e, 2e) process, and Ψ_f^{N-1} and Ψ_i^N are the total wavefunctions for the final ion state and the initial target ground state, respectively. The quantity $|T_f|^2$ in Eq. (2.46) is therefore the probability of a transition from the initial state prior to collision to the final ion state. Within the binary encounter and impulse approximations (see Section 2.2.1 above) the operator T_f depends only on the coordinates of the incident and target electrons so that Eq. (2.46) becomes [12]:

$$\sigma_{\mathrm{EMS}} = (2\pi)^4 \frac{p_1 p_2}{p_0} \sum_{\mathrm{ave}} \left| \left\langle \chi^{(-)}(\boldsymbol{p}_1)\chi^{(-)}(\boldsymbol{p}_2) \middle| T(E) \middle| \left\langle \Psi_f^{N-1} \middle| \Psi_i^N \right\rangle \chi^{(+)}(\boldsymbol{p}_0) \right\rangle \right|^2 \tag{2.48}$$

The Σ_{ave} in Eq. (2.48) represents a sum over final ion state degeneracies and an average over initial state degeneracies (i.e. a sum over vibrational, rotational and electronic states). However, rotational and vibrational effects are too small to be observed experimentally

because of the relatively broad instrumental energy resolution (see Chapter 3). Using the Born-Oppenheimer approximation, the ion and target wavefunctions Ψ_f^{N-1} and Ψ_i^N can be expressed as the product of electronic, vibrational and rotational wavefunctions and the sums over final vibrational and rotational states can be eliminated from Eq. (2.46) via a closure relation [12]. In addition, the EMS reaction is typically done in the gas phase so that a spherical average given by $(4\pi)^{-1}\int d\Omega$ is included in the EMS cross-section to account for the random orientation of the gaseous target molecules. Vibrational effects are commonly approximated by evaluating the cross-section at the molecular equilibrium geometry of the target molecule [12] (a study by Leung et al. [128] has shown this to be a reasonable approximation for calculating the valence shell momentum profiles for the water molecule). The average over initial electronic state effects is generally approximated by evaluation of the cross-section in the initial ground electronic state. The sum over degenerate final electronic states taken into account by assuming that all of the degenerate final ion states give the same σ_{EMS} and therefore the sum can be replaced by a factor g_f equal to the degeneracy of the final ion state. Taking all of these considerations into account, the EMS-cross-section is given by:

$$\sigma_{EMS} = 4\pi^3 \frac{p_1 p_2}{p_0} g_f \int \left| \left\langle \chi^{(-)}(\boldsymbol{p}_1)\chi^{(-)}(\boldsymbol{p}_2) \middle| T(E) \middle| \Psi_f^{N-1} \middle| \Psi_i^N \right\rangle \chi^{(+)}(\boldsymbol{p}_0) \right\rangle \Big|^2 d\Omega \qquad (2.49)$$

where Ψ_f^{N-1} and Ψ_i^N are now the total ion and neutral electronic wavefunctions , respectively.

2.2.3 The Distorted Wave Impulse Approximation

In the distorted wave impulse approximation (DWIA), the wavefunctions $\chi^{(-)}(\boldsymbol{p}_1)$, $\chi^{(-)}(\boldsymbol{p}_2)$ and $\chi^{(+)}(\boldsymbol{p}_0)$ of the incident and outgoing electrons are represented by distorted waves and the EMS cross-section in Eq. (2.49) becomes [12]:

$$\sigma_{EMS} = 4\pi^3 \frac{p_1 p_2}{p_0} \sigma_{Mott} g_f \int \left| \left\langle \chi^{(-)}(\boldsymbol{p}_1)\chi^{(-)}(\boldsymbol{p}_2) \middle| \Psi_f^{N-1} \middle| \Psi_i^N \right\rangle \chi^{(+)}(\boldsymbol{p}_0) \right\rangle \Big|^2 d\Omega \qquad (2.50)$$

where σ_{Mott} is the Mott scattering cross-section for electron-electron collisions. An explicit form for the Mott scattering cross-section in the symmetric non-coplanar geometry is given in Ref. [12]. This cross-section has been shown to be effectively constant [129] for the symmetric non-coplanar geometry with the electron angles and valence binding energies commonly used in EMS. For example, at $\theta = 45°$ and $E_0 = 1215.6$ eV in the symmetric non-coplanar geometry, the variation of σ_{Mott} over the range of azimuthal angle $\phi = \pm 30°$ is small (< 2%) and effectively negligible [129]. In addition, although greater differences (~13%) result in σ_{Mott} if the impact energy is varied by 50 eV [49], the impact energy dependence of the Mott scattering factor is usually neglected (such a choice has been made in this thesis). Therefore, the EMS cross-section can be considered to be proportional to the electronic structure factor given by the integral in Eq. (2.50).

The main advantage of the DWIA cross-section is that the distorted waves in Eq. (2.50) allow for the perturbation (distortion) of the incoming and outgoing electron waves by the target and the ion. In EMS studies of the p and s type valence orbitals of atoms at E_0 ~ 1200 eV, distortion effects have been found to be significant at higher momenta ($p \geq 1.5$ au) and the DWIA has been found to give an excellent description of the EMS cross-section for atoms up to p ~ 3 au [12,33]. In addition, in agreement with the physical argument that the electron waves should be influenced less by the target and ion as their energy increases, such distortion effects have been shown to decrease as the impact energy and outgoing electron energies are increased [12].

Although the DWIA model is physically reasonable, the calculation of the transition amplitude using this equation is often prohibitively difficult . Only spherical potentials are feasible in calculations and thus DWIA calculations have only been done for atomic targets of spherical symmetry such as the noble gases [36,130,131], the Cd atom [132] and the Cr, Mo and Ti atoms studied in this thesis (see Chapter 7). DWIA calculations have thus far been found to be intractable for molecules.

2.2.4 The Plane Wave Impulse Approximation

Due to the limitations in calculating the distorted wave cross-section for molecules, the plane wave impulse approximation (PWIA) must be used to provide a description of the EMS cross-section. In the PWIA, the incident and outgoing electrons are assumed to have sufficiently high energies such that they may be represented by plane waves ($\chi = e^{i\boldsymbol{p}\cdot\boldsymbol{r}}$). Therefore, it is assumed that the electron waves are not distorted by the molecular potential. With the use of plane waves and the binary encounter approximation (and hence the impulse approximation), the EMS cross-section is [12]:

$$\sigma_{\mathrm{EMS}} = 4\pi^3 \frac{p_1 p_2}{p_0} \sigma_{\mathrm{Mott}} g_f \int \left| \left\langle \boldsymbol{p}\Psi_f^{N-1} \middle| \Psi_i^N \right\rangle \right|^2 d\Omega \tag{2.51}$$

where $\boldsymbol{p}$ represents the plane-wave target electron with momentum given by Eq. (2.45). Similar to Eq. (2.50) for the DWIA, the Mott scattering cross-section in Eq. (2.51) is effectively constant for the electron angles and energies used in the present work. Thus, the cross-section observed in an EMS experiment is essentially directly proportional to $\int \left| \left\langle \boldsymbol{p}\Psi_f^{N-1} \middle| \Psi_i^N \right\rangle \right|^2 d\Omega$, the spherically averaged square of the overlap of the final ion and initial target electronic wavefunctions. It should also be noted that the ion-neutral overlap is in momentum (p) space.

In the PWIA model, the collision is viewed effectively as a binary encounter between two hard spheres (i.e. like the collision of two billiard balls). It is assumed that the ejected electron does not feel the potential due to the target or the effect of the incoming electron until it is knocked out. Similarly, the incoming electron does not feel the target potential or the effects of the other electron until the collision takes place. Collision events are also reasonably treated as instantaneous so that geometry changes within the neutral target molecule and the resulting ion are assumed to be negligible during the collision time. Although it may initially appear that these approximations are so restrictive and that they might limit the quality of the results from the PWIA model, extensive EMS studies over more than 20 years have shown [12]

the PWIA model to be generally adequate for describing the shapes of orbital momentum profiles at values of $p \leq 1.5$ au. If the energies of the incoming and outgoing electrons are kept sufficiently high (> 1000 eV) so that the momentum transfer is large (this is the case for the symmetric non-coplanar geometry with E_0 = 1200 eV + binding energy and $E_1 = E_2$ = 600 eV that is typically used in EMS studies and in this thesis), the PWIA has been shown to be an effective and reliable model for the interpretation of EMS cross-section [11,12,37-40]. However, it should be noted that the PWIA begins to break down for target electron momenta (ion recoil momenta) above approximately 1.5 au. Beyond this value of momenta, distortion effects tend to result in greater experimental cross-section than that predicted with the PWIA and therefore momentum profiles calculated with the DWIA provide generally better agreement with experiment in this region (although DWIA calculations are only feasible for atomic systems at this time).

The interpretation of the EMS cross-section given by Eq. (2.51) relates to calculated wavefunctions from theory in the following manner. In theoretical quantum chemistry, the overlap of final ion and initial target electronic wavefunctions is often referred to as a Dyson orbital Φ_f [60,62]. Dyson orbitals may be obtained directly as solutions of Dyson's quasiparticle equation, or indirectly by calculating the N and (N-1) electron wavefunctions (e.g. by CI or many-body perturbation theory (MBPT)) and then computing the overlap. The Dyson orbitals are also normalized such that:

$$\Phi_f(\boldsymbol{p}) = \frac{1}{S_f}\left\langle \boldsymbol{p}\Psi_f^{N-1} \middle| \Psi_i^N \right\rangle \tag{2.52}$$

where S_f is the normalization factor [60,62]. Therefore, the EMS cross-section simplifies to:

$$\sigma_{\mathrm{EMS}} \propto g_f S_f^2 \int \left|\Phi_f(\boldsymbol{p})\right|^2 d\Omega \tag{2.53}$$

The S_f^2 factor in Eq. (2.53) is known as the spectroscopic factor or pole strength of the ionization and is given by:

$$S_f^2 = \sum_j S_j^f \tag{2.54}$$

and the quantity S_j^f is the square of the overlap between Ψ_f, the ion wavefunction, and $\Psi_i^{(j)}$, the target wavefunction with a hole in orbital ψ_j:

$$S_j^f = \left| \left\langle \Psi_f \middle| \Psi_i^{(j)} \right\rangle \right|^2 \tag{2.55}$$

Therefore, S_j^f is the probability of finding the $(\psi_j)^{-1}$one-hole configuration in the final ion state *f*. For the case of a many-body wavefunction, removal of one electron from the system always results in more than one "hole" (i.e. a range of hole states) and thus the total probability S_f^2 is the sum of all the individual S_j^f (Eq. (2.54)). Each hole left by an electron that has been removed is described as having been "split up" into poles, each of which has a different binding energy. It should also be noted that the S_j^f for ionization of the j^{th} electron obey the spectroscopic sum rule:

$$\sum_f S_j^f = 1 \tag{2.56}$$

where the sum is over all final states *f*. Therefore, for each electron ionized, the removal of one electron always results in the creation of one complete hole, even if the hole is fragmented. The Dyson orbital and eigenvalue with the largest spectroscopic factor for any hole associated with the removal of a certain electron is generally referred to as the main pole, while all others are usually referred to as "satellites" because of their lower spectroscopic factor (lower probability) and because they are often found close in energy to the parent peak.

A theoretical momentum profile evaluated using the quantity $\int \left| \Phi_f(\boldsymbol{p}) \right|^2 d\Omega$ in Eq. (2.53) is often referred to as the ion-neutral overlap distribution (OVD). As discussed above, computation of the OVD with many-body calculations (such as the configuration interaction treatments described in Section 2.1.3) for the neutral and ion wavefunctions can be used to assess the effects of electron correlation and electronic relaxation effects in the measured cross-section [11,12,37-40]. However, it should be noted that instrumental

momentum (angle) resolution effects (discussed below) must first be incorporated into the OVD before it can be compared to the experimental momentum profile.

2.2.5 The Target Hartree-Fock Approximation

Calculating the full OVD in Eq. (2.53) is often highly computationally intensive. A simpler alternative to calculating the full OVD is to modify Eq. (2.53) using the target Hartree-Fock approximation (THFA). The THFA [12] assumes that electron correlation effects are negligible in the initial state (i.e. neutral ground state molecule) and thus the many-body wavefunction Ψ_i^N can be replaced by the single determinant Hartree-Fock wavefunction Ψ_{HF} of canonical HF molecular orbitals. Within this model, the many-body ion wavefunction Ψ_f^{N-1} is also represented as a linear combination of independent particle determinants of ground state target HF orbitals. In addition, it is assumed that, for a given ion state manifold *f*, only one of the S_j^f is appreciably different from zero. If the one significant S_j^f is the one given by $j = j(f)$, then the expression for the EMS cross-section is given by:

$$\sigma_{\mathrm{EMS}} \propto g_f S_j^f \int \left|\psi_j(\boldsymbol{p})\right|^2 d\Omega \tag{2.57}$$

where $\psi_j(\boldsymbol{p})$ is the momentum space canonical Hartree-Fock orbital *j* from which the electron is ionized (the Fourier transform of the more familiar one-electron position space orbital wavefunction $\psi_j(\boldsymbol{r})$). It should also be noted that the spectroscopic factor (pole strength of ionization) has been reduced to S_j^f in Eq. (2.57), which is the probability of finding the $(\psi_j)^{-1}$ one-hole configuration in the final ion state *f*.

The integral in Eq. (2.57) is known as the spherically averaged one-electron momentum distribution (MD) and thus, within the PWIA and THFA approximations, electron momentum spectroscopy provides imaging of the canonical Hartree-Fock orbital electron density in momentum space. Therefore, within the THFA, the EMS cross-section is an initial state property and is independent of the final state of the ion. Theoretical calculations of the EMS cross-section are thus simplified because only one calculation (of the electronic structure of the

neutral molecule) need be done for comparison to experiment. In should also be noted that, within the THFA as described by Eq. (2.57), all momentum profiles within the ionization manifold from the same target orbital j will have the same shape, regardless of the final state f. Therefore, the assignment and interpretation of satellite structure in the EMS binding energy is greatly simplified. The relative intensities of the ionization peaks within a manifold are given by the spectroscopic factors S_j^f. In addition, the spectroscopic sum rule in Eq. (2.56) implies that by summing all the observed intensity of each final ion state manifold, all the orbitals in a molecule can be normalized to a common relative intensity scale, with appropriate allowances for degeneracies. A further approximation is that, if final state correlation is negligible, then S_j^f will be unity for primary hole ion states and zero for all other states (this is equivalent to the frozen orbital or Koopmans approximation). This is often a reasonable model for outer valence orbital ionizations which have been found in previous EMS studies [12] to have pole strengths near unity (i.e. only a single ionization peak typically arises from each outer valence orbital). However, ionization from inner valence orbitals has been observed to often produce a multitude (or manifold) of "satellite" ionization peaks due to the substantial electron correlation effects in these processes. Therefore, inner valence XMPs from the same ionization manifold are more likely to differ in their individual shapes than those from outer valence orbitals. In addition, theoretical momentum profiles calculated within the THFA may have more noticeable shape discrepancies with inner valence XMPs because of these final ion state correlation effects.

2.2.6 The Target Kohn-Sham Approximation

Dyson orbitals obtained from configuration interaction calculations according to Eq. (2.53) above have been shown to provide highly accurate predictions of the EMS cross-section [11,12,37-40]. In particular, in those cases where distortion effects are negligible and correlation effects are necessary to model the experimental cross-section, the Dyson orbital within the PWIA has often provided the most accurate theoretical interpretation of the

experimental momentum profile [11,12,37-40]. However, such CI calculations are often demanding and scale at least as N^5, where N is the basis set size. Therefore, CI calculations for EMS studies (via Eq. (2.53)) are often limited to small molecules. The target Hartree-Fock approximation (Section 2.2.5) is an alternative calculation that scales as ~ N^4, although the quality of the resulting momentum profile is generally lower than that obtained from CI. While the THFA allows calculations for somewhat larger molecules than are possible with the CI overlap, THFA calculations still rapidly become computationally difficult for many large molecules that are of interest in EMS. The desired results for larger molecules are instead much more feasible with Kohn-Sham DFT because such calculations scale approximately as ~ N^3. In addition, despite the lowered computational complexity, the properties predicted by Kohn-Sham DFT are generally comparable to or better than Hartree-Fock [60,111,133,134] since some accounting of electron correlation effects in the target ground state is included in DFT via the exchange correlation potential (see Section 2.1.4). However, it should be noted that the extension of Kohn-Sham DFT to EMS studies was not practical until recently because the Kohn Sham orbitals were originally introduced [110] as purely mathematical constructs to simplify calculations instead of as physically meaningful quantities. The necessary connection between Kohn-Sham orbitals and the EMS cross-section was provided by Casida [135] and Duffy et al. [60], who reinterpreted Eq. (2.53) in the context of Kohn-Sham density functional theory and the target Kohn-Sham approximation (TKSA). It was proposed [60,135] that the *true* Kohn-Sham orbitals (i.e. those that would arise from the *exact* exchange-correlation functional) could be interpreted as approximations to Dyson orbitals. Therefore, the TKSA gives a result similar to Eq. (2.57) in which the canonical Hartree-Fock orbital is replaced by a momentum space Kohn-Sham orbital $\psi_j^{KS}(\boldsymbol{p})$:

$$\sigma_{\mathrm{EMS}} \propto g_f \int \left|\psi_j^{KS}(\boldsymbol{p})\right|^2 d\Omega \tag{2.58}$$

In the justification for using Kohn-Sham orbitals as approximations to Dyson orbitals, Casida [135] showed that the Kohn-Sham equation is the variationally best local

approximation to Dyson's quasiparticle equation. However, while the direct solution of Dyson's equation can in principle yield an infinite number of solutions (Dyson orbitals), only N occupied Kohn-Sham orbitals result from solution of the KS equation for an N electron molecule. Therefore, there is a spectroscopic factor included in the PWIA model of the EMS cross-section (Eq. (2.53)), but no corresponding factor in the TKSA cross-section (Eq. (2.58)).

Although the EMS cross-sections within the THFA and TKSA have similar forms (Eqs. (2.57) and (2.58)), it should be stressed that they differ when electron correlation is considered. The THFA neglects initial target electron correlation effects while the TKSA includes such effects within the chosen form of the exchange-correlation functional. Therefore, the quality of the comparisons of the TKSA momentum profiles to experiment is often highly dependent on the choice of exchange-correlation functional (i.e. local, non-local or hybrid) and the computational methods (i.e. auxiliary basis sets, grid size, fitting procedures) used to evaluate it.

It should be noted that even if the "exact" exchange-correlation functional could somehow be known, the resulting exact Kohn-Sham orbitals would still be, within the TKSA, *approximations* to Dyson orbitals. Thus, there are really two approximations included in practical DFT calculations of momentum profiles. The exact KS orbitals are approximations to the full Dyson overlap, but DFT calculations also involve approximate functionals (and limited basis set size) so that one can never actually compute the exact KS orbitals. Although these considerations may appear to be extremely restricting, it has been shown in several EMS studies [45,53-55,60-62] that the use of approximate Kohn-Sham orbitals as approximations to Dyson orbitals provides reasonable (and often excellent) comparisons with the XMPs. The accuracy of such approximations has been evaluated by comparison of the TKSA momentum profiles with experiment and theoretical momentum profiles computed within the PWIA (Eq. (2.53)) and THFA (Eq. (2.57)) models [45,53-55,60-62]. The TKSA momentum profiles have been shown to generally provide results comparable to or better than those from the THFA and gives similar results to those from CI in cases where electron correlation effects are

important (e.g. H_2O, NH_3 and HF [60]). Such comparisons of the TKSA, PWIA and THFA momentum profiles will also be continued in this thesis.

Despite the fact that Kohn-Sham orbitals are frequently good approximations to Dyson orbitals, it has often been noted that the Kohn-Sham orbital and total energies differ from those obtained from Dyson's equation [60,111,136]. Therefore, orbital and total energies from Kohn-Sham DFT are not readily comparable to those from Hartree-Fock and post-Hartree-Fock (e.g. CI) methods. The shift in Kohn-Sham orbital energies relative to the values for the Dyson orbitals has been discussed in detail by Duffy et al. [60].

2.2.7 Fourier Transform

The usual wavefunctions produced by the variational method are position space wavefunctions $\psi(\boldsymbol{r})$. However, as given by Eqs. (2.57) and (2.58), the EMS experimental results are more directly related to momentum space wavefunctions $\psi(\boldsymbol{p})$. Although the Schrödinger equation can in principle be solved directly in momentum space, the integrals involved are difficult to evaluate and therefore the usual approach is to solve the Schrödinger equation in position space and Fourier transform the resulting wavefunctions to momentum space according to the following equation:

$$\psi(\boldsymbol{p}) = (2\pi)^{-3/2} \int e^{-i\boldsymbol{p}\cdot\boldsymbol{r}} \psi(\boldsymbol{r})\, d\boldsymbol{r} \tag{2.59}$$

For this purpose, a FORTRAN program (HEMS) has been developed in this laboratory to perform the necessary transformation and evaluation of the spherically averaged momentum profiles. This program is based on equations reported by Kaijser and Smith Jr. [137]. The chosen basis functions are transformed into momentum space according to Eq. (2.59), the value of $|\psi_j|^2$ is computed (where either HF or KS orbitals are used) and then spherically averaged so that, according to Eqs. (2.57) and (2.58), it is related to the EMS experimental cross-section. However, it should be noted that experimental angular (i.e. momentum) resolution effects (described in the next section) must be incorporated before the calculations can be compared to

the XMP. Computation of the OVD (Eq. (2.53)) also involves a Fourier transform to p space, followed by the incorporation of momentum resolution effects.

2.2.8 Resolution Folding Effects

Like all spectrometers, the EMS spectrometer does not have perfect resolution, but rather has some finite resolutions for instrumental polar (θ) and azimuthal (ϕ) angles. This angular resolution is reflected in the shape of the XMPs. Therefore, for meaningful comparison of theory and experiment, the calculated DWIA cross-sections (Eq. (2.50)), PWIA overlap distributions (Eq. (2.53)) or HF and TKSA momentum distributions (Eqs. (2.57) and (2.58)) must be momentum resolution folded by taking into account the finite instrumental acceptance angles [58,59]. Because the Gaussian-weighted planar grid (GW-PG) method of Duffy et al. [59] has been shown to incorporate these angular resolution effects and to provide excellent agreement between high-level theory and experiment, it has been used for momentum resolution folding in the present work. For the multichannel energy-dispersive EMS spectrometer used to collect the data presented in this thesis, finite instrumental half angles of $\Delta\theta = \pm 0.6°$ and $\Delta\phi = \pm 1.2°$ have been used in the GW-PG calculations (thus, the FWHM momentum resolution is approximately 0.1 atomic units). After momentum resolution folding, the OVD (Eq. (2.53)) or the MD (Eqs. (2.57) and (2.58)) is referred to as a theoretical momentum profile (TMP) and is then suitable for comparison with the experimental momentum profile (XMP). The resolution folded DWIA cross-section in Eq. (2.50) may also be compared with experimental measurements in the case of atoms but it should be noted that this is a cross-section and not a momentum profile.

Chapter 3

Experimental Method

3.1 The Multichannel Energy-Dispersive Spectrometer

The construction and operation of the multichannel energy-dispersive EMS spectrometer used in the present work has been described in detail in earlier publications [45,46]. A schematic of the spectrometer is shown in Fig. 3.1. Briefly, a high energy (1200 eV + binding energy) electron beam (25-30 μA) is produced from a directly heated thoriated tungsten filament (F) and an oscilloscope electron gun containing a grid (G) and accelerating anode (A). The beam is aligned and focussed into the collision region by three sets of electrostatic quadrupole deflectors (D1-D3) and two Einzel lenses (F1 and F2). The electron beam alignment and collimation are monitored by the currents on four spray plates (P1-P4) and a Faraday cup (FC). In the present work, the current of a well-focussed incident beam (~ 1 mm in diameter) into the Faraday cup is about 25-30 μA.

The electron beam undergoes ionizing collisions with the target gas and produces two outgoing electrons which are sampled at the polar angles θ (45°) by electron lenses and decelerated into the hemispherical electrostatic electron analyzers. One analyzer is fixed while the other is movable under computer control through a -35° to +35° range of azimuthal angles φ (see Fig. 1.1) to vary the measured electron momentum (see Eq. (2.45)). The analyzer pass energy is 50 eV. An 8 eV range of outgoing electron energies (i.e. 600 ± 4 eV) is sampled by a double chevron configuration microchannel plate (MCP) detector [138-140] located in the exit plane of each analyzer. Coincidence events are recorded from the many electrons striking

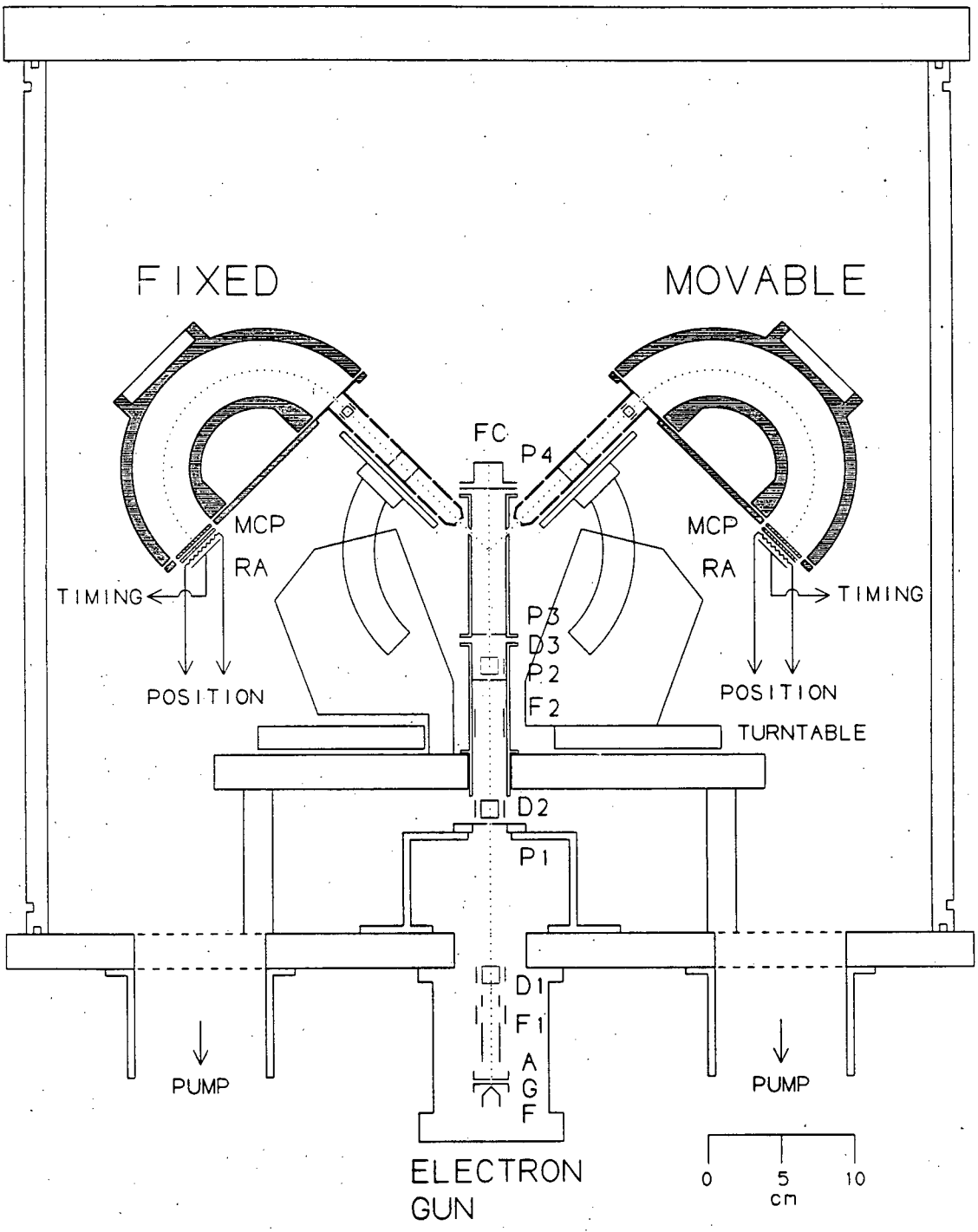

Fig. 3.1: Schematic of the energy-dispersive multichannel EMS spectrometer used in the present work. The two analyzers are kept at fixed polar angles $\theta = 45°$ and the out-of-plane azimuthal angle ϕ of the movable analyzer is variable. This figure is from Refs. [45,46].

F	Filament	F1,F2	electron lenses	D1-D3	quadrupole deflectors
G	Grid	P1-P4	spray plate apertures	RA	resistive anode
A	Anode	FC	Faraday cup	MCP	microchannel plates

the detectors. The position (energy) information is determined using a Gear-type [141] resistive anode (RA) encoder at the back of each MCP array and charge division circuitry. The timing information is determined using a time-to-amplitude converter (TAC). It should be noted that the details of the position and timing signal processing as well as the computer control have been described previously in great detail [45,46]. An overall schematic of the signal processing electronics is shown in Fig. 3.2. Fig. 3.3 shows a typical time spectrum obtained from the TAC output with time resolution of 16 ns.

The aluminum vacuum housing is evacuated by two Seiko-Seiki TMP 450 Maglev turbomolecular pumps (base pressure ~ 10^{-7} torr) backed by a rotary pump. The electron gun is differentially pumped by a Seiko-Seiki TMP 300 Maglev turbomolecular pump. Ambient magnetic fields are reduced below 1 mGauss by hydrogen-annealed μ-metal shields placed inside the vacuum chamber.

Gas samples and volatile liquid samples are introduced into the spectrometer using a gas line that connects to the interaction region. The pressure within the spectrometer is controlled by use of a variable leak valve (sample pressures of approximately 6×10^{-6} torr are typically employed for gaseous targets). Solids of low vapour pressure can be directly introduced through a vacuum lock using a solid sample probe [55]. Use of this sample probe was necessary to obtain sufficient gas density at room temperature for the measurements of $W(CO)_6$ in this work.

Data collection is carried out in either the non-binning or binning modes [45]. Typical results are shown in Fig. 3.4 for Ar 3p ionization. The non-binning coincidence binding energy spectrum is obtained at a fixed impact energy with triangular response functions in both the true coincidence window (CW, open circles) and background random coincidence window (BW, filled circles). In the non-binning mode the detection efficiency is different at each collected energy (i.e. higher in the top region of the triangle and lower near the two ends). Due to this non-uniform detection efficiency, the non-binning mode provides relatively rapid data

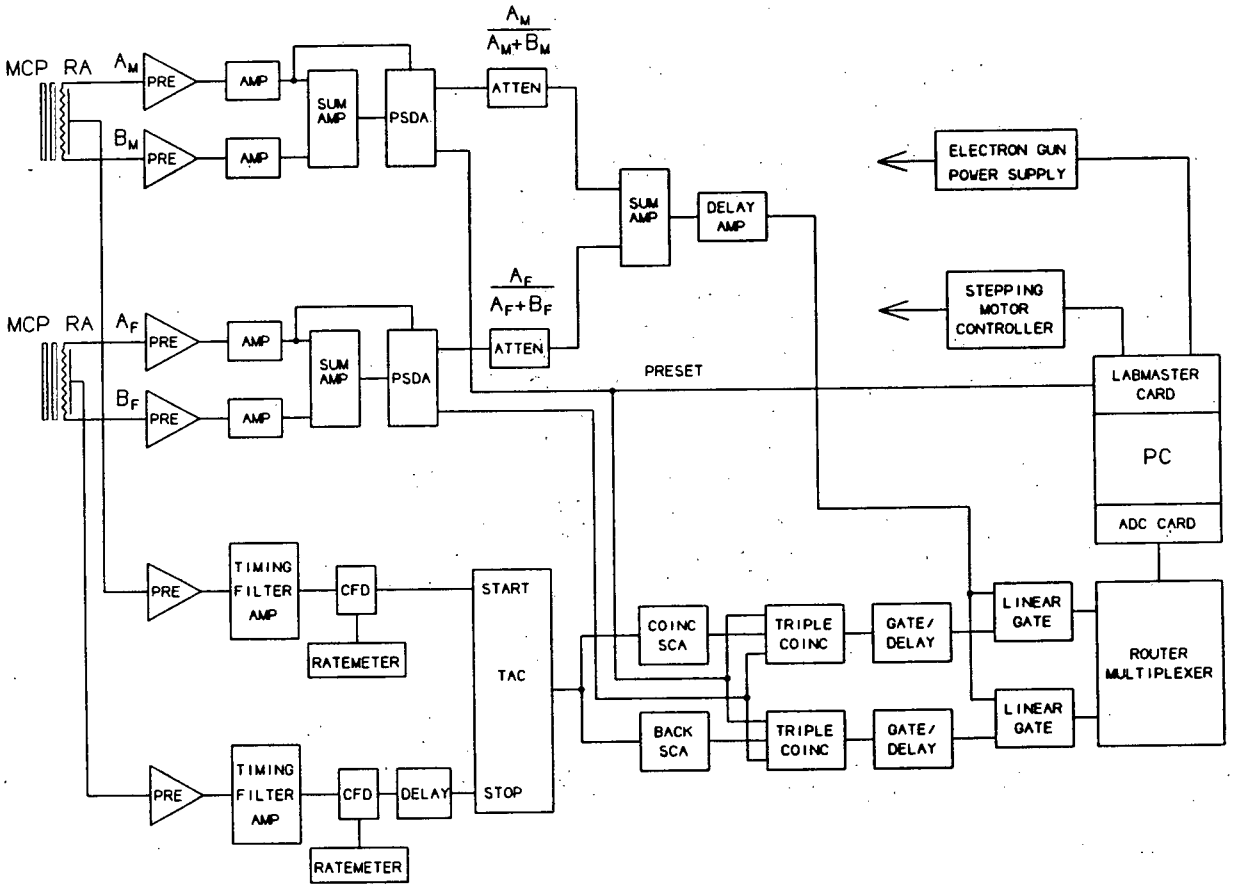

Fig. 3.2: Schematic diagram of the position sensitive detectors and signal processing electronics for the EMS spectrometer. Each position sensitive detector consists of a pair of microchannel plates (MCP) and a resistive anode (RA). Also shown are: position sensitive detector analyzer (PSDA), constant fraction discriminator (CFD); time-to-amplitude converter (TAC), single-channel analyzer (SCA), analogue-to-digital converter computer card (ADC), and personal computer (PC). This figure is from Refs. [45,46].

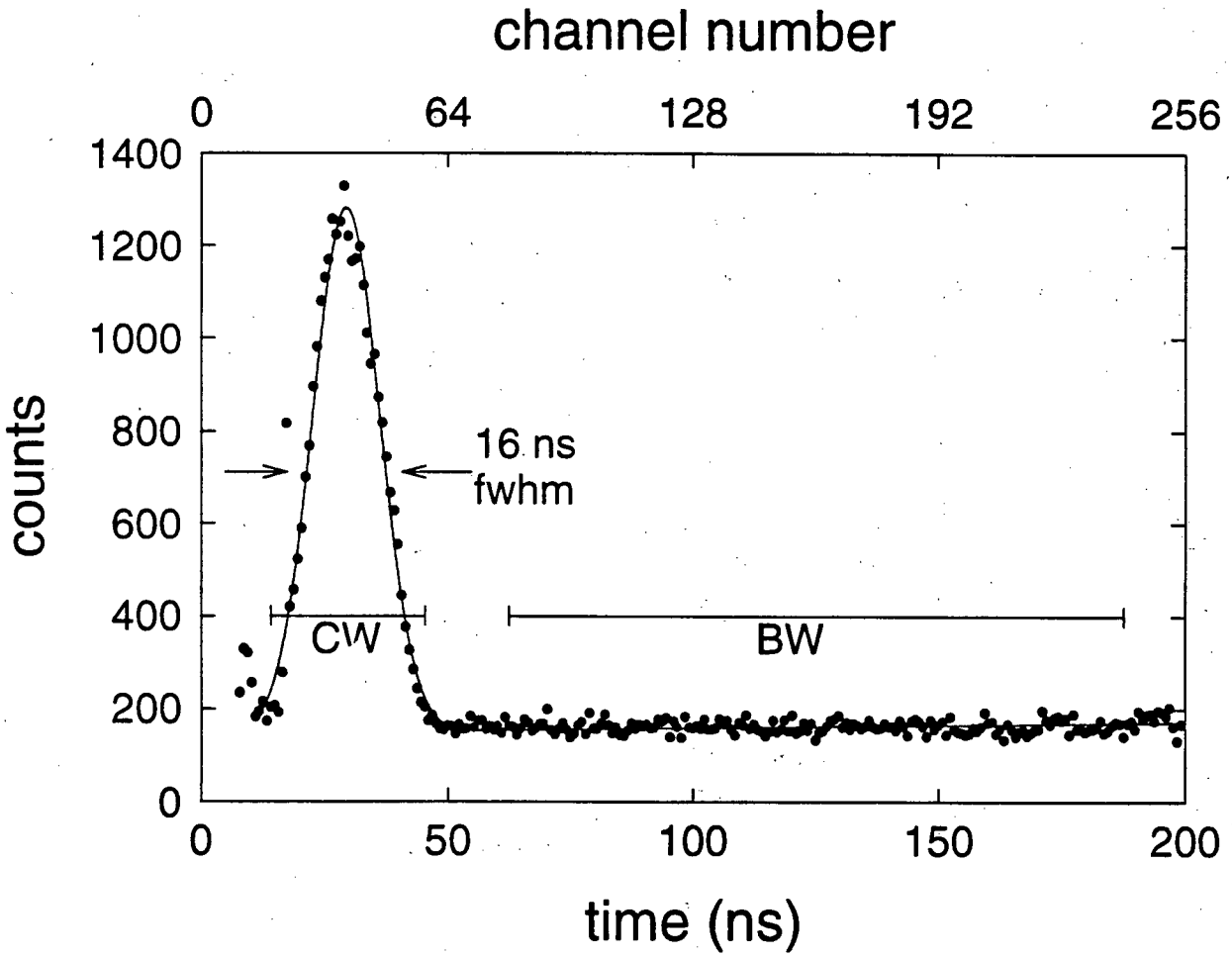

Fig. 3.3: Time spectrum output by the TAC and collected by the ADC computer card. The time ranges of the true coincidence window (CW) and background window (BW) as set by the single channel analyzers (SCA) are indicated. It should be noted that the CW is set by the SCA to collect true coincidence + random coincidence events while the BW is set by the SCA to collect random coincidence events. The data in the figure were collected in 45 minutes from non-binning mode measurements of the Ar 3p ionization process. This figure is from Ref. [46].

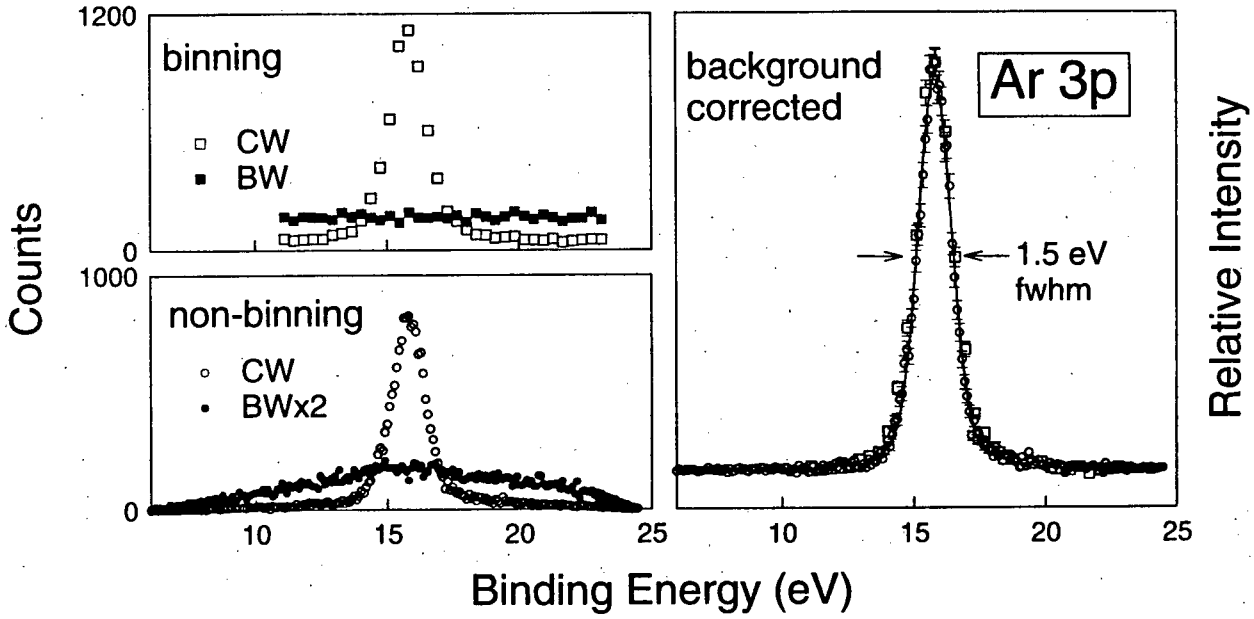

Fig. 3.4: Non-binning mode (squares) and binning mode (circles) Ar 3p binding energy spectra. The non-binning data shown are the sum of BES collected in a period of 17 hours at 27 out-of-plane azimuthal angles ranging from -30° to +30°. The binning data are the sum of 21 BES collected in 21 hours. The binning and non-binning mode raw data (CW designates the coincidence window while BW designates the background window) are shown in the upper-left and lower-left panels, respectively. The BW data are of greater intensity than the CW data because of the greater width of the background window (as shown in Fig. 3.3). This is accounted for in the background correction procedure (see Section 3.2). The binning mode and non-binning mode background corrected BES are shown in the right panel, normalized for height to allow direct shape comparison of the two spectra. The result of a least-squares fit of a pair of Gaussian functions to the ionization peak is indicated by the solid line. This figure is from Ref. [46].

collection for situations where the ionization energy for a single orbital is well-separated in energy from those for the remaining orbitals (e.g. the low-lying HOMOs of NO, NO_2, O_2 and the metal hexacarbonyls studied in the present work - see Chapters 4, 5 and 7). However, the non-binning data collection mode is not well suited for the simultaneous study of several ionization processes at different binding energies because the relative intensities of each process are not easily determined with high accuracy from such a non-linear background. In contrast, the binning data collection mode (see Fig. 3.4 and Ref. [45]) is used to collect binding energy spectra with a flat overall response function (see the open and filled squares in the CW and BW windows in Fig. 3.4). In the binning mode, the total energy range of the detector and the binding energy range to be measured are divided into a number of narrow energy ranges called "energy bins" that are measured for equal times (the width of each energy bin is typically ~ 0.3 eV) as the impact energy is scanned. In this manner, all BES ionization peaks obtained at all ϕ angles have a common intensity scale and several ionization processes may be studied in the same experiment. Therefore, the binning mode has been used to obtain the measurements for the full valence shell regions of molecular oxygen and methanol presented in Chapters 5 and 8 of this work, respectively.

The overall instrumental energy resolution is monitored by measuring the BES for a calibration gas in the binning mode. The He $(1s)^{-1}$ ionization peak at 24.6 eV or the Ar 3p ionization peak at 15.8 eV are typically chosen for this purpose. As demonstrated by the data in Fig. 3.4 for the Ar 3p ionization process, an energy resolution of ~ 1.5 eV FWHM is typically obtained. It should also be noted that the value of the spectrometer energy resolution is required for further analysis of the experimental data (see Chapters 5 and 8). The Ar 3p ionization process is also used to monitor the angular resolution of the spectrometer. As can be seen from Fig. 3.5, the momentum profile for this ionization process is "p-type" (i.e. the maximum of the profile is at a value of $p > 0$). If a spectrometer with perfect angular resolution existed, measurement of the Ar 3p ionization process with such a spectrometer would give a p-type momentum profile with zero intensity at $p = 0$ au due to orbital symmetry

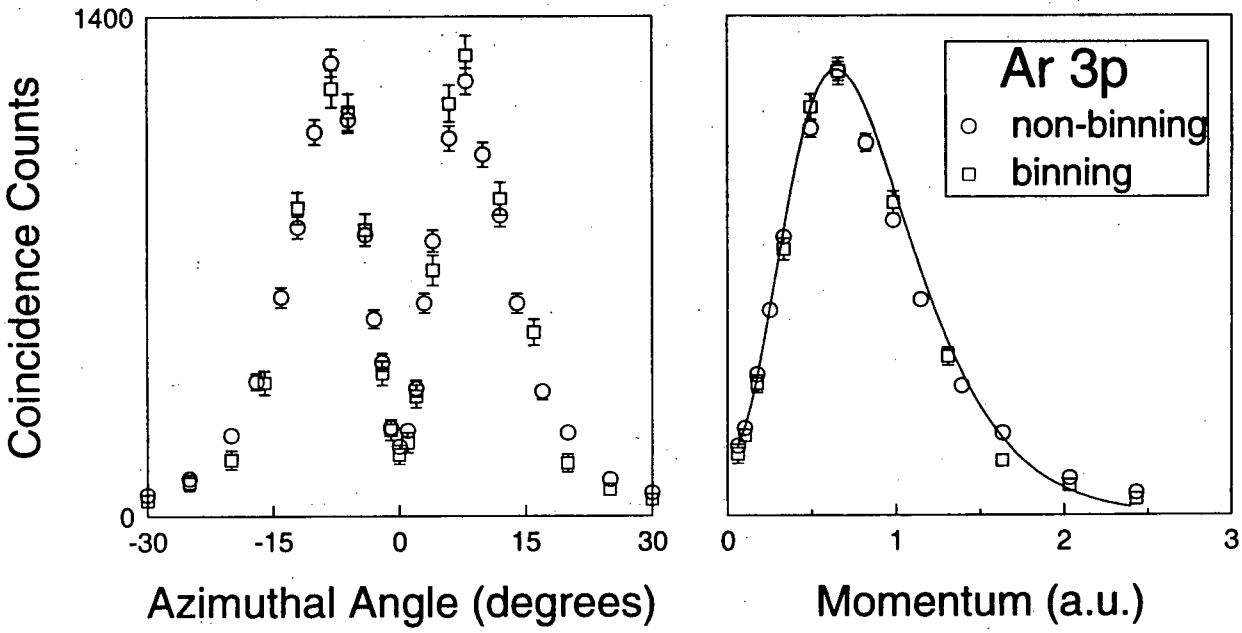

Fig. 3.5: Non-binning mode (open circles) and binning mode (open squares) angle measurements (left) and momentum profiles (right) for Ar 3p ionization. The data sets were collected in 17 and 21 hours, respectively. The binning mode data has been scaled by a factor of 1.9 to normalize the two data sets at the maximum of the momentum profile. The solid line in the right panel is the calculated Ar 3p theoretical momentum profile from the CI ion-neutral overlap calculation of Davidson and co-workers [142]. The experimental angular resolution ($\Delta\theta = 0.6°$, $\Delta\phi = 1.2°$) has been incorporated into the TMP using the GW-PG method [59] and the TMP has been normalized to the experimental data at the maximum of the momentum profile. This figure is from Ref. [46].

considerations. However, as can be seen in Fig. 3.5, some experimental intensity is always observed at $p = 0$ au due to finite instrumental angular resolution effects (i.e. effects due to the finite acceptance angles about the nominal values of θ and ϕ for each analyzer). The angular resolution parameters for the spectrometer have been determined to be $\Delta\theta = 0.6°$ and $\Delta\phi = 1.2°$ by comparison of the Ar 3p experimental momentum profile with a high quality CI calculated momentum profile [142] that incorporates the GW-PG resolution folding method [59]. As can be seen in Fig. 3.5, excellent agreement is obtained between theory and experiment using these parameters. To ensure that the spectrometer is operating properly, results similar to those shown in Fig. 3.5 should be obtained each time the instrumental angular resolution is monitored. It should be noted that the above tests of the energy and angular resolution of the spectrometer are generally performed before and after each experiment or following any adjustments to the spectrometer.

3.2 Background (Random Coincidence) Correction

A coincidence event results in two electrons arriving at the detectors at the same time (i.e. the two electrons are "correlated" with respect to time). However, it is possible that two electrons that do not come from the same ionization event can strike the detectors at the same time. These "uncorrelated" electrons give a random coincidence event that must be taken into account. The random coincidence background (see Fig. 3.3) has a constant amplitude because all time differences for uncorrelated electron pairs have equal probability. Therefore, the total coincidence peak in Fig. 3.3 has two components: those from actual (e, 2e) coincidence events ("true" coincidences) in the peak and the constant underlying background resulting from random uncorrelated electron pairs ("random" coincidences). The random coincidences must be removed from the total coincidences in the peak to determine the number of true coincidence events. The amplitude of the background is determined by use of coincidence and background windows (CW and BW in Fig. 3.3) that encompass the coincidence peak and a large background region, respectively. The background window is typically a factor r larger in

width than the coincidence window in order to obtain the random coincidence rate with greater precision. If the number of total coincidence counts in the CW window is N_c and the number of non-coincident counts in the BW window is N_b, then the number of true coincidence counts N_t is obtained as follows:

$$N_t = N_c - N_b / r \tag{3.1}$$

The error in the number of true coincidence counts is:

$$\Delta N_t = \sqrt{N_c^2 + \frac{N_b^2}{r^2}} \tag{3.2}$$

Chapter 4

The HOMOs of NO and NO_2

4.1 Introduction

The technique of EMS has been extensively applied to closed-shell molecules [11,12,37-40]. In contrast, open-shell molecules have received much less attention experimentally because of their reactive nature and theoretically because of the more challenging nature of quantum mechanical calculations for such species. In view of the challenging experimental and theoretical problems associated with open-shell molecules, a detailed experimental and theoretical investigation of the electron momentum profiles for the outermost (HOMO) orbitals of NO and NO_2 has been carried out in this laboratory. These are benchmark molecules for quantum chemistry and are among the most common stable open-shell species. These molecules are also of importance in processes such as nitrogen fixation [143], neurotransmission [144], smog and acid rain [143].

Previously reported EMS studies of the HOMOs of NO [145-147] show limited statistics and considerable scatter due to the low cross-sections involved for ionization from these partially filled orbitals. The Hartree-Fock wavefunctions employed in the earlier work on NO by Brion et al. [145] involved only minimal and double-zeta basis sets and more advanced calculations were not considered. Furthermore, the instrumental momentum resolution was not always taken into account in previous work when comparing the experimental and theoretical momentum profiles. The adequate incorporation of finite angular acceptances (i.e. momentum resolution effects) has been found to be essential for the meaningful comparison of experiment

and theory, particularly at lower momentum [39,58,59]. The experimental and theoretical study of NO by Fantoni et al. [146] included the use of the same Kouba and Ohrn unrestricted Hartree-Fock (UHF) wavefunction [148] presented in the work of Brion et al. [145]. In contrast, the theoretical treatment presented in the work of Tossell et al. [147] was limited in that calculations were presented only with small basis sets at the restricted open-shell Hartree-Fock (ROHF) level which may not provide an adequate computational model for open-shell molecules (see Section 2.1.2 for descriptions of the ROHF and UHF methods).

In order to obtain improved EMS measurements for the HOMO of NO, the energy-dispersive multichannel EMS spectrometer [45] described in Chapter 3 was used in the present work. All multichannel measurements in the present work were obtained using the non-binning mode [45] (see Section 3.1). The differential detection efficiency of the non-binning mode (higher in the middle of the triangle and lower near the two ends) was advantageous for measurements on the single, well-separated binding energy peak of the HOMO of NO. The measurements for NO_2 were carried out with an earlier single channel instrument at a binding energy of 11.2 eV and the present results are the first to be reported for this molecule. The NO and NO_2 samples were obtained from Matheson gas products. All gas samples were of $> 99.0\%$ purity. Some additional considerations regarding the handling of the NO gas sample are discussed in the next section.

Much larger basis sets and more complex theoretical methods have been used in the present work for NO to calculate theoretical momentum profiles which also incorporate the improved resolution folding procedures [59]. Theoretical momentum profiles at the target Hartree-Fock approximation (THFA) level from both the UHF and ROHF methods are shown for both molecules. Momentum profiles from post Hartree-Fock methods such as multi-reference singles and doubles configuration interaction (MRSD-CI) methods, averaged coupled-pair functional (ACPF) [149] and quasi-degenerate variational perturbation theory (QDVPT) [150,151] are also presented in order to assess the role of electron correlation and relaxation effects. In addition, no published work to date has compared EMS momentum

profiles for open-shell molecules with momentum profiles from DFT. Thus, TKSA-DFT calculations using the local functional of Vosko, Wilk and Nusair [112], the non-local correlation functional of Perdew and Wang [115,117] and a non-local combination of the Perdew correlation and Becke exchange functional [116] are shown for the HOMOs of both molecules in the present work.

4.2 Gas Samples and Sample Handling for NO

Experience in the present work has shown that great care is needed in handling and introducing NO gas samples into the spectrometer. In the initial phases of the present experimental study of the HOMO XMP of NO using a single channel EMS spectrometer, surprising and unexpected results were obtained as shown by the open triangles in Fig. 4.1a. Previous experimental measurements [145-147] of the momentum profile of the 2π HOMO of NO display considerable scatter and uncertainties due to the very low EMS cross-section arising from the single occupancy of the 2π orbital and the broad nature of the momentum profile. This can be seen in Fig. 4.1b where the previous results from Brion et al. [145] (filled squares), Fantoni et al. [146] (open inverted triangles), and Tossell et al. [147] (filled diamonds) are shown. The data from Fantoni et al. [146] is that collected at 800 eV, although some data were also presented at 2600 eV. Within the limited statistics the three experimental results appear to be in reasonable agreement with each other and with the theoretical momentum profile (TMP) from the Kouba and Ohrn (K&O-U) calculation [148]. In the original publications, the K&O-U TMP was thought by Brion et al. [145] and also by Fantoni et al. [146] to agree well for shape with the HOMO momentum profiles as shown in Fig. 4.1b. It should be noted, however, that while it was reported [145] that the K&O-U wavefunction was a CI calculation, it has since been found that the momentum profile reported in Ref. [145] and presumably also that in Ref. [146] was calculated from the leading configuration of the CI wavefunction only and thus was in fact a Hartree-Fock and not a CI treatment

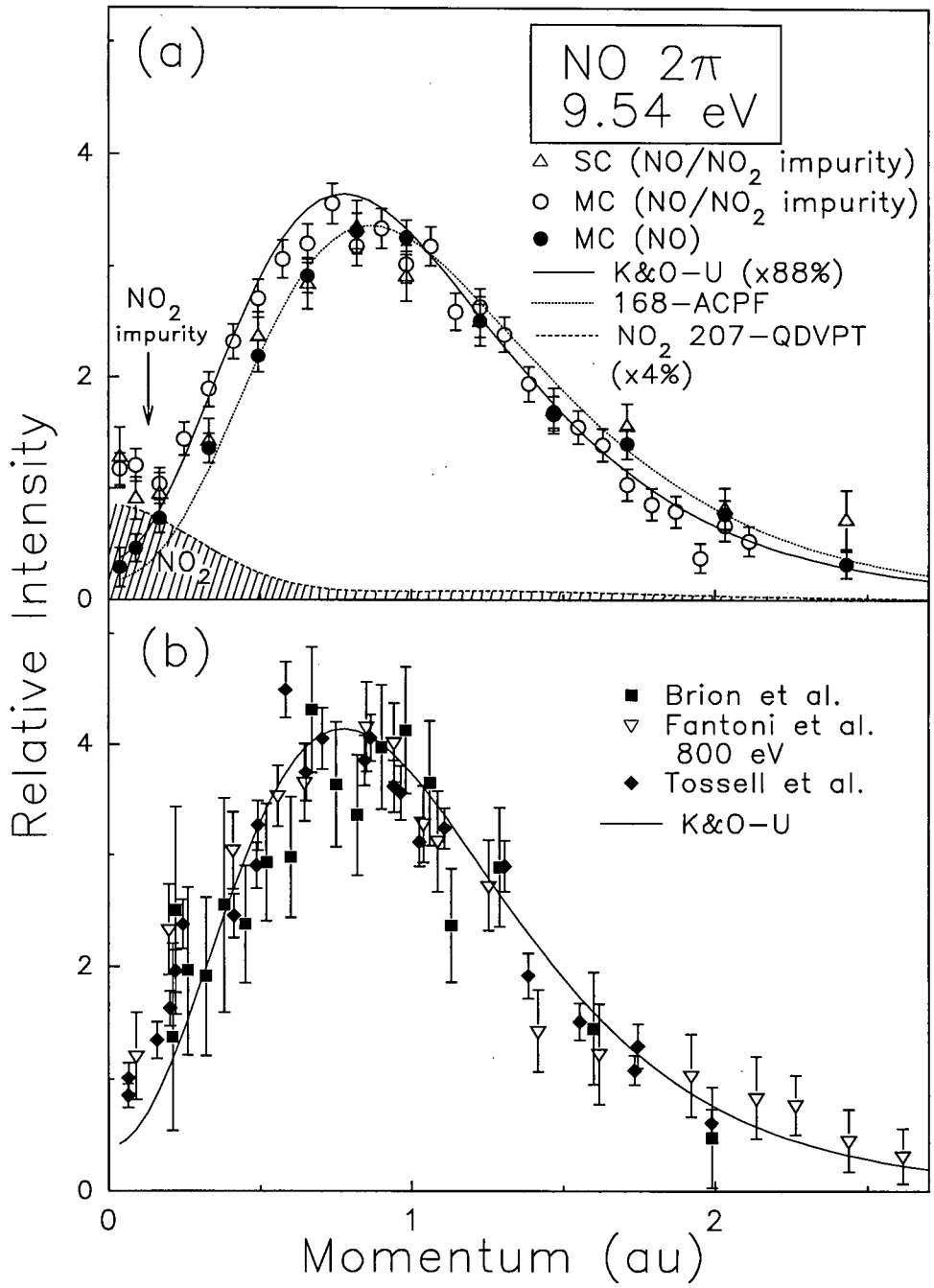

Fig. 4.1: (a) Experimental momentum profiles for the 2π orbital of NO from the present work. Shown are the XMPs from a single channel EMS spectrometer (open triangles), a multichannel momentum dispersive multichannel EMS spectrometer (open circles) and a multichannel energy-dispersive EMS spectrometer (filled circles). The single channel and momentum dispersive results contain some degree of contamination from NO_2 (see Section 4.2 for details). The estimated contribution due to NO_2 impurity is represented by the NO_2 207-QDVPT momentum profile (long dashed line) multiplied by 0.04. Also shown are the calculated theoretical spherically averaged K&O-U momentum profile [145] (multiplied by a factor of 0.88) and the 168-ACPF momentum profile for NO. **(b)** Previous experimental momentum profiles for the 2π orbital of NO. Shown are the XMPs from Brion et al. [145] (filled squares), Fantoni et al. [146] (open inverted triangles) and Tossell et al. [147] (filled diamonds). The calculated spherically averaged K&O-U momentum profile is also shown. See text for further details.

The K&O-U momentum profile shown in Fig. 4.1a is also from the leading configuration only. It should also be noted that the previous measurements [145,146] show very little data in the low momentum region below $p \sim 0.2$ au and that nearly all data points below 0.5 au are higher than predicted by the K&O-U theory. The measurements of Tossell et al. [147] which are reasonably consistent with the other experiments [145,146] were in poor agreement with calculations based on the Hartree-Fock wavefunction of Cade and Wahl [152].

A consideration of Figs. 4.1a and 4.1b shows that in the region above ~ 0.3 au the present single channel measurements (open triangles) are generally consistent with the three earlier published experiments [145-147]. However, below ~ 0.3 au the data points unexpectedly rise as zero momentum is approached. This is in marked contrast to all calculations (see Fig. 4.1a and also Fig. 4.2 below) which, as expected from symmetry considerations, show a decreasing cross-section as zero momentum is approached. The high data points at low momentum persisted in repeated measurements, not withstanding the poor statistics inherent in the case of the single channel spectrometer. A further measurement in our laboratory (open circles in Fig. 4.1a) using the high precision and improved statistics of a recently built momentum dispersive multichannel EMS spectrometer [47] produced similar spuriously high results at low momentum. It is noteworthy that above ~ 0.2 au these measurements (like the earlier data [145-147] in Fig. 4.1b) are in close conformity with the less accurate K&O-U calculation but not with the very accurate and highly correlated 168-ACPF ion-neutral overlap calculation (dotted line in Fig. 4.1a) described in Section 4.3.2 below.

The anomalous behaviour in the experimental results which is manifested particularly at lower momenta has been found to be due to NO_2 impurities in the sample gas introduced to the collision chamber. Consideration of the respective Franck-Condon widths and the fact that the HOMO ionization potential of NO_2 is close to that of NO indicate that any small NO_2 impurity would cause the observed spurious effects particularly at the lowest momenta because of the very intense s-type NO_2 HOMO momentum profile (see Fig. 4.3 below). Careful consideration of the purity of the commercial gas cylinders and the results of other spectroscopic experiments

[153] indicated that the NO_2 impurity observed in the EMS measurements was not present in the NO cylinders. Clearly, the NO_2 impurity was being generated in the stainless steel sample handling and introduction system of the EMS spectrometers. Since, as is well-known, NO is readily oxidized to NO_2 by atmospheric oxygen an obvious possibility would be a leak in the sample system. However, careful leak testing eliminated this as the cause. A further possibility would be reaction of NO with oxygen containing species (e.g. H_2O, O_2, previously studied molecules, etc.) adsorbed on the walls of the inlet manifold, valves and leak valve. Initial measurements for NO on the energy-dispersive multichannel EMS instrument [45] also showed a similar "turning-up" at low momentum. However, after repeated flushing to remove suspected NO_2 impurities, overnight stagnation (to allow reaction) and evacuation, very different results, as indicated by the solid circles in Fig. 4.1a, were eventually obtained. These procedures were repeated daily during the measurements. It can be seen from this high precision data that the low momentum "turning-up" has essentially gone and also that the XMP is shifted over to higher momentum below 1.0 au Furthermore these measurements are in generally very good agreement with the shape of the high-level 168-ACPF overlap calculation for NO (see Section 4.4.1) and in poor agreement with the shape of the K&O-U treatment. Note that the two calculations are separately height normalized to the experimental data sets in Fig. 4.1a. It can be concluded that the gas sample for the solid circle data points in Fig. 4.1a is dominantly NO. However, some minimal pollution from residual NO_2 cannot be discounted and this may be the reason for the remaining small discrepancy between the 168-ACPF theory and experiment at the lowest momenta. The estimated contribution from the (s-type - see Fig. 4.3) NO_2 impurity in the earlier open circle and open triangle data sets is shown by the shaded area under the long-dashed line in Fig. 4.1a. This long dashed line is the 207-QDVPT calculation for the HOMO of NO_2 (see Section 4.3.2 for a description of this calculation) scaled appropriately. Based on these observations and a consideration of the presently reported very high level calculations, we suggest that the earlier published measurements for NO [145-147] were also complicated by varying degrees of NO_2 impurity. It should be noted

(Fig. 4.1b) that these earlier measurements [145-147] all show higher cross-sections at lower momenta than even the K&O-U calculation. The present work indicates that the apparently good agreement of earlier measurements with the K&O-U calculation is fortuitous due to the probable presence of NO_2 impurities.

4.3 Calculations

4.3.1 Hartree-Fock Calculations

Spherically averaged theoretical momentum profiles have been calculated for the HOMOs of NO and NO_2 using several basis sets of varying quality within the plane wave impulse and the target Hartree-Fock approximations (via Eq. (2.57)). Both the UHF and ROHF methods have been used for all basis sets. The instrumental angular (momentum) resolution was included in the calculations using the Gaussian-weighted planar grid method [59] (see Section 2.2.8). Various other calculated and experimental electronic properties are listed in Tables 4.1 and 4.2. The experimentally derived geometries for NO [154] and NO_2 [155] were used in all calculations.

The dipole moment of NO is of special interest in quantum mechanical calculations because the predicted dipole moment reversal [156-158] gives a N^-O^+ polarity which is counter to that from intuitive electronegativity arguments. An experimental measurement of the dipole moment [159,160] gave a value of 0.15872 Debye with an N^-O^+ polarity as reported by Gray et al. [161]. While the sign of the dipole moment for NO is often incorrectly predicted by Hartree-Fock calculations, correlated treatments generally give the correct polarity [157]. Thus, a positive dipole moment for NO in Table 4.1 implies a polarity of N^-O^+. The experimental dipole moment for NO is from Ref. [160].

When considering the properties in Tables 4.1 and 4.2, it should be noted (see Section 2.1.2) that the UHF methods and ROHF methods give different values for the total energy and spin contamination. The increased variability of the UHF method causes the UHF

Table 4.1: Calculated and experimental properties for NO $X\ ^2\Pi$

	Basis Set and Calculation Method[a]	Total Energy (hartree)	$\langle \hat{S}^2 \rangle$	μ (Debye)[b]	p_{max} (au)[c]
	Hartree-Fock Calculations				
1u	STO-3G-U	-127.530	0.9660	+0.2492	1.27
1r	STO-3G-R	-127.526	0.7500	+0.1559	1.20
2u	6-311+G*-U	-129.284	0.8104	-0.3019	0.94
2r	6-311+G*-R	-129.277	0.7500	-0.3617	0.89
3u	AUG5-U	-129.304	0.8024	-0.2391	0.91
3r	AUG5-R	-129.296	0.7500	-0.2873	0.85
4u	168-U	-129.309	0.7984	-0.2440	0.91
4r	168-R	-129.299	0.7500	-0.2753	0.86
6u	210-U	-129.307	0.7981	-0.2397	0.91
6r	210-R	-129.297	0.7500	-0.2689	0.89
	Post-Hartree-Fock Calculations				
4c	168-CI	-129.713	0.7500	+0.1388	0.86
4a	168-ACPF	-129.730	0.7500	+0.1779	0.85
6c	210-CI	-129.712	0.7500	+0.1432	0.88
6a	210-ACPF	-129.728	0.7500	+0.1805	0.86
	DFT Calculations[d]				
3*l*	AUG5-L	-128.981	—	+0.2536	0.77
3p	AUG5-P	-130.088	—	+0.2322	0.76
3b	AUG5-BP	-129.967	—	+0.2316	0.79
	Experimental	-129.900[e]		+0.1587[f]	0.85[g]

[a] Calculations performed at the experimental equilibrium bond length of 1.151 Å (2.175 au), Ref. [154].

[b] A positive dipole moment μ implies a polarity of N^-O^+. Calculated dipole moments are for a non-relativistic, non-vibrating, non-rotating molecule.

[c] The p_{max} corresponds to the value of momentum where the intensity of the momentum profile is at a maximum (see Fig. 4.2).

[d] The total energy from Kohn-Sham DFT has been suggested to be in error because of shifted orbital energies relative to ionization potentials from Dyson's equation [60] - see also Section 2.2.6.

[e] The "experimental" total energy is the estimated non-relativistic, non-vibrating, infinite nuclear mass total energy. Total energy obtained by adding the atomic energies from Ref. [162] to the D_0 values from Ref. [159] plus the zero point energy from the frequencies in Ref. [159]. A numerical Hartree-Fock calculation with the ROHF method was also reported to give a total energy of -129.2991 hartree for NO [163].

[f] Refs. [159-161].

[g] Present work, ± 0.05.

Table 4.2: Calculated and experimental properties for NO_2 $X\,^2A_1$

	Basis Set and Calculation Method[a]	Total Energy (hartree)	$\langle \hat{S}^2 \rangle$	μ (Debye)[b]
	Hartree-Fock Calculations			
1u	STO-3G-U	-201.273	0.7619	+0.2435
1r	STO-3G-R	-201.268	0.7500	+0.2758
2u	6-311+G*-U	-204.087	0.7702	+0.7187
2r	6-311+G*-R	-204.078	0.7500	+0.8073
3u	AUG5-U	-204.121	0.7712	+0.6610
3r	AUG5-R	-204.112	0.7500	+0.7446
5u	207-U	-204.129	0.7713	+0.6584
5r	207-R	-204.120	0.7500	+0.7629
	Post-Hartree-Fock Calculations			
5c	207-CI	-204.752	0.7500	+0.4373
5a	207-ACPF	-204.795	0.7500	+0.4740
5q	207-QDVPT	-204.806	0.7500	+0.4857
	DFT Calculations[c]			
3*l*	AUG5-L	-203.710	—	+0.2689
3p	AUG5-P	-205.400	—	+0.2668
3b	AUG5-BP	-205.217	—	+0.2463
	Experimental	-205.085[d]		+0.289[e]

[a] Calculations performed at the experimental equilibrium bond length of 1.19455 Å (2.25737 au) and bond angle of 133.851°, Ref. [155].

[b] A positive dipole moment implies a polarity of $N^+O_2^-$. Calculated dipole moments are for a non-relativistic, non-vibrating, non-rotating molecule.

[c] The total energy from Kohn-Sham DFT has been suggested to be in error because of shifted orbital energies relative to ionization potentials from Dyson's equation [60]. See also Section 2.2.6.

[d] The "experimental" total energy is the estimated non-relativistic, non-vibrating, infinite nuclear mass total energy. Total energy obtained by adding the atomic energies from Ref. [162] to the D_0 values from Ref. [164] plus the zero point energy from the frequencies in Ref. [164].

[e] Ref. [165].

total energy for a given molecule and basis set to be generally lower than the ROHF total energy. However, spin contamination can be problematic for UHF wavefunctions [57,97,98,108] and thus UHF wavefunctions are not true eigenfunctions of the total spin operator $\hat{S}^2$. A measure of the spin contamination is found by calculation of the expectation value of $\hat{S}^2$. The value of $\langle \hat{S}^2 \rangle$ is 0.75 for NO and NO_2 when no spin contamination is present and it can be seen that for all the UHF calculations in Tables 4.1 and 4.2 this value is exceeded due to interference from states of higher multiplicity. Spin contamination does not arise in the ROHF method and thus all ROHF calculations give $\langle \hat{S}^2 \rangle$ values of exactly 0.75 for NO and 2.0 for NO_2. A large amount of spin-contamination in any wavefunction may cause inaccuracy in computed properties. There is a high degree of spin contamination for the STO-3G-U and 6-311+G*-U calculations for NO (Table 4.1). However, the spin contamination for UHF calculations on NO_2 is reasonably small (Table 4.2).

Further details of the Hartree-Fock calculation methods and basis sets are described below. The total number of contracted Gaussian-type orbital functions (CGTO) used is also given. All calculations with the STO-3G, 6-311+G* and AUG5 basis sets (described below) were done at the University of British Columbia with the Gaussian 92 program [124] while the calculations with the 168-GTO, 210-GTO and 207-GTO basis sets were done by Prof. E.R. Davidson at Indiana University with the MELD program. Those calculations employing the UHF method have the "-U" extension added to the basis set symbol while the "-R" extension indicates the ROHF method. The ROHF calculations done at Indiana University involve both symmetry and equivalence restriction (i.e. all molecular orbitals are pure σ and π orbitals). This symmetry and equivalence restriction affects the results for NO, making the π_x and π_y orbitals equivalent partner functions in the Π irreducible representation of the $C_{\infty v}$ point group. Symmetry or equivalence restrictions were not done with the UHF calculations from the University of British Columbia or those from Indiana University.

(1u) STO-3G-U and (1r) STO-3G-R: These calculations employed a minimal basis set (effectively single zeta). Each function is a contraction of three primitive Gaussian functions. Both the nitrogen and oxygen atoms have a (6s,3p)/[2s,1p] contraction and thus 10 CGTO are used for NO while 15 CGTO are employed for NO_2. This basis was designed by Pople and co-workers [101].

(2u) 6-311+G*-U and (2r) 6-311+G*-R: These calculations used an augmented version of the 6-311G basis of Pople and co-workers [103]. The 6-311+G* basis is formed by augmenting the 6-311G with diffuse s- and p-functions [105] and spherical d-type polarization functions [104] on both the nitrogen and oxygen atoms to produce a (12s,6p,1d)/[5s,4p,1d] contraction per atom. A total of 44 CGTO are employed for NO while 66 CGTO are used for NO_2.

(3u) AUG5-U and (3r) AUG5-R: The basis set for these calculations was taken from the work of Dunning et al. [166-169]. The AUG5 basis set used in the present work is actually a truncated form of Dunning's aug-cc-pV5Z basis set in which all f-, g- and h-functions have been removed. This truncation was adopted to provide compatibility with the density functional calculations since the DFT program (deMon) cannot handle the higher *l* functions in its present form. Thus, the AUG5 consists of a (33s,13p,5d)/[7s,6p,5d] contraction per atom. In addition, the d functions have been changed from spherical to Cartesian so that the Hartree-Fock results from this basis set can be directly compared with the DFT results from this basis. Thus, a total of 110 CGTO are used for NO while 165 CGTO are used for NO_2.

(4u) 168-U and (4r) 168-R: The 168 CGTO basis set for NO has a contraction of (19s,14p,3d,2f,1g)/[7s,8p,3d,2f,1g] per atom. The primary (19s,14p) functions are taken from Partridge [170], while the (3d,2f,1g) polarization functions are from Dunning [166]. The first fourteen s functions were contracted into two s functions using the first fourteen 1s and 2s atomic orbital coefficients. Similarly, the first seven p functions are contracted into one p function using the first seven 2p atomic orbital coefficients. This contracted basis set is further augmented by additional diffuse s and p functions from Partridge's supplementary functions for

$O^-(^2P)$ and $N^-(^3P)$ [170]. All components of the d, f and g functions are kept in the calculations.

(5u) 207-U and (5r) 207-R: The 207 CGTO basis set for NO_2 is obtained by removing all the g functions from the 168-CGTO basis set, thus giving a (19s,14p,3d,2f)/[7s,8p,3d,2f] contraction per atom.

(6u) 210-U and (6r) 210-R: This 210 CGTO basis set for NO is the augmented correlation-consistent, polarized valence quadruple-zeta basis set (aug-cc-pVQZ) of Dunning and co-workers [166-169]. The basis set consists of a (13s,7p,4d,3f,2g)/[6s,5p,4d,3f,2g] contraction per atom.

4.3.2 MRSD-CI, ACPF and QDVPT Calculations

(4c) 168-CI and (4a) 168-ACPF: The near Hartree-Fock limit 168-R calculation (described above in Section 4.3.1) was chosen as the initial reference calculation. The frozen-core, multi-reference singles and doubles excitations configuration interaction (MRSD-CI) and average coupled-pair functional (ACPF) [149] calculations were then performed (by Prof. E.R. Davidson at Indiana University with the MELD program) on both the neutral molecules and cation radicals with the neutral symmetry restricted ROHF K-orbitals [171-173]. The full ion-neutral overlap distributions were then calculated in the plane wave impulse approximation of the EMS cross-section via Eq. (2.53) to investigate the role of electron correlation and relaxation effects on the TMPs. The instrumental angular (momentum) resolution was included in the TMPs using the Gaussian-weighted planar grid method [59]. Various other electronic properties from these calculations are listed in Tables 4.1 and 4.2. The experimentally derived geometry for NO [154] was used in all calculations.

(5c) 207-CI, (5a) 207-ACPF and (5q) 207-QDVPT: The Hartree-Fock 207-R calculation (described above in Section 4.3.1) was chosen as the initial reference calculation. MRSD-CI and ACPF calculations were performed (by Prof. E.R. Davidson at Indiana University) with this basis set for NO_2 at the experimental geometry [155] according to the same procedure

described above for calculations 4c and 4a for NO. In addition, frozen-core, quasi-degenerate variational perturbation theory (QDVPT) calculations were also performed for the NO_2 molecule with this basis set.

(6c) 210-CI and (6a) 210-ACPF: The Hartree-Fock 210-R calculation (described above in Section 4.3.1) was chosen as the initial reference calculation. MRSD-CI and ACPF calculations were performed (by Prof. E.R. Davidson at Indiana University) with this basis set for NO at the experimental geometry [154] according to the same procedure described above for calculations 4c and 4a.

4.3.3 DFT Calculations

(3*l*) AUG5-L, (3p) AUG5-P and (3b) AUG5-BP: Three density functional calculations were carried out at UBC using the deMon program [122,123] and the large AUG5 orbital basis set (described above in Section 4.3.1 for calculations 3u and 3r) at the experimental geometries for NO [154] and NO_2 [155]. All calculations used a random extra-fine grid and the energy convergence was set at 10^{-7} hartree. The auxiliary basis set for fitting the charge density and exchange-correlation potential was the N/O (5,4;5,4) from the deMon program [122,123]. The AUG5-L calculation employs the local density approximation of Vosko et al. [112] while the AUG5-P calculation uses the non-local correlation functional of Perdew and Wang [115,117]. The AUG5-BP calculation uses a non-local combination of the correlation functional of Perdew and Wang [115,117] and the exchange functional of Becke [116]. The Kohn-Sham orbitals have been extracted from the result and the momentum profiles have been calculated using the TKSA via Eq. (2.58). The instrumental angular resolution effects [59] were also incorporated into the TMPs. Various other electronic properties from the DFT calculations are listed in Tables 4.1 and 4.2. However, as noted in Section 2.2.6, DFT total energies differ from the exact result [60] and thus the DFT total energies in Tables 4.1 and 4.2 are not readily comparable to those from Hartree-Fock methods, CI, ACPF and QDVPT. In addition, while the DFT calculations reported in the present work result in separate α and β molecular orbitals

and thus contain some degree of spin contamination, the $\langle \hat{S}^2 \rangle$ values are not tabulated in Tables 4.1 and 4.2 because the deMon program does not compute this expectation value (see Section 4.3.1 above for a discussion on spin contamination).

4.4 Results and Discussion

4.4.1 Comparison of Experimental and Theoretical Momentum Profiles

High momentum resolution measurements have been made of the outermost valence electron experimental momentum profiles (XMPs) for NO (2π, Fig. 4.2) and NO_2 ($6a_1$, Fig. 4.3). The XMP for NO was collected on the energy-dispersive multichannel EMS spectrometer (see Chapter 3) while the XMP for NO_2 was collected with a single channel instrument. On each figure the mean binding energy at which each particular XMP was measured is noted (9.54 eV for NO and 11.23 eV for NO_2). These values correspond to the vertical ionization potentials of the lowest lying peaks observed in the photoelectron spectra [174]. The outermost XMP for each molecule is well separated in energy from the rest of the valence ionization manifold, which ensures that all the observed intensity of the momentum profile is due to ionization to the lowest lying ion state only and contains no mixing with other ionization processes. While NO_2 is known to exist in equilibrium with its dimer N_2O_4 in the gas phase, photoelectron spectroscopy [175] has shown that the dimer concentration is negligible at low pressures (0.01 torr) and room temperature. Furthermore, the first PES peak from the dimer has been recorded at low temperatures and does not overlap extensively with the band from the HOMO of the monomer [175]. Since the present EMS experiments were done at even lower pressures (~ 10^{-4} torr) and the dimer peak at 12.39 eV was not observed in the EMS binding energy spectra, the present results contain no detectable contributions from N_2O_4.

Much better statistics have been obtained in the present work on NO compared to previous results [145-147]. In addition, the comparison of theory and experiment was

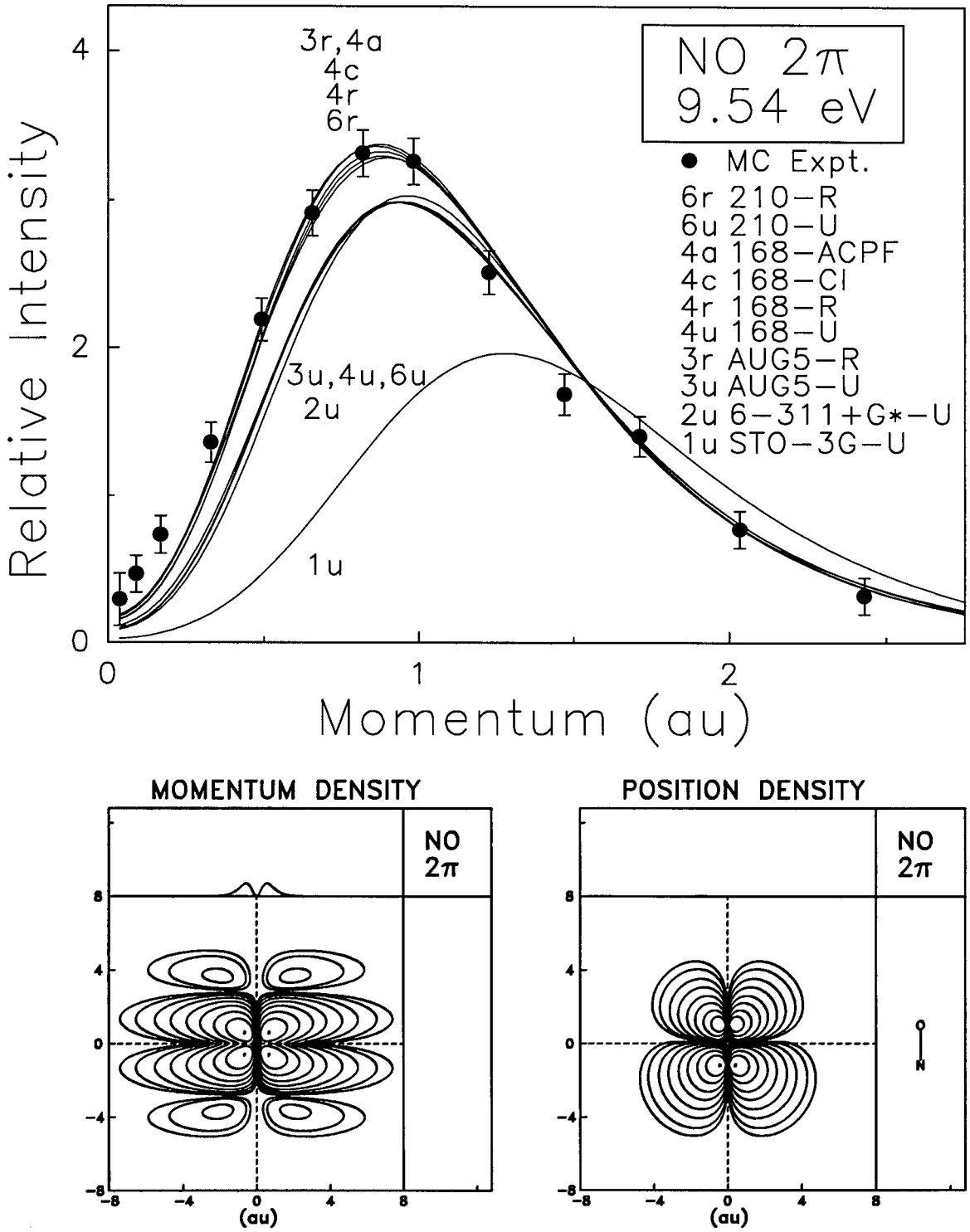

Fig. 4.2: Measured and calculated spherically averaged Hartree-Fock and post-Hartree-Fock momentum profiles for the 2π orbital of NO (upper panel). The lower panels show the momentum and position density contour maps for an oriented NO molecule calculated at the Hartree-Fock level using the 168-R basis set. The contours represent 0.01, 0.03, 0.1, 0.3, 1.0, 3.0, 10.0, 30.0, and 99.0% of the maximum density.

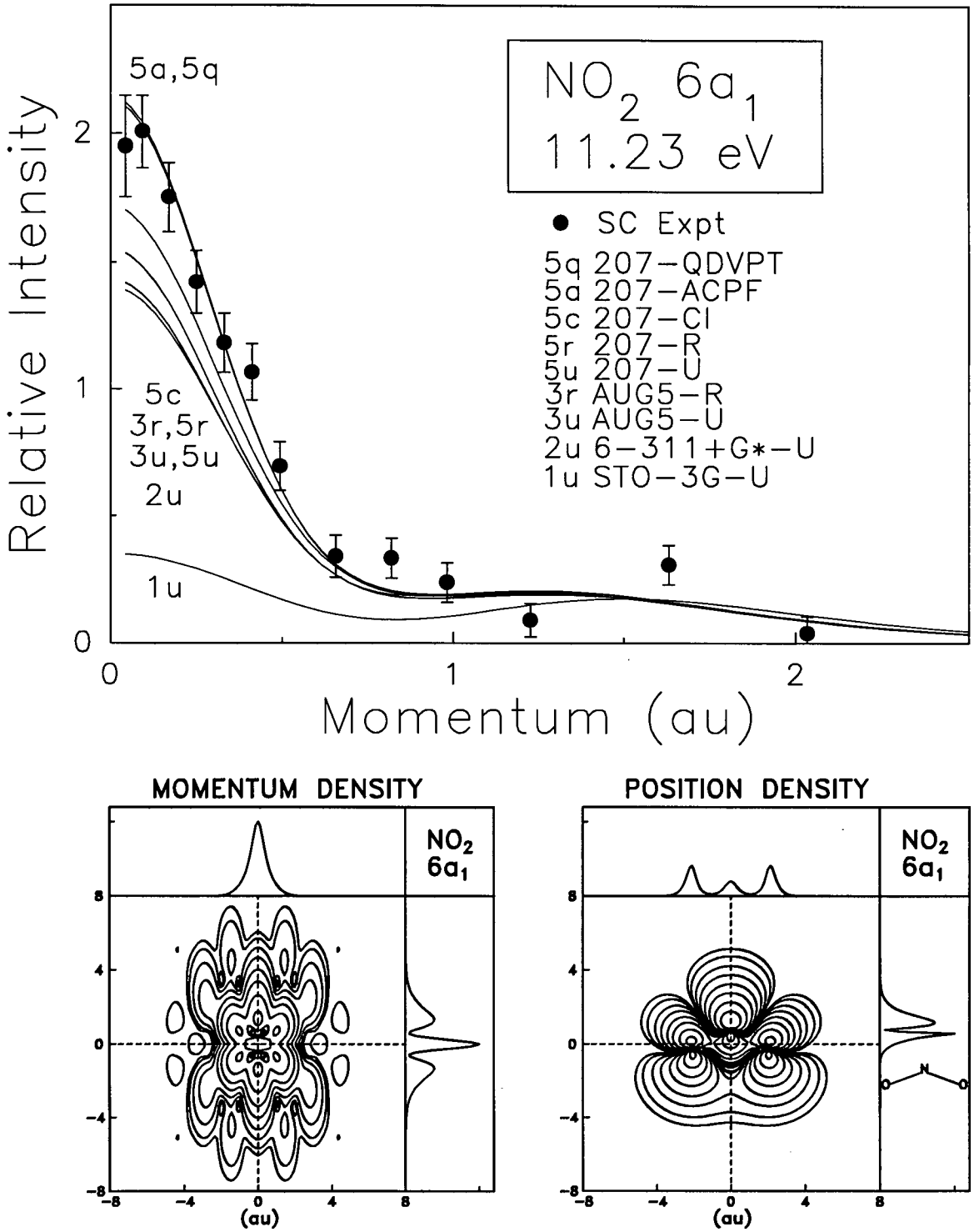

Fig. 4.3: Measured and calculated spherically averaged Hartree-Fock and post-Hartree-Fock momentum profiles for the $6a_1$ orbital of NO_2 (upper panel). The lower panels show the momentum and position density contour maps for an oriented NO_2 molecule calculated at the Hartree-Fock level using the 207-R basis set. The contours represent 0.01, 0.03, 0.1, 0.3, 1.0, 3.0, 10.0, 30.0, and 99.0% of the maximum density.

much more limited in previous work [145-147] because of the small basis sets used and also because no post-Hartree-Fock calculations were done. In the present work, the experimental momentum profiles are compared on Figs. 4.2 and 4.3 with the theoretical momentum profiles (TMPs) calculated at the UHF and ROHF Hartree-Fock level and also with MRSD-CI, ACPF and QDVPT ion-neutral overlaps as described in Sections 4.3.1 and 4.3.2 above. Selected properties for each calculation and corresponding experimental values are shown in Tables 4.1 and 4.2. The Hartree-Fock basis sets used range from a very modest minimal STO-3G basis to the very much larger 168-GTO, 207-GTO and 210-GTO basis sets developed in the course of the present work. The effects of many-body correlation and electronic relaxation are also seen on Figs. 4.2 and 4.3 from the MRSD-CI, ACPF and QDVPT calculations of the TMPs. The TMPs from the 210-CI and 210-ACPF treatments are very similar to their 168-CI and 168-ACPF counterparts and therefore these calculations are not shown on Fig. 4.2 but the properties are listed in Table 4.1. It should be noted that the experimental instrumental angular resolution has been accounted for in all theoretical momentum profiles in Figs. 4.2 and 4.3 using the GW-PG method [59].

Experiment and theory are placed on a common intensity scale for each molecule by normalizing the experiment to the 168-ACPF momentum profile for NO (Fig. 4.2) and to the 207-QDVPT momentum profile for NO_2 (Fig. 4.3), assuming unit pole strength. Since the wavefunctions are normalized all of the calculations are on a common relative intensity scale for each molecule. However, for profiles such as the NO_2 HOMO where s character is dominant (Fig. 4.3), it is often more difficult to distinguish the quality of TMPs than for p-type profiles such as the 2π orbital of NO. A change in relative intensity at low p is often the only major distinguishing characteristic between two TMPs for dominantly s-type momentum profiles such as the NO_2 HOMO. As such, other normalizations to the NO_2 XMP could be selected.

The UHF calculations of the momentum profiles in Figs. 4.2 and 4.3 show a trend of improving agreement with experiment as the basis set quality improves from the STO-3G

(curve 1u) which fits the observed XMPs very poorly, to the intermediate quality results (6-311+G*-U) to the large basis sets (curves 3u, 4u, 5u and 6u). There is a "UHF basis set limit" at which these Hartree-Fock momentum profiles tend to converge and little or no further improvement in shape fit with experiment is seen upon an increase in basis set size. An improvement in shape and/or intensity fit is brought about only by use of the ROHF method (curves 3r, 4r, 5r and 6r). ROHF calculations were also obtained for both molecules with the STO-3G and 6-311+G* basis sets (calculations 1r and 2r, respectively) and the results are given in Tables 4.1 and 4.2 (these TMPs are not shown in Figs. 4.2 and 4.3). The STO-3G-R momentum profile for NO_2 is identical to the STO-3G-U momentum profile. However, in all other cases in the present work the ROHF momentum profiles displayed a higher relative intensity at low momentum than their UHF counterparts. This effect is thought to be due to the influence of the energy minimization constraint in constructing Hartree-Fock wavefunctions. For an optimized UHF wavefunction, the additional flexibility introduced by different α and β spin manifolds leads to a lower total energy and a more contracted *r*-space HOMO density than an ROHF wavefunction with the same basis set. Thus, the ROHF method leads to a more diffuse *r*-space density distribution because of its additional orbital constraint. For the s-type HOMO of NO_2 (Fig. 4.3), the increased intensity is concentrated near $p = 0$ and no significant shape difference results between ROHF and UHF TMPs although ROHF leads to higher intensity at low p than UHF. As noted in Section 4.3.1 above, other calculated properties such as spin contamination differ considerably in the UHF and ROHF methods.

Turning to a more detailed consideration of the various UHF and ROHF calculations, it can be seen that the minimal basis set STO-3G-U results are in very poor agreement with both the observed experimental momentum profiles (curves 1u on Figs. 4.2 and 4.3) and electronic properties (Tables 4.1 and 4.2). For NO_2 in particular the STO-3G-U momentum profile exhibits a very different s to p ratio from the XMP and the other TMPs. The poor total energies for both molecules reflect the low degree of basis set saturation in the STO-3G-U calculations. While the dipole moments for NO and NO_2 are closer to experiment than those from several

large basis sets, it is well known that the STO-3G often produces accurate dipole moments because of a fortuitous error cancellation [57].

The 6-311+G*-U intermediate size basis set calculation (curve 2u on Figs. 4.2 and 4.3), including diffuse and polarization functions, provides a better description than the STO-3G-U wavefunction for each molecule. However, the low momentum regions of both XMPs are still underestimated. For NO_2 the 6-311+G*-U momentum profile is comparable to the results of the larger basis set Hartree-Fock (UHF and ROHF) calculations. With the exception of the dipole moment, general improvements are also obtained for other calculated properties for both molecules (Tables 4.1 and 4.2) relative to the STO-3G-U calculation.

The AUG5-U TMP (curves 3u on Figs. 4.2 and 4.3) provides a further small improvement in shape compared to the 6-311+G*-U momentum profile for NO. The AUG5-U momentum profile for NO_2 differs only in intensity from the 6-311+G*-U TMP. Improvements are also seen in most other properties in Tables 4.1 and 4.2.

As mentioned above, the UHF and ROHF momentum profiles from larger basis sets (curves 3u, 4u, 5u and 6u on Figs. 4.2 and 4.3) tend to converge. However, there is still some fluctuation in other properties with basis set size (Tables 4.1 and 4.2). In particular, there is still variation in total energy at the millihartree level. The dipole moments of NO and NO_2 also vary significantly with change in basis set size. Of the UHF calculations, the 168-U provides generally the best description of the range of properties considered here for NO while the 207-U provides the best description of the properties of NO_2. The 168-R and 210-R calculations provide good ROHF descriptions of the properties of NO while the 207-R gives the best ROHF description of the properties of NO_2 (due to its lowest total energy).

Post-Hartree-Fock methods such as CI calculations [11,12,37-40] have often provided a further significant improvement in the shape fit with the XMP over Hartree-Fock level calculations, particularly where second row atoms are involved. However, from Fig. 4.2 it can be seen that a comparably good description of the observed momentum profile of NO is achieved by the larger basis set restricted Hartree-Fock (AUG5-R (3r), 168-R (4r) and

210-R (6r)) and post-Hartree-Fock (168-CI (4c) and 168-ACPF (4a)) calculations. Although not shown on Fig. 4.2, the 210-CI and 210-ACPF TMPs give very similar results (see Table 4.1). There is still a small discrepancy between the NO XMP and all theory at low momentum below $p \sim 0.4$ au. This could be due to a very small amount of impurity NO_2 (see Section 4.2) but this is thought to be unlikely after an analysis of the experimental and theoretical momentum profiles. Although the 207-CI (5c), 207-ACPF (5a) and 207-QDVPT (5q) post-Hartree-Fock calculations for NO_2 are reasonably similar in shape to the ROHF momentum profiles (3r and 5r), they do show higher intensity at lower p and fit the XMP quite well within the statistical precision of the data. Despite the only small differences in the shapes of the TMPs relative to the near-Hartree-Fock limit TMPs, it should be noted that the post-Hartree-Fock calculations provide significant improvement in the total energies and dipole moments of both molecules (Tables 4.1 and 4.2). Since the post-Hartree-Fock calculations are based on initial ROHF Hartree-Fock results, they are free of spin contamination. It should also be noted that the post-Hartree-Fock calculations for NO using the 168-GTO basis set generally yield better values of the properties than those using the 210-GTO basis set for a given type of calculation.

The experimental momentum profiles are also compared on Figs. 4.4 and 4.5 with the DFT TMPs (see Section 4.3.3 above for a description of the calculation methods). For purposes of comparison, MRSD-CI, ACPF and QDVPT momentum profiles are also shown on Figs. 4.4 and 4.5. The XMPs have been normalized to the AUG5-BP DFT theoretical momentum profiles for the present comparisons in Figs. 4.4 and 4.5 (note that different normalizations were selected for Figs. 4.2 and 4.3). It can be seen that the DFT momentum profiles are more intense than the MRSD-CI, ACPF and QDVPT results. This can occur because overly spatially diffuse orbitals may result from some choices for the exchange-correlation functional in the Kohn-Sham calculations [60] and thus the momentum profile may be more intense at low p (by the reciprocity of r- and p-space).

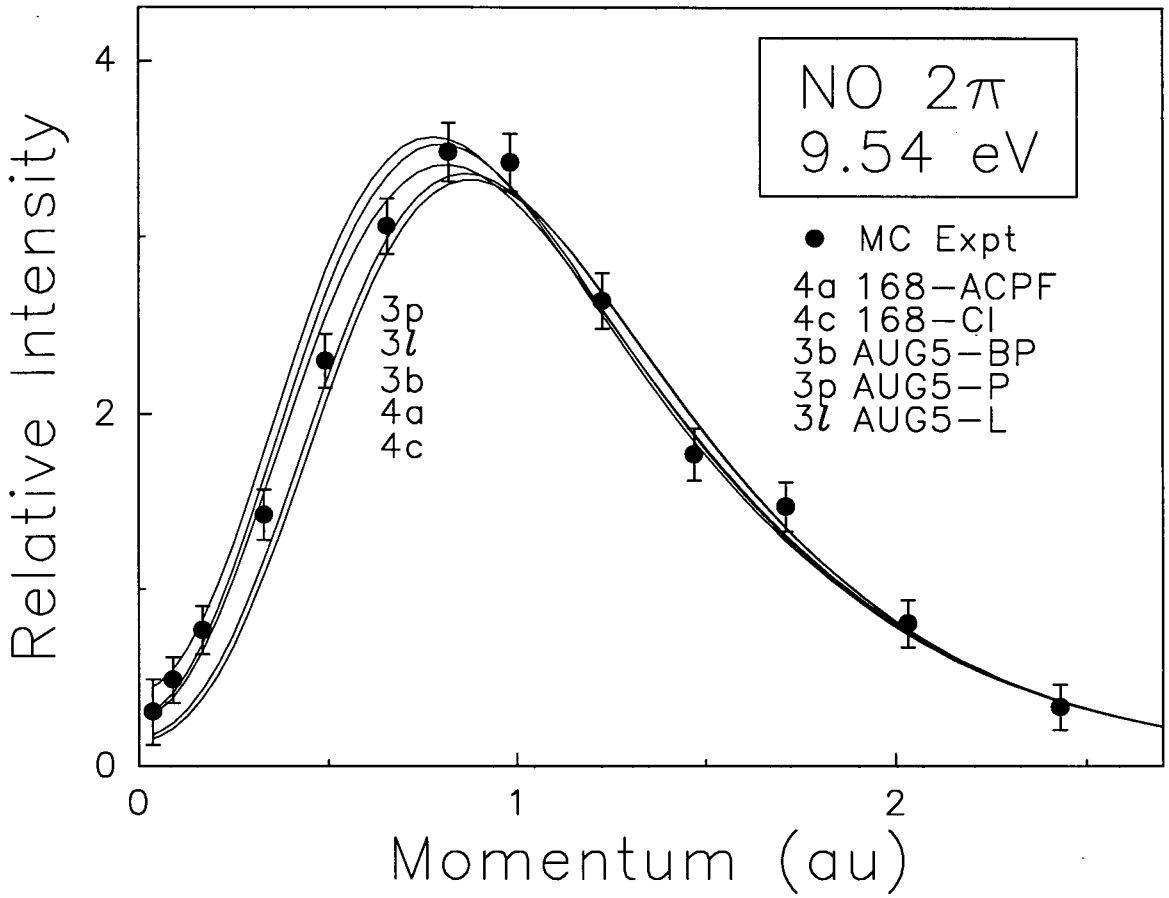

Fig. 4.4: Measured and calculated spherically averaged DFT momentum profiles for the 2π orbital of NO. The solid circles represent the experimental multichannel or single channel measurements also shown on Fig. 4.2. Selected MRSD-CI and ACPF calculated momentum profiles are also shown for comparison with the DFT momentum profiles. Note that the normalization of experiment to theory differs from that used in Fig. 4.2. See text for details.

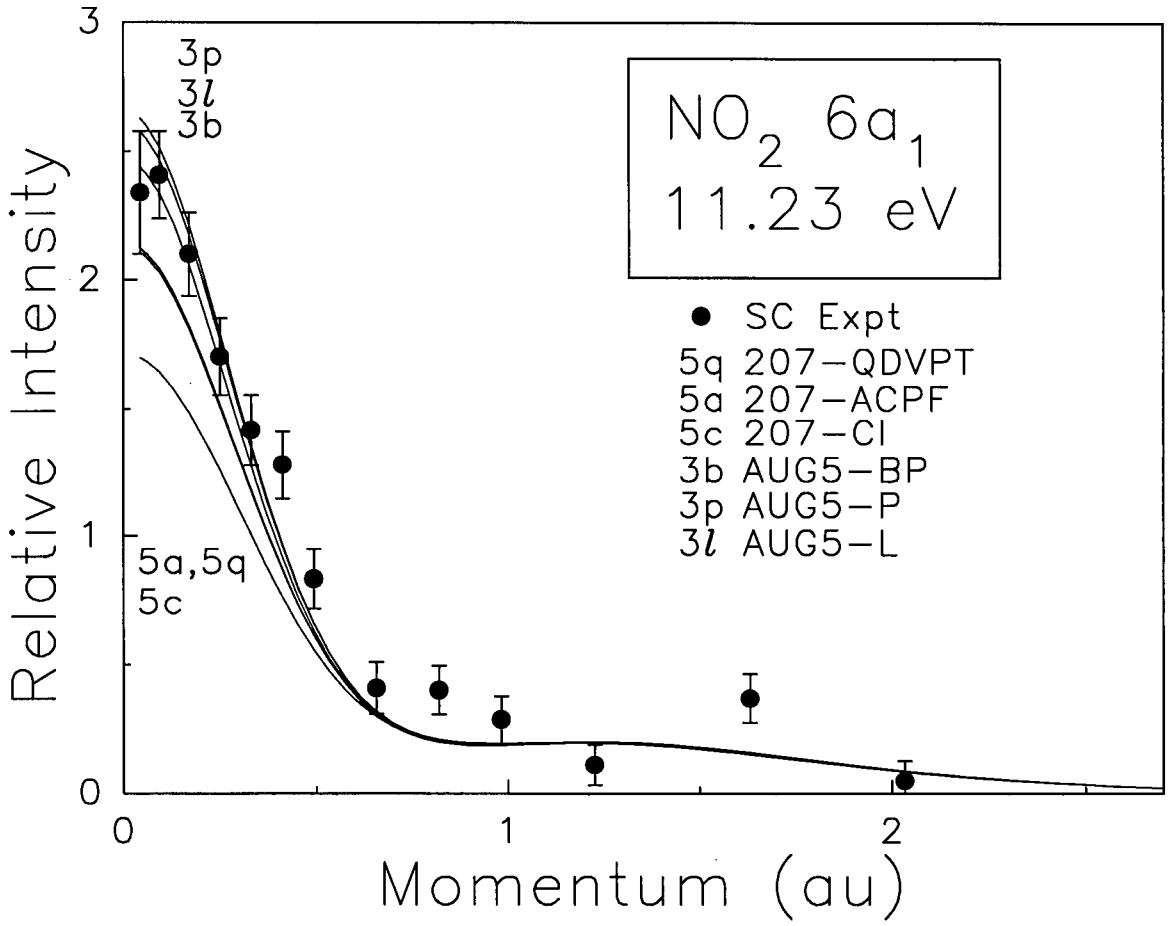

Fig. 4.5: Measured and calculated spherically averaged DFT momentum profiles for the $6a_1$ orbital of NO_2. The solid circles represent the experimental multichannel or single channel measurements also shown on Fig. 4.3. Selected MRSD-CI, ACPF and QDVPT calculated momentum profiles are also shown for comparison with the DFT momentum profiles. Note that the normalization of experiment to theory differs from that used in Fig. 4.3. See text for details.

It can be seen from Figs. 4.4 and 4.5 that there is quite good overall agreement between the DFT target Kohn-Sham momentum profiles and the experimental momentum profiles of both molecules. In terms of intensity of the DFT momentum profiles, the ordering is AUG5-P (curve 3p), AUG5-L (curve 3*l*) and AUG5-BP (curve 3b) for both molecules. For NO, there are some noticeable shape differences between the three DFT TMPs, with the Becke-Perdew non-local calculation (curve 3b) fitting the best. However, for NO_2 the shape differences between the DFT TMPs from the local density approximation and those from the non-local potentials are minimal. Thus, the local density approximation results appear to be at least as good a model of the momentum profiles for the HOMO of NO_2 as the more sophisticated non-local potential treatments.

Somewhat better agreement with the shape of the observed XMP of NO is given by the DFT curve 3b (Fig. 4.4) in the low momentum region (< 0.5 au) than for the high-level post-Hartree-Fock calculations (see Fig. 4.4, and also refer to curves 4c and 4a on Fig. 4.2). For NO_2, though, the intensities are more different and the shape fit with the XMP is roughly comparable to those from the Hartree-Fock and post-Hartree-Fock TMPs (compare Figs. 4.3 and 4.5). On comparing other properties, dipole moments from the DFT calculations (Tables 4.1 and 4.2) are within 0.1 Debye of experiment. While the DFT dipole moments for NO_2 are closer to experiment than those from MRSD-CI or ACPF, the opposite is true for the dipole moment of NO. It should be noted that some degree of spin contamination is present in the DFT calculations for open-shell molecules that is not present for the CI results but, as noted in Section 4.3.3, $\langle \hat{S}^2 \rangle$ from DFT was not computed. However, despite the spin contamination and the well-known problem of obtaining absolute energies from DFT, it can be said that the DFT treatments provide quite good values of the other properties in the present work.

4.4.2 Density Maps in Momentum and Position Space

The momentum and position space density contour maps corresponding to oriented NO and NO_2 molecules presented in Figs. 4.2 and 4.3 (bottom panels) are of pedagogical interest

and also provide some insight into the (spherically averaged) experimental and theoretical momentum profiles. These maps are slices of the orbital electron density $|\psi|^2$ through the molecular plane of each oriented molecule in position space and with momentum perpendicular and parallel with respect to the molecular plane in momentum space. The calculations are based on the near Hartree-Fock limit results for both molecules (168-R for NO and 207-R for NO_2) which have been found to provide good descriptions of the XMPs of these molecules at the Hartree-Fock level. The origin for the position space maps is the molecular center of mass and all dimensions are in atomic units. The side panels on each map show slices of the momentum or position space density along the vertical (right panel) and horizontal (top panel) dotted lines.

The HOMO of NO is predicted (from simple Hartree-Fock theory) to be a completely antibonding π^* orbital with no s-type contributions. Accordingly, the *r*-map (Fig. 4.2) for this molecule displays an orbital consisting mainly of atomic p-type functions on each atom. The p-type orbital components for NO are not of equal intensity on N and O. In addition, there is a "filling-in" along the perpendicular "nodal" plane in *p*-space. Since the Kouba and Ohrn treatment [148] was erroneously considered (see Section 4.2) to give the best fit to the momentum profiles in earlier work [145] the fact that the corresponding HOMO *r*-map of NO became more non-bonding (and hence less antibonding) as the amount of nodal character in the orbital decreased was thought to be significant. However, it has been found in the present work that the K&O-U wavefunction does not provide an acceptable fit to the NO XMP once the NO_2 impurity has been eliminated (see Section 4.2 and Fig. 4.1a). Thus any deductions [145] arising from the non-bonding or antibonding character of this orbital predicted using the Kouba and Ohrn wavefunction are inappropriate. It should also be noted that while there is some filling in along the perpendicular plane, the intensity at the origin of the *p*-map is exactly zero (see top panel). Thus, spherical averaging of this momentum density should give a momentum profile with zero intensity at $p = 0$. In this regard it should be noted that the calculated spherically averaged momentum profiles in Fig. 4.2 have non-zero intensity at $p = 0$ due to the

fact that they have been folded with the instrumental resolution function to compare with experiment.

The p-map for the $6a_1$ orbital of the triatomic species NO_2 (Fig. 4.3) is more complex than those for the diatomic NO molecule. The complexity of the p-map indicates the difficulties that often arise in interpreting momentum space representations for larger molecules. The multicenter nature of this molecule is reflected in the complex oscillatory behaviour in momentum space. It should be noted that the momentum space wavefunction contains all the symmetry characteristics of the position space wavefunction with the addition of an inversion center and thus the p-map contains a center of symmetry (even though such a symmetry element is not present in the C_{2v} point group). Finally, on the p-map there is a large momentum density at $p = 0$ (top and right panels in the p-map) and thus the spherically averaged NO_2 $6a_1$ momentum profile (Fig. 4.3) is strongly s-type in contrast to the p-type momentum profiles of NO (Fig. 4.2). In the r-map, the HOMO displays the a_1 symmetry characteristic of a totally symmetric orbital in the C_{2v} molecular point group.

Chapter 5

Molecular Oxygen

5.1 Introduction

The electronic structure of the oxygen molecule has been the subject of many theoretical and experimental studies. This interest is due in part to the great abundance of the molecule and to the important role it plays in living systems and in atmospheric processes [143]. The open-shell nature of O_2 adds a challenging aspect to quantum mechanical calculations that is not present for closed-shell molecules. Experimentally, He I and He II experiments [174,176-179] using high-resolution photoelectron spectroscopy (PES) for the valence shell ionization processes of O_2 have been reported up to ~ 28 eV binding energy. Gardner and Samson [180] extended the valence shell He II PES studies to ~ 40 eV binding energy and high resolution threshold PES studies using synchrotron radiation have also been reported [181]. In addition, x-ray photoelectron spectroscopy (XPS) studies up to ~ 32 eV [182] and ~ 60 eV [183] have been reported. The full valence shell binding energy spectrum has also been measured at low resolution (1 eV FWHM) by dipole (e, 2e) spectroscopy [184] and by electron momentum spectroscopy (2 eV FWHM) [185] out to ~ 60 eV.

The first reported study of O_2 by EMS was the early single channel experimental work of Suzuki et al. [185] in which valence electron momentum distributions corresponding to the major features in the binding energy spectrum up to 60 eV were obtained. However, no calculated binding energy spectra or theoretical momentum profiles were reported [185].

While no theoretical momentum profiles were presented in the work of Suzuki et al. [185], experimental momentum profiles were obtained for binding energies up to 60 eV. In some cases, the experimental momentum profiles corresponding to the production of the individual quartet and doublet ion states arising from ionization of the same orbital were obtained. The $a^4\Pi_u$ and $A^2\Pi_u$ ion states were difficult to deconvolute because of the limited statistics even with the higher energy resolution (1.2 eV FWHM) available at impact energies of 400 eV. In addition, the $1\pi_u$ ionization satellite peak at 23.7 eV could not be resolved from the nearby $c^4\Sigma_u^-$ state. On the basis of the shapes of the observed momentum profiles, the peaks at 39 and 47 eV were assigned to $^4\Sigma_g^-$ and $^2\Sigma_g^-$ ion states from $2\sigma_g$ ionization although no accounting for the total $2\sigma_g$ pole strength and the high binding energy region out to 60 eV was made. A further limitation was the limited statistical precision of the data due to low instrumental sensitivities [185]. In particular, the momentum profiles corresponding to the $C^2\Sigma_u^-$ and 33.0 eV final ion states showed large scatter [185].

Subsequent EMS work on O_2 by Tossell et al. [147] presented both experimental and theoretical momentum profiles for the five valence orbitals of O_2 but no binding energy spectra were reported. However, although the shapes of the observed momentum profiles agreed qualitatively with theory, the calculations used very limited basis set size [147]. Very limited statistics were also apparent and the momentum profiles corresponding to individual quartet and doublet states were not resolved [147].

The binding energy spectra of oxygen are more complex than for closed-shell cases because of the presence of both quartet and doublet final ion states which make the deconvolution and interpretation of the spectra more difficult. The ability of theory to predict the relative intensity of the quartet and doublet ion states in the EMS spectrum of oxygen (or other open-shell molecules) and their corresponding momentum profiles has not been investigated.

The initial orbital origin of the peak in the 33 eV region of the O_2 binding energy spectrum has been the subject of considerable dispute. Gardner and Samson [180] did not

include this energy region in their experiment while the XPS study of Siegbahn et al. [183] attributed the 33 eV peak to shake-up or more likely characteristic energy losses. The fact that the peak was observed at a comparable intensity in dipole (e, 2e) work [184], which was done at much lower pressure than the XPS study [183], suggested that energy losses undergone by ejected photoelectrons could be ruled out and that the peak at 33 eV was more likely due to final ion states arising from shake-up mechanisms. The propagator techniques used by Cederbaum and Domcke [65] calculated all of the $^2\Pi_u$ intensity to be at energies $\leq$ 27.3 eV while Dixon and Hull [186] predicted all the $^2\Pi_u$ intensity to be at $\leq$ 22.7 eV. Other theory by Honjou et al. [187,188] using configuration interaction wavefunctions placed all of the $^2\Pi_u$ intensity at energies $\leq$ 24.3 eV and predicted that the peak at 33.0 eV was mainly due to $^2\Sigma_u^-$ and (to a lesser extent) $^2\Sigma_g^-$ poles. The multiconfigurational electron propagator calculations of Yeager and co-workers [189,190] predicted that almost all the intensity due to ionization of $1\pi_u$ electron is below 24.56 eV and also indicated that a transition at ~ 34.7 eV is due to a $^2\Sigma_u^-$ state. The electron propagator techniques by Purvis and Öhrn [191] did not predict any poles in the 33 eV region. Gerwer et al. [192] suggested that the 33 eV peak be assigned as $^2\Pi_u$ since this led to reasonable agreement between their calculated total electronic ion state cross-sections for formation of $(1\pi_u)^{-1}$ ions and those obtained by measurements using dipole (e, 2e) spectroscopy [184] as well as He I PES experiments using a many line light source [193]. However, many corrections were required [192] for unresolved experimental final ion state cross-sections and the agreement between theory and experiment was only moderately good. On the basis of the observed p-type momentum profile and peak area arguments, Suzuki et al. [185] suggested that the peak at 33 eV was due to a $^2\Pi_u$ satellite associated with the $1\pi_u$ ionization process. However, this assignment [185] was not definitive since poles from $2\sigma_u$ ionization with $c^4\Sigma_u^-$ or $C^2\Sigma_u^-$ parent final ion states would also have p-type momentum distributions similar to those from poles corresponding to $^2\Pi_u$ ionic states. No momentum profiles were reported for the 33 eV region in the EMS work of Tossell et al. [147].

The above history indicates that improved experimental and more detailed theoretical investigations of O_2 are desirable. In the intervening years since the previous EMS studies on O_2 [147,185] large improvements in sensitivity have been achieved with the development of multichannel EMS spectrometers [42,44,45,47]. In addition, a range of much more sophisticated calculation methods using large basis sets are now possible with current computing devices. The present work now reports multichannel energy-dispersive electron momentum spectroscopy measurements of all valence orbital momentum profiles and complete valence shell binding energy spectra (up to 59 eV) for O_2 with improved statistical precision compared with previous work. The comparison of theoretical intensities to the experimental EMS binding energy spectrum and the subsequent theoretical modelling of the measured momentum profile intensities has also been carried out using a range of computational methods and basis sets. The EMS binding energy spectra including the more complex inner valence region are compared with the results of a new multi-reference singles and doubles configuration interaction (MRSD-CI) calculation of the ionic states using very large basis sets. The measured orbital momentum profiles are compared with a variety of Hartree-Fock treatments ranging from a minimal STO-3G basis to near Hartree-Fock limit quality basis sets including a 168 contracted Gaussian type orbital (168-GTO) calculation developed in the course of the present collaborative work. Both the Unrestricted Hartree-Fock (UHF) and Restricted Open-shell Hartree-Fock (ROHF) methods have been used to calculate momentum profiles in the present work. In addition, the effects of correlation and electronic relaxation on all of the valence orbital momentum profiles are also investigated with new MRSD-CI ion-neutral overlap calculations (168-G(CI)). In the case of the outermost $1\pi_g$ orbital ($^2\Pi_g$ final ion state) an averaged coupled-pair functional (ACPF) [149] calculation using the 168-GTO basis is also reported. Many-electron effects on all O_2 momentum profiles are further investigated with density functional methods, using the target Kohn-Sham approximation of the EMS cross-section [60] with local and non-local (gradient corrected) functionals.

In the present work, careful attention has also been given to obtaining individual experimental momentum profile measurements corresponding to the separate quartet and doublet final ion state exit channels arising from a common initial orbital origin. Experimental momentum profiles are provided for all of the orbital ionizations leading to the $X^2\Pi_g$, $a^4\Pi_u$, $A^2\Pi_u$, $b^4\Sigma_g^-$, $B^2\Sigma_g^-$, $^2\Pi_u(3)$, $c^4\Sigma_u^-$ and $C^2\Sigma_u^-$ final ion states as well as for the peak at 33 eV. The inner valence $2\sigma_g$ ionization ($^4\Sigma_g^-$ and $^2\Sigma_g^-$ final ion states) pole strengths have been studied by an analysis of the binding energy and momentum profiles for the high energy 36-59 eV region. The comparison of the calculated momentum profiles with individual experimental momentum profiles has been used to determine pole strengths for the $1\pi_u$ ionization peaks corresponding to the $A^2\Pi_u$ parent state and the $^2\Pi_u(3)$ satellite state (23.7 eV) and these pole strengths have been compared with previously published experimental [177,185] and theoretical [65,186-192] results. In a similar way, pole strengths for production of the $c^4\Sigma_u^-$ and $C^2\Sigma_u^-$ states from $2\sigma_u$ ionization have also been determined. An assignment of the peak at 33 eV in the binding energy spectra is provided by an analysis of the measured EMS and calculated MRSD-CI binding energy spectra and the pole strengths in the $(1\pi_u)^{-1}$ and $(2\sigma_u)^{-1}$ manifolds.

Multichannel measurements in the present work were obtained using the binning mode [45] of the EMS spectrometer (see Section 3.1). In addition, earlier non-binning mode (see Section 3.1) measurements were obtained for the $1\pi_g$ (HOMO) orbital of O_2 that is well-separated from the rest of the valence ionization spectrum (these non-binning measurements have been published in Ref. [94] with the results for NO and NO_2 shown in Chapter 4). The O_2 sample was obtained from Medigas gas products and was of > 99.0% purity. No impurities were observed in any of the spectra.

5.2 Hartree-Fock, MRSD-CI, ACPF and DFT Calculations

The basis sets for the O atom, calculation methods and calculation notation for O_2 are the same as described for NO in Sections 4.3.1-4.3.3 (with the exception that the calculations involving the 210-GTO basis set were for NO only). The number of CGTO for a given calculation method is the same for both NO and O_2. For example, the AUG5-U calculation for O_2 is designated as 3u, uses the same basis set for each O atom as described for the 3u calculation for NO in Section 4.3.1 and therefore employs a total of 110 CGTO. It should also be noted that calculations 1u, 1r, 2u, 2r, 3u, 3r, 3*l*, 3p and 3b for O_2 were performed at the University of British Columbia while calculations 4u, 4r, 4c and 4a were performed by Prof. E.R. Davidson at Indiana University with the MELD program. The experimentally derived geometry for O_2 [194] was used in all calculations. Various other calculated and experimental electronic properties for O_2 are listed in Table 5.1. The same considerations regarding total energy and spin contamination from the UHF, ROHF and DFT methods discussed in Sections 4.3.1 and 4.3.3 also apply to oxygen. It can be seen from Table 5.1 that all ROHF calculations (no spin contamination) give an $\langle \hat{S}^2 \rangle$ value of exactly 2.0 for O_2 while this value is exceeded in the UHF calculations. A large amount of spin-contamination in any wavefunction may cause inaccuracy in computed properties, but the spin contamination of the UHF wavefunctions in Table 5.1 is reasonably small (< 3%).

Because of the two unpaired α electrons in the $X^3\Sigma_g^-$ ground state of neutral oxygen, the calculation of the TMPs (and therefore also the theoretical binding energy spectra) corresponding to a given orbital electron ionization and final ion state is more detailed than for a closed-shell molecule. If an orbital other than the $1\pi_g$ (HOMO) orbital is ionized and a quartet final ion state is produced, then the ion state spin eigenfunction must result in a total spin of 3/2. One possible spin eigenfunction corresponds to the $\alpha(1)\alpha(2)\alpha(3)$ configuration for the three unpaired electrons in the ion. In this case it can be said that a β electron ionization process from the orbital of interest contributes to the TMP corresponding to the quartet ion

Table 5.1: Calculated and experimental properties for O_2 $X\,^3\Sigma_g^-$

	Basis Set and Calculation Method[a]	Total Energy (hartree)	$\langle \hat{S}^2 \rangle$	Θ_{zz} (au)[b]	$\langle r^2 \rangle_e$ (au)[c]	p_{max} (au)[d]
	Hartree-Fock Calculations					
1u	STO-3G-U	-147.634	2.0034	-0.9307	40.652	1.36
1r	STO-3G-R	-147.632	2.0000	-0.9258	40.649	1.36
2u	6-311+G*-U	-149.660	2.0488	-0.4304	43.744	1.10
2r	6-311+G*-R	-149.638	2.0000	-0.4708	43.673	1.07
3u	AUG5-U	-149.686	2.0488	-0.1574	43.446	1.07
3r	AUG5-R	-149.663	2.0000	-0.2304	43.385	1.05
4u	168-U	-149.691	2.0484	-0.2178	43.446	1.07
4r	168-R	-149.667	2.0000	-0.2768	43.386	1.05
	Post-Hartree-Fock Calculations					
4c	168-CI	-150.133	2.0000	-0.2766	43.337	1.03
4a	168-ACPF	-150.146	2.0000	-0.2716	43.410	1.03
	DFT Calculations[e]					
3*l*	AUG5-L	-149.338	—	-0.3259	43.878	0.96
3p	AUG5-P	-150.547	—	-0.3390	43.924	0.95
3b	AUG5-BP	-150.418	—	-0.3224	43.708	0.98
	Experimental	-150.326[f]		-0.29[g]	44.4±0.2[h]	1.0[i]

[a] Calculations performed at the experimental equilibrium bond length of 1.20748 Å (2.28181 au), Ref. [194].

[b] The quadrupole moment is defined as $\Theta_{zz} = (1/2)\left\langle \sum q_i (3z_i^2 - r_i^2) \right\rangle$, summing over all nuclei and electrons Calculated quadrupole moments are for a non-relativistic, non-vibrating, non-rotating molecule.

[c] The electronic spatial extent is defined as $\langle r^2 \rangle = \left\langle \sum r_i^2 \right\rangle$, summing over all electrons.

[d] The p_{max} corresponds to the value of momentum where the intensity of the momentum profile is at a maximum (see Figs. 5.4a and 5.4b).

[e] The total energy from Kohn-Sham DFT has been suggested to be in error because of shifted orbital energies relative to ionization potentials from Dyson's equation [60] - See also Section 2.2.6.

[f] The "experimental" total energy is the estimated non-relativistic, non-vibrating, infinite nuclear mass total energy. Total energy obtained by adding the atomic energies from Ref. [162] to the D_0 values from Ref. [159] plus the zero point energy from the frequencies in Ref. [159].

[g] Recommended value from Ref. [195].

[h] Ref. [196].

[i] Present work.

state [197]. However, a spin eigenfunction with total spin of 3/2 can also be constructed from a particular linear combination of the $\alpha(1)\alpha(2)\beta(3)$, $\alpha(1)\beta(2)\alpha(3)$ and $\beta(1)\alpha(2)\alpha(3)$ electron configurations for the ion. Thus, α electron ionization from the orbital of interest also makes a contribution to the TMP corresponding to the quartet final ion state. The relative contributions of these β and α electron ionizations to the TMP corresponding to a quartet ion state are 1 and 1/3, respectively [197]. Similarly, for ionization from an orbital (other than the HOMO) producing a doublet final ion state, the ion state spin eigenfunctions must result in a total spin of 1/2. The ion state spin eigenfunction corresponds to a linear combination of $\alpha(1)\alpha(2)\beta(3)$, $\alpha(1)\beta(2)\alpha(3)$ and $\beta(1)\alpha(2)\alpha(3)$ electron configurations only and therefore it can be said that only α electron ionization from the orbital of interest contributes to the TMP corresponding to a doublet final ion state. Lastly, the case for the HOMO $1\pi_g$ orbital is much simpler since only α electrons may be ionized and used for calculation of the TMP.

TMPs for closed-shell molecules are simply multiplied by the respective orbital occupancies (number of electrons) to put the TMPs for all orbitals on the same intensity scale. However, the situation for an open-shell molecule is more complicated. The rules for predicting relative intensities of final ion states for open-shell molecules have been well-noted in the PES literature [63,64,198]. The relative intensity for a given ion state with total spin S is proportional to the degeneracy of the final ion state g_f given by the product of the spin degeneracy factor P_{spin} equal to $(2S+1)$ and orbital factor P_{orbit} equal to the orbital degeneracy of the ion state [63,64,198]:

$$g_f \propto P_{\text{spin}} \cdot P_{\text{orbit}} \tag{5.1}$$

It should also be noted that where several states arise from ionization of an orbital of an open-shell molecule (i.e. doublets and quartets for O_2), the sum of the g_f factors associated with the various final ion states must equal the number of electrons in the orbital of origin [64]. This allows the intensities of the TMPs arising from ionization from the various orbitals of O_2 to be placed on a common scale. Thus in constructing the TMPs corresponding to the $^2\Pi_g$, $^4\Pi_u$,

$^2\Pi_u$, $^4\Sigma_g^-$, $^2\Sigma_g^-$, $^4\Sigma_u^-$ and $^2\Sigma_u^-$ final ion states of O_2 the factors g_f of 2, 8/3, 4/3, 4/3, 2/3, 4/3 and 2/3, respectively, are used to put them on a common relative intensity scale.

The various TMPs of the valence orbitals were obtained using Eq. (2.53) for the MRSD-CI and ACPF calculations (4c and 4a, respectively), Eq. (2.57) for the Hartree-Fock calculations (1u, 1r, 2u, 2r, 3u, 3r, 4u and 4r) and Eq. (2.58) for the DFT calculations (3*l*, 3p and 3b) according to the above considerations of the α and β electron ionization contributions to the quartet and doublet final ion states and the factors g_f for the various final ion states. The finite experimental momentum resolution (Δp ~ 0.1 au) was folded into all TMPs using the GW-PG method [59].

5.3 Results and Discussion

5.3.1 Binding Energy Spectra

Oxygen belongs to the $D_{\infty h}$ point group and its (open-shell) ground state valence shell electronic configuration in the Hartree-Fock approximation is

$$\underbrace{2\sigma_g^2 2\sigma_u^2}_{\text{inner valence}}\ \underbrace{3\sigma_g^2 1\pi_u^4 1\pi_g^2}_{\text{outer valence}}\quad X^3\Sigma_g^- \tag{5.2}$$

Removal of an electron from the valence orbitals gives the following experimentally reported O_2^+ ionic states [174,176-183]:

configuration	**ionic state**
$2\sigma_g^2 2\sigma_u^2 3\sigma_g^2 1\pi_u^4 1\pi_g^1$	$X^2\Pi_g$
$2\sigma_g^2 2\sigma_u^2 3\sigma_g^2 1\pi_u^3 1\pi_g^2$	$a^4\Pi_u, A^2\Pi_u, {}^2\Pi_u(3)$
$2\sigma_g^2 2\sigma_u^2 3\sigma_g^1 1\pi_u^4 1\pi_g^2$	$b^4\Sigma_g^-, B^2\Sigma_g^-$
$2\sigma_g^2 2\sigma_u^1 3\sigma_g^2 1\pi_u^4 1\pi_g^2$	$c^4\Sigma_u^-, C^2\Sigma_u^-$
$2\sigma_g^1 2\sigma_u^2 3\sigma_g^2 1\pi_u^4 1\pi_g^2$	$^4\Sigma_g^-, {}^2\Sigma_g^-, {}^4\Sigma_g^-(2), {}^2\Sigma_g^-(2)$

(5.3)

In addition, a satellite peak of disputed origin has been observed at 33.0 eV (labelled Q in the present work).

The $X^2\Pi_g$ ground ionic state from $1\pi_g$ ionization has a vertical ionization potential of 12.30 eV and is well resolved in the measured photoelectron spectra [174,176-180]. The valence shell ionization potentials reported in the He(I) and He(II) studies of Edqvist et al. [177] and Baltzer et al. [179] and the XPS results of Siegbahn et al. [183] are presented in Table 5.2. Results from the earlier EMS study of Suzuki et al. [185] are also shown in Table 5.2.

Ionization from orbitals other than the $1\pi_g$ HOMO results in an ion with three singly occupied orbitals and thus both quartet and doublet ion states are observed. Ionization of the $1\pi_u$ orbital gives the $a^4\Pi_u$ state at 16.7 eV, the parent $A^2\Pi_u$ state at 17.6 eV and a higher energy $^2\Pi_u(3)$ pole at 23.9 eV [179]. The presence of a $^2\Pi_u(2)$ pole of very low intensity is predicted to be at ~ 20 eV by theory [65,186,189,190]. This weak $^2\Pi_u(2)$ pole has not been identified experimentally [174,176-180]. It should be noted that other notation systems have been used for the predicted $^2\Pi_u(2)$ pole at ~ 20 eV [65,186,189,190] and the experimentally observed $^2\Pi_u(3)$ pole at ~ 23.7 eV. Baltzer et al. [179] employed a similar notation of $2\,^2\Pi_u$ and $3\,^2\Pi_u$ for these states, respectively, while Suzuki et al. [185] chose to ignore the predicted pole at ~ 20 eV and instead applied the notation $^2\Pi_u(2)$ to their experimentally observed pole at 23.7 eV. Suzuki et al. [185] also assigned the peak at ~ 33 eV in the EMS binding energy spectrum to $1\pi_u$ ionization and labelled the final ion state of this peak as $^2\Pi_u(3)$. In the present work, we label the peak at 33 eV simply as Q and discuss its possible orbital origin on the basis of the present experimental results and calculations in Section 5.3.2.4.

Ionization of a $3\sigma_g$ electron likewise leads to the separate quartet $b^4\Sigma_g^-$ and doublet $B^2\Sigma_g^-$ states which are observed in the photoelectron spectra at binding energies of 18.17 and 20.43 eV, respectively [174,177]. Similarly, removal of an electron from the inner closed shell $2\sigma_u$ orbital produces the O_2^+ $c^4\Sigma_u^-$ and $C^2\Sigma_u^-$ states. Baltzer et al. [179] have assigned these

Table 5.2: Experimental ionization energies and peak widths[a] for O_2

orbital origin[b]	final ion state[b]	Vertical ionization energies					Peak width
		PES [177]	PES [179]	XPS [183]	EMS [185]	EMS this work[c]	EMS this work[d]
$1\pi_g$	$X^2\Pi_g$	12.30	12.31	13.1	12.5	12.30	0.80
$1\pi_u$	$a^4\Pi_u$	16.70	16.70	17.0	16.8	16.7	1.00
$1\pi_u$	$A^2\Pi_u$	17.73	17.64		16.8	17.5	0.90
$3\sigma_g$	$b^4\Sigma_g^-$	18.17	18.17	18.8	18.1	18.2	0.52
$3\sigma_g$	$B^2\Sigma_g^-$	20.43	20.30	21.1	20.3	20.3	0.70
$1\pi_u$	$^2\Pi_u(3)$	24.0	23.9		23.7	23.7	1.50
$2\sigma_u$	$c^4\Sigma_u^-$	24.58	24.56	25.3	24.5	24.5	0.40
$2\sigma_u$	P,"$C^2\Sigma_u^-$"		27.3	27.9	27.5	27.4	2.40
	Q			33.6	32.5	33.0	1.40
$2\sigma_g$	$^4\Sigma_g^-$			39.6	39	38.9	2.25
$2\sigma_g$	$^2\Sigma_g^-$			41.6	39	40.9	2.00
$2\sigma_g$	$^4\Sigma_g^-(2)$			46	47	45.2	3.00
$2\sigma_g$	$^2\Sigma_g^-(2)$			48	47	48.4	3.00

[a] All ionization energies and peak widths are in eV.
[b] Assignments from Refs. [174,177,179,183,185] with the exception of the peak at 33.0 eV which has been labelled Q in the present work.
[c] Energy position of the maximum of the Gaussian function width for this final ion state used in the deconvolution procedure.
[d] Natural half-width of the Gaussian function for this final ion state used in the deconvolution procedure.

processes to ionization potentials of 24.56 eV and 27.3 eV, respectively. However, the present MRSD-CI results (Table 5.3) and other calculations [187-190] predict the presence of strong $^4\Sigma_u^-$ poles that overlap the peak traditionally associated with the $C^2\Sigma_u^-$ ionic state. This predicted dual character is supported by the present experiments and therefore we label the peak at 27.3 eV as peak P in the present work and discuss its composition in Section 5.3.2.4. The $^2\Pi_u(3)$ and $c^4\Sigma_u^-$ states are difficult to separate because of their closeness in energy. The observed ionization potentials for the peak corresponding to the $c^4\Sigma_u^-$ final ion state reported by high resolution experiments [177,179,180] are ~ 0.9 eV less than that reported in the XPS work of Siegbahn et al. [183].

Ionization of the inner-valence $2\sigma_g$ orbital produces the $^4\Sigma_g^-$ and $^2\Sigma_g^-$ states. Due to the more limited energy resolution of XPS, the vertical ionization potentials of these states are not as well-characterized as the lower energy states. Siegbahn et al. [183] reported $^4\Sigma_g^-$ and $^2\Sigma_g^-$ vertical ionization potentials of 39.6 and 41.6 eV, respectively, while Gardner and Samson [180] reported values of 39.7 and 40.3 eV. The threshold PES experiments of Ellis et al. [181] gave similar values of 39.5 and 40.8 eV. In addition, the pole strength of these states is thought to be further split into several satellite processes both from considerations of experiment [181,183,184,185] and theory [187-191]. The earlier studies [181,183,184,185] all showed that the inner valence region of the binding energy spectrum of O_2 is split into satellite peaks at ~ 46 and 48 eV. In Table 5.2 these states are labelled [185] as $^4\Sigma_g^-(2)$ and $^2\Sigma_g^-(2)$. However, additional satellite processes must occur since the intensity continues out to the limit of the data at 59 eV.

Fig. 5.1 shows the binding energy spectra of O_2 from 9 to 59 eV for measurements at relative azimuthal angles of (a) $\phi = 0.5°$ and (b) $\phi = 8.5°$ (impact energy of 1200 eV + binding energy) on a common intensity scale and at an energy resolution of 1.5 eV FWHM. Fig. 5.1c shows the summed binding energy spectra of O_2 from 9 to 59 eV for azimuthal ϕ angles of 0.5°, 1.5°, 3.5°, 5.5°, 8.5°, 9.5°, 12.5°, 13.5°, 16.5°, 17.5°, 20.5°, 24.5° and 30.5°. The energy scale was calibrated with respect to the $1\pi_g$ vertical ionization potential as measured by high

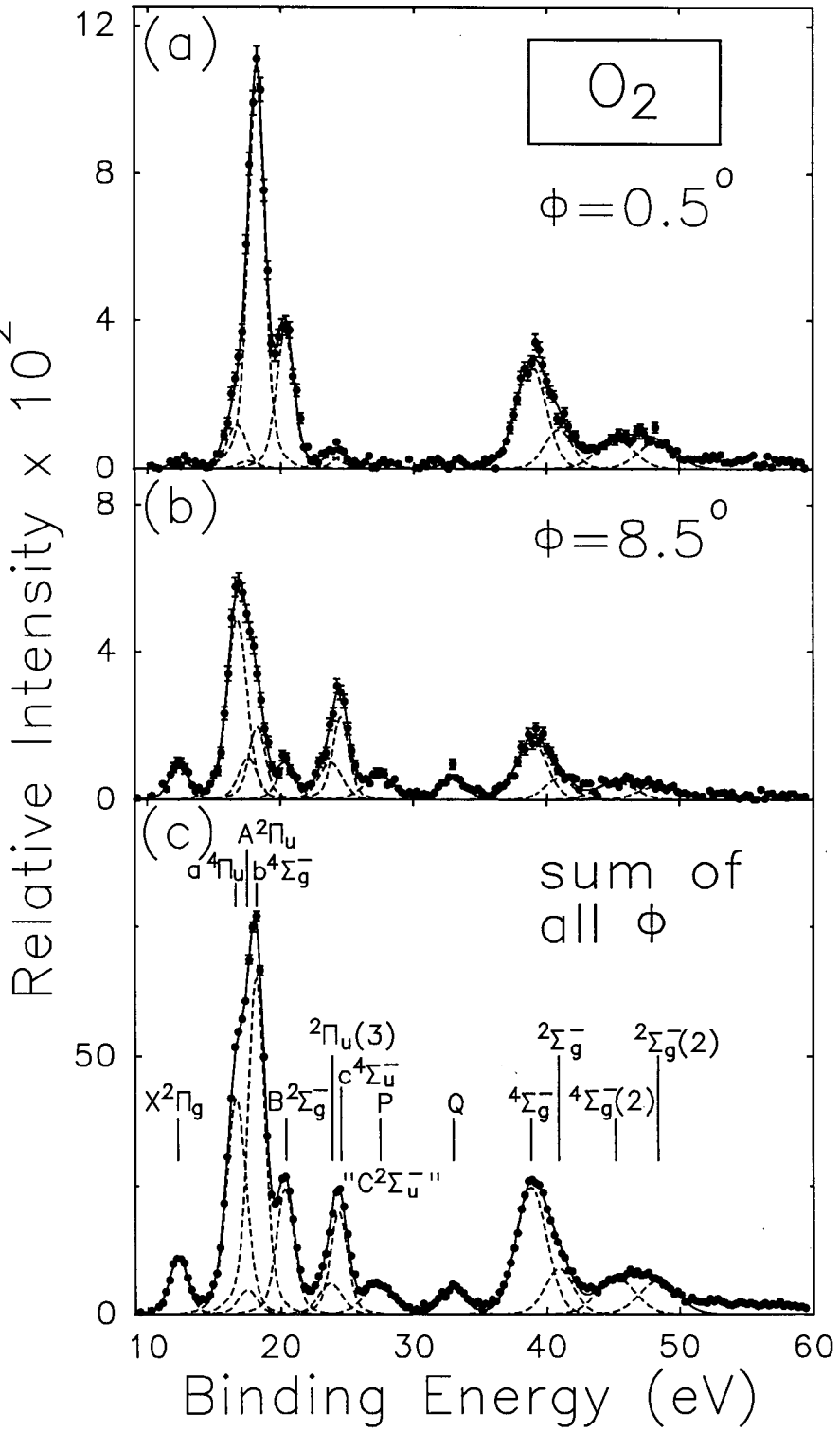

Fig. 5.1: EMS binding energy spectra of O_2 from 9 to 59 eV at **(a)** ϕ = 0.5°, **(b)** ϕ = 8.5° and **(c)** over all thirteen ϕ angles, obtained at an impact energy of (1200 eV + binding energy). The dashed lines represent Gaussian fits to the peaks and the solid curve is the summed fit. See text for details.

resolution photoelectron spectroscopy [174,177]. Gaussian peak shapes have been fitted to the main peaks throughout the spectra in Fig. 5.1a-c using vertical ionization potentials and Franck-Condon widths (folded with the EMS instrumental energy width of 1.5 eV FWHM) estimated from photoelectron spectroscopy measurements [174,177,179,183]. The relative energy spacings of the Gaussian peaks were estimated from the vertical ionization potentials, with small adjustments to compensate for the asymmetries in the shapes of the Franck-Condon envelopes. For the states above 30 eV, energies and widths were more difficult to determine because of the lower energy resolution of the XPS studies [183]. Measured and calculated ionization potentials from the literature and those used in the present work are shown in Table 5.2. The peak widths used in the present work to fit the experimental EMS binding energy spectra in Fig. 5.1 are also given in Table 5.2.

In the outer valence region of the $\phi = 0.5°$ and $\phi = 8.5°$ experimental binding energy spectra, several features can be seen in each spectrum. A peak due to the $1\pi_g$ ionization process (the $X^2\Pi_g$ state) is observed at a binding energy of 12.30 eV, which is consistent with the results of photoelectron spectroscopy [174,177,179]. This peak displays characteristic "p-type" behaviour, having a greater intensity at $\phi = 8.5°$ than at $\phi = 0.5°$. The band from 15 to 21 eV contains four ionization processes. The quartet and doublet states arising from $1\pi_u$ ionization (the $a^4\Pi_u$ and $A^2\Pi_u$ states) are observed at 16.7 and 17.5 eV, respectively, in agreement with the observed PES spectrum [174,177,179]. These two states are clearly p-type and are difficult to deconvolute because of their close spacing [177,179] and because of the low intensity of the $A^2\Pi_u$ state. The next two quartet and doublet states ($b^4\Sigma_g^-$ and $B^2\Sigma_g^-$) arise from ionization of the $3\sigma_g$ orbital. The energies of these peaks are also consistent with the literature values of 18.17 eV and 20.43 eV [174,177,179]. The $b^4\Sigma_g^-$ state is very intense and "s-type" so that it has greater intensity at $\phi = 0.5°$ than at $\phi = 8.5°$. Thus, although the $b^4\Sigma_g^-$ state is very close to the $A\,^2\Pi_u$ state, the separation of the two states is aided in the EMS binding energy spectra by their different symmetries (i.e. s-type and p-type, respectively). Since the B $^2\Sigma_g^-$ state also arises from the $3\sigma_g$ orbital, it is likewise s-type.

The presence of the $^2\Pi_u(3)$ satellite peak arising from $1\pi_u$ ionization has been reported to be at 23.90 eV [179]. The EMS binding energy spectra and associated curve fit in Fig. 5.1 show a p-type momentum profile at an energy of 23.7 eV which can be identified with the $^2\Pi_u(3)$ satellite. This process is close in energy to the nearby $c^4\Sigma_u^-$ state at 24.56 eV [179] and it is clear from Fig. 5.1b that two ionization processes are present in this energy region. The $c^4\Sigma_u^-$ state arises from $2\sigma_u$ ionization and is also p-type. The closeness of these two states (and the fact that both are p-type) complicates the deconvolution of the spectrum in this region.

A further ionization process, traditionally labelled [174,176-183] as the $C^2\Sigma_u^-$ state from $2\sigma_u$ ionization has been observed at 27.3 eV using high resolution photoelectron spectroscopy [179]. However, the present work (see Section 5.3.2.4 below) indicates that an additional ion state ($^4\Sigma_u^-$) contributes to the ionization in this energy region. In view of this situation the peak observed (Fig. 5.1) at 27.4 eV is referred to as peak P. In addition, the satellite peak labelled Q in the present work is observed at 33.0 eV in Fig. 5.1. The photoelectron study of Siegbahn et al. [183] gives a vertical ionization potential of 33.6 eV for this peak while the value of 32.5 eV from Suzuki et al. [185] is in better agreement with the present work.

The observed binding energy spectra (Fig. 5.1) in the high energy region from 36-59 eV are complex. An XPS study by Siegbahn et al. [183] assigned the broad peak at ~ 39 eV to contain the two $^4\Sigma_g^-$ and $^2\Sigma_g^-$ states from $2\sigma_g$ ionization at vertical ionization energies of 39.6 and 41.6 eV, respectively. However, it should be noted that energy positions are more difficult to determine with the lower energy resolution of XPS. Deconvolution of the EMS binding energy spectra in the present work gives slightly different results (Table 5.2) of 38.9 and 40.9 eV. Both states are clearly s-type, which is consistent with earlier EMS measurements [185]. Siegbahn et al. [183] also observed states in the high energy region at 46 and 48 eV which they assigned to be $^4\Sigma_g^-(2)$ and $^2\Sigma_g^-(2)$ satellite states from $2\sigma_g$ ionization. Suzuki et al. [185] supported this conclusion by measurement of the EMS momentum profiles. The EMS binding energy spectra in the present work also show intensity in this region and Gaussian peaks have been fitted to these dominantly s-type peaks at 45.2 and 48.4 eV

(Table 2). In addition, the spectra in Fig. 5.1 show a high energy tail (mainly s-type) out to the limit of the data at 59 eV.

Calculated binding energy spectra are compared with the measured binding energy spectra in Fig. 5.2. Theory and experiment have been area normalized below 36 eV binding energy in the $\phi = 8.5°$ spectrum The calculated spectra are obtained by using the pole energies and pole strength S_f^2 values given by the presently reported 168-CI MRSD-CI calculation (see Table 5.3) as well as the angular dependence from the presently reported 168-CI theoretical momentum profiles for each pole at each angle. The measured EMS instrumental energy resolution function, as well as the widths of the transitions as observed in the experimental EMS binding energy spectra (see Fig. 5.1 and Table 5.2) have been folded into the calculated spectra. Good agreement is obtained between experiment and theory for the $1\pi_g$ orbital ($X^2\Pi_g$ final ion state). The correct shapes and positions are also reasonably well predicted at both angles for the band from 15 to 21 eV which contains four closely spaced ion states with two different symmetries. The intensity of the peak at ~ 20.5 eV corresponding to the $B^2\Sigma_g^-$ state (Table 5.2) is underestimated by theory at $\phi = 8.5°$ with the present normalization. In addition, the widths and positions in the 23-25 eV energy region are not well reproduced by theory (the closely-spaced $^2\Pi_u(3)$ and $c^4\Sigma_u^-$ states are observed in this region - see Fig. 5.1 and Table 5.2). The experimental and theoretical intensities for peaks P and Q observed experimentally at ~ 27.5 eV and ~ 33 eV are in agreement, but the energy positions predicted by theory are about 1 eV too high. Large discrepancies in energy positions and intensities also occur at both angles for the $^4\Sigma_g^-$ and $^2\Sigma_g^-$ states at ~ 39 eV. The difference in intensity between experiment and theory in this region can likely be attributed to the presence of higher energy satellite processes clearly visible in the experimental spectra out to the 59 eV limit not taken into account by the MRSD-CI calculation. The MRSD-CI calculation in the present work only takes into account states up to ~ 42 eV (see Table 5.3). In this regard, it should be noted that the MRSD-CI calculations are not expected to be accurate above the double ionization potential of O_2

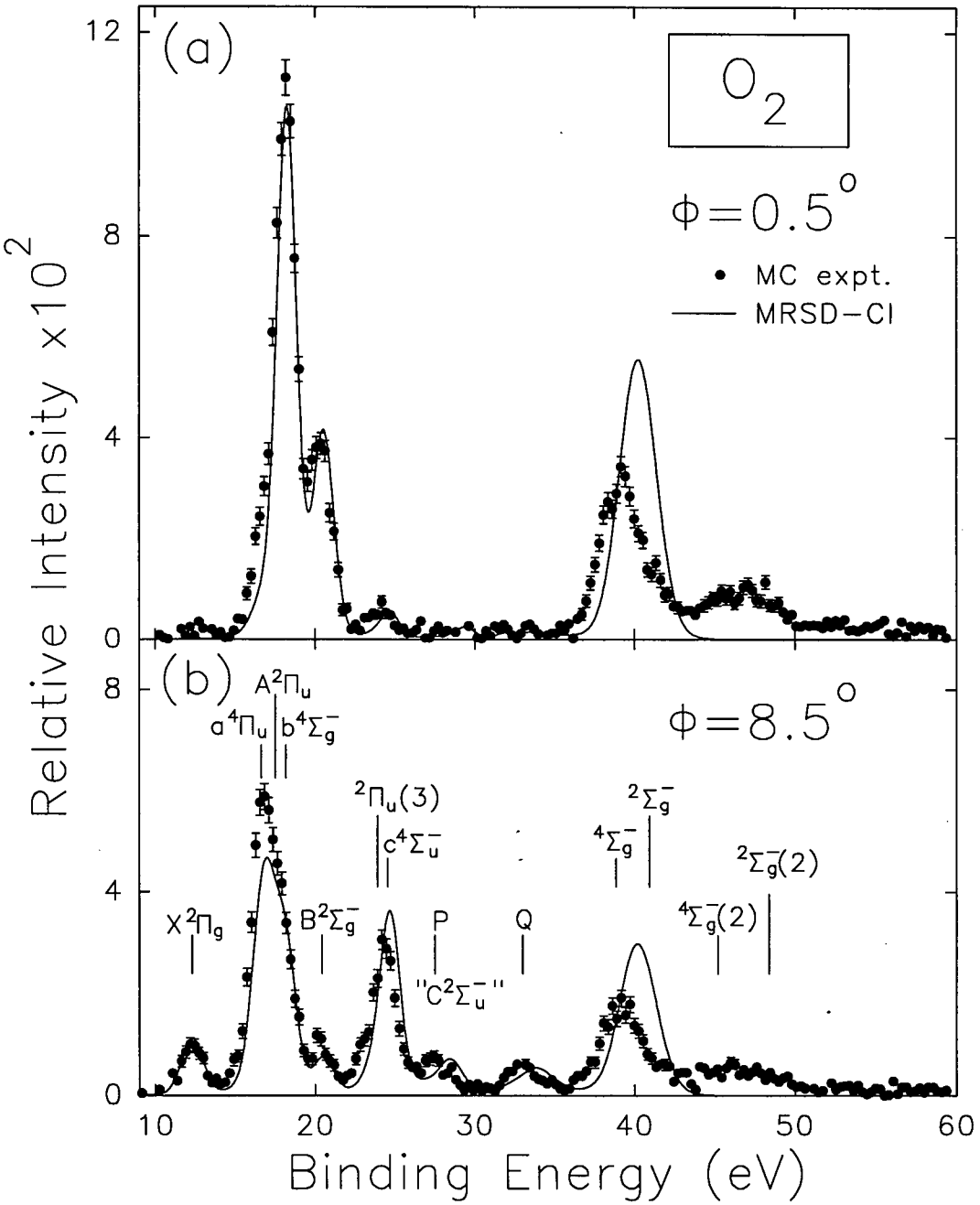

Fig. 5.2: Measured and calculated binding energy spectra of O_2 from 9 to 59 eV at **(a)** ϕ = 0.5° and **(b)** ϕ = 8.5°. The solid curves indicate the synthesized theoretical binding energy spectra with pole energies and pole strengths (Table 5.3) given by the 168-CI MRSD-CI calculation which was also used for the angular dependence. The same energy peak widths as used in Fig. 5.1 have been folded into the synthesized spectra. The theoretical and experimental binding energy spectra are area normalized on the 9-36 eV region at ϕ = 8.5°. See text for details.

Table 5.3: MRSD - CI states and intensities (pole strengths) for O_2^+

State	Energy (au)	Energy (eV)	S_f^2 [a]	$1.23S_f^2$ [b]	Excitation	Coefficient
$^2\Sigma_g^-$	-149.3924	20.53	0.807	0.993	$(3\sigma_g)^{-1}$	0.91
	-148.9729	31.94	0.039	0.048	$(\pi_u)^{-1}(\pi_g)^{-1}(3\sigma_u)^1$	0.82
	-148.9360	32.94	0.020	0.025	$(\pi_u)^{-1}(2\sigma_u)^{-1}(\pi_g)^1$	0.80
	-148.9023	33.86	0.053	0.065	$(3\sigma_g)^{-1}(\pi_u)^{-2}(\pi_g)^2$	0.63
					$(\pi_u)^{-1}(2\sigma_u)^{-1}(\pi_g)^1$	0.53
	-148.6451	40.86	0.182	0.224	$(3\sigma_g)^{-1}(\pi_u)^{-2}(\pi_g)^2$	0.49
					$(2\sigma_g)^{-1}(2\sigma_u)^1(\pi_u)^{-1}(\pi_g)^1$	0.52
					$(2\sigma_g)^{-1}$	0.45
$^2\Sigma_u^-$	-149.2367	24.76	0.059	0.039	$(3\sigma_g)^{-1}(1\pi_u)^{-1}(1\pi_g)^1$	0.91
	-149.1290	27.69	0.270	0.332	$(3\sigma_g)^{-1}(1\pi_u)^{-1}(1\pi_g)^1$	0.74
					$(2\sigma_u)^{-1}$	0.55
	-148.9011	33.89	0.375	0.461	$(2\sigma_u)^{-1}$	0.61
					$(3\sigma_g)^{-1}(1\pi_u)^{-1}(1\pi_g)^1$	0.52
	-148.7611	37.70	0.029	0.036	$(1\pi_u)^{-2}(3\sigma_u)^1$	0.89
$^4\Sigma_u^-$	-149.2387	24.71	0.652	0.802	$(2\sigma_u)^{-1}$	0.84
	-149.1007	28.46	0.102	0.125	$(3\sigma_g)^{-1}(1\pi_u)^{-1}(1\pi_g)^1$	0.77
	-148.6945	39.52	0.025	0.031	$(3\sigma_g)^{-2}(3\sigma_u)^1$	0.71
	-148.5913	42.32	0.006	0.007	$(1\pi_u)^{-2}(2\sigma_u)^{-1}(1\pi_g)^2$	0.82
$^4\Sigma_g^-$	-149.4768	18.23	0.853	1.049	$(3\sigma_g)^{-1}$	0.92
	-149.0655	29.42	0.019	0.023	$(\pi_u)^{-1}(\pi_g)^{-1}(3\sigma_u)^1$	0.86
	-148.7941	36.81	0.009	0.011	$(\pi_u)^{-1}(2\sigma_u)^{-1}(\pi_g)^1$	0.66
					$(3\sigma_g)^{-1}(\pi_u)^{-2}(\pi_g)^2$	0.48
	-148.6705	40.17	0.773	0.951	$(2\sigma_g)^{-1}$	0.85
$^2\Pi_g$	-149.6947	12.30	0.815	1.002	$(1\pi_g)^{-1}$	0.91
	-149.2016	25.72	0.021	0.026	$(1\pi_u)^{-2}(1\pi_g)^1$	0.91
	-148.8933	34.11	0.011	0.014	$(1\pi_u)^{-2}(1\pi_g)^1$	0.80

Table 5.3: Continued

State	Energy (au)	Energy (eV)	S_f^2 [a]	$1.23S_f^2$ [b]	Excitation	Coefficient
$^2\Pi_u$	-149.4860	17.98	0.303	0.373	$(1\pi_u)^{-1}$	0.93
	-149.4366	19.16	0.004	0.005	$(1\pi_u)^{-1}$	
	-149.2561	24.23	0.477	0.587	$(1\pi_u)^{-1}$	0.73
	-148.8406	35.54	0.023	0.028	$(3\sigma_g)^{-1}(1\pi_g)^{-1}(3\sigma_u)^1$	0.59
					$(3\sigma_g)^{-2}(1\pi_u)^{-1}(1\pi_g)^2$	0.43
$^4\Pi_u$	-149.5291	16.81	0.838	1.031	$(1\pi_u)^{-1}$	0.94

[a] In the present work renormalized pole strengths are used when comparing with experiment - see discussion in Section 5.3.2.

[b] The renormalized pole strength is equal to $1.23 \times S_f^2$. The factor of 1.23 is the scaling factor used to normalize the MRSD-CI calculation in Fig. 5.3a (see Section 5.3.2).

(~ 36.3 eV) because of the presence of highly excited Rydberg states of O_2^+ converging on the double ionization limit.

5.3.2 Comparison of Experimental and Theoretical Momentum Profiles

Experimental and theoretical spherically averaged momentum profiles have been obtained for each of the valence orbitals of O_2. The experimental momentum profiles are extracted from the multichannel binning mode binding energy spectra. The relative intensities for the different transitions are maintained by the sequential, angular-correlated data collection process. The Gaussian fitting procedure, described above in Section 5.3.1 for the binding energy spectra, is used to determine the relative intensities of the various transitions at each azimuthal angle ϕ. The experimental momentum profile corresponding to a particular final ion state is obtained by plotting the area under the corresponding fitted peak for each electronic state of the ion as a function of p (i.e. ϕ angle). With this procedure all experimental momentum profiles are automatically placed on a common relative intensity scale. The theoretical momentum profiles are obtained as described in Section 5.2.

The experimental and theoretical momentum profiles (shown on an angle (ϕ) scale because of the wide range of binding energy included - see Eq. (2.45)) have been placed on a common intensity scale by normalizing the experimental data, summed from 9-36 eV, to the AUG5-BP theory summed over the outer valence orbitals ($1\pi_g$, $1\pi_u$, $3\sigma_g$) plus the $2\sigma_u$ orbital as shown in Fig. 5.3a. The $2\sigma_g$ orbital has been left out of the summation on Fig. 5.3a because:

(1) as can be clearly seen on Fig. 5.1, there is apparently $2\sigma_g$ intensity beyond the limit of the experimental data which extends out to 59 eV

(2) little or no $2\sigma_u$ intensity is predicted [187-191] above 36 eV

(3) the momentum profile analysis of the $2\sigma_u$ ionization processes giving $^4\Sigma_u^-$ and $^2\Sigma_u^-$ final ion states as shown in Figs. 5.6 and 5.7 and discussed in Section 5.3.2.4 below accounts for essentially all the intensity below 36 eV.

(4) this range is below the double ionization potential of O_2 - see discussion in Section 5.3.1 above.

It should be noted that all the TMPs in Fig. 5.3a are shown at unit pole strength except for the 168-CI momentum profile (curve 4c) which was constructed using the MRSD-CI poles in Table 5.3 each with their respective pole strength (S_f^2) value. It is clear from Fig. 5.3a that only the density functional theory calculations predict the correct shape of the observed XMP from 9-36 eV, especially in the low momentum region (below $\phi = 10°$). A shape very different from experiment is predicted at lower momenta (angles) by the Hartree-Fock and CI calculations. The AUG5-BP density functional theory calculation which includes both correlation and exchange has been chosen for normalization of the experimental data. However, the local (AUG5-L) and correlation-only (AUG5-P) density functional theory calculations give very similar results. The normalization factor obtained in the above procedure for Fig. 5.3a has been used for each individual orbital for all experimental and all theoretical comparisons (see Figs. 5.4-5.7) in the present work. The CI calculation (curve 4c) has much lower intensity than experiment because the chosen normalization to the AUG5-BP curve assumes that virtually all of the ionization intensity for the orbitals lies within the energy range 9-36 eV. The CI calculation however predicts typically only ~ 80% of each ionization manifold in the binding energy range below 36 eV (see Table 5.3) with the "missing" pole strength unaccounted for and presumably located at higher binding energies. In order to treat the CI calculation in a manner consistent with the above normalization scheme, a second curve (4C, equal to 1.23×4c) has been constructed on Fig. 5.3a to provide the best intensity and shape fit between CI and experiment at least in the region above $\phi = 10°$. At lower ϕ angles the CI calculation provides a poor shape fit to experiment. It should be noted that this factor corresponds to the same normalization of CI to experiment as was used for the binding energy spectra in Fig. 5.2. Similarly, the summed experimental and theoretical momentum profiles over the entire measured binding energy range from 9-59 eV (Fig. 5.3b) for the valence orbitals ($1\pi_g$, $1\pi_u$,

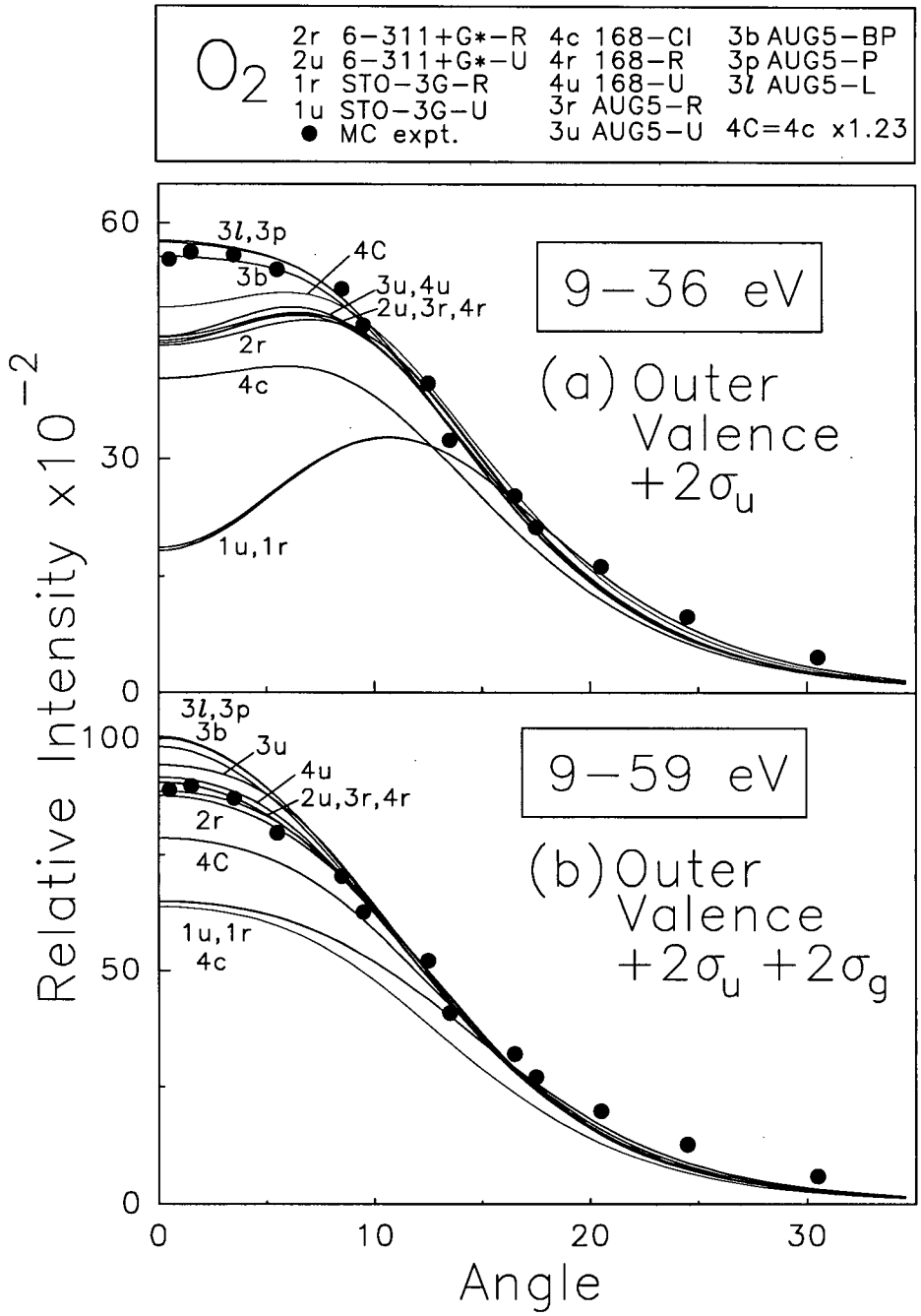

Fig. 5.3: Summed experimental and calculated spherically averaged momentum profiles for the **(a)** outer valence + $2\sigma_u$ orbital and **(b)** outer valence + $2\sigma_u$ + $2\sigma_g$ orbitals of O_2. The experimental data points are obtained by summing the measured binding energy spectra from 9 to 36 eV (Fig. 5.3a) and 9 to 59 eV (Fig. 5.3b) at each azimuthal angle (momentum). The solid curves are the sum of the respective momentum profiles calculated by several quantum mechanical methods and a wide variety of basis sets (see Section 5.2 for descriptions of the calculations). It should be noted that the summed theoretical curves take into account the g_f factors for quartet and doublet states (see text for details). The momentum resolution has been folded into all calculations using the GW-PG method [59] before summation. The experimental data has been normalized to the AUG5-BP calculation in Fig. 5.3a and this same normalization factor has been applied to the data in Fig. 5.3b and all individual orbital momentum profiles (see Figs. 5.4-5.7). Note that the 168-CI calculation (curve 4c) is also shown as 1.23 × 4c (curve 4C). See text for details.

$3\sigma_g$, $2\sigma_u$ and $2\sigma_g$) have also been constructed using the same normalization factor for experiment and theory from Fig. 5.3a. The 168-CI momentum profile (curve 4c in Fig. 5.3b) was constructed using the MRSD-CI poles in Table 5.3 each with their respective S_f^2 value. Good agreement for shape is obtained between experiment and all calculations over the entire angular range of the data in Fig. 5.3b. Although the better Hartree-Fock calculations are close to the summed experimental data, the DFT calculations predict slightly greater intensity than experiment, particularly at the lower momenta. In this regard, additional extra $2\sigma_g$ intensity is expected above the upper limit of the experimental binding energy (59 eV) as discussed above. The discrepancy between theory and experiment above $\phi = 20°$ is likely due to distorted wave effects [12] at higher momenta. The 168-CI momentum profile predicts a lower intensity than experiment and this may be due to the remaining pole strength (S_f^2) which is likely located in the high energy range above 36 eV. In a manner similar to Fig. 5.3a, a second CI curve (4C) has been constructed by multiplying curve 4c by a factor of 1.23. This curve matches the experiment better than curve 4c, although it still does not predict all the experimental intensity. The renormalized MRSD-CI pole strengths ($1.23\times S_f^2$) are also shown in Table 5.3.

The experimental and theoretical momentum profiles corresponding to each of the various ion states associated with the five valence orbitals of O_2 (see Section 5.3.1) are presented in Figs. 5.4-5.7 using the above normalization. The energies shown on Figs. 5.4-5.7 correspond to the binding energy peak maxima of the ion states observed in the present work (see Fig. 5.1 and also Table 5.2). The Hartree-Fock and DFT TMPs are presented at unit pole strength on Figs. 5.4a-d, 5.5a-d and 5.7b-d. In the other panels of Figs. 5.4-5.7, the Hartree-Fock and DFT TMPs are presented at a pole strength scaled by a factor to shape fit the XMP and to determine an experimental pole strength (the factor required in each case is indicated in each panel). The ACPF profile has only been calculated for the HOMO (see Figs. 5.4a and 5.4b) and is presented at unit pole strength. The MRSD-CI theoretical momentum profiles (curves 4C) in Figs. 5.4-5.7 are presented at their renormalized pole strengths ($1.23\times S_f^2$) from Table 5.3.

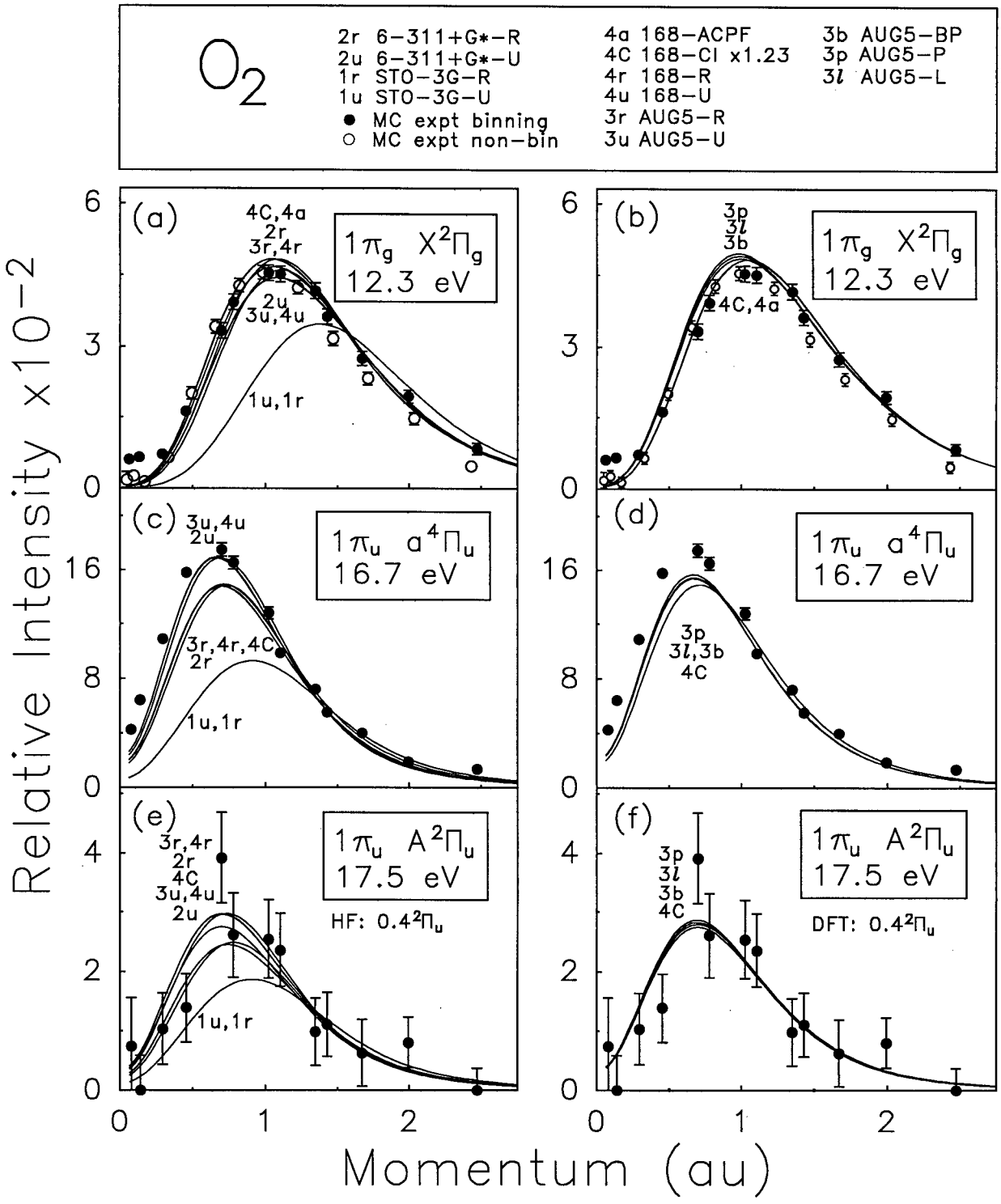

Fig. 5.4: Measured and calculated spherically averaged momentum profiles for the $1\pi_g$ ($X^2\Pi_g$) and $1\pi_u$ ($a^4\Pi_u$, $A^2\Pi_u$) orbitals of O_2. The solid circles represent the experimental energy-dispersive multichannel measurements obtained in the present work with the binning mode of the EMS spectrometer. The open circles represent the experimental energy-dispersive multichannel measurements obtained earlier in this laboratory using the non-binning mode of the same EMS spectrometer. All calculations have been spherically averaged and folded with the experimental momentum resolution. See text for details.

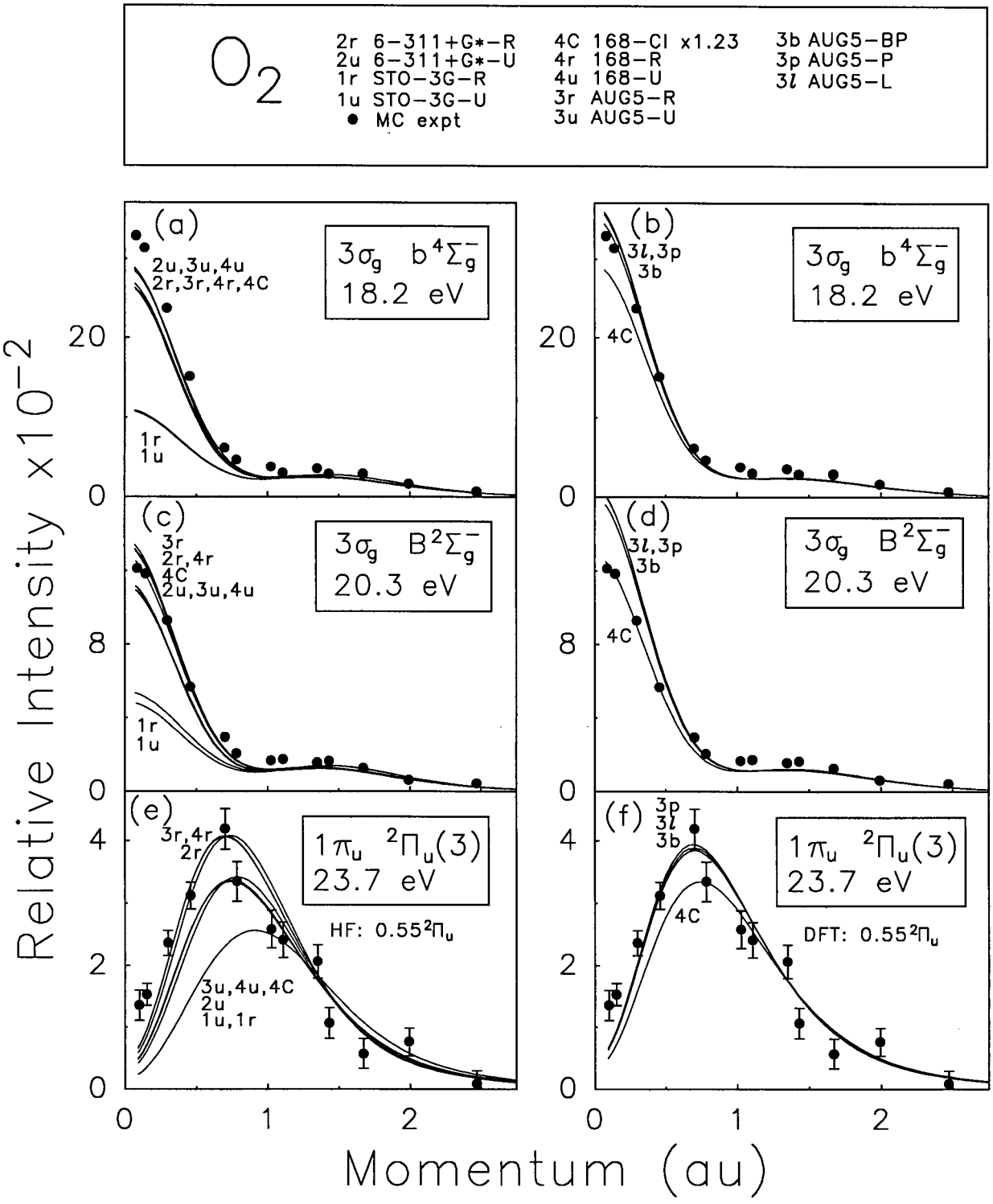

Fig. 5.5: Measured and calculated spherically averaged momentum profiles for the $3\sigma_g$ ($b^4\Sigma_g^-, B^2\Sigma_g^-$) and $1\pi_u$ ($^2\Pi_u(3)$) orbitals of O_2. The solid circles represent the experimental energy-dispersive multichannel measurements obtained in the present work with the binning mode of the EMS spectrometer. All calculations have been spherically averaged and folded with the experimental momentum resolution. See text for details.

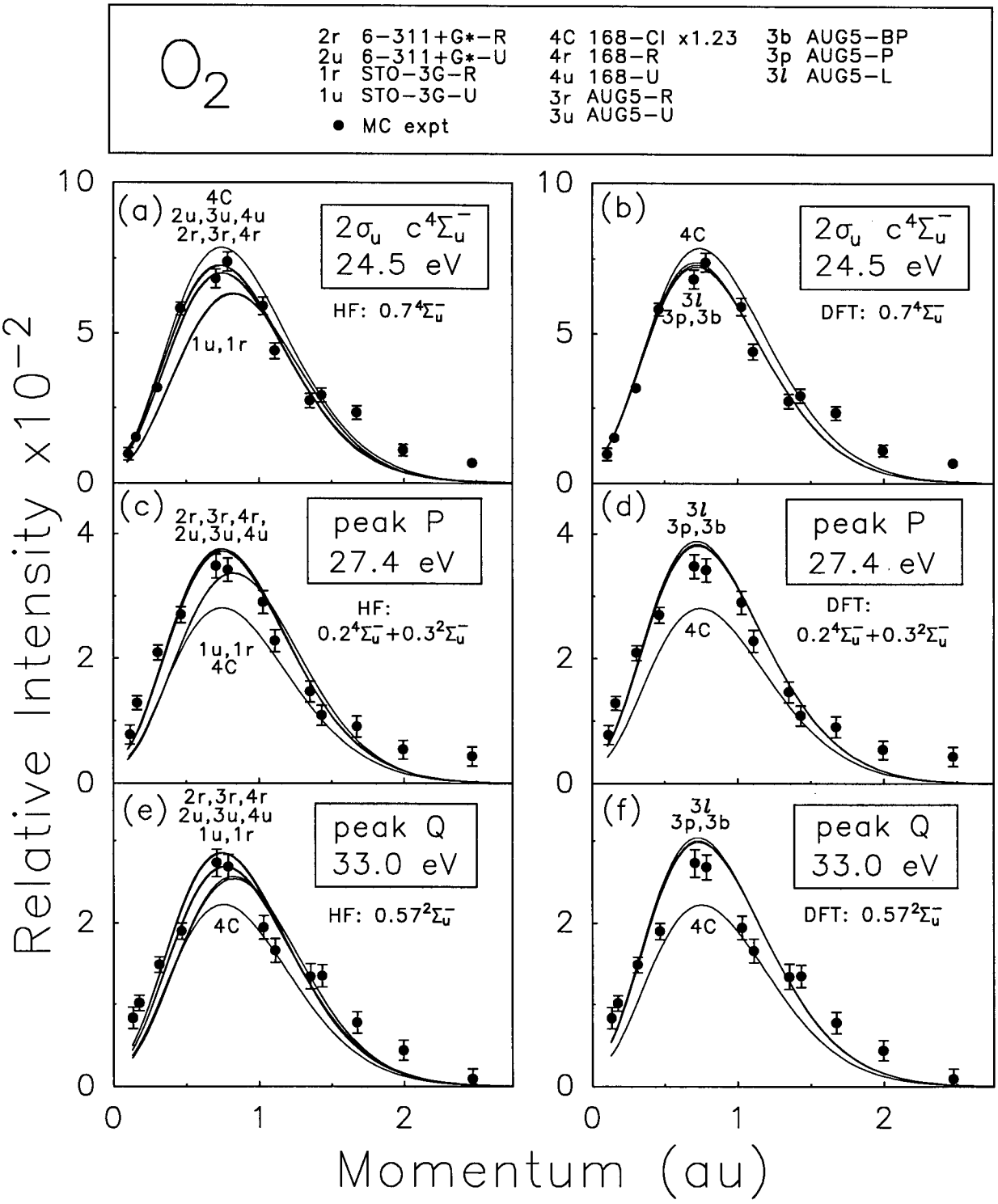

Fig. 5.6: Measured and calculated spherically averaged momentum profiles for the $2\sigma_u$ ($c^4\Sigma_u^-$, P, Q) orbital of O_2. The solid circles represent the experimental energy-dispersive multichannel measurements obtained in the present work with the binning mode of the EMS spectrometer. All calculations have been spherically averaged and folded with the experimental momentum resolution. See text for details.

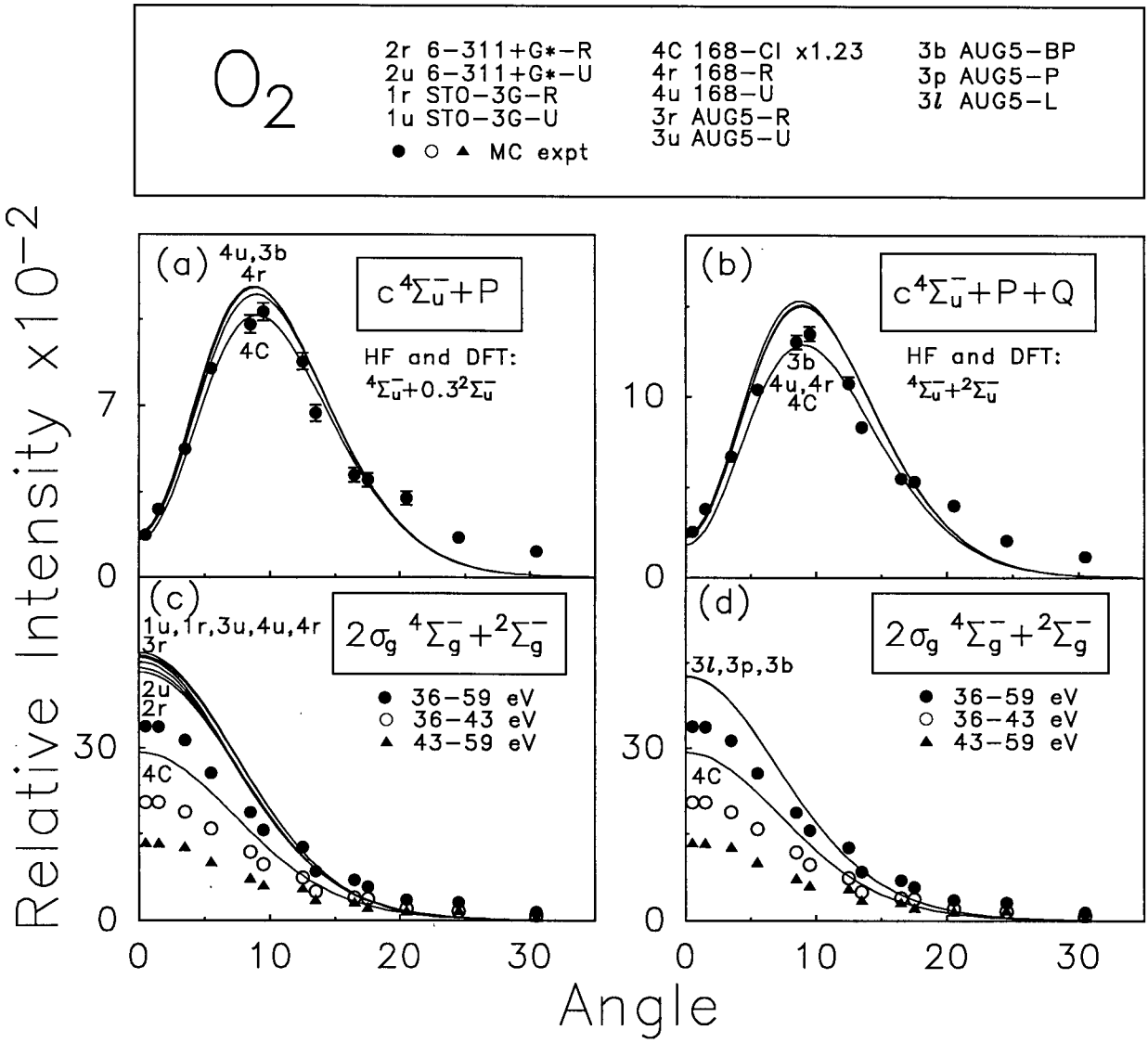

Fig. 5.7: Measured and calculated spherically averaged momentum profiles corresponding to sums of states as indicated and for the $2\sigma_g$ ($^4\Sigma_g^-$, $^2\Sigma_g^-$) orbital of O_2. The solid circles represent the experimental energy-dispersive multichannel measurements obtained in the present work with the binning mode of the EMS spectrometer. All calculations have been spherically averaged and folded with the experimental momentum resolution. See text for details.

5.3.2.1 The $1\pi_g$ Orbital ($X^2\Pi_g$ Final Ion State)

The experimental momentum profile for the $1\pi_g$ orbital of O_2 ($X^2\Pi_g$ final ion state) is shown in Figs. 5.4a and 5.4b. The outermost XMP is well separated in energy from the rest of the valence ionization manifold, which ensures that all the observed intensity of the momentum profile is due to ionization to the lowest lying ion state only and contains no mixing with other ionization processes. The solid circles in Figs. 5.4a and 5.4b represent the experimental energy-dispersive multichannel measurements obtained for the HOMO in the present work with the binning mode of the EMS spectrometer (see Section 3.1). The open circles in Figs. 5.4a and 5.4b represent experimental energy-dispersive multichannel measurements for the HOMO obtained earlier in this laboratory using the same EMS spectrometer in the non-binning mode (see Section 3.1). In Figs. 5.4a and 5.4b the non-binning data have been renormalized to the presently obtained measurements (solid circles) in the region of the maximum.

The $1\pi_g$ experimental momentum profile is compared on Fig. 5.4a with the various theoretical momentum profiles (TMPs) calculated at the UHF and ROHF Hartree-Fock level and also with the MRSD-CI and ACPF ion-neutral overlaps as described in Section 5.2 above. Selected properties for each calculation and corresponding experimental values are shown in Table 5.1. The Hartree-Fock basis sets used range from a minimal STO-3G basis to the very much larger 168-GTO basis set. The effects of many-body correlation and electronic relaxation are also seen on Fig. 5.4a from the MRSD-CI and ACPF calculations of the TMPs. The 168-CI momentum profile in Fig. 5.4a corresponds to the $^2\Pi_g$ MRSD-CI pole at 12.30 eV (Table 5.3). The slightly higher cross-section than is expected from theory or symmetry considerations at very low p was persistently observed. The reason for this is not at present understood. Calibration using the Ar 3p orbital showed the expected nodal behaviour at the lowest momenta.

As might be expected, there is a large disagreement between the STO-3G minimal basis set calculations (curve 1u and 1r) and the observed shape and intensity of the XMP. The intermediate size basis set 6-311+G*-U calculation (curve 2u) gives better agreement with

experiment than the STO-3G calculations but it still underestimates the $p < 1$ au region of the XMP. The larger size basis set UHF calculations (curves 3u and 4u) are in better agreement with experiment with regard to shape and the similarity of curves 3u and 4u suggests that the UHF momentum profiles are essentially converged at this level of basis set size. Similarly, the higher level ROHF momentum profiles generally agree better with experiment as the basis set size is increased. The ROHF momentum profiles with intermediate and large size basis sets for this orbital generally display a higher relative intensity at low momentum than UHF calculations (of the same basis set size). The converged ROHF momentum profiles (curves 3r and 4r) match the shape and intensity of the XMP well but it should be noted that the UHF method predicts some other electronic properties (such as total energy, see Table 5.1) better than the ROHF method. It should be noted that, on the basis of the present normalization, the CI (curve 4C) and ACPF (curve 4a which is shown at unit pole strength) calculations fit the shape of the XMP comparably well and only slightly overestimate the intensity.

The density functional momentum profiles for the HOMO $1\pi_g$ orbital ($X^2\Pi_g$ final ion state) are shown on Fig. 5.4b. It can be seen that all three DFT calculations give quite similar results and display slightly more intensity at low momentum than is observed experimentally. The MRSD-CI and ACPF calculations (curves 4C and 4a) most closely fit the experimental data for shape and intensity. However, all DFT calculations for the $1\pi_g$ orbital also provide a good description of the shape of the XMP.

5.3.2.2 The $1\pi_u$ Orbital ($a^4\Pi_u$, $A^2\Pi_u$ and $^2\Pi_u(3)$ Final Ion States)

Experimental and theoretical momentum profiles for the $1\pi_u$ orbital of O_2 ($a^4\Pi_u$ final ion state) are shown in Figs. 5.4c and 5.4d. The best results for shape and intensity compared to the XMP are clearly the intermediate and large basis set UHF calculations of AUG5-U (curve 3u) and 168-U (curve 4u). The ROHF calculations from these basis sets are adequate for shape comparison, but the intensity is much too low. This is in contrast to the HOMO (Fig. 5.4a) and the results for the HOMOs of NO and NO_2 in Chapter 4 where ROHF

calculations gave better shape comparisons with the XMP than UHF calculations. As noted above, the 168-CI momentum profile in Figs. 5.4c and 5.4d corresponds to the $^4\Pi_u$ MRSD-CI pole predicted at 16.81 eV (Table 5.3). This 168-CI calculation predicts results (curve 4C) that are closer in intensity and shape to the intermediate and large basis sets ROHF results than UHF calculations. The DFT momentum profiles (Fig. 5.4d) are more intense than the 168-CI calculation (curve 4C), but are still unable to account for the experimental intensity at $p < 1.2$ au. The DFT momentum profiles predict the shape of the observed XMP well but not the intensity. If the density functional TMPs are multiplied by a factor of ~ 1.2, an excellent shape fit with experiment is obtained. The choice of functional has little effect on the overall shape of the TMPs.

Experimental and theoretical momentum profiles for the $1\pi_u$ orbital of O_2 corresponding to the $A^2\Pi_u$ final ion state are shown in Figs. 5.4e and 5.4f. The 168-CI momentum profile in Figs. 5.4e and 5.4f corresponds to the $^2\Pi_u$ MRSD-CI pole at 17.98 eV (Table 5.3). The statistics for this final ion state are very limited due to the low intensity of this state and the difficulty in deconvoluting it from the energetically close and intense $a^4\Pi_u$ and $b^4\Sigma_g^-$ states. The Hartree-Fock and DFT theoretical momentum profiles in Figs. 5.4e and 5.4f have been scaled by a factor of 0.4 to provide reasonable agreement with the intensity of the XMP and because of the additional $1\pi_u$ satellite intensity at higher energy discussed below (i.e. the $^2\Pi_u(3)$ peak at 23.7 eV). Within the rather limited precision of the experimental data, this experimentally obtained pole strength of 0.4 derived from a comparison of the intensities of the XMP and TMPs is consistent with the theoretical estimates of 0.44 by Cederbaum and Domcke [65], 0.34 by Dixon and Hull [186] and 0.35 by Honjou et al. [187,188]. The MRSD-CI calculation of the present work (see Table 5.3) predicts a normalized pole strength of 0.373 in excellent agreement with the experimental value. It should also be noted that the ROHF momentum profiles in Fig. 5.4e generally predict more intense TMPs than their UHF counterparts. The 168-CI momentum profile (curve 4C) predicts a shape and intensity more

similar to the ROHF limit curves 3r and 4r than the UHF limit curves 3u and 4u. The DFT momentum profiles (Fig. 5.4f) are very similar in shape and intensity to the 168-CI calculation.

The experimental and theoretical momentum profiles for the $1\pi_u$ orbital corresponding to the $^2\Pi_u(3)$ satellite state are shown in Figs. 5e and 5f. As expected, the XMP and TMPs are similar to the momentum profiles corresponding to the parent $A^2\Pi_u$ state at 17.5 eV (see Figs. 5.4e and 5.4f). It should also be noted that the 168-CI momentum profile in Figs. 5.5e and 5.5f corresponds to the $^2\Pi_u$ MRSD-CI pole at 24.23 eV (Table 5.3). The peak is of low EMS intensity and is close in energy to the peak corresponding to the $c^4\Sigma_u^-$ state and thus deconvolution leads to some scatter in the data. The satellite splitting has been accounted for by scaling the Hartree-Fock and DFT TMPs by a factor of 0.55 to give the large basis set ROHF calculations (curves 3r and 4r) reasonable agreement with the experimental intensity. Other choices could be made for the normalization of experiment to theory, but curves 3r and 4r were chosen since ROHF momentum profiles agreed well for the intensities of other doublet states (see Figs. 5.4a and 5.5c). It should be noted that this experimentally derived pole strength of 0.55 is identical to the calculated pole strength reported by Cederbaum and Domcke [65]. The experimental pole strength from Figs. 5.5e and 5.5f also agrees quite well with the MRSD-CI calculation of the present work which predicts a normalized $^2\Pi_u$ pole strength of 0.589 at 24.23 eV (see Table 5.3). Dixon and Hull [186] predicted a slightly higher pole strength of 0.64. On comparing the relative fits of the various TMPs in Figs. 5.5e and 5.5f, it is obvious that the minimal basis set STO-3G-U and STO-3G-R profiles are in poor agreement with the measured intensity and shape of the XMP. The large basis set UHF calculations (curves 3u and 4u) and the 168-CI calculation (curve 4C) predict reasonable shapes for the XMP, but have low intensity with the present normalization factor of 0.55. The DFT momentum profiles are all very similar and all fit the experiment well within the limited experimental statistics for this ionization process. The DFT momentum profiles adequately predict the experimental intensity in a manner similar to the large basis set ROHF calculations (curves 3r and 4r).

Previous work [185,192] assigned peak Q as $^2\Pi_u$ in character. However, a consideration of the theoretical and experimentally derived $^2\Pi_u$ pole strengths rules out the possibility that the 33 eV peak consists of $1\pi_u$ processes. The MRSD-CI theory of the present work (Fig. 5.2 and Table 5.3) predicts three $^2\Pi_u$ poles below ~ 24.3 eV. The MRSD-CI poles at 17.98 eV (normalized pole strength 0.373) and 24.23 eV (normalized pole strength 0.589) can be identified with the $A^2\Pi_u$ and $^2\Pi_u(3)$ states observed in the PES [174,177,179]. As mentioned previously, the $^2\Pi_u(2)$ state has not been observed experimentally but has been predicted to be formed with a very low cross-section at ~ 20 eV [65,186,189,190]. The weak $^2\Pi_u$ MRSD-CI pole at 19.16 eV in Table 5.3 (normalized pole strength of 0.005) can be identified with this predicted $^2\Pi_u(2)$ state. The three MRSD-CI $^2\Pi_u$ energies and normalized pole strengths (0.373, 0.005 and 0.589) below 24.3 eV in the present work are in reasonable agreement with previous predictions [65,186-188]. The propagator technique work of Cederbaum and Domcke [65] gave $A^2\Pi_u$, $^2\Pi_u(2)$ and $^2\Pi_u(3)$ energies of 17.47, 19.75 and 27.32 eV with relative intensities of 0.44, 0.01 and 0.55. The semi-empirical CI calculations of Dixon and Hull [186] predicted energies of 17.56, 19.97 and 22.72 eV with relative intensities of 0.34, 0.001 and 0.64. Honjou et al. [187,188] predicted energies of 17.84, 20.7 and 24.44 eV and relative intensities of 0.35, 0.000, and 0.47 for these states, respectively. In addition, Yeager and co-workers [189,190] obtained calculated ionization energies of 17.77, 20.82 and 24.56 eV for the $A^2\Pi_u$, $^2\Pi_u(2)$ and $^2\Pi_u(3)$ ionic states, respectively. It should be noted that all previous calculations [65,186-190] and the present MRSD-CI results place virtually all the $^2\Pi_u$ intensity below ~ 27.3 eV and, in most cases, below 24.5 eV. However, the $^2\Pi_u$ assignments of the previously published theory [65,186-190] and the presently reported calculation differ from those of Suzuki et al. [185] who designated the observed 23.7 eV peak as $^2\Pi_u(2)$ and then used this assignment to characterize the peak at ~ 33 eV as $^2\Pi_u(3)$ on the basis of the comparison of experimental intensity ratios with those from theory [65,186-188] and the theoretical study of Gerwer et al. [192]. It is suggested in the present work that the theoretical $^2\Pi_u$ intensity ratios were not compared with the correct experimental intensities in

the previous EMS work [185] due to the predicted $^2\Pi_u(2)$ intensity at ~ 20 eV being incorrectly compared with the 23.7 eV experimental peak (and thus the theoretical $^2\Pi_u(3)$ intensity being incorrectly compared with the 33 eV experimental peak intensity). The ionization energies and pole strengths listed above from previously published theory [65,186-190], the MRSD-CI calculation of the present work and the photoelectron study by Baltzer et al. [179] all indicate that the peak at 23.7 eV in the EMS binding energy spectra should be assigned as $^2\Pi_u(3)$ and that no significant $^2\Pi_u$ intensity is present at 33 eV. The only predicted MRSD-CI $^2\Pi_u$ pole above 24.3 eV is of too low intensity (0.028 normalized pole strength) and too high energy (35.54 eV) to account for peak Q. In addition, while Gerwer et al. [192] included the 33 eV peak in the total $1\pi_u$ photoionization cross-section for comparison of their theory to experiment, the agreement was only moderately good and several correction procedures were required for the summation of unresolved peaks in the dipole (e, 2e) and line-source data. In the present work, the experimentally derived pole strengths for the peaks corresponding to the $A^2\Pi_u$ and $^2\Pi_u(3)$ states are found to be 0.4 and 0.55, respectively (Figs. 5.4e, 5.4f, 5.5e and 5.5f) and even with the limited statistics for these profiles these values correspond well with theory [65,186-188] and the presently reported MRSD-CI calculation. Thus, at least 0.95 of the experimental $^2\Pi_u$ pole strength has been accounted for at energies much lower than 33 eV and this represents essentially all the $^2\Pi_u$ pole strength, given the experimental statistics.

5.3.2.3 The $3\sigma_g$ Orbital ($b^4\Sigma_g^-$ and $B^2\Sigma_g^-$ Final Ion States)

The experimental and theoretical momentum profiles for the $3\sigma_g$ orbital of O_2 ($b^4\Sigma_g^-$ final ion state) are shown in Figs. 5.5a and 5.5b. All profiles are similar in shape except that the STO-3G calculations (curves 1u and 1r) are in serious disagreement, as might be expected. The intermediate and large ROHF calculations (curves 2r, 3r and 4r) show much better agreement with the shape and intensity of the observed XMP than the STO-3G-R calculation. It should be noted that the 168-CI momentum profile in Figs. 5.5a and 5.5b corresponds to the

$^4\Sigma_g^-$ MRSD-CI pole at 18.23 eV (Table 5.3). The MRSD-CI calculation (curve 4C) is formed from an initial ROHF reference state and thus the intensity of the 168-CI momentum profile is similar to curves 2r, 3r and 4r. Similar to the XMP corresponding to the quartet ($a^4\Pi_u$) ionic state in Figs. 5.4c and 5.4d, the best fit to the shape and intensity of the XMP corresponding the quartet $b^4\Sigma_g^-$ ion state in Fig. 5.5a is given by the higher level UHF calculations (curves 2u, 3u and 4u). However, these UHF TMPs still underestimate the experimental intensity slightly. The high momentum region (p > 1 au) is modelled reasonably well by all calculations. Excellent agreement for both shape and intensity is obtained for the DFT and experimental momentum profiles (Fig. 5.5b). All the DFT profiles are very similar in shape and intensity and provide the best match to the experimental intensity.

The experimental and theoretical momentum profiles for the $3\sigma_g$ orbital of O_2 corresponding to the $B^2\Sigma_g^-$ final ion state are shown in Fig. 5.5c and 5d. Both the STO-3G-U and STO-3G-R momentum profiles are poor predictions of the XMP shape and intensity. The higher level UHF calculations (curves 2u, 3u and 4u) show reasonable agreement with the shape of the observed XMP but slightly underestimate its intensity. In contrast, the ROHF calculations (curves 2r, 3r and 4r) show excellent agreement with the experimental shape and intensity, particularly in the low momentum region. It appears that large basis set UHF calculations are best for predicting the shape and intensity of XMPs associated with quartet final ion states (Figs. 5.4c, 5.4d, 5.5a and 5.5b) while large basis set ROHF calculations are a better model for the XMPs corresponding to doublet final ion states (Figs. 5.4a, 5.4b, 5.5c and 5.5d). The 168-CI momentum profile (curve 4C) in Figs. 5.5c and 5.5d corresponds to the $^2\Sigma_g^-$ MRSD-CI pole at 20.53 eV (Table 5.3). This MRSD-CI momentum profile provides excellent agreement with the experimental shape and intensity of the XMP. The DFT momentum profiles are too intense (Fig. 5.5d) although the shape of the XMP is adequately predicted.

5.3.2.4 The $2\sigma_u$ Orbital ($c^4\Sigma_u^-$ Final Ion State, Peak P and Peak Q)

The experimental and theoretical momentum profiles for the $2\sigma_u$ orbital of O_2 ($c^4\Sigma_u^-$ final ion state) are shown in Figs. 5.6a and 5.6b. The $^4\Sigma_u^-$ MRSD-CI pole at 24.71 eV (Table 5.3) has been chosen for the calculation of the 168-CI momentum profile (curve 4C). It is clear from Figs. 5.6a and 5.6b that the experimental and theoretical intensities are very different since the Hartree-Fock and DFT TMPs as shown have been multiplied by a factor of 0.7 to match the experimental intensity. This experimentally estimated pole strength of 0.7 is in good agreement with the (renormalized) pole strength of 0.802 at 24.71 eV calculated by the MRSD-CI method (Table 5.3). It is suggested that the ~ 30% difference in intensity between the TMPs and the XMP in Figs. 5.6a and 5.6b is due to splitting of the $2\sigma_u$ ionization process into additional $^4\Sigma_u^-$ satellite states or "poles" due to electron correlation effects.

Considering next the broad peak Q at 33 eV, it should be noted that no $^4\Sigma_u^-$ states are predicted in this energy region by the present MRSD-CI calculations (see Table 5.3) or by any of the other earlier published theoretical studies [187-190]. It should also be noted that the region of the binding energy spectrum (Fig. 5.1) above 36 eV is dominantly due to s-type $(2\sigma_g)^{-1}$ processes as discussed in Section 5.3.1 and therefore any contributions from p-type processes (i.e. $^4\Sigma_u^-$ and $^2\Sigma_u^-$) in this region are very small or negligible. Peak Q must therefore contain essentially only $^2\Sigma_u^-$ states and a $0.57^2\Sigma_u^-$ fraction of the Hartree-Fock and DFT TMPs is found to fit the XMP for this peak (Figs. 5.6e and 5.6f). This fraction is in quite good agreement with the (renormalized) MRSD-CI $^2\Sigma_u^-$ pole strength of 0.461 predicted at 33.89 eV (Table 5.3). Honjou et al. [187,188] also predicted strong $^2\Sigma_u^-$ poles at 34.9 and 36.6 eV while Yeager and co-workers [189,190] identified the experimentally observed peak in the region of 33 eV with a $^2\Sigma_u^-$ ionization process calculated at 34.70 eV.

The above analysis leaves experimental pole strengths of $0.3^4\Sigma_u^-$ and $0.43^2\Sigma_u^-$ unaccounted for and this intensity must therefore be mostly in peak P at 27.4 eV since all other regions of the binding energy spectrum have been assigned (see Section 5.3.2.5 and Fig. 5.7 below for a discussion of the $(2\sigma_g)^{-1}$ contributions which are located above 36 eV). Peak P is

well-fitted by the TMP linear combination of ($0.2\,^4\Sigma_u^-$ and $0.3\,^2\Sigma_u^-$) as shown in Figs. 5.6c and 5.6d. The above analysis of the $c^4\Sigma_u^-$ ionic state and peaks P and Q therefore account for ~ 90% (0.7+0.2 for $^4\Sigma_u^-$ and 0.57+0.3 for $^2\Sigma_u^-$) of the pole strength of the $^4\Sigma_u^-$ and $^2\Sigma_u^-$ manifolds. The above assignment of peak P is further supported by the present MRSD-CI and earlier calculations [187-190] which all predict both $^4\Sigma_u^-$ and $^2\Sigma_u^-$ ionization strength in the region of ~ 27 eV with relatively minor additional strength located in the higher energy region above 36 eV. Finally, it should be noted that 0.72 of the $^4\Sigma_u^-$ pole strength would be needed for a good fit if peak P was due to the quartet state and this is clearly not the case since ~ 0.7 of the $^4\Sigma_u^-$ pole strength is already contained in the $c^4\Sigma_u^-$ state at 24.5 eV.

Figs. 5.7a and 5.7b give further evidence that almost all of the $^4\Sigma_u^-$ and $^2\Sigma_u^-$ pole strength is accounted for if there are significant $^4\Sigma_u^-$ processes in peak P and if peak Q has mainly $^2\Sigma_u^-$ character. Fig. 5.7a shows the experimental data for the peak corresponding to the $c^4\Sigma_u^-$ ionic state (24.5 eV) and peak P (27.4 eV) added together and compared to several high-level calculated $2\sigma_u$ momentum profiles. The individual Hartree-Fock and DFT TMPs corresponding to $^4\Sigma_u^-$ final ion states are included in the sum with a unit pole strength while a pole strength of 0.3 has been used for the TMPs corresponding to $^2\Sigma_u^-$ final ion states. The CI calculation (curve 4C) in Fig. 5.7a consists of the summation of the poles at 24.71, 27.69 and 28.46 eV, each with their respective renormalized S_f^2 values. Good shape and intensity agreement is obtained for the TMPs and summed XMP in Fig. 5.7a, especially for the CI calculation. In Fig. 5.7b, the experimental data for the peak at 24.5 eV corresponding to the $c^4\Sigma_u^-$ ionic state, peak P (27.4 eV) and peak Q (33 eV) have been summed and compared to several high-level Hartree-Fock and DFT $2\sigma_u$ momentum profiles corresponding to $^4\Sigma_u^-$ and $^2\Sigma_u^-$ final ion states each with unit pole strength. The CI calculation (curve 4C) in Fig. 5.7b consists of the summation of the poles at 24.71, 27.69, 28.46 and 33.89 eV, each with their respective renormalized S_f^2 values. Within the statistics of the data it can be seen that experiment and theory are in good agreement for total intensity, indicating that essentially all of

the $^4\Sigma_u^-$ and $^2\Sigma_u^-$ pole strength lies within the energy region containing the three peaks ($c^4\Sigma_u^-$, P and Q).

5.3.2.5 The $2\sigma_g$ Orbital ($^4\Sigma_g^-$ and $^2\Sigma_g^-$ Final Ion States)

The experimental and theoretical momentum profiles for the $^4\Sigma_g^-$ and $^2\Sigma_g^-$ parent and satellite states from $2\sigma_g$ orbital ionization are shown in Figs. 5.7c and 5.7d. Siegbahn et al. [183] gave vertical ionization potentials of 39.6 and 41.6 eV for the $^4\Sigma_g^-$ and $^2\Sigma_g^-$ states, but the present EMS work gives slightly lower ionization potentials (Table 5.2). Gardner and Samson obtained ionization potentials of 39.7 and 40.4 for these states [180]. Due to the limited knowledge of the positions and widths of these states, an energy slice from 36-43 eV (open circles in Figs. 5.7c and 5.7d) encompassing the main peak centered at ~ 39 eV has been taken. The same normalization factor determined for all other orbitals (see Fig. 5.3) has been used in Figs. 5.7c and 5.7d. The MRSD-CI $^4\Sigma_g^-$ and $^2\Sigma_g^-$ poles at 40.17 and 40.86 eV (Table 5.3) have been chosen for the calculation of the 168-CI momentum profile (curve 4C) since their energies and pole strengths correspond most closely with the experimentally observed parent ion states. While the XMP is clearly s-type, it does not match the theoretical intensity and thus additional $2\sigma_g$ ionization intensity must occur in higher energy poles. All calculations (Hartree-Fock, MRSD-CI and DFT) model the experimental shape and intensity in a similar manner. A second energy slice from 43-59 eV (filled triangles in Figs. 5.7c and 5.7d) shows the same s-type shape and this is consistent with previous observations [183,185] indicating that the higher energy region is predominantly composed of $(2\sigma_g)^{-1}$ poles. The peak centered at ~ 47 eV accounts for the majority of the intensity in the 43-59 eV region (see Fig. 5.1) and the states assigned as $^4\Sigma_g^-(2)$ and $^2\Sigma_g^-(2)$ are found within this peak (see Refs. [183,185] and also Table 5.2). Results from the MRSD-CI calculation in the present work only extend to ~ 42 eV and do not take into account the very high energy region because of complications involving the modelling of double ionization. While the shape of the 36-59 eV binding energy slice

(filled circles in Figs. 5.7c and 5.7d) agrees well with that of the summed theory for $2\sigma_g$ ionization, some experimental intensity is apparently missing. However, as noted in Section 5.3.2, there is still missing intensity (Fig. 5.3) at a binding energy of 59 eV and therefore additional $2\sigma_g$ intensity remains at higher binding energies.

5.3.3 Density Maps in Momentum and Position Space

The momentum and position space density contour maps corresponding to each of the five valence orbitals of an oriented O_2 molecule are presented in Figs. 5.8 and 5.9. These density maps provide some insight into the corresponding (spherically averaged) experimental and theoretical momentum profiles. The position space maps are slices of the orbital electron density $|\psi|^2$ through a plane containing both nuclei. The momentum space maps show momenta perpendicular and parallel to the molecular plane. The calculations are based on the 168-R near-Hartree-Fock limit results which have been found to provide generally good descriptions of the XMPs of O_2 at the Hartree-Fock level. The origin for the position space maps is the molecular center of mass and all dimensions are in atomic units. The side panels on each map show slices of the momentum or position space density along the vertical (right panel) and horizontal (top panel) dotted lines.

The momentum and position density maps for the $1\pi_g$ orbital of O_2 are shown in Figs. 5.8a and 5.8b. Simple molecular orbital Hartree-Fock models describe this MO as an antibonding π^* orbital involving out-of-phase (destructive interference) overlap of atomic O 2p orbitals. The expected shape of a pure π^* orbital can be seen from the *r*-map in Fig. 5.8b (i.e. four lobes of density and nodal planes both along the internuclear axis and perpendicular to the internuclear axis). The highly nodal character of this orbital in *r*-space is also reflected in *p*-space (*r*-space symmetry characteristics are conserved upon transformation to *p*-space and thus there are also two nodal planes in the *p*-map). In view of this high degree of nodal

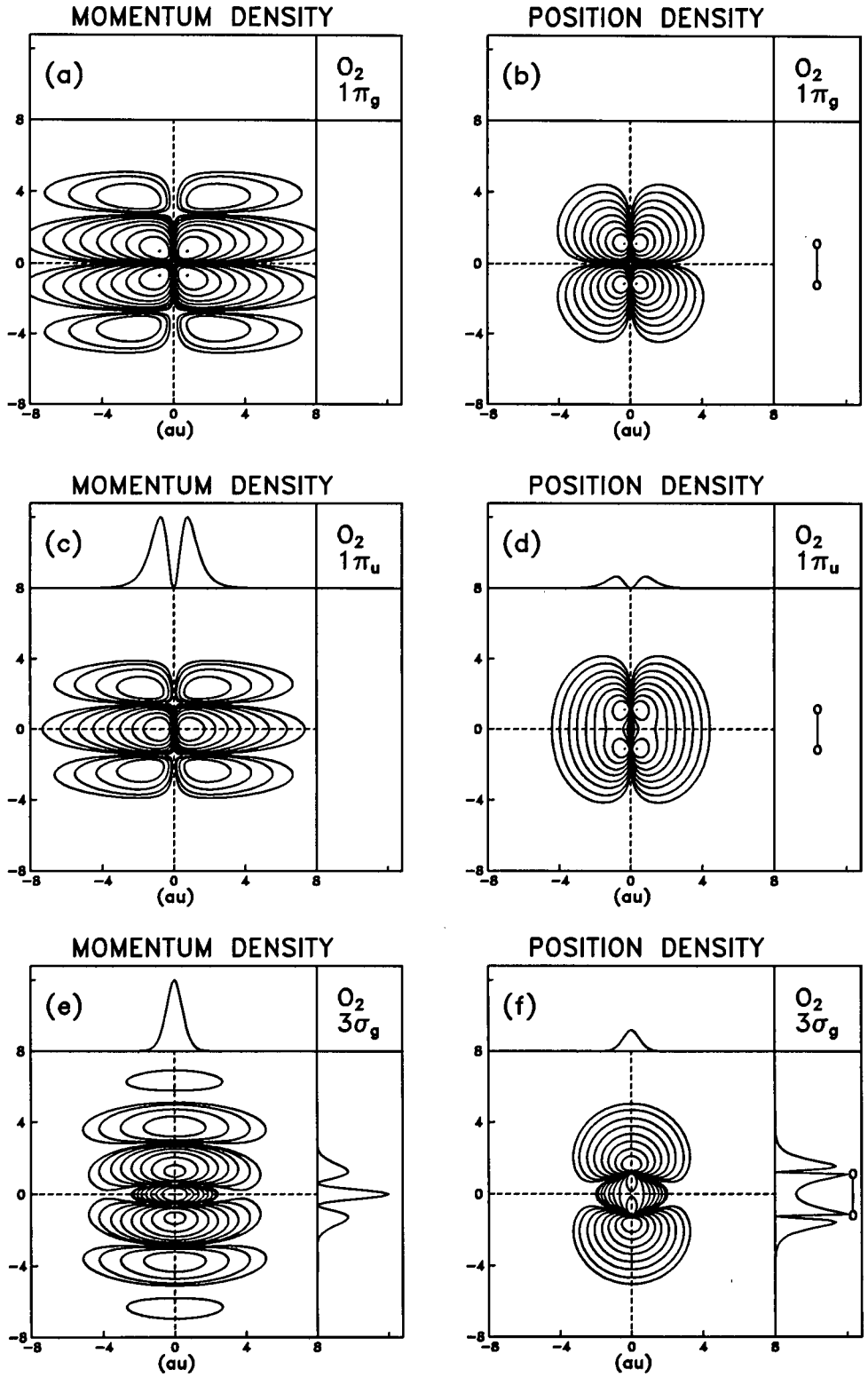

Fig. 5.8: Momentum and position density contour maps for the $1\pi_g$, $1\pi_u$ and $3\sigma_g$ orbitals of an oriented O_2 molecule calculated at the Hartree-Fock level using the 168-R basis set. The contour values represent 0.01, 0.03, 0.1, 0.3, 1.0, 3.0, 10.0, 30.0, and 99.0% of the maximum density. The side panels (top and right side) show the density along the dashed lines (dashed vertical and horizontal lines) for each density map.

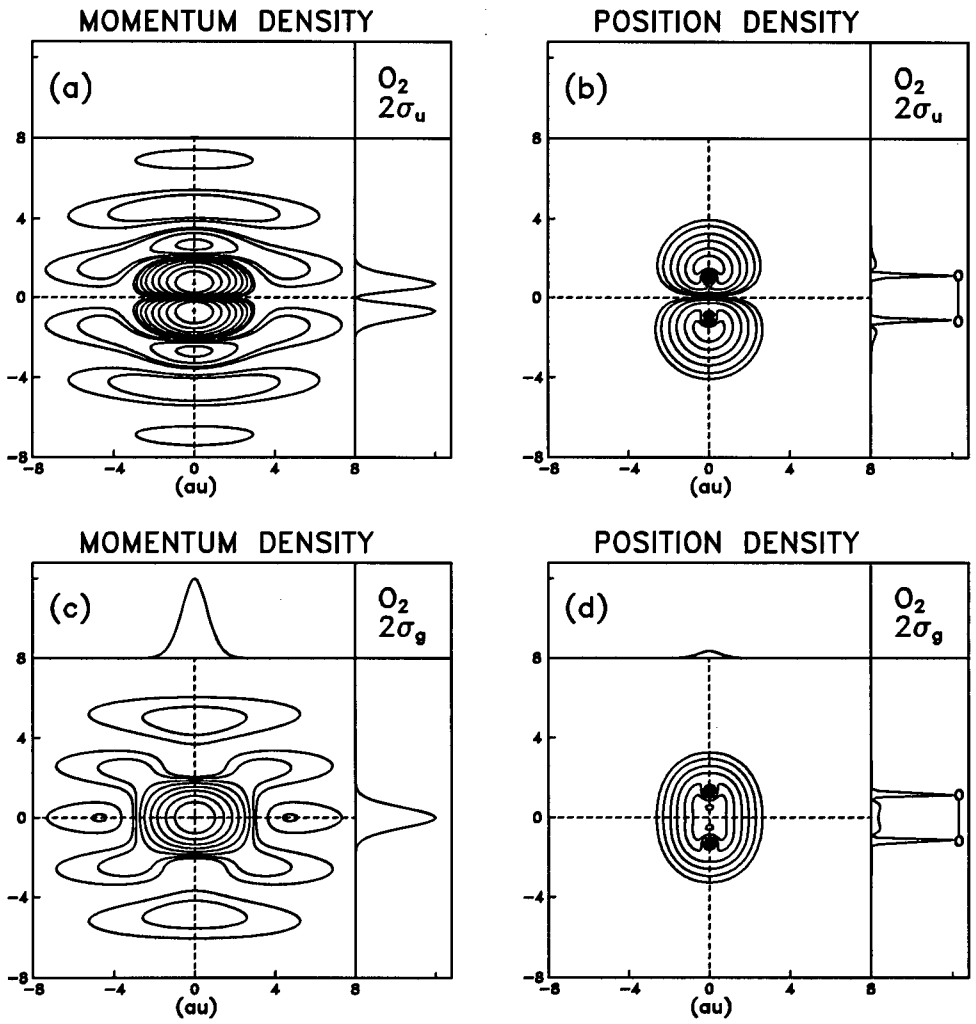

Fig. 5.9: Momentum and position density contour maps for the $2\sigma_u$ and $2\sigma_g$ orbitals of an oriented O_2 molecule calculated at the Hartree-Fock level using the 168-R basis set. The contour values represent 0.01, 0.03, 0.1, 0.3, 1.0, 3.0, 10.0, 30.0, and 99.0% of the maximum density. The side panels (top and right side) show the density along the dashed lines (dashed vertical and horizontal lines) for each density map.

behaviour it is not surprising that the experimental and theoretical momentum profiles for this orbital display such a high p_{max} value of 1.0 au in view of the relation $p=i\hbar\partial(\psi)/\partial x$ [145,199]. The interference of wavefunctions on the atomic centers is also reflected in the momentum density map as additional lobes called "bond oscillations" [78,200,201].

The momentum and position density maps for the $1\pi_u$ orbital of O_2 are shown in Figs. 5.8c and 5.8d. The $1\pi_u$ orbital is a bonding orbital resulting from in-phase (constructive interference) side-on overlap of atomic O 2p orbitals. The expected two-lobed shape of the orbital can be seen from the *r*-map (Fig. 5.8d). Because the overlap is off the internuclear axis and because the lobes are of opposite sign, a nodal plane exists along this axis. Similarly, one nodal plane is observed in the *p*-map in the $p_{parallel}$ direction (Fig. 5.8c). The momentum density at $p = 0$ is identically zero so that all (non-momentum resolution folded) profiles for this orbital have zero intensity at $p = 0$. The small intensity near $p = 0$ in the TMPs shown in Figs. 5.4a and 5.4b is due to momentum resolution folding effects.

The momentum and position density maps for the $3\sigma_g$ orbital of O_2 are shown in Figs. 5.8e and 5.8f. Constructive overlap of atomic orbital components is clearly seen in the region between the O atoms to produce a σ bond. The multiple lobes in the *p*-map are further evidence of this bonding behaviour. The large amount of momentum density at $p = 0$ (see top and side slices in the *p*-map) indicates the strongly s-type character of the experimental and theoretical momentum profiles for this orbital (see Figs. 5.5a-d). In addition, the small secondary maxima in the momentum density (see side slice in the *p*-map) are reflected in the spherically averaged momentum profiles as small p-type behaviour with maxima of $p \sim 1.4$ au.

The $2\sigma_u$ orbital of O_2 is predicted from molecular orbital theory to be antibonding and this is reflected by the momentum and position density maps for this orbital (Figs. 5.9a and 5.9b). The *r*-map displays a nodal plane perpendicular to the internuclear axis. Strong multiple lobes are observed in the *p*-map and no momentum density is observed at $p = 0$.

Maxima in the momentum density observed at $p \sim 0.8$ au in the side slice of the p-map are reflected in the p-type shapes of the observed XMP and TMPs for this orbital.

The weakly bonding character of the $2\sigma_g$ orbital of O_2 is indicated by the σ density between the oxygen atoms in the r-map (Figs. 5.9c and 5.9d). The inner valence $2\sigma_g$ orbital is mostly composed of atomic-like O 2s character. On comparing with the density maps for the $3\sigma_g$ orbital (Figs. 5.8e and 5.8f) it is also clear that the $2\sigma_g$ is more spatially contracted (and hence more diffuse in momentum space) than the $3\sigma_g$ orbital. This is reflected by the broader momentum profiles for $2\sigma_g$ ionization in Figs. 5.7c and 5.7d than for the momentum profiles for $3\sigma_g$ ionization in Figs. 5.5a-d. The observed strongly s-type momentum profiles from $2\sigma_g$ ionization are also reflected by the presence of a large amount of momentum density in the $2\sigma_g$ p-map at $p = 0$.

Chapter 6

The HOMOs of PH_3, PF_3 and $P(CH_3)_3$

6.1 Introduction

Inductive effects in NH_3, NF_3 and the methyl-substituted amines $N(CH_3)_nH_{3-n}$ where n = 0-3, have been studied previously by EMS and quantum mechanical calculations [39,70,80-82,202]. According to intuitive hybridization concepts based on simple Valence Bond Theory, the "lone pair" on the N atom would be expected to become more "p-type" as the ligand-N-ligand bond angle increases. Since the bond angles of $N(CH_3)_3$, NH_3 and NF_3 are 111°, 107° and 102°, respectively, these intuitive concepts predict that the lone pair of $N(CH_3)_3$ should show a higher degree of p-type character than the lone pair in NH_3 while the lone pair in NF_3 should show increased s character relative to NH_3. The experimental momentum profile (XMP) for NF_3 was in qualitative agreement with these intuitive expectations, but the results for $N(CH_3)_3$ were completely contrary to those predicted [81,82]. However, the correct qualitative trends were given by even the simplest MO (delocalized) treatments such as STO-3G minimal basis set calculations [81]. Improved basis sets gave better quantitative agreement [82]. The increase in s-type character for NF_3 compared to NH_3 was attributed to an increase in the N 2s contribution to the molecular orbital while the observed increase in s-character upon methyl substitution was related to the large H 1s contribution *trans* to the nitrogen "lone pair" [81,82]. Upon further methylation, more *trans*-H 1s character contributes to the molecular orbital and thus, the $3a_1$ orbital of NH_3 loses its localized "lone pair" character and becomes increasingly delocalized with each methyl substitution [81,82]. It was also suggested [81,82] that this delocalization of the HOMO

charge density caused by methyl substitution implies that the methyl group is an electron-withdrawing substituent (relative to hydrogen) when bonded to N. Other EMS studies on methyl substitution in the series H_2CO, CH_3COH and $(CH_3)_2CO$ [83] and H_2O [69], CH_3OH [84] and CH_3OCH_3 [85,86] have also shown this delocalization effect of the methyl group on the frontier orbitals. These results are in contrast to the well-known and often invoked methyl-inductive effect in organic chemistry, where concepts such as basicity and the stability of carbocations have traditionally been rationalized by considering the methyl group to be electron-donating relative to hydrogen [203]. However, consideration of other properties such as the decrease in the dipole moment of substituted amines upon increasing methylation give further evidence of the electron-withdrawing ability of the methyl group [82]. The latter view is also strongly supported by the ^{14}N and ^{15}N NMR chemical shifts which are moved downfield by increasing methylation, thus indicating a deshielding of the nitrogen nucleus [204,205]. Much earlier low level MO calculations by Hehre and Pople [206] also suggested that methyl groups are electron attracting relative to hydrogen when bonded to nitrogen or oxygen.

To further investigate the inductive effects of the methyl group relative to hydrogen and fluorine, the experimental momentum profiles for the HOMOs of PF_3 and $P(CH_3)_3$ are studied in the present work and compared with experimental results for PH_3 previously reported from this laboratory [74]. A knowledge of whether methyl groups are intrinsically electron-donating or electron-attracting in these phosphorus compounds and the behaviour relative to the corresponding nitrogen compounds is of importance in predicting the general properties of alkyl groups in many compounds and chemical reactions. Furthermore, intuitive arguments based on geometry and hybridization concepts would predict the so-called "lone-pair' of a PX_3 molecule to range from 100% s-type character (for an XPX bond angle of 90°) to 100% p-type character (for an XPX bond angle of 120°, i.e. when the molecule is planar). The experimental ligand-P-ligand bond angles are 98.6°, 96.9° and 93.3° for $P(CH_3)_3$, PF_3 and PH_3, respectively [207-209]. Thus, intuitive arguments predict the HOMOs of $P(CH_3)_3$ and PF_3 to contain more

p-type character than the HOMO of PH_3. However, the bond angles in the phosphorus compounds are smaller than in the corresponding amines and thus, according to intuitive concepts, the substituted phosphorus compounds should show greater s-type character in their HOMO electron momentum profiles than in their nitrogen analogs.

The experimental momentum profiles for PH_3 [74], PF_3 and $P(CH_3)_3$ are compared to theoretical momentum profiles at the target Hartree-Fock approximation (THFA) level (see Section 2.2.5). For PH_3, a post-Hartree-Fock momentum profile from the multi-reference single and doubles configuration interaction (MRSD-CI) method taken from the work of Clark et al. [74] is also presented in order to assess the role of electron correlation and relaxation effects. Due to the increasing difficulty of applying the Hartree-Fock and CI methods to larger molecules, the ability of density functional theory (DFT) calculations to predict momentum profiles for PX_3 molecules is also investigated in the present work. As discussed in Section 2.2.6, DFT allows considerable computational savings for calculations on larger molecules [60] such as those studied in the present work. Thus, TKSA-DFT calculations of the momentum profiles using (i) the local density approximation of Vosko et al. [112], (ii) the non-local correlation functional of Perdew and Wang [115,117] and (iii) a non-local combination of the Perdew correlation functional and Becke exchange functional [116] have been carried out for the HOMOs of all three molecules in the present work.

EMS momentum profile measurements for the HOMOs of PF_3 and $P(CH_3)_3$ were obtained with a single channel EMS spectrometer [78] at binding energies of 12.2 eV and 8.6 eV, respectively. The PF_3 sample was obtained from Ozark Mahoning gas products while the $P(CH_3)_3$ sample was obtained from Aldrich Chemicals. Both samples were of > 99.0% purity.

6.2 Calculations

6.2.1 Hartree-Fock Calculations

Spherically averaged theoretical momentum profiles have been calculated within the plane wave impulse and the target Hartree-Fock approximations (via Eq. (2.57)) for the HOMO of each of the three molecules using several basis sets of varying quality. In addition to p_{max}, the maximum of the theoretical or experimental momentum profile, other calculated and experimental electronic properties for the three molecules are also listed in Table 6.1. The experimentally derived geometries for PH_3 [207], PF_3 [208] and $P(CH_3)_3$ [209] were used in all calculations and C_{3v} molecular symmetry was assumed for each molecule.

Details of the calculation methods are described below. The total number of contracted Gaussian-type orbital functions (CGTO) used is also given. All calculations were performed at the University of British Columbia using the Gaussian 92 program [124] with the exception of the 136-GTO calculation which is taken from the work of Clark et al. [74].

(1) STO-3G: A calculation employing a minimal basis set (effectively single zeta). Each function is a contraction of three Gaussian functions and thus it consists of P(9s,6p)/[3s,2p], C/F(6s,3p)/[2s,1p] and H(3s)/[1s] contractions. Therefore, a total of 12 CGTO are employed for PH_3, 24 CGTO for PF_3 and 33 CGTO for $P(CH_3)_3$. This basis was designed by Pople and co-workers [101].

(2) 4-31G: This is a split-valence basis developed by Ditchfield, Hehre and Pople [102]. It uses a minimal basis for each of the core orbitals on P, C and F and essentially a double zeta description of the valence orbitals. This basis set has limited flexibility, with only one extra s and p wavefunction added to account for polarization and diffuseness. It consists of a P(12s,8p)/[4s,3p], C/F(8s,4p)/[3s,2p] and H(4s)/[2p] contraction. The number of CGTO is then 19 for PH_3, 40 for PF_3 and 58 for $P(CH_3)_3$.

(3) 6-311G: The 6-311G basis of Pople and co-workers [103] is a split-valence basis

Table 6.1: Calculated and experimental properties for PH_3, PF_3 and $P(CH_3)_3$

Molecule[a]		Wavefunction	Total Energy (hartree)	μ (Debye)[b]	p_{max} (au)[c]
PH_3	1	STO-3G	-338.634	0.537	0.62
	2	4-31G	-342.022	1.171	0.55
	3	6-311G	-342.423	1.159	0.42
	4	6-311+G*	-342.468	0.757	0.47
	5	6-311++G**	-342.477	0.755	0.47
	6	AUG3	-342.486	0.684	0.45
	7	AUG5	-342.493	0.665	0.44
	8	136-GTO	-342.493[d]	0.665[d]	0.45[d]
	8c	136-G(CI)	-342.683[d]	0.624[d]	0.45[d]
	6*l*	AUG3-L	-341.854	0.701	0.44
	6p	AUG3-P	-343.333	0.528	0.43
	6b	AUG3-BP	-343.174	0.592	0.45
		Experimental	-343.42[e]	0.578[f]	0.5[d]
PF_3	1	STO-3G	-631.019	1.334	
	2	4-31G	-638.294	2.723	
	3	6-311G	-639.059	2.680	
	4	6-311+G*	-639.230	1.678	
	6	AUG3	-639.287	1.246	
	7	AUG5	-639.327	1.228	
	6*l*	AUG3-L	-637.981	0.907	
	6p	AUG3-P	-641.554	0.897	
	6b	AUG3-BP	-641.144	0.866	
		Experimental		1.13[g]	
$P(CH_3)_3$	1	STO-3G	-454.401	0.458	
	2	4-31G	-458.983	1.192	
	3	6-311G	-459.517	1.606	
	4	6-311+G*	-459.609	1.429	
	5	6-311++G**	-459.623	1.438	
	6	AUG3	-459.642	1.461	
	7	AUG5	-459.656	1.464	
	6*l*	AUG3-L	-458.744	1.405	
	6p	AUG3-P	-461.476	1.301	
	6b	AUG3-BP	-461.202	1.384	
		Experimental		1.192[h]	

[a] Calculations used the experimental equilibrium geometry for PH_3 [207], PF_3 [208] and $P(CH_3)_3$ [209].
[b] Calculated dipole moments are for a non-relativistic, non-vibrating, non-rotating molecule.
[c] The p_{max} corresponds to the value of momentum where the intensity of the momentum profile is at maximum (see Fig. 6.1).
[d] Ref. [74].
[e] Ref. [210].
[f] Ref. [224].
[g] Ref. [208].
[h] Ref. [223].

comprised of an inner shell of six s-type Gaussians and an outer valence shell that has been split into three parts represented by three, one and one primitives, respectively. Thus, it consists of a P(13s,9p)/[6s,5p], C/F(11s,5p)/[4s,3p] and H(5s)/[3s] contraction. The number of CGTO is then 30 for PH_3, 60 for PF_3 and 87 for $P(CH_3)_3$.

(4) 6-311+G*: This is an augmented version of the 6-311G basis of Pople and co-workers [103]. The 6-311+G* basis is formed by augmenting the 6-311G with diffuse s- and p-functions [105] and spherical d-type polarization functions [104] on all heavy (non-hydrogen) atoms. A (14s,10p,1d)/[7s,6p,1d] contraction is then used for P, a (12s,6p,1d)/[5s,4p,1d] contraction for C and F, and a (5s)/[3s] contraction for H to give a total of 39 CGTO for PH_3, 96 CGTO for PF_3 and 123 CGTO for $P(CH_3)_3$.

(5) 6-311++G:** A split valence basis set in which the 6-311+G* basis set has been further augmented by the addition of a diffuse sp shell and a p-type polarization function to all hydrogen atoms [104,105]. The contractions are thus P(14s,10p,1d)/[7s,6p,1d], C(12s,6p,1d)/[5s,4p,1d] and H(6s,1p)/[4s,1p] to provide a total of 51 CGTO for PH_3 and 159 CGTO for $P(CH_3)_3$.

(6) AUG3: The AUG3 basis set used in the present work is a truncated form of Dunning's aug-cc-pVTZ basis set [166-169] in which all f-, g- and h-functions have been removed. This truncation was adopted to provide compatibility with the density functional calculations since the present version of the DFT program (deMon) cannot handle these higher l functions. In addition, the d functions have been changed from spherical to Cartesian so that the Hartree-Fock results are comparable to DFT results with this basis. Thus, it consists of a P(48s,21p,3d)/[6s,5p,3d], C/F(23s,8p,3d)/[5s,4p,3d] and H(5s,3p)/[4s,3p] contraction. A total of 78 CGTO are employed for PH_3, 144 CGTO for PF_3 and 261 CGTO for $P(CH_3)_3$.

(7) AUG5: The basis set for these calculations was taken from the work of Dunning and co-workers [166-169]. The AUG5 basis set used in the present work is actually a truncated form of Dunning's aug-cc-pV5Z basis set in which all f-, g- and h-functions have been removed. Thus, the AUG5 consists of the atomic contractions of (65s,24p,5d)/[8s,7p,5d] for P,

(33s,13p,5d)/[7s,6p,5d] for C/F and (13s,5p)/[6s,5p] for H. The d functions are spherical. Thus, a total of 177 CGTO are used for PH_3, 204 CGTO for PF_3 and 393 CGTO for $P(CH_3)_3$.

(8) 136-GTO: The 136 CGTO extended basis set for PH_3 designed by Davidson and Boyle and reported in the work of Clark et al. [74] consists of P(21s,14p,4d,2f)/[12s,10p,4d,2f] and H(10s,3p,2d)/[6s,3p,1d] contractions. This basis set was designed to saturate the diffuse basis function limit and to give improved representation of the *r*-space tail of the orbitals [74].

6.2.2 MRSD-CI Calculation

(8c) 136-G(CI): The 136-G(CI) calculation for PH_3 is from the earlier work of Clark et al. [74] and a much more detailed discussion of the calculation can be found in that paper. Briefly, the Hartree-Fock singly and doubly excited configuration interaction (HF SDCI) and MRSD-CI wavefunctions for the neutral and ion species were constructed from the 136-GTO basis set (described above in Section 6.2.1). The Hartree-Fock virtual orbitals were transformed into K orbitals to improve the CI convergence. The configuration space for the neutral MRSD-CI calculations was chosen from the largest coefficients of an initial HF SDCI calculation. In addition, the molecular orbitals for the neutral molecule were also used for the ion state calculations.

6.2.3 DFT Calculations

(6*l*) AUG3-L, (6p) AUG3-P and (6b) AUG3-BP: These three density functional calculations were carried out at the University of British Columbia using the deMon program [122,123] and the large AUG3 orbital basis set (described above in Section 6.2.1 for calculation 6) at the experimental geometries for PH_3 [207], PF_3 [208] and $P(CH_3)_3$ [209] and C_{3v} molecular symmetry. All calculations used a random extra-fine grid and the energy convergence was set at 10^{-7} hartree. The auxiliary basis sets for fitting the charge density and exchange-correlation potential were the P(6,4;6,4), F/C(5,4;5,4), and H(4,1;4,1) from the deMon program [122,123]. The AUG3-L calculation employs the local density approximation of Vosko et al. [112] while

the AUG3-P calculation uses the gradient corrected correlation functional of Perdew and Wang [115,117]. The AUG3-BP calculation uses a combination of the correlation functional of Perdew and Wang [115,117] and the exchange functional Becke [116]. The Kohn-Sham orbitals have been extracted from the result and the momentum profiles have been calculated using the TKSA via Eq. (2.58). The instrumental angular resolution effects [59] were also incorporated into the TMPs. Various other electronic properties from the DFT calculations are listed in Table 6.1. However, as noted in Section 2.2.6, the use of inexact functionals in practical DFT calculations causes the total energies to differ from the exact result [60] and thus the DFT total energies in Table 6.1 are not readily comparable to those from Hartree-Fock methods and MRSD-CI.

6.3 Results and Discussion

6.3.1 Comparison of Experimental and Theoretical Momentum Profiles

The experimental momentum profile (XMP) for the outermost orbital ($5a_1$) of PH_3, obtained earlier by Clark et al. [74] using a single-channel EMS spectrometer [78] is compared in Fig. 6.1 with both earlier and presently performed calculations. In addition, the outermost XMPs for PF_3 ($8a_1$, Fig. 6.2) and $P(CH_3)_3$ ($8a_1$, Fig. 6.3) have been measured in the present work with the same single-channel spectrometer [78]. On each figure, the mean binding energy at which each particular XMP was measured is noted (10.6 eV for PH_3, 12.29 eV for PF_3 and 8.65 eV for $P(CH_3)_3$). The values correspond to the vertical ionization potentials of the lowest lying peaks observed in the photoelectron spectra [211-213] for these molecules. Even at the modest EMS energy resolution, the outermost ionization process for each molecule is well separated in energy from the rest of the valence ionization manifold, and this ensures that all the observed intensity in each momentum profile is due solely to ionization to the lowest lying ion state with no contribution from higher ionization processes.

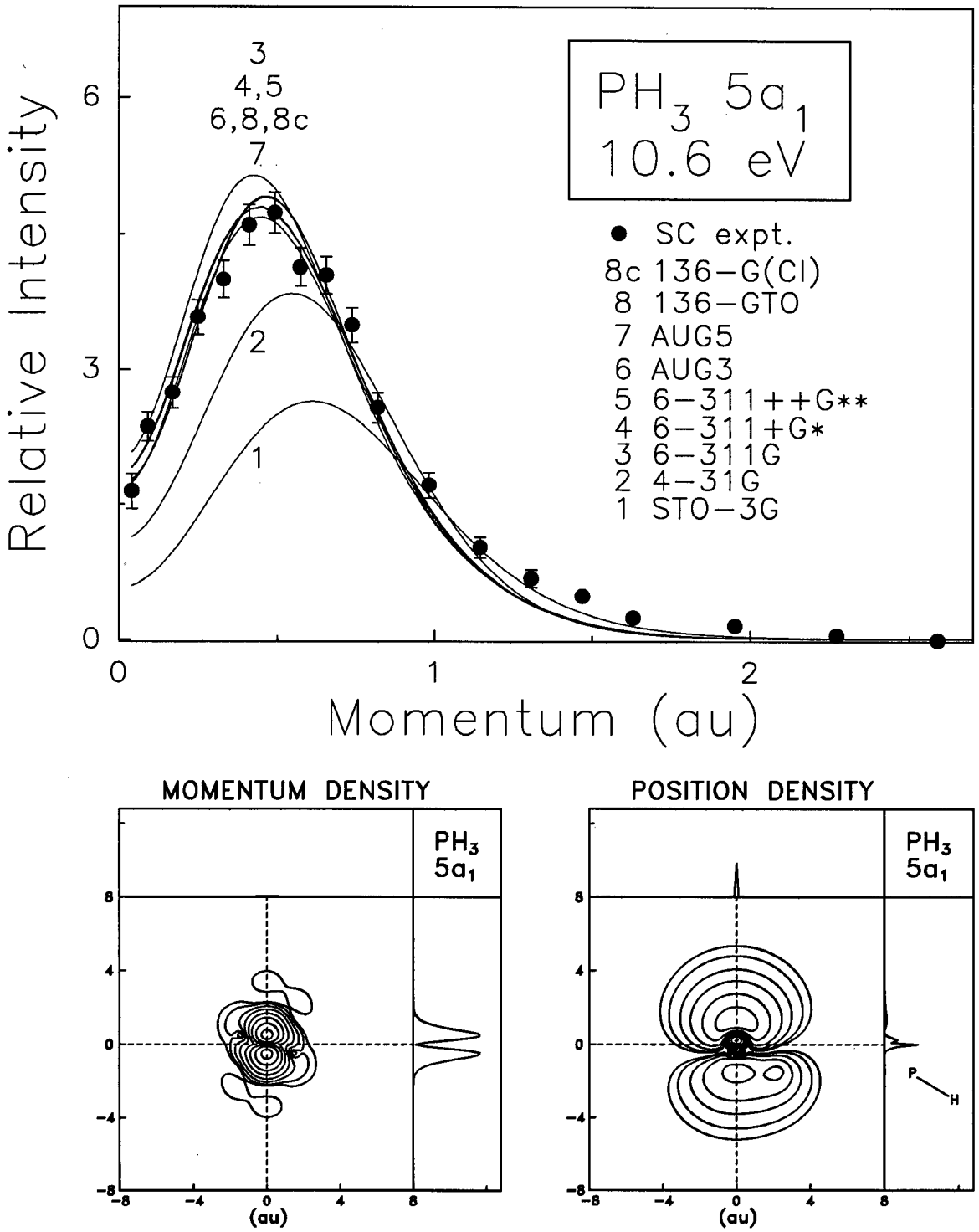

Fig. 6.1: Measured and calculated spherically averaged Hartree-Fock and MRSD-CI momentum profiles for the $5a_1$ orbital of PH_3 (upper panel). The lower panels show the momentum and position density contour maps for an oriented PH_3 molecule calculated at the Hartree-Fock level using the AUG3 basis set. The position density map shows the shape of the molecular orbital in one plane through the molecule containing PH and bisecting the angle between the other two ligands. The P atom is situated at the origin. The momentum map shows momenta perpendicular and parallel to the defined planes in position space. The contours represent 0.01, 0.03, 0.1, 0.3, 1.0, 3.0, 10.0, 30.0, and 99.0% of the maximum density.

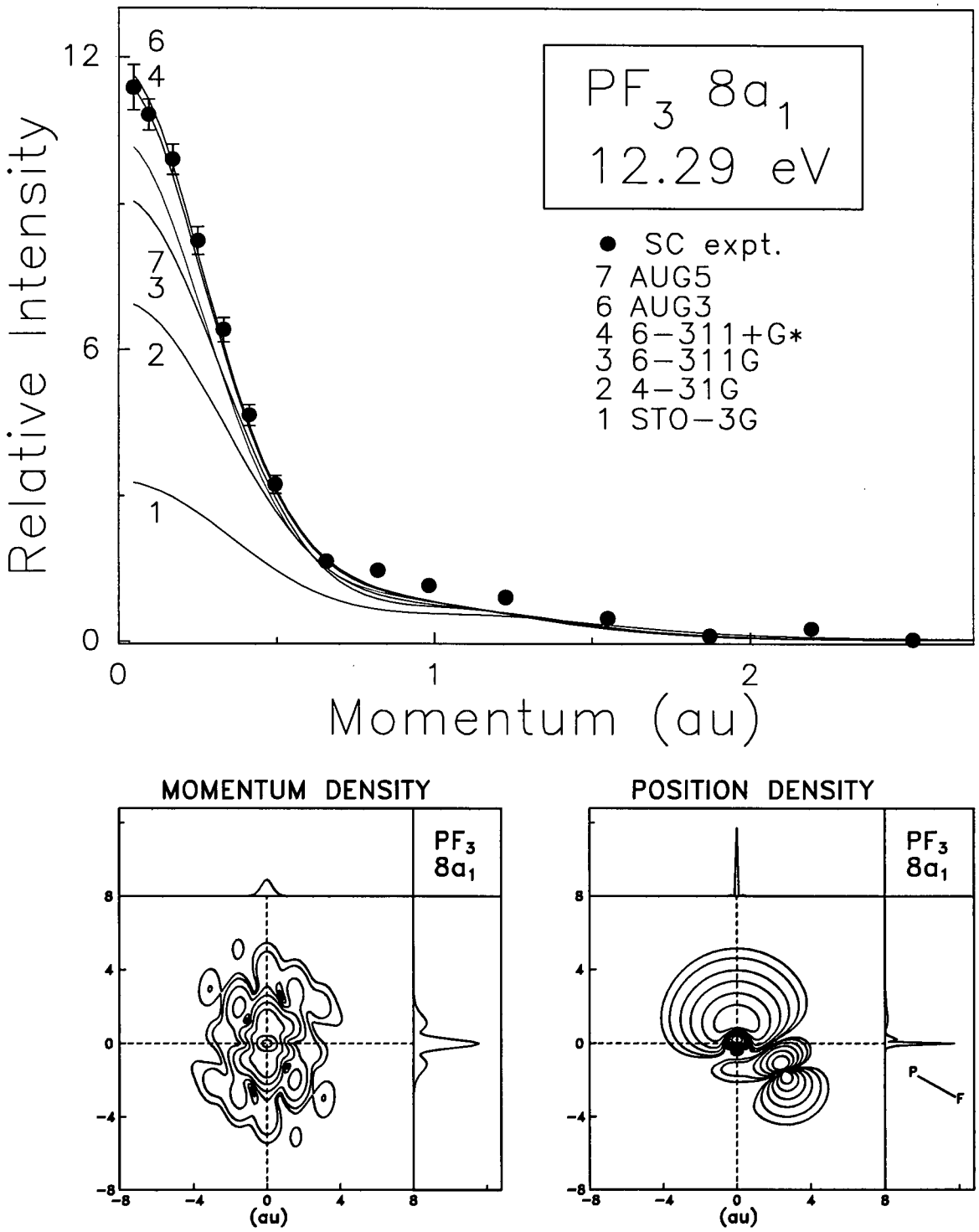

Fig. 6.2: Measured and calculated spherically averaged momentum profiles for the $8a_1$ orbital of PF_3 (upper panel). The lower panels show the momentum and position density contour maps for an oriented PF_3 molecule calculated at the Hartree-Fock level using the AUG3 basis set. The position density map shows the shape of the molecular orbital in one plane through the molecule containing PF and bisecting the angle between the other two ligands. The P atom is situated at the origin. The momentum map shows momenta perpendicular and parallel to the defined planes in position space. The contours represent 0.01, 0.03, 0.1, 0.3, 1.0, 3.0, 10.0, 30.0, and 99.0% of the maximum density.

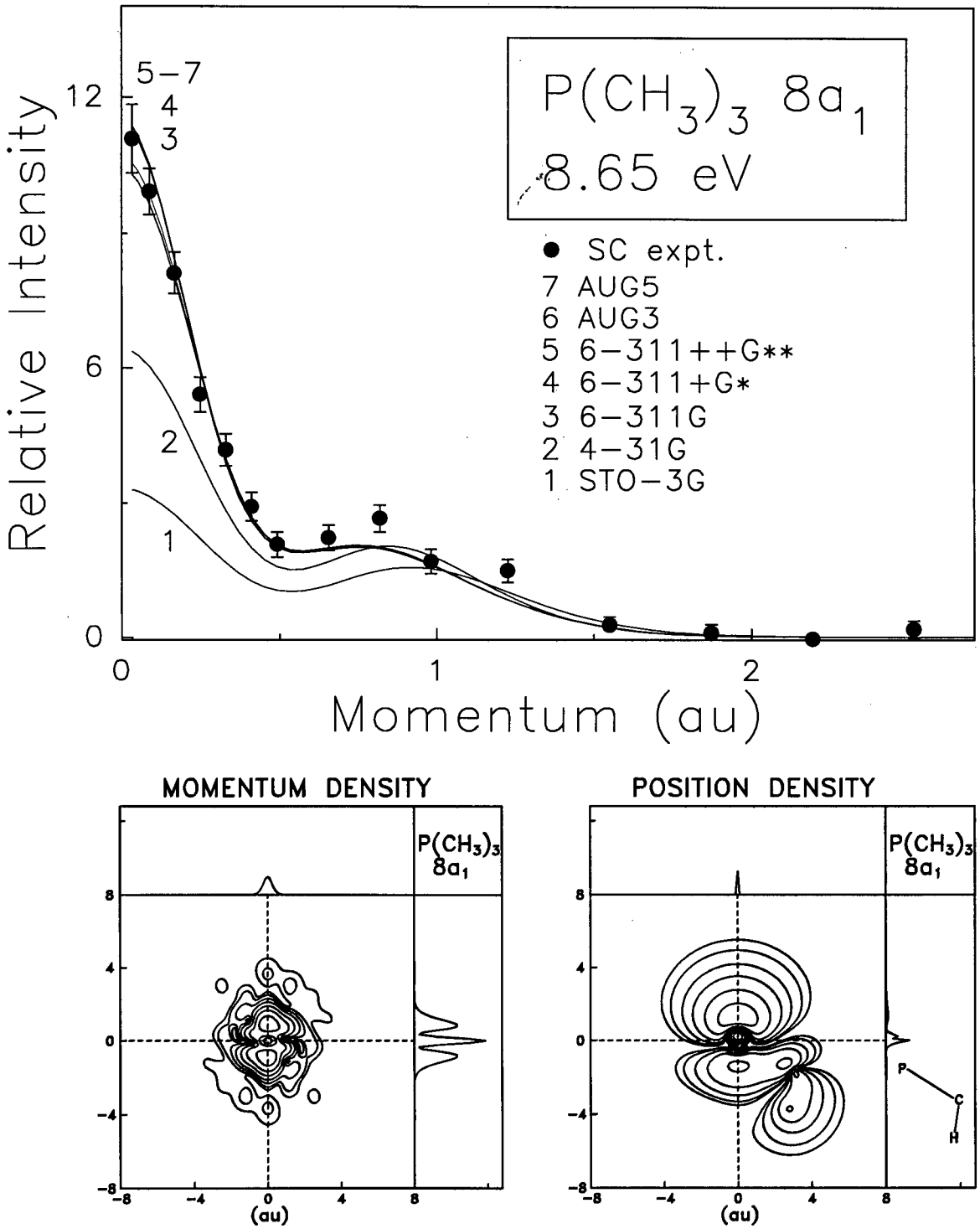

Fig. 6.3: Measured and calculated spherically averaged momentum profiles for the $8a_1$ orbital of $P(CH_3)_3$ (upper panel). The lower panels show the momentum and position density contour maps for an oriented $P(CH_3)_3$ molecule calculated at the Hartree-Fock level using the AUG3 basis set. The position density map shows the shape of the molecular orbital in one plane through the molecule containing PCH and bisecting the angle between the other two ligands. The P atom is situated at the origin. The momentum map shows momenta perpendicular and parallel to the defined planes in position space. The contours represent 0.01, 0.03, 0.1, 0.3, 1.0, 3.0, 10.0, 30.0, and 99.0% of the maximum density.

The experimental momentum profiles for PH_3, PF_3 and $P(CH_3)_3$ are compared on Figs. 6.1-6.3 respectively with a range of theoretical momentum profiles (TMPs) calculated at the Hartree-Fock level. Selected properties from each calculation and the corresponding experimental values are shown in Table 6.1. The Hartree-Fock basis sets used range from a very modest minimal STO-3G basis to the very much larger AUG5 and 136-GTO basis sets. The effects of many-body correlation and electronic relaxation are also seen on Fig. 6.1 from the MRSD-CI ion-neutral overlap reported earlier [74]. It should be noted that the experimental instrumental angular resolution has been accounted for in all theoretical momentum profiles in Figs. 6.1-6.3 using the GW-PG method [59].

Experiment and theory have been placed on a common intensity scale for each molecule by normalizing the experiment to the 136-G(CI) momentum profile for PH_3, the AUG3 momentum profile for PF_3 and the AUG5 momentum profile for $P(CH_3)_3$ (assuming unit pole strength). This places the calculations for each molecule on a common relative intensity scale. However, for dominantly s-type profiles such as the PF_3 and $P(CH_3)_3$ HOMOs (Figs. 6.2 and 6.3), it is more difficult to assess the quality of different TMPs than in the case of p-type profiles such as the $5a_1$ orbital of PH_3. This is because a change in relative intensity at low p is often the only major distinguishing characteristic between two TMPs for dominantly s-type momentum profiles such as the PF_3 and $P(CH_3)_3$ HOMOs. As such, other normalizations to the XMP could be employed instead of the choices made in the present work.

As in previous studies on the substituted amines, intuitive arguments fail to predict the correct amount of s- and p-type contributions to the HOMO momentum profiles of PF_3 and $P(CH_3)_3$. Specifically, the momentum profiles for PF_3 and $P(CH_3)_3$ display far more s-type character than phosphine. Intuitive arguments based on their larger bond angles (see introduction) predict that these orbitals would have more p-type character than the HOMO of PH_3. While the presence of a small second maximum in the momentum profile at $p \sim 0.8$ au for $P(CH_3)_3$ indicates a small amount of p-type character in this orbital, it is obvious (Fig. 6.3) that s-type character is dominant in this XMP. Thus, as might be expected, intuitive arguments

involving hybridization and localized bonding are unreliable. However, as can be seen from Figs. 6.1-6.3, delocalized molecular orbital concepts including even the simplest STO-3G molecular orbital description clearly provide a more realistic description of the HOMOs. The general shapes of the experimental momentum profiles are similar to those of their respective amine analogs [70,80-82]. The HOMO of NF_3 displays relatively more p-type character than the HOMO of PF_3 as shown by the prominent maxima at $p \sim 1.3$ au that is clearly observed in the NF_3 XMP [81,82]. In contrast, the XMP of PF_3 shows no strong second maxima in this region. For $N(CH_3)_3$ and $P(CH_3)_3$, the ratio of s to p character is similar in both momentum profiles.

A more detailed examination of the momentum profiles calculated using Hartree-Fock and MRSD-CI procedures will now be presented. The minimal basis set STO-3G result (curve 1 on Figs. 6.1-6.3) has generally the poorest agreement for shape and intensity with the experimental momentum profiles and the properties listed in Table 6.1. For example, the STO-3G calculation gives a seriously incorrect prediction of the s to p ratio for the $P(CH_3)_3$ XMP. The STO-3G total energy for all molecules is also very poor, as expected from the low degree of basis set saturation in this calculation. While the STO-3G dipole moment for PH_3 is better than those from several large basis sets, it is well known that the STO-3G calculation often produces fairly good dipole moments because of a fortuitous error cancellation [57]. In addition, the STO-3G dipole moment for $P(CH_3)_3$ is clearly in error. The split-valence description using the small 4-31G basis set calculation (curve 2 on Figs. 6.1-6.3) provides a moderately better description of the XMPs of all molecules than the STO-3G momentum profile. For other properties, the 4-31G total energies (Table 6.1) are surpassed by those from larger basis sets. However, the 4-31G dipole moments are interesting in that those for PH_3 and PF_3 are clearly in error while the 4-31G dipole moment for $P(CH_3)_3$ is in agreement with experiment.

The TMPs from the intermediate size 6-311G calculation (curve 3 on Figs. 6.1-6.3) provide slightly better energies and an improved fit to the XMPs of PH_3, PF_3 and $P(CH_3)_3$

compared with the low-level minimal basis set and 4-31G calculations. For other properties, the 6-311G values are easily surpassed by those from larger basis sets (Table 6.1). The next level of calculation is the addition of diffuse and polarization character to the 6-311G basis set. While the 6-311+G* momentum profile (curve 4 on Figs. 6.1-6.3) gives a better shape fit than the 6-311G TMP for PH_3, little shape difference is seen for these two calculated TMPs for PF_3 and $P(CH_3)_3$. For other properties, though, the 6-311+G* gives lower total energies and much improved dipole moments compared with the 6-311G value (Table 6.1). The 6-311++G** momentum profiles for PH_3 and $P(CH_3)_3$ (curve 5 on Figs. 6.1 and 6.3) show little or no shape change from the 6-311+G* momentum profiles, thus indicating that added diffuse and polarization of the H atom basis sets has little effect on the calculated momentum profiles. Instead, the main improvements are in total energies and dipole moments for PH_3 and $P(CH_3)_3$.

Despite the larger size of the AUG3 calculation, the 6-311++G** (curve 5) and AUG3 (curve 6) momentum profiles for $P(CH_3)_3$ are almost identical (see Fig. 6.3). Generally good shape agreement with experiment is provided by the AUG3 and 6-311+G* TMPs for PF_3 (Fig. 6.2). The AUG3 calculation provides a slightly better momentum profile (see p_{max}) for PH_3 than that from the 6-311++G** result.

The AUG3 and AUG5 momentum profiles (curves 6 and 7, respectively, on Figs. 6.1-6.3) are similar in shape for each molecule, although there are some differences in intensity, especially for PF_3. It can be noted that the AUG5 calculation for PH_3 involves an even larger basis set than the 136-GTO calculation thought to be near the Hartree-Fock limit in the work of Clark et al. [74]. The AUG5 and 136-GTO TMPs are in excellent agreement for shape and also give reasonably similar total energies and dipole moments. This again indicates that the Hartree-Fock limit is closely approached at this level. The AUG5 also gives the lowest total energies for PF_3 and $P(CH_3)_3$. The AUG5 dipole moments for all molecules are also generally good, especially for PH_3 and PF_3.

The inclusion of electron correlation causes virtually no change in the TMP for PH_3 (compare the 136-GTO and 136-G(CI) momentum profiles in Fig. 6.1). TMPs for the valence orbitals of other third row heavy atom containing molecules such as HCl [76] and H_2S [75] have also shown little change with inclusion of CI. This is in contrast to the equivalent second row heavy atom containing molecules such as NH_3, HF and H_2O [39,69,72]. However, in all cases electron correlation and relaxation have a significant effect on the total energy and dipole moment (see Refs. [39,56,69] and calculations 8 and 8c in Table 6.1). The 136-G(CI) calculation gives the lowest total energy for PH_3 and provides a dipole moment within 0.05 Debye of experiment.

The XMPs for the outermost orbitals of PH_3, PF_3 and $P(CH_3)_3$ are also compared to the DFT theoretical momentum profiles in Figs. 6.4-6.6. The XMPs have been normalized to the DFT TMPs in Figs. 6.4-6.6 (it should be noted that different normalizations were selected for Figs. 6.1-6.3). For purposes of comparison, Hartree-Fock momentum profiles for each molecule and the post-Hartree-Fock 136-G(CI) momentum profile for PH_3 are also shown. It can be seen that the DFT momentum profiles are slightly more intense than the Hartree-Fock and post-Hartree-Fock results in Fig. 6.4, with the exception of curve 6b for PH_3.

The DFT target Kohn-Sham momentum profiles on Figs. 6.4-6.6 provide very good overall agreement with the experimental momentum profiles of all three molecules. The correlation-only AUG3-P TMP (curve 6p) is the most intense for PF_3 and $P(CH_3)_3$, followed by the local density approximation AUG3-L TMP (curve 6*l*). Curves 6p and 6*l* are identical for PH_3. For all molecules, the exchange and correlation AUG3-BP TMP (curve 6b) has the lowest intensity of the DFT TMPs. It should also be noted that there are only very small shape differences between the three DFT TMPs for PH_3, with the Becke-Perdew non-local calculation (curve 6b) fitting the best. However, for PF_3 and $P(CH_3)_3$, the shape differences between the DFT TMPs from the local density approximation and those from the non-local potentials are minimal.

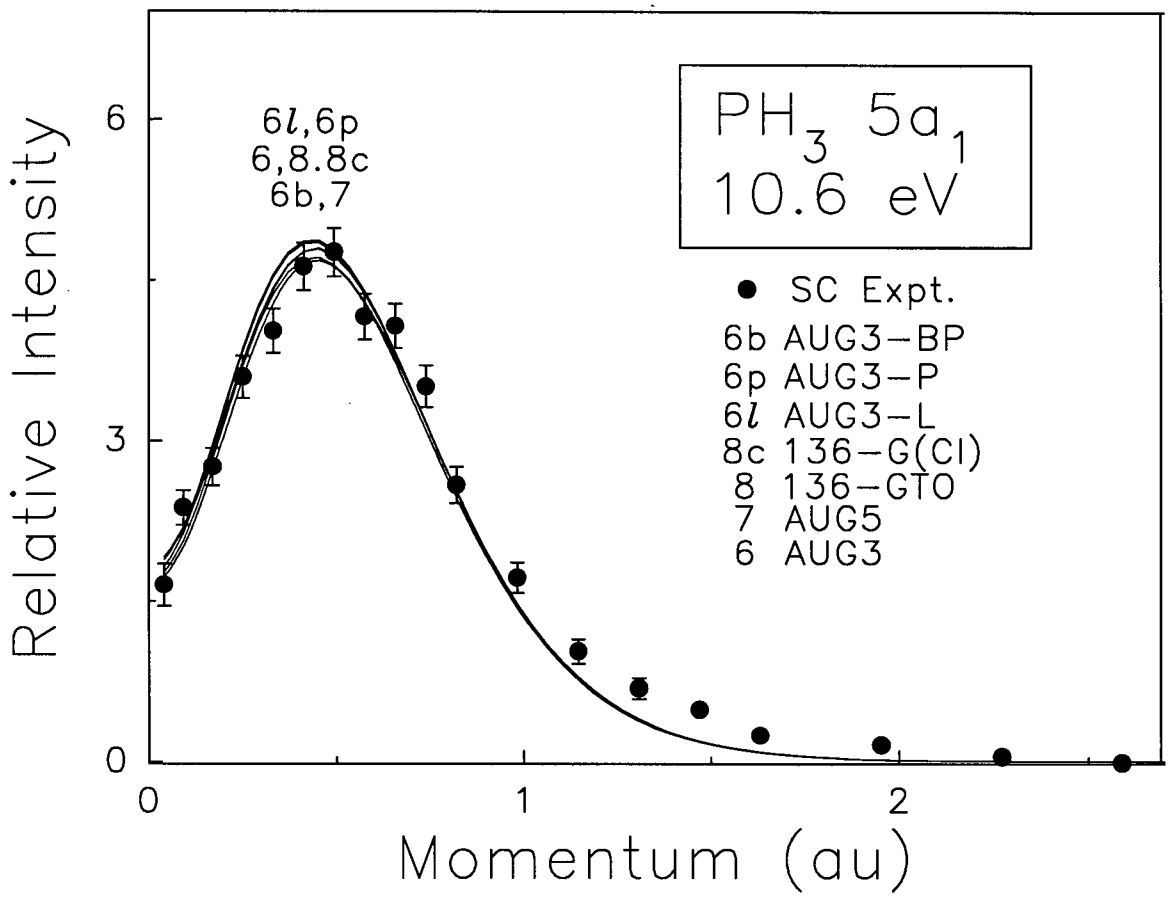

Fig. 6.4: Measured and calculated spherically averaged DFT momentum profiles for the $5a_1$ orbital of PH_3. The solid circles represent the single channel measurements also shown on Fig. 6.1. Selected Hartree-Fock and MRSD-CI calculated momentum profiles are also shown for comparison with the DFT momentum profiles. All calculations have been spherically averaged and folded with the experimental momentum resolution. See text and Table 6.1 for details of the wavefunctions and normalization procedures. Note that the normalization of experiment to theory differs from that used in Fig. 6.1.

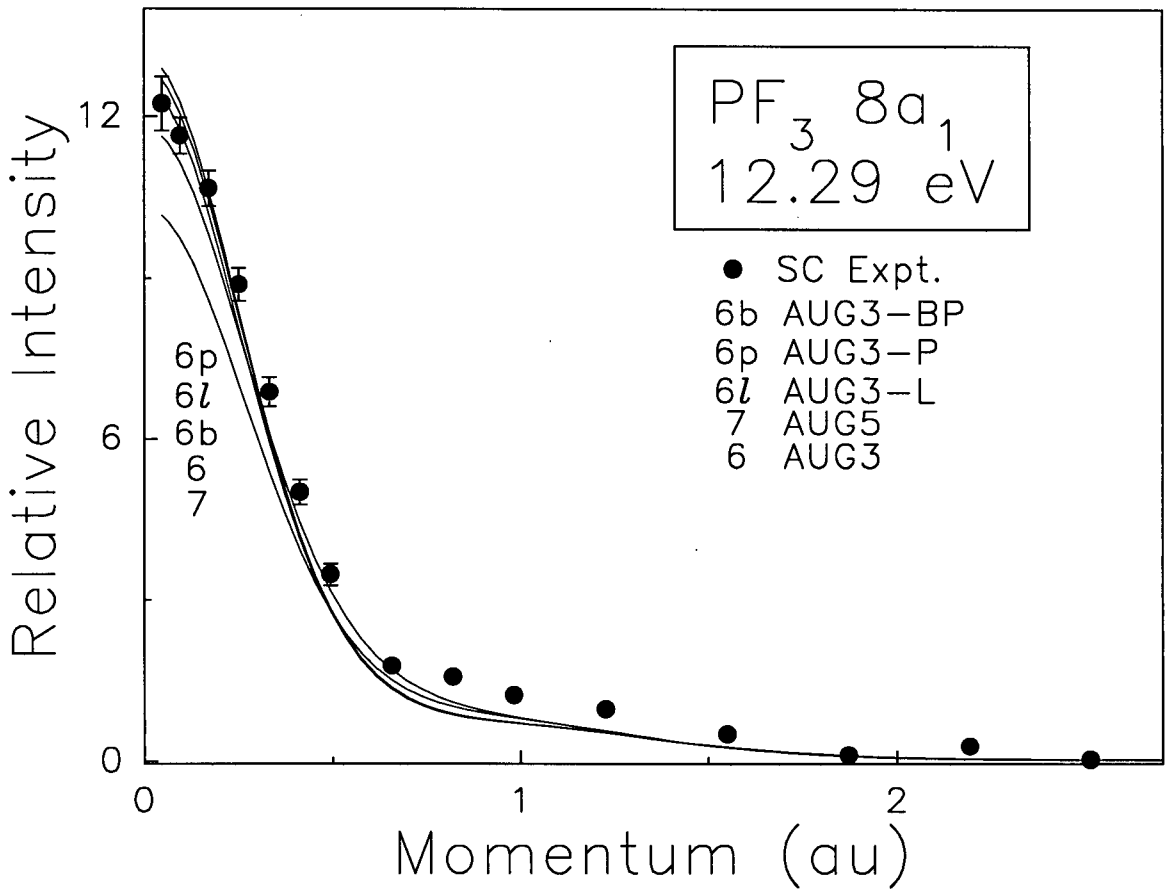

Fig. 6.5: Measured and calculated spherically averaged DFT momentum profiles for the $8a_1$ orbital of PF_3. The solid circles represent the single channel measurements also shown on Fig. 6.2. Selected Hartree-Fock calculated momentum profiles are also shown for comparison with the DFT momentum profiles. All calculations have been spherically averaged and folded with the experimental momentum resolution. See text and Table 6.1 for details of the wavefunctions and normalization procedures. Note that the normalization of experiment to theory differs from that used in Fig. 6.2.

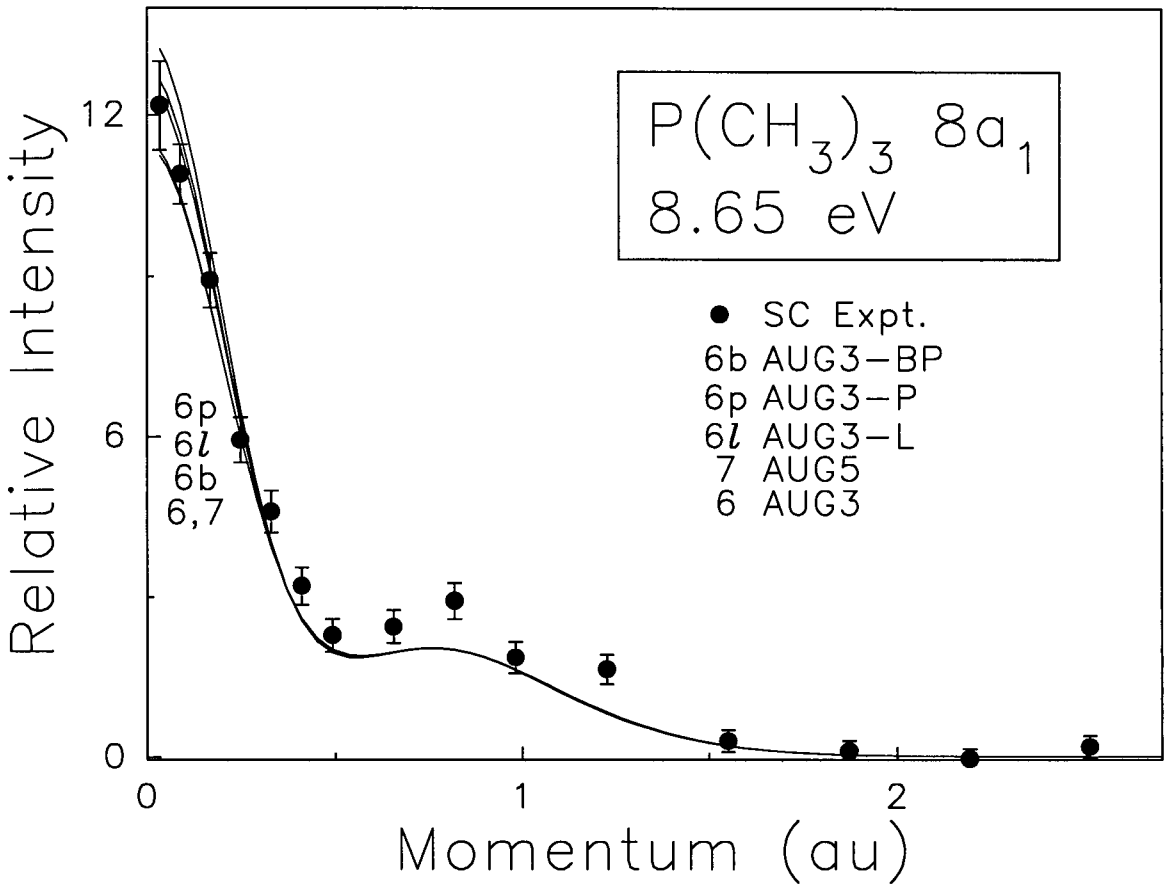

Fig. 6.6: Measured and calculated spherically averaged DFT momentum profiles for the $8a_1$ orbital of $P(CH_3)_3$. The solid circles represent the single channel measurements also shown on Fig. 6.3. Selected Hartree-Fock calculated momentum profiles are also shown for comparison with the DFT momentum profiles. All calculations have been spherically averaged and folded with the experimental momentum resolution. See text and Table 6.1 for details of the wavefunctions and normalization procedures. Note that the normalization of experiment to theory differs from that used in Fig. 6.3.

Of the DFT momentum profiles for PH_3, the AUG3-BP momentum profile (curve 6b on Fig. 6.4) provides generally the best shape fit with the observed XMP. While this profile provides an acceptable fit to the XMP, it is difficult to see any improvement for shape compared to the high-level Hartree-Fock and post-Hartree-Fock momentum profiles for PH_3 (compare to curves 6-8c on Fig. 6.4). Similarly, all of the DFT momentum profiles for PF_3 presented in Fig. 6.5 fit the XMP well for shape, but these results are roughly comparable to those from the Hartree-Fock momentum profiles (curves 6 and 7 on Fig. 6.5, and also refer to Fig. 6.2).

The DFT momentum profiles for $P(CH_3)_3$ also provide good fits to the XMP (Fig. 6.6) although there is some discrepancy in the region of the second maximum from p = 0.5 au to p = 1.3 au where the TMPs underestimate the XMP. As mentioned above, much of the problem in determining the "goodness" of a TMP for this orbital arises from the characteristics of an sp-type momentum profile. A slightly better shape fit is achieved by normalization to the Hartree-Fock momentum profile from the AUG3 calculation in Fig. 6.3. For other electronic properties, DFT dipole moments from the AUG3-P and AUG3-BP for PH_3 and $P(CH_3)_3$ are in good agreement with experiment and are generally more accurate than those from Hartree-Fock and post-Hartree-Fock calculations (Table 6.1). DFT dipole moments for PF_3 are also accurate (within 0.27 Debye of experiment), although better dipole moments are obtained from the Hartree-Fock AUG3 and AUG5 calculations. In addition, as discussed in Section 2.1.4, there is the well-known problem of obtaining absolute energies from DFT [111,214]. However, it can be said that the DFT treatments provide quite good values of the other properties in the present work.

6.3.2 Density Maps in Momentum and Position Space

Calculated momentum and position space density contour maps for the HOMOs of PH_3, PF_3 and $P(CH_3)_3$ are presented in Figs. 6.1-6.3 above. These maps are slices of the

orbital electron density $|\psi|^2$ in momentum and position space, respectively. It should be noted that these maps are for oriented molecules, whereas the momentum profiles in Figs. 6.1-6.3 are for randomly oriented (i.e. spherically averaged) molecules. The maps were produced with the AUG3 Hartree-Fock calculation since this provides a reasonably adequate description for all three molecules (see Section 6.3.1). The position density maps show the shapes of the molecular orbitals in one plane through the molecule containing PH, PF or PCH, respectively, and bisecting the angle between the other two ligands. The P atom is situated at the origin. The momentum maps show momenta perpendicular and parallel to the defined planes in position space. The side panels on each map show slices of the momentum or position space density along the vertical (right panel) and horizontal (top panel) axes. All dimensions for the *p*- and *r*-maps are in atomic units.

The *p*- and *r*-maps in Figs. 6.1-6.3 are helpful in understanding the shapes of the experimental and theoretical momentum profiles. It is obvious from the *p*-maps of PF_3 and $P(CH_3)_3$ that the intensity is largest at $p = 0$ and thus (after spherical averaging) there is maximum intensity at $p = 0$ in the momentum profile (Figs. 6.2 and 6.3). However, for PH_3 there is only a small amount of intensity at $p = 0$ as indicated by the side panels on the momentum density map (Fig. 6.1). While some small degree of s-type character (due to the H atoms) is seen in the PH_3 momentum profile, p-type character is dominant for this orbital. The two maxima centered at $p = \pm 0.5$ au in the right side panel of the PH_3 *p*-map are also reflected in the momentum profile as a p_{max} (after spherical averaging) occurring at ~ 0.5 au. Similarly, the two other large maxima in the $P(CH_3)_3$ *p*-map at $p = \pm 0.8$ au (right panel) account for the p-type behaviour and second maxima at $p \sim 0.8$ au in the momentum profile after spherical averaging.

Similar to previous work on the methylamines [80-82], the observed increase in s-character upon methyl substitution in PH_3 to give $P(CH_3)_3$ can be related to an increased H 1s contribution to the MO from the H *trans* to the "lone pair". A consideration of the MO

coefficients in both the AUG3 wavefunction and the simpler 4-31G wavefunction indicates that although the H 1s contribution in PH_3 is relatively small the *trans*-H 1s contribution to the HOMO in $P(CH_3)_3$ is quite large. In addition, the calculated increased intensity at p = 0 au must be solely due to these increased s orbitals contributions. This is more readily understood if one considers the Fourier transformation between position and momentum space given by Eq. (2.59). Eq. (2.59) may be simplified to give the momentum space wavefunction at p = 0 au:

$$\psi(\boldsymbol{p})\big|_{p=0} = (2\pi)^{-3/2} \int \psi(\boldsymbol{r})\, d\boldsymbol{r} \tag{6.1}$$

Thus, only s-type orbitals can contribute at p = 0 au since pure p-type or d-type orbitals have equal lobes of opposite sign [27] with a node at the origin (i.e. they have zero integrated "area" in both position and momentum space). The increased contribution of trans-H 1s to the $P(CH_3)_3$ HOMO relative to the PH_3 HOMO thus corresponds to greater intensity at p = 0 according to Eq. (6.1) and thus the momentum profile is expected to be more s-type as is observed (Fig. 6.3). A similar effect (i.e. decreased %p character and increased %s character following methyl substitution) has also been observed in the comparison of the outermost orbitals of HCHO, CH_3CHO and $(CH_3)_2CO$ [83]. The implications of these results for the methyl inductive effect in organic chemistry will be discussed in Section 6.3.3.

The increase in s-character in PF_3 relative to PH_3 occurs for a different reason than that for $P(CH_3)_3$ and PH_3. Analysis of the density maps and an examination of the MO coefficients reveals a sharp increase in the P 3s atomic orbital contribution to the HOMO of PF_3 compared to the 3s contribution to the HOMO of PH_3. The higher P 3s contribution in PF_3 relative to the P 3s contribution in PH_3 is clearly seen in the top and right panels of the r-maps for these molecules as increased density at zero atomic units for PF_3. These results are analogous to the sharp increase in N 2s contribution to the MO observed for NF_3 relative to NH_3 in previous work [81].

Bawagan and Brion [82] commented on the "secondary" p_{max} for the methyl-substituted amines and noted that increasing methyl substitution led to an increase of p_{max} from 0.52 au in NH_3 to ~ 1.1 au in $N(CH_3)_3$. Although no experimental momentum profiles are available for $PH_2(CH_3)$ and $PH(CH_3)_2$, the momentum profiles for PH_3 and $P(CH_3)_3$ also follow this trend (p_{max} for PH_3 is 0.5 au while the secondary p_{max} for $P(CH_3)_3$ occurs at ~ 0.8 au). The shift of p_{max} towards higher momentum has earlier been associated with additional nodal surfaces [83,199,215]. Tossell et al. [80] and Bawagan and Brion [82] suggested that the higher momentum components observed in the methyl-substituted amines compared to NH_3 were due to these extra nodal surfaces. These nodes were attributed to the trans-H 1s which is *antibonding* with respect to the N 2p. Similarly, it is suggested in the present work that the shift of p_{max} of $P(CH_3)_3$ towards higher momentum relative to p_{max} of PH_3 is due to the increased trans-H 1s character in the $P(CH_3)_3$ HOMO relative the trans-H 1s character in the PH_3 HOMO. The increase in number of nodal surfaces with increasing methyl substitution can be seen by considering the corresponding position space density maps for PH_3 and $P(CH_3)_3$ (Figs. 6.1 and 6.3, respectively).

6.3.3 The Methyl Inductive Effect

To provide more insight into the relatively large amount of s-type character in the HOMOs of PF_3 and $P(CH_3)_3$ and the inability of geometry and hybridization arguments to rationalize the results, two-dimensional position (charge) density difference maps for the outermost orbitals of PF_3 and PH_3, and also $P(CH_3)_3$ and PH_3 are shown in Fig. 6.7 calculated with the 4-31G and AUG3 wavefunctions. These maps are slices of the orbital electron density differences $\rho_{PF_3} - \rho_{PH_3}$ and $\rho_{P(CH_3)_3} - \rho_{PH_3}$ in position space. The position density difference maps show the shapes of the molecular orbitals in one plane through the molecule containing PH, PF or PCH, respectively, and bisecting the angle between the other two ligands. The P atom is situated at the origin. Slices of the position space density difference along the vertical

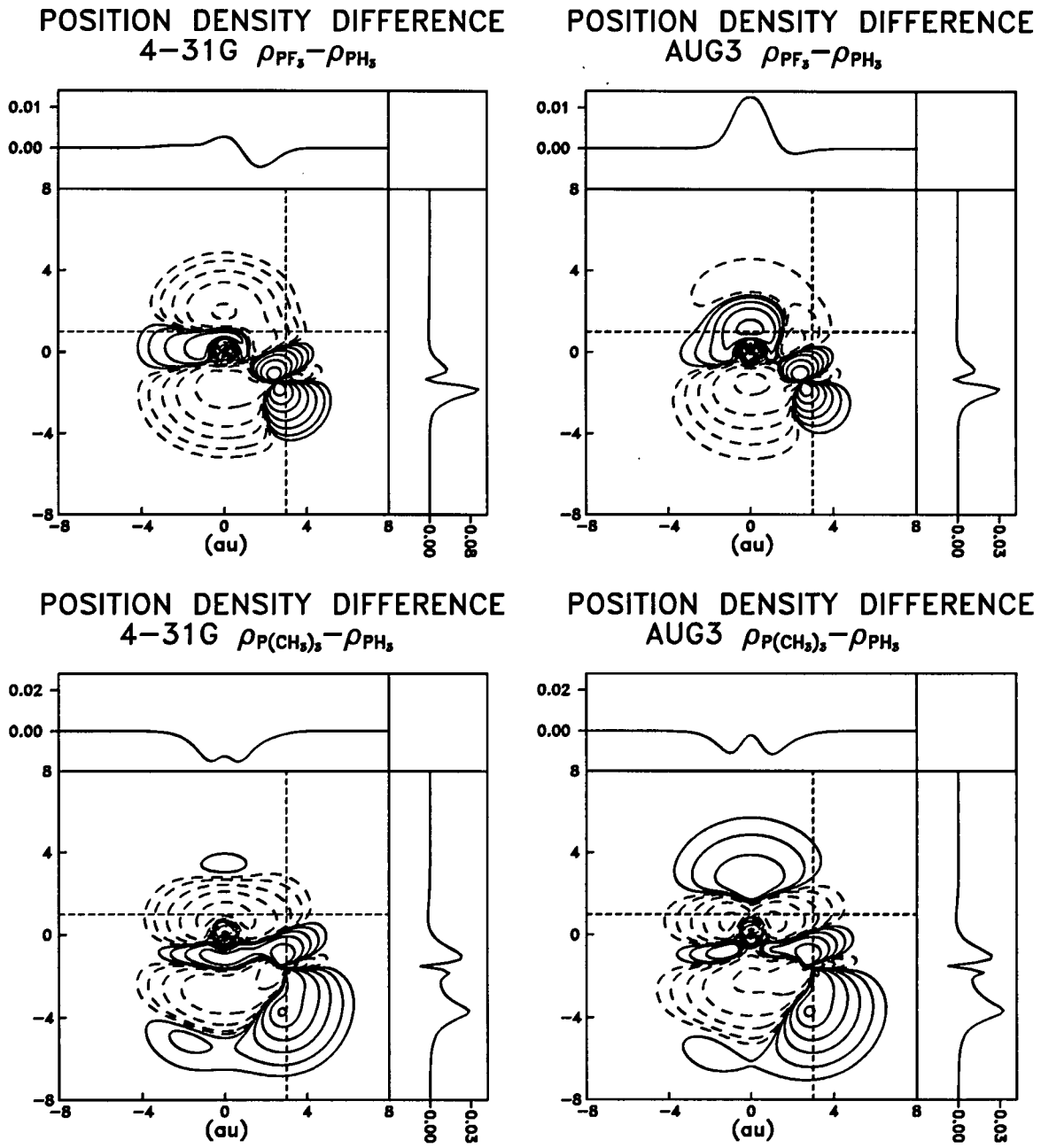

Fig. 6.7: Position (charge) density difference maps for substituted phosphines. The contour maps were generated with the 4-31G and AUG3 wavefunctions and all maps show the density for oriented molecules. The position density difference maps show the shapes of the molecular orbitals in one plane through the molecule containing PH, PF or PCH, respectively, and bisecting the angle between the other two ligands. The P atom is situated at the origin. The contour values represent ±0.01, ±0.03, ±0.1, ±0.3, ±1.0, ±3.0, ±10.0, ±30.0 and ±99.0% of the maximum intensities. Positive difference is shown by solid contour lines while negative difference is shown as dashed lines. The side panels (top and right side) show the density difference along the dashed lines (horizontal and vertical) in the density map.

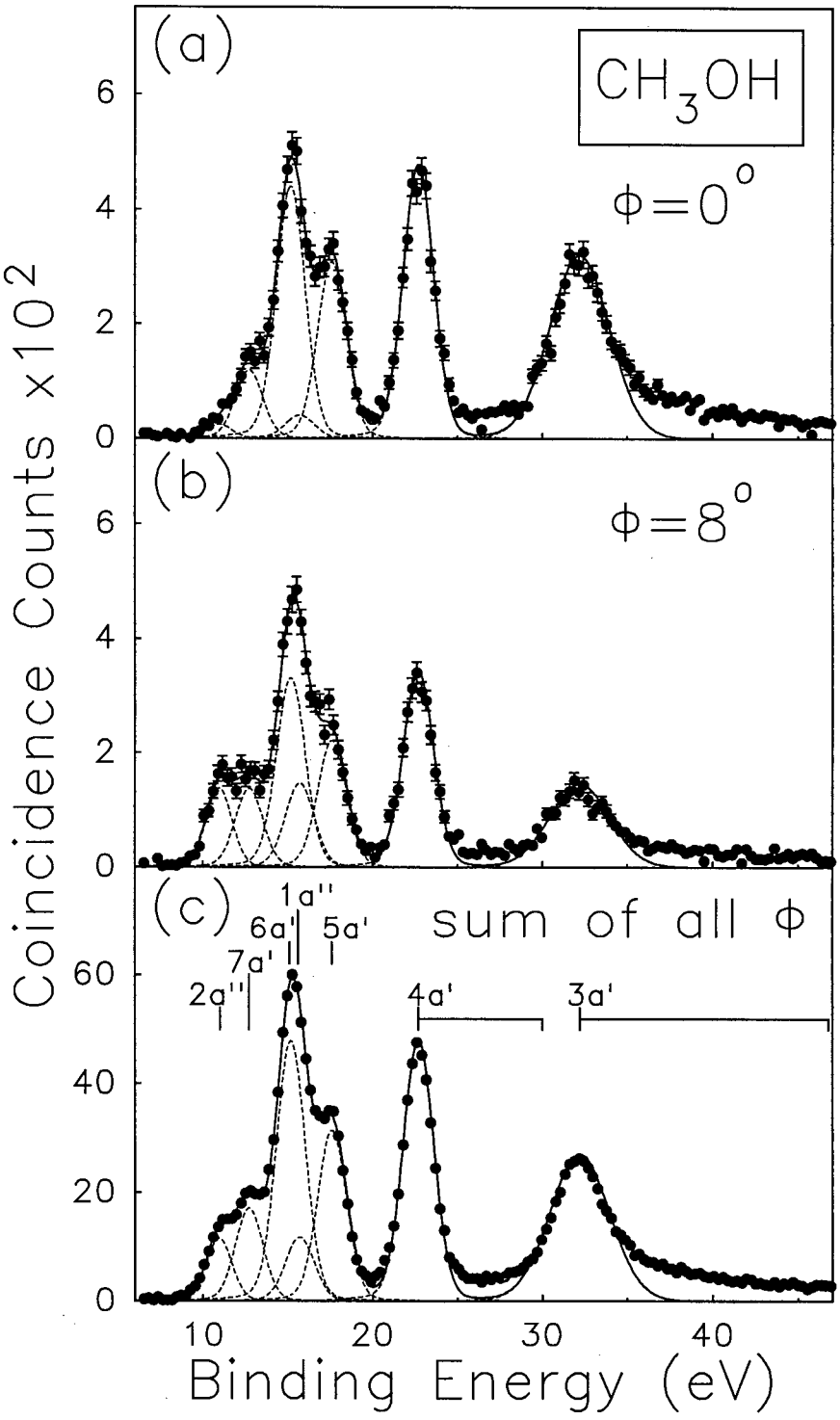

Fig. 8.1: EMS binding energy spectra of CH_3OH from 6 to 47 eV at **(a)** $\phi = 0°$, **(b)** $\phi = 8°$ and **(c)** summed over sixteen ϕ angles, obtained at an impact energy of (1200 eV + binding energy). The dashed lines represent Gaussian fits to the peaks and the solid curve is the summed fit.

by high resolution ultraviolet photoelectron spectroscopy [174,260] for the six outermost orbitals. However, the $(1a'')^{-1}$ and $(6a')^{-1}$ bands are only partially resolved even at high resolution. A low resolution X-ray photoelectron spectroscopy experiment [183] gave an ionization potential of 32.2 eV for the main inner valence peak corresponding to the $(3a')^{-1}$ state. The work of von Niessen et al. [260] has compiled the experimental ionization potential data up to 1979 together with the results of many-body Green's function calculations of the binding energy spectrum. Measured ionization potentials from the literature [174,183,260], the EMS ionization potentials from Minchinton et al. [84], and those used in the present work are shown in Table 8.2. Also given in Table 8.2 are calculated MRSD-CI ionization energies from the present work and Green's function ionization energies obtained by von Niessen et al. [260]. For the inner valence 3a′ and 4a′ orbitals, the corresponding spectroscopic strengths from the Green's function calculations [260] results are also shown.

The removal of the least tightly bound (i.e. HOMO) 2a″ electron leads to the ground state of the ion corresponding to the band at 11.0 eV in the EMS binding energy spectrum (Fig. 8.1). The nodal "p-type" character of this orbital which would be expected for such an oxygen "lone pair" of electrons is confirmed by the fact that the intensity is much larger at $\phi = 8°$ than at $\phi = 0°$. However, the second "lone pair" (i.e. 7a′ orbital) results in the band at 12.7 eV which has only slightly larger intensity at $\phi = 8°$ than at $\phi = 0°$, indicating a mixed s-p type character. The band at ~ 15.5 eV results from ionization from both the 6a′ and 1a″ orbitals while the $(5a')^{-1}$ ionization accounts for the partially resolved shoulder at 17.7 eV. The $(4a')^{-1}$ process produces the large bands in the inner valence region at 22.7 eV. Other than for the 2a″ (HOMO) band, the intensities of each of the other bands are quite similar both at $\phi = 0°$ and $\phi = 8°$ thus indicating that these all have appreciable totally symmetric ("s-type") components in the wavefunctions of the corresponding molecular orbitals. The region above 25 eV which has been studied earlier both by XPS [183] and EMS [84] shows a prominent peak at 32.2 eV due to the $(3a')^{-1}$ process. However, there is considerable additional ionization strength both between 25-29 eV and also spread out over the binding energy spectrum above the 32.2 eV

peak to the limit of the data at 47 eV. The many-body Tamm-Dancoff Green's function inner valence calculations reported by von Niessen et al. [260] predict the $(4a')^{-1}$ process to be dominated by two poles at 23.01 and 23.38 eV each with a spectroscopic factor of 0.44 (Table 8.2). The calculations [260] also predict that the $(3a')^{-1}$ process is severely split into at least nine poles spread over a wide energy range with the main intensity in the ~ 33 eV region, in reasonable agreement with experiment. However, the remaining intensity observed above 36 eV is not predicted [260].

Calculated binding energy spectra are compared with the measured binding energy spectra in Fig. 8.2. Theory and experiment have been normalized at 15.2 eV in the $\phi = 8°$ spectrum The calculated spectra are obtained by using the pole energies and pole strengths given by von Niessen et al. [260] in Table 8.2, and the Trun-pV5Z theoretical momentum profiles for each pole at each angle. For the first six main peaks below 25 eV, the measured EMS instrumental energy resolution function, as well as the widths of the transitions as observed in the experimental EMS binding energy spectra (see Fig. 8.1 and Table 8.2) have been folded into the calculated spectra. For the $(3a')^{-1}$ ionization parent and satellite processes and their corresponding poles, both the EMS energy resolution and an width of 2.00 eV based on the observed XPS [183] have been folded into the calculated spectra.

The region containing the 2a″ and 7a′ orbitals is overestimated at $\phi = 8°$ and underestimated at $\phi = 0°$. However, the correct shapes and positions are also reasonably well predicted at both angles for the 14 to 17 eV energy region containing the $(6a')^{-1}$ and $(1a'')^{-1}$ ionization processes. The energy position of the $(5a')^{-1}$ ionization process is also predicted well, especially at $\phi = 8°$, but the experiment has greater intensity at $\phi = 0°$ than predicted (i.e. more s-type character than predicted). The predicted energy of the $(4a')^{-1}$ ionization process is about 0.5 eV too high, thus causing the leading edge of the experimental peak at 22.7 eV to be underestimated. In addition, the peak maxima of the $(4a')^{-1}$ peak is also overestimated by the calculation at both angles while no poles model the experimental intensity in the 25-30 eV region, thus suggesting that the theory should contain lower pole strength at the

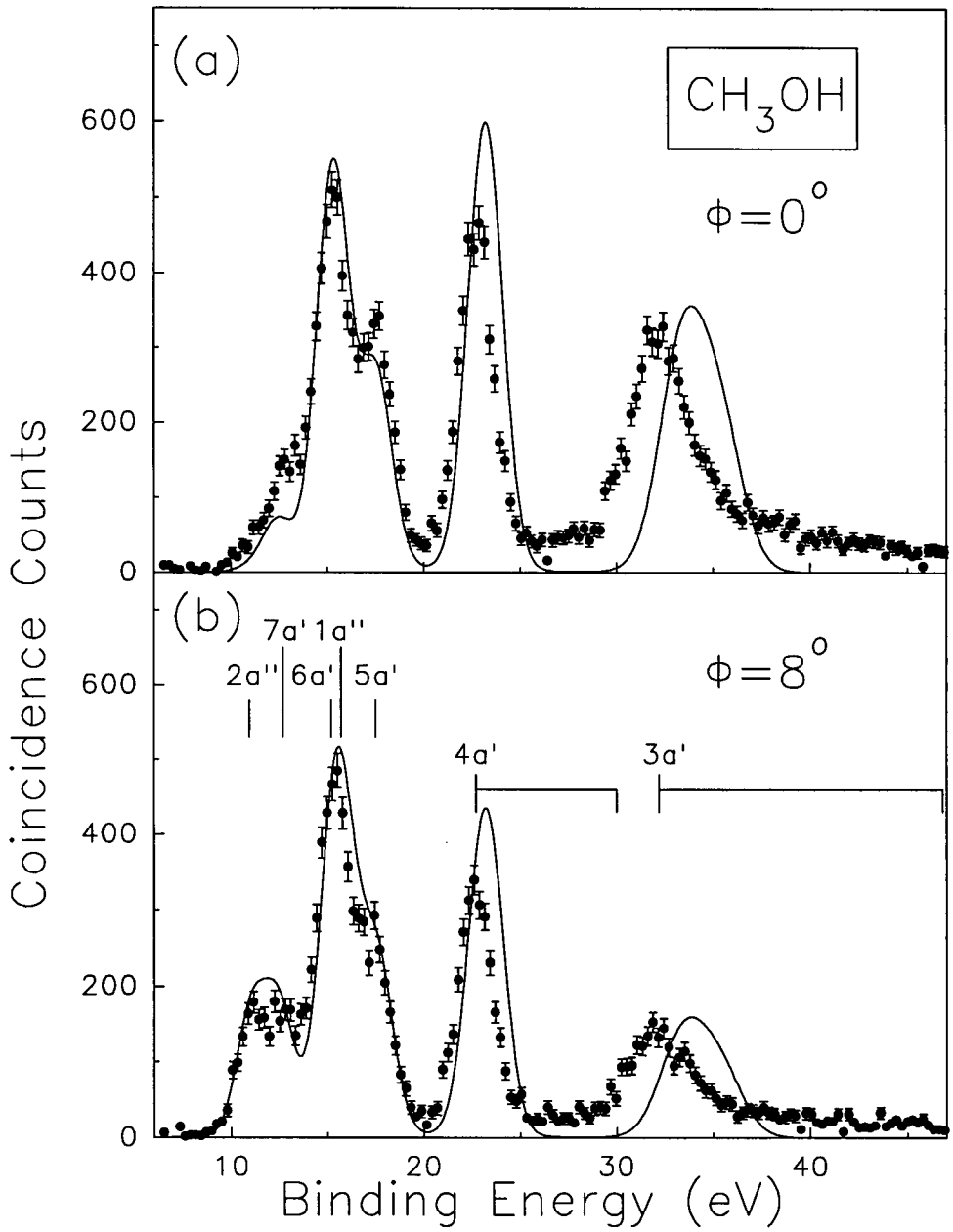

Fig. 8.2: Measured and calculated binding energy spectra of CH_3OH from 6 to 47 eV at **(a)** $\phi = 0°$ and **(b)** $\phi = 8°$. The solid curves indicate the synthesized theoretical binding energy spectra with pole energies and pole strengths (Table 8.2) given by the Green's function calculation [260] and including the angular dependence from the Trun-pV5Z Hartree-Fock calculation. The same energy peak widths as used in Fig. 8.1 have been folded into the synthesized spectra. See text for details.

stated energies of 23.01 and 23.38 eV (Table 8.2) and instead place more $(4a')^{-1}$ poles in the region 25-30 eV. The intensity of the theory in the region > 30 eV is in good agreement (at both angles) with the main peak corresponding to $(3a')^{-1}$ parent ionization at an experimental ionization energy of 32.2 eV. However, the theoretical peak is ~ 0.8 eV too high in energy and this can be attributed to the energies of the major $(3a')^{-1}$ poles predicted at 32.82 and 33.08 eV (Table 8.2). While the shape of the parent peak is well-predicted, the overall asymmetry and observed non-zero intensity of the experimental data out to 47 eV is not well-modelled by theory. The highest energy predicted for any pole is 35.62 eV and it is clear from the experiment that more poles with considerable pole strength are needed at higher energies.

8.3.2 Comparison of Experimental and Theoretical Momentum Profiles

High momentum resolution measurements have been made of the valence electron experimental momentum profiles (XMPs) for CH_3OH (Figs. 8.3-8.5) at each ϕ angle. The fitted peak areas in the binding energy spectra (see Section 8.3.1) have been used for the relative intensities of the seven valence orbitals. On each figure the mean binding energy for each XMP is noted. These values correspond to the energy position of the main Gaussian function used to fit this peak in the deconvolution procedure.

Although much improved statistics have been obtained in the present multichannel work for CH_3OH, the shapes and relative intensities obtained in the present work are consistent with the previous measurements [84]. The most significant improvements are for the two outermost (2a″ and 7a′) orbitals and for the inner valence 4a′ orbital. In addition, the level of theory was much more limited in the earlier work [84] in that only a single Hartree-Fock calculation with a small basis set was used and no post-Hartree-Fock calculations were performed. In the present work, the experimental momentum profiles are compared on Figs. 8.3-8.5 respectively with the theoretical momentum profiles (TMPs) calculated using a range of basis sets from the very modest minimal STO-3G basis set to the near-Hartree-Fock limit level (110-GTO and Trun-pV5Z) as described in Section 8.2.1. The effects of electron

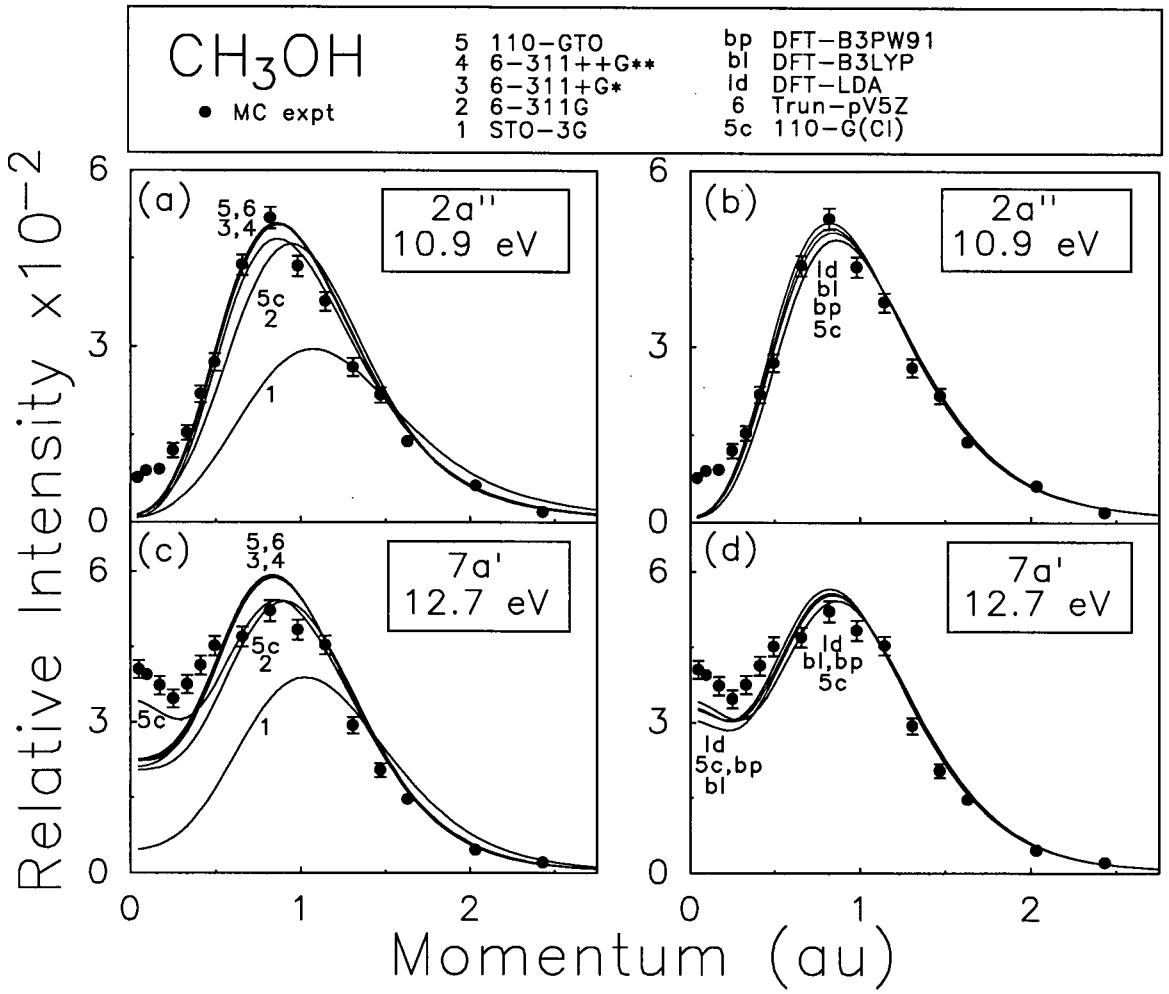

Fig. 8.3: Measured and calculated spherically averaged momentum profiles for the 2a″ and 7a′ orbitals of methanol. The solid circles represent the experimental energy-dispersive multichannel measurements. All calculations have been spherically averaged and folded with the experimental momentum resolution. See text and Table 8.1 for details of the wavefunctions and normalization procedures.

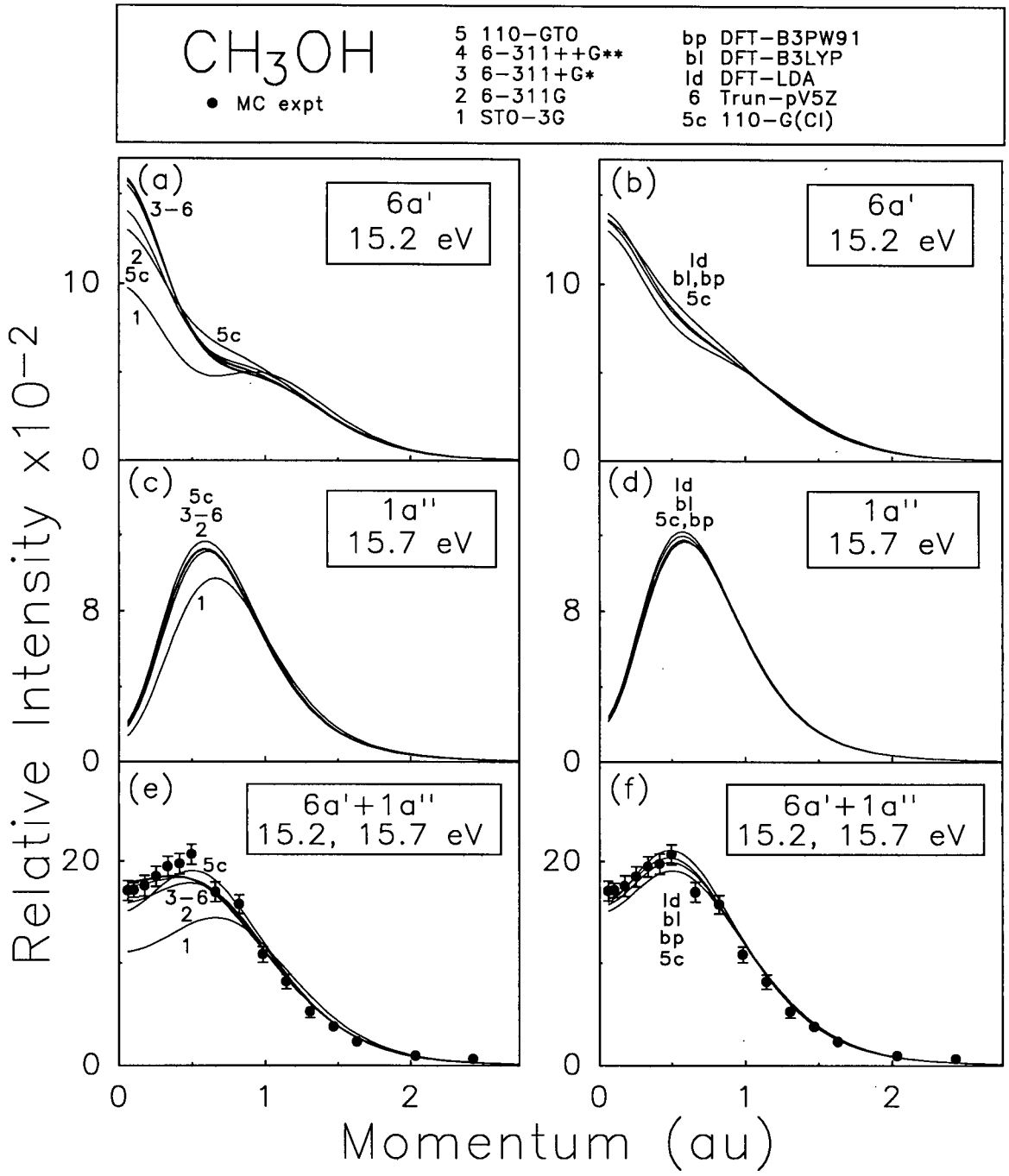

Fig. 8.4: Calculated spherically averaged momentum profiles for the 6a′, 1a″ and sum of the 6a′ and 1a″ orbitals of methanol. All calculations have been spherically averaged and folded with the experimental momentum resolution. See text and Table 8.1 for details of the wavefunctions and normalization procedures.

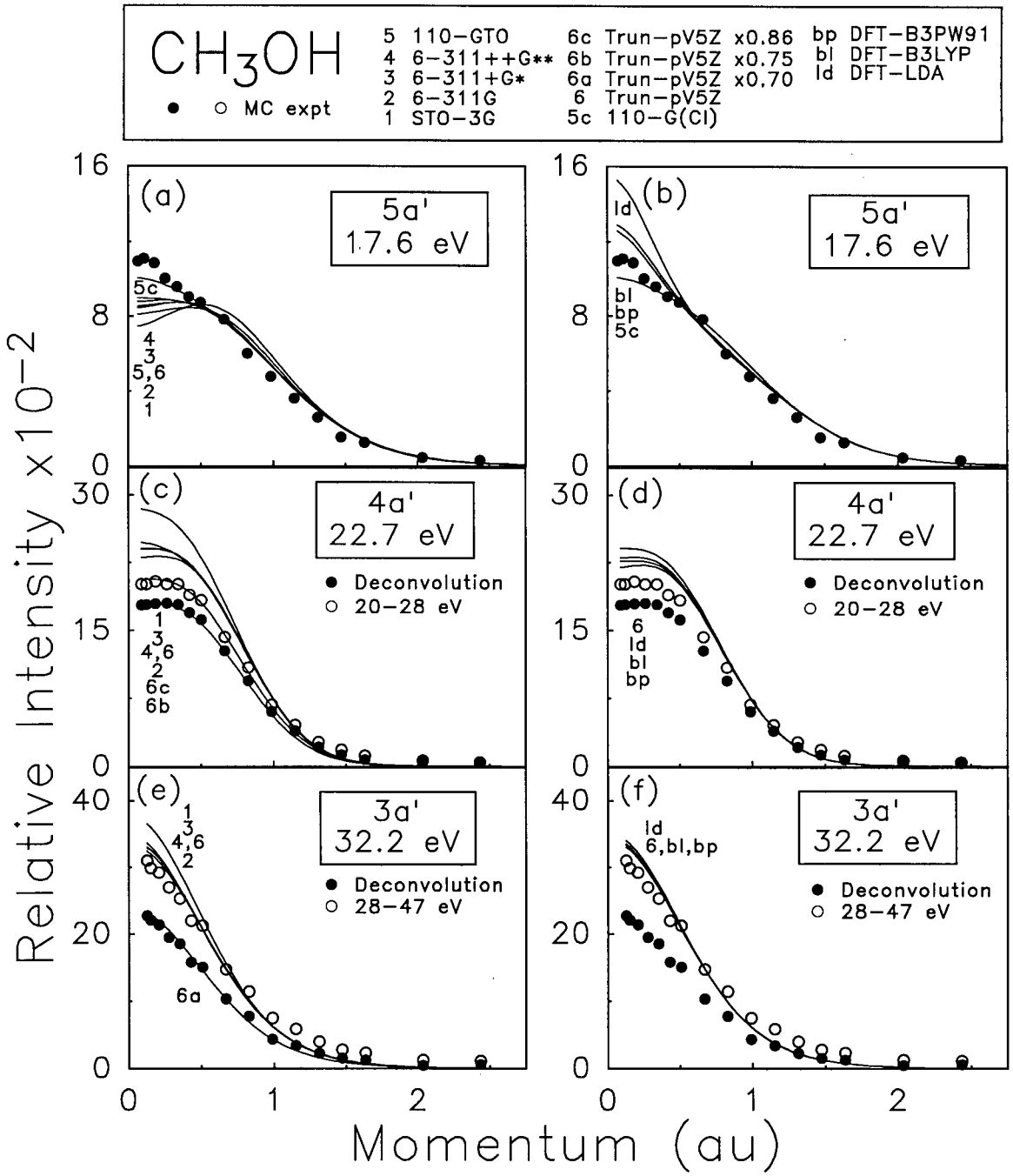

Fig. 8.5: Measured and calculated spherically averaged momentum profiles for the 5a′, 4a′ and 3a′ orbitals of methanol. The solid circles represent the experimental energy-dispersive multichannel measurements from the deconvolution procedure. The open circles for the 4a′ orbital represent the experimental energy-dispersive multichannel measurements taken by summing over all angles within the energy "slice" of 20-28 eV while the open circles for the 3a′ orbital represent the experimental energy-dispersive multichannel measurements taken by summing over all angles within the energy "slice" of 28-47 eV. See text and Table 8.1 for details of the wavefunctions and normalization procedures. Curves 6a, 6b and 6c are constructed by scaling curve 6 by factors of 0.70, 0.75 and 0.86, respectively.

correlation and electronic relaxation effects are also investigated in Figs. 8.3-8.5 by the 110-G(CI) MRSD-CI ion-neutral overlaps described in Section 8.2.2 above. The DFT TMPs calculated according to Section 8.2.3 are also shown on Figs. 8.3-8.5. A pole strength of unity has been used in the presentation of all TMPs including the MRSD-CI theoretical momentum profiles in Figs. 8.3-8.5. The experimental instrumental angular resolution has been accounted for in all theoretical momentum profiles using the GW-PG method [59]. Experiment and theory have been placed on a common intensity scale for each molecule by normalizing the experiment to the 110-GTO theoretical momentum profile for the 2a″ (HOMO) orbital. It should be noted that alternative normalizations (e.g. on the 110-G(CI)) could be chosen. Selected other properties for each calculation and corresponding experimental values are shown in Table 8.1.

The observed experimental momentum profile for the 2a″ orbital (Figs. 8.3a and 8.3b) displays some intensity at low momentum below $p \sim 0.3$ au that is not accounted for by even the more sophisticated theoretical treatments. The only intensity that the TMPs in Figs. 8.3a and 8.3b have at $p = 0$ is due to the very small effects of the resolution folding procedure [59]. Minchinton et al. [84] also observed similar low momentum discrepancies between their experimental data for the 2a″ orbital and theory, although the differences were larger due to the use of the small double-zeta basis set which does not reproduce the low momentum region below 0.6 au. From the present work it is clear that the discrepancies at low momentum for the 2a″ orbital are significantly decreased by the use of high-level wavefunctions. The use of electron correlation and relaxation in the 110-G(CI) calculation (curve 5c) only decreases the intensity of the TMP slightly compared to curve 5, but there are no large differences in shape between these curves. This is in sharp contrast to the XMP and TMPs for the outermost $1b_1$ orbital of H_2O [37,39,69] in which electron correlation and relaxation effects are necessary to predict correctly the region of the XMP below the maximum ($p_{max} = 0.5$ au). Although slightly better agreement is obtained by the DFT momentum profiles in Fig. 8.3b,

some experimental intensity still remains unaccounted for in the very low momentum region ($p < 0.3$ au).

The experimental and theoretical momentum profiles for the 7a′ orbital are shown in Figs. 8.3c and 8.3d. In contrast to the situation for the 2a″ orbital, the calculation of the ion-neutral overlap including electronic correlation and relaxation by the MRSD-CI method produces a very significant improvement over the near Hartree-Fock limit calculations in the level of agreement between the measured and calculated 7a′ momentum profiles below 1 au (compare curves 5, 6 and 5c). The 110-G(CI) momentum profile is the only calculation in Fig. 8.3c that reasonably models both the shape and intensity of the 7a′ XMP. However, even this high-level post-Hartree-Fock calculation is not able to account for all the experimental intensity at low momentum ($p \leq 0.5$ au). The DFT momentum profiles for the 7a′ orbital (Fig. 8.3d) are slightly more intense than experiment in the region of the maximum about ~ 0.9 au. However, the DFT momentum profiles for the 7a′ orbital predict a similar shape at low momentum as the 110-G(CI) momentum profile and provide an even further improved fit to the experimental data in this region. This effect can be attributed to the inclusion of electron correlation in the DFT exchange-correlation potential.

The theoretical momentum profiles for the 6a′ and 1a″ orbitals of CH_3OH are shown in Figs. 8.4a-d. The summed (6a′+1a″) experimental and theoretical momentum profiles are shown in Figs. 8.4e and 8.4f. The shape and intensity of the (6a′+1a″) XMP is well-reproduced by the 110-G(CI) calculation although the intensity at low momentum is slightly underestimated. The Hartree-Fock momentum profiles do not predict the correct shape of the XMP in this region in that curves 2-6 tend to "flatten out" at low p while the XMP displays stronger p-type character. It is clear that the improved fit of the 110-G(CI) momentum profile for the (6a′+1a″) orbitals is due to the different shape it gives for the 6a′ momentum profile in Figs. 8.4a and 8.4b, placing less intensity in the region $p \leq 0.3$ au and more in the region $0.3 \leq p \leq 1.0$ au than the large basis set Hartree-Fock calculations. Except for the STO-3G momentum profile, all Hartree-Fock TMPs for the 1a″ orbital (Fig. 8.4c) are similar in shape.

Similar effects occur for the DFT and CI momentum profiles for the (6a′+1a″) orbital (Fig. 8.4f) and excellent shape and intensity fits with experiment are obtained.

The experimental momentum profile for the 5a′ orbital (Figs. 8.5a and 8.5b) is predominantly s-type. All the calculated profiles for the 5a′ molecular orbital show considerably less s-type contributions at low p than is observed experimentally. Minchinton et al. [84] also observed this discrepancy between simple Hartree-Fock theory and experiment in the low p region of the 5a′ orbital. In the present work the discrepancies between experiment and theory at low momentum are somewhat decreased by the use of larger basis set Hartree-Fock calculations and, in particular, by using the MRSD-CI method. It should be noted that in Fig. 8.5a the only TMP that provides reasonably adequate shape and intensity compared to the XMP is the high-level 110-G(CI) momentum profile. This suggests that electron correlation effects are important in the low momentum regions of the EMS cross-section for this orbital. All other calculations "flatten out" at low p or even predict a more p-type momentum profile in the case of very simple wavefunctions (STO-3G). The DFT momentum profiles for the 5a′ orbital (Fig. 8.5b) do not agree with experiment well in that the low momentum region near $p = 0$ is seriously overestimated. It appears that an overly spatially diffuse orbital has resulted from the DFT calculations, especially for the DFT-LDA results (see curve ld on Fig. 8.5b). While the shapes of Kohn-Sham DFT momentum profiles are often in reasonable agreement with experiment, but it has been observed that the use of approximate functionals in DFT calculations may result in overestimations of the "diffuseness" of the electron density [60,265]. These momentum profile overestimations have also been observed more frequently from DFT calculations employing the local density approximation functionals [60,265] which are generally considered to be of lower quality relative to gradient corrected functionals.

The experimental and theoretical momentum profiles for the 4a′ inner valence orbital of CH_3OH are shown in Figs. 8.5c and 8.5d. The filled circles show the experimental energy-dispersive multichannel EMS measurements for the peak at 22.7 eV obtained from the

deconvolution procedure. In addition, the open circles show the multichannel data taken from summing the experimental binning mode data over all angles within the given energy slice of 20-28 eV that contains the main peak centered at 22.7 eV in Fig. 8.1.. The theoretical momentum profiles in Fig. 8.5c are presented at 100% relative intensity with the exception of curves 6b and 6c. Curve 6b represents the Trun-pV5Z TMP for the 4a′ orbital multiplied by a factor of 0.75 while curve 6c represents the Trun-pV5Z momentum profile multiplied by a factor of 0.86. It can be seen in Fig. 8.5c that all of curves 1-6 provide reasonable shape comparisons to the XMPs. The best shape fits for the 4a′ XMP are given by the 6-311++G** and Trun-pV5Z momentum profiles. The 6-311G momentum profile (curve 2) for the 4a′ orbital also provides a reasonable shape fit. However, the most noticeable difference between experiment and curves 1-6 is that all of these curves greatly overestimate the deconvoluted experimental data (filled circles) and slightly overestimate the energy slice data (open circles). If curve 6 is multiplied by 0.75 to produce curve 6b, excellent shape and intensity agreement with the deconvoluted data is obtained. The intensities of the experimental deconvoluted and theoretical momentum profiles thus suggest that the 4a′ parent peak at 22.7 eV has a pole strength of 0.75 while the remaining 0.25 pole strength is split into higher energy "satellite" ionization processes up to 28 eV and beyond. A consideration of the data for energy region from 20-28 eV (open circles) accounts for most of the remaining pole strength. This data has the same shape as the filled circles, which indicates that the energy region from ~ 25-28 eV beyond the parent peak centered at 22.7 eV is composed of mainly $(4a')^{-1}$ satellite ionization processes. If curve 6 is multiplied by 0.86 to produce curve 6c, excellent shape and intensity agreement is obtained with the energy slice data from 20-28 eV. Thus, 86% of the $(4a')^{-1}$ intensity can be accounted for over this energy region. This is in agreement with the discussion of Section 8.3.1, in which the spectroscopic strength for the inner valence 4a′ orbital was found to be severely split. In the earlier study of methanol [84], a parent pole strength of 0.6 was indicated for the 4a′ orbital when comparing the intensities of the XMPs with the lower quality double-zeta Snyder and Basch [266] calculation. The DFT momentum profiles for the 4a′

orbital are shown in Fig. 8.5d along with the experimental data for the energy region 20-28 eV. The density functional TMPs all agree exceptionally well for the shape of the 4a′ XMP. In addition, DFT predicts intensities which are lower and more in agreement with experiment than the Hartree-Fock curve 6 and thus are consistent with essentially all of the $(4a')^{-1}$ pole strength being in the 20-28 eV region.

The experimental and theoretical momentum profiles for the 3a′ inner valence orbital of CH_3OH are shown in Figs. 8.5e and 8.5f. The filled circles represent the experimental multichannel EMS measurements obtained from the deconvolution procedure by fitting a Gaussian peak to the main $(3a')^{-1}$ parent ionization peak centered at 32.2 eV (see Fig. 8.1 and also Table 8.2). The open circles show the data for the entire high energy region of 28-47 eV which contains the parent peak and the satellite processes present at energies > 35 eV in the EMS binding energy spectra (Fig. 8.1). It can be seen from Figs. 8.5e and 8.5f that all calculations provide reasonable shape comparisons to the two XMPs. However, curves 1-6 all overestimate the intensity of the experimental data from the deconvolution procedure. If curve 6 is be multiplied by a factor of 0.70 (i.e. curve 6a), excellent agreement is obtained for shape and intensity with the experimental data. On this basis the 3a′ parent peak would have a pole strength of 0.70 with the remaining ~ 0.30 pole strength being split into higher energy satellite ionization processes. A similar parent pole strength of 0.6 was found in the earlier work [84]. This is consistent with the severe splitting of the inner valence 3a′ orbital predicted by theory [260]. The fact that the 28-47 eV data (open circles) has the same shape as the deconvoluted data (solid circles) suggests that the EMS cross-section in the 35-47 eV region is dominantly due to $(3a')^{-1}$ satellite processes. The intensity of the 28-47 eV region is also only slightly less than predicted by the higher-level TMPs (curves 4 and 6) and thus nearly all of the $(3a')^{-1}$ pole strength is accounted for within this energy region. The small amount of remaining $(3a')^{-1}$ pole strength is presumably located above 47 eV. The DFT momentum profiles for this orbital (Fig. 8.5f) generally provide excellent shape agreement with experiment and intensities similar to those obtained with the higher level Hartree-Fock calculations.

For accurate computations of chemical phenomena, it is important to use a wavefunction that gives good calculated values for a range of properties (e.g. total energy, dipole moment and momentum profile) that emphasize different regions of phase space [39,69]. On considering the other properties obtained from the various wavefunctions (Table 1), it can be seen that the poor STO-3G total energy and low dipole moment value reflect the low degree of basis set saturation in this calculation. Much better total energies and dipole moments are obtained with larger basis sets that incorporate diffuse and polarization functions (the 6-311G, 6-311+G* and 6-311++G** calculations). The 110-GTO and Trun-pV5Z calculations provide the largest Hartree-Fock results in the present work. It appears that the Hartree-Fock limit is being closely approached by these calculations (5 and 6) since they provide momentum profiles (see Figs. 8.3-8.5) with much the same shape and intensity as well as similar energies, although the dipole moment is still converging (Table 8.1). In addition to the improved agreement it provides between theory and experiment for several XMPs, a significant improvement is made in the total energy with the 110-G(CI) calculation. While little can be said regarding the DFT total energies [60], it can be seen from Table 8.1 that the dipole moments predicted by the DFT calculations are generally excellent and within 0.1 Debye of experiment.

8.3.3 Density Maps in Momentum and Position Space

The momentum and position space density contour maps corresponding to an oriented CH_3OH molecule presented in Figs. 8.6-8.8 provide some information regarding the complementary nature of *p*- and *r*-space. Some knowledge of the shapes and intensities of the (spherically averaged) XMPs and TMPs can also be gained by an analysis of these maps. These maps are slices of the orbital electron density $|\psi|^2$ through the molecular plane of an oriented molecule in position space and with momentum perpendicular and parallel with respect to the molecular plane in momentum space. The molecular planes chosen are indicated

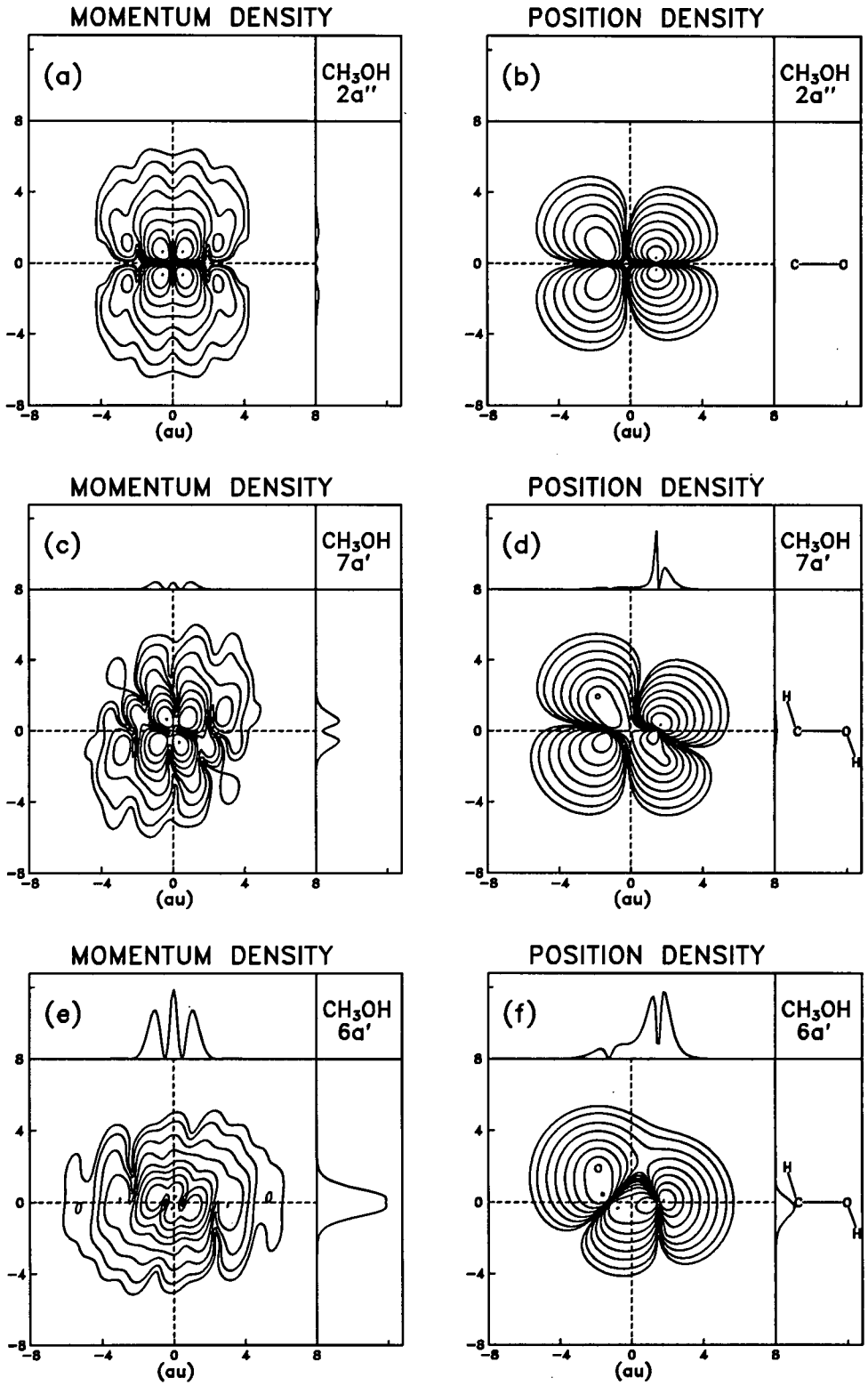

Fig. 8.6: Momentum and position density contour maps for the 2a″, 7a′ and 6a′ orbitals of an oriented methanol molecule calculated at the Hartree-Fock level using the Trun-pV5Z basis set. The contour values represent 0.01, 0.03, 0.1, 0.3, 1.0, 3.0, 10.0, 30.0, and 99.0% of the maximum density. The side panels (top and right side) show the density along the dashed lines (dashed vertical and horizontal lines) for each density map.

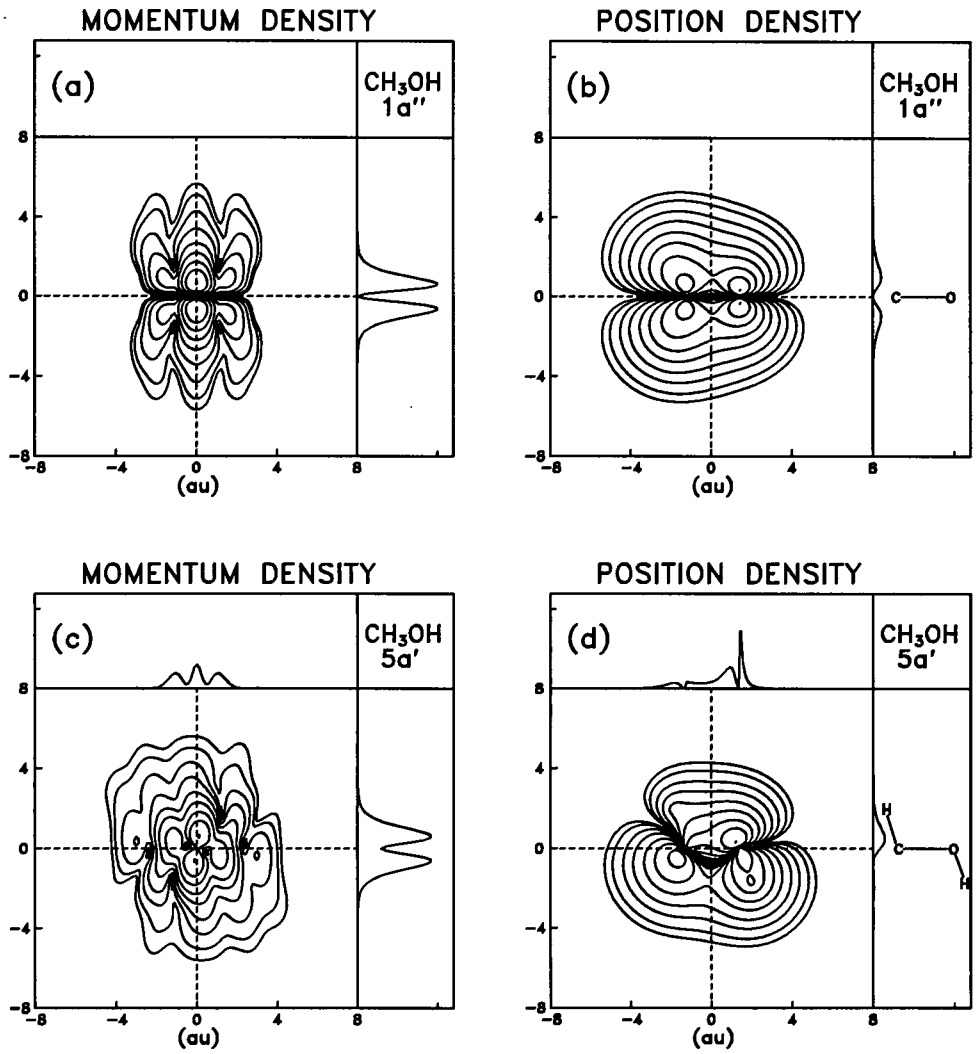

Fig. 8.7: Momentum and position density contour maps for the 1a″ and 5a′ orbitals of an oriented methanol molecule calculated at the Hartree-Fock level using the Trun-pV5Z basis set. The contour values represent 0.01, 0.03, 0.1, 0.3, 1.0, 3.0, 10.0, 30.0, and 99.0% of the maximum density. The side panels (top and right side) show the density along the dashed lines (dashed vertical and horizontal lines) for each density map.

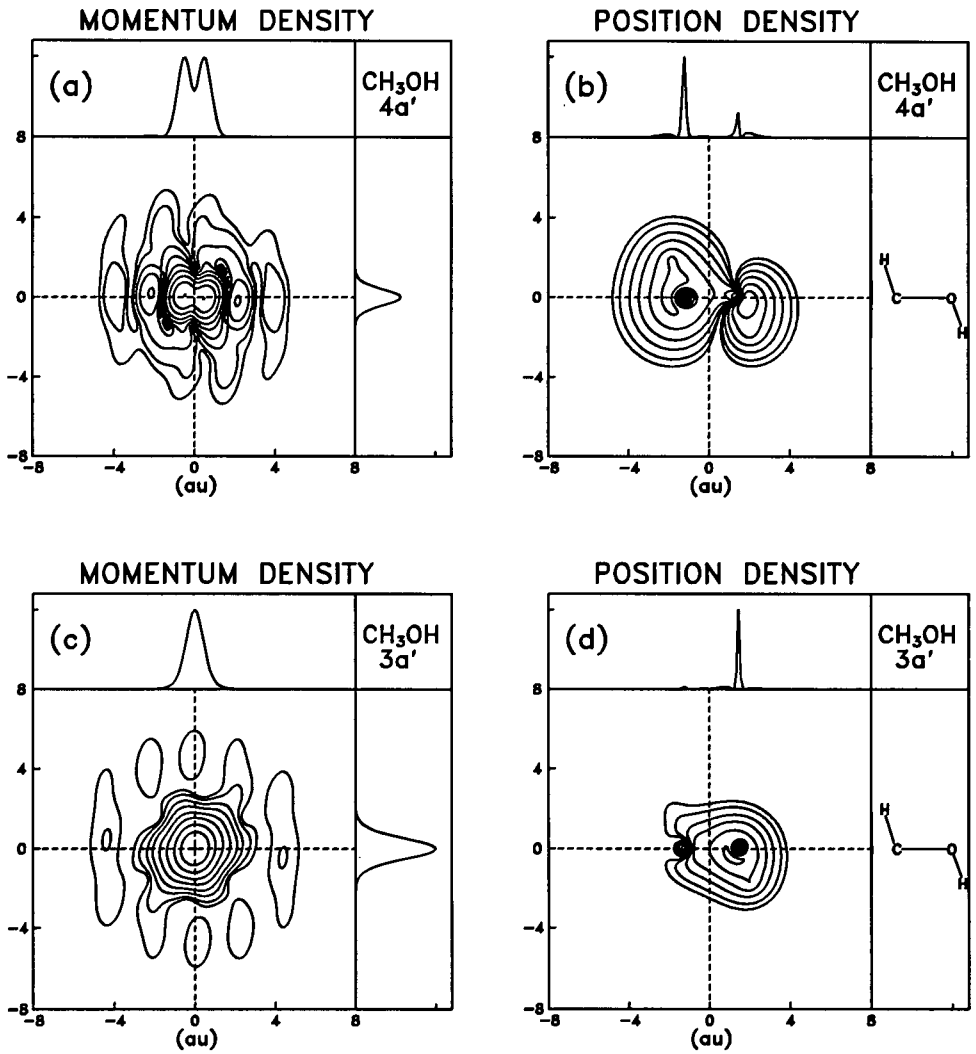

Fig. 8.8: Momentum and position density contour maps for the 4a′ and 3a′ orbitals of an oriented methanol molecule calculated at the Hartree-Fock level using the Trun-pV5Z basis set. The contour values represent 0.01, 0.03, 0.1, 0.3, 1.0, 3.0, 10.0, 30.0, and 99.0% of the maximum density. The side panels (top and right side) show the density along the dashed lines (dashed vertical and horizontal lines) for each density map.

in the right-hand side panels of Figs. 8.7-8.8. The calculations for each molecule are based on the near Hartree-Fock limit results (Trun-pV5Z) which has been found to provide good descriptions of the XMPs at the Hartree-Fock level. The origin for the position space maps is the molecular center of mass and all dimensions are in atomic units. The side panels on each map show slices of the momentum or position space density along the vertical (right panel) and horizontal (top panel) dotted lines. Position space three dimensional molecular orbital representations for the valence orbitals of methanol have been published by Jørgensen and Salem [267] and these are also shown in Ref. [84].

The 2a″ HOMO of methanol is predicted in simple valence bond terminology to be an oxygen lone pair. Accordingly, the *r*-map (Fig. 8.6b) for this orbital mainly consists of atomic p-type functions concentrated on oxygen. However, there is a partial delocalization of the 2a″ electron density away from a pure O lone pair onto the C atom. While the general shape of this orbital is similar to that of a π^* orbital, the p-type orbital components are not of equal intensity on C and O. In addition, there is only one nodal plane in *p*-space (Fig. 8.6a) due to the heteroatomic nature and asymmetry of CH_3OH [268]. The momentum density along the other plane in *p*-space is very small and is identically zero at zero momentum. Thus, spherical averaging of this momentum density should give a momentum profile with zero intensity at $p = 0$. In this regard it should be noted that the calculated spherically averaged momentum profiles in Figs. 8.3a and 8.3b have a very small non-zero intensity at $p = 0$ which is entirely due to the fact that they have been folded with the instrumental resolution function to compare with experiment. However, as noted in Section 8.3.2 and shown in Figs. 8.3a and 8.3b, the experimental intensity is somewhat larger than theory below $p \sim 0.3$ au.

The 7a′ orbital is also considered (at least according to simple valence bond concepts) to be an oxygen lone pair. The more complex molecular orbital Trun-pV5Z wavefunction used in this work, however, predicts lobes of electron density on both C and O which interfere constructively or destructively (see *r*-map on Fig. 8.6d). Unlike the 2a″ orbital, the *p*-map for the 7a′ orbital contains no nodal planes and the momentum density at zero momentum is non-

zero. Thus, a significant s-type component to the momentum profile is predicted by all TMPs, in accordance with experiment. However, p-type components in the wavefunction still dominate.

The *r*-map for the 6a′ molecular orbital (Fig. 8.6f) shows that significant σ_{CO} density exists while σ_{CH} density due to the in-plane hydrogen of the methyl group is also present. In addition, the methyl and hydroxyl hydrogen density adds in-phase to produce a spatially diffuse electron density and thus, according to the reciprocity of *r*- and *p*- space, appreciable electron density exists at low momentum in *p*-space (see *p*-map). This electron density at low p is reflected in the predominantly s-type shape of the momentum profiles for this orbital.

The 1a″ orbital is considered to be basically an out-of-plane orbital with lobes like a π orbital involving the out-of-plane hydrogens of the methyl group, the C 2p and some lobes of lesser density on O. Thus, the MO coefficients show that C 2p, O 2p and H 1s components dominate the electron density. The out-of-plane character is reflected by the nodal plane along the C-O axis (see *r*-map in Fig. 8.7b). The momentum density is zero at $p = 0$ and the side slice in the *p*-map also indicates appreciable electron density with a maximum at ±0.6 au. Thus, after spherical averaging, the momentum profiles for this orbital have zero intensity at zero momentum and a p_{max} at ~ 0.6 au. It should be noted that, similar to situation for the 2a″ momentum profile, the calculated momentum profiles in Fig. 8.4c and 8.4d have non-zero intensity at low momentum due to folding with the experimental angular resolution function.

The 5a′ orbital shows two main regions of density (see *r*-map in Fig. 8.7d). Density between the out-of-plane hydrogens and the σ_{OH} density adds to produce the region below the C-O bond axis. The density in the top region involves C, O and the in-plane methyl group H. The *p*-map is complex, reflecting the multicenter nature of this orbital. In addition, the top and side slices of the *p*-map reflect large amounts of both s- and p-type components in the molecular orbital. Thus, a large amount of s-type character appears in the calculated momentum profiles for this orbital. It should be noted, however, that the Hartree-Fock

Trun-pV5Z wavefunction used to construct these maps underestimates the s-type character in the XMP (Fig. 8.5a).

Two boundary surfaces appear in the 4a′ *r*-map (Fig. 8.8b) with maximum density on the C and O atoms. An analysis of the molecular orbital coefficients reveals that O 2s and C 2s atomic components dominate this MO. It is not unexpected that such an inner valence orbital would display mostly atomic character. There is considerable density at $p = 0$ in the *p*-map. Some p-type components are also prevalent in the wavefunction as seen by the two maxima at ±0.4 au in the top slice of the *p*-map. The calculated momentum profiles for this orbital (Figs. 8.5c and 8.5d) are thus predominantly s-type with some levelling off of the profile below 0.4 au.

The large electron density on O indicated in the top slice of the 3a′ *r*-map (Fig. 8.8d) is due to large s-orbital components in the wavefunction. The MO coefficients reveal that this inner valence orbital is mostly composed of atomic-like O 2s character. The *p*-map contains very large momentum density at $p = 0$ and the TMPs for this orbital are very strongly s-type (Figs. 8.5e and 8.5f).

Chapter 9

Concluding Remarks

This work has presented EMS measurements of the binding energy spectra and all valence momentum profiles for molecular oxygen and methanol. In addition, the momentum profiles for the highest occupied molecular orbitals have been studied for NO and NO_2, the series PH_3, PF_3 and $P(CH_3)_3$ and the series $Cr(CO)_6$, $Mo(CO)_6$ and $W(CO)_6$. Most of these measurements were obtained using the energy-dispersive multichannel spectrometer described in Chapter 3. For the studies of the low ionization cross-sections for the open-shell molecules, the larger molecules and some orbitals of methanol, the increased sensitivity of this multichannel spectrometer made possible the completion of the measurements in a reasonable amount of time and to good statistical precision. The experimental results have been compared with a range of Hartree-Fock calculations performed at the University of British Columbia. In addition, comparisons have been made with high-level Hartree-Fock and post-Hartree-Fock (e.g. MRSD-CI) calculations carried out in collaboration work by Professor E.R. Davidson and co-workers at Indiana University. The present work has also provided quantitative assessments of the recently developed DFT target Kohn-Sham approximation (TKSA) method for the calculation of momentum profiles.

The present EMS results for NO are an improvement over previous measurements and the data show considerably less scatter. The results for NO are significantly different from previously published measurements in the low momentum region and the differences can be attributed to contamination by NO_2 in the earlier work. In addition, the first measurements and

calculations for the XMP for the $6a_1$ HOMO of NO_2 are reported. A wide range of Hartree-Fock and high level post-Hartree-Fock (MRSD-CI, ACPF and QDVPT) calculations have also been performed and generally good agreement was obtained between theoretical and experimental momentum profiles for both open-shell molecules. At a given Hartree-Fock level, ROHF calculations are found to give more intense momentum profiles than UHF methods. Post-Hartree-Fock calculations produce changes in the intensity of the momentum profiles of NO and NO_2 but only small changes in the shape. The small but significant discrepancies remaining between theory and experiment for NO at lower momentum even at the post-Hartree-Fock level are reduced slightly by the density functional theory calculations.

The presently reported experimental momentum profiles of O_2 display considerably improved statistics compared with previously published EMS results. The oxygen binding energy spectra in the 9-59 eV range have been compared with MRSD-CI calculations. Strong splittings corresponding to $^4\Sigma_g^-$ and $^2\Sigma_g^-$ satellite states are observed experimentally and also predicted by the MRSD-CI calculations for the inner valence region. The measured momentum profiles are compared with cross-sections calculated using both unrestricted (open-shell) and restricted methods using basis sets ranging from minimal basis to near Hartree-Fock limit in quality. In addition, the effects of correlation and relaxation on the calculated momentum profiles are investigated using MRSD-CI calculations. Electron correlation effects in the ground state are further examined using several density functional approaches for the momentum profiles. The present EMS measurements and MRSD-CI calculations clearly show that the binding energy peak P at ~ 27.3 eV has significant contributions from both $^4\Sigma_u^-$ and $^2\Sigma_u^-$ processes in contrast to earlier assignments which have attributed this peak to the $C^2\Sigma_u^-$ state alone. Similarly, the binding energy peak at 33 eV is shown to be due to $^2\Sigma_u^-$ satellite intensity rather than the earlier assignment of $^2\Pi_u$ character.

Previous EMS measurements for PH_3 [74] have been extended to include experimental and theoretical studies of the orbital momentum profiles for the HOMOs of PF_3 and $P(CH_3)_3$. New calculations with larger basis sets have also been presented for the HOMO of PH_3. As in

the case of NH_3, NF_3 and $N(CH_3)_3$, intuitive arguments fail to predict the correct amounts of s- and p-type character in the momentum distributions of PH_3, PF_3 and $P(CH_3)_3$. A consideration of the EMS results and calculations together with an analysis of the respective HOMO density difference maps suggests that the methyl group is electron withdrawing relative to H when bonded to phosphorus. These results are analogous to the situation found previously [81,82] for the corresponding nitrogen compounds.

EMS measurements for the metal hexacarbonyls $M(CO)_6$, where M = Cr, Mo or W, are compared with a range of Hartree-Fock and DFT calculations. The present measurements for $Cr(CO)_6$ are in good agreement with previously published work, particularly in the low momentum region where some unexpected intensity is observed in the experimental momentum profile contrary to symmetry expectations. The measurements of the XMPs of the $2t_{2g}$ HOMOs of $Mo(CO)_6$ and $W(CO)_6$ are the first to be reported. The large discrepancies remaining between theory and experiment at low momentum for all molecules cannot be accounted for by any of the PWIA Hartree-Fock or DFT calculations. Vibrational effects distorting the symmetry of the ground state molecules are a possible explanation for the discrepancies at low momentum. Comparison of PWIA and DWIA calculations for atomic Cr 3d and Mo 4d orbitals suggest that the discrepancies in the metal hexacarbonyl molecules may be due to distorted wave effects. At present DWIA calculations are not possible for molecular targets and clearly such theoretical developments are desirable.

The methanol binding energy spectra in the 6-47 eV range have been compared with Green's function calculations [260]. In the inner valence region strong splitting of the 4a′ and 3a′ orbitals due to final electron state correlation is observed experimentally and predicted by the calculations. The experimental momentum profiles of the complete valence orbitals have been used to evaluate various theoretical models including Hartree-Fock wavefunctions ranging from the minimal basis set to the near Hartree-Fock limit, many-body MRSD-CI treatments with large basis sets, and Kohn-Sham DFT calculations a large basis set and several exchange-correlation potentials. Inclusion of electron correlation using the MRSD-CI and DFT

methods is found to be necessary for reasonable predictions of the shapes and intensities of the outer spatial regions of the valence electron momentum profiles of the 7a′, (6a′+1a″) and 5a′ orbitals. Some small discrepancy between theory and experiment remains at low momentum for the 2a″, 7a′ and 5a′ orbitals. For the 5a′ orbital in particular, all theory severely underestimates the s-type character in the XMP. The shapes of the inner valence 4a′ and 3a′ momentum profiles are well predicted by theory, but the theoretical momentum profiles must be multiplied by a factor of 0.75 for the 4a′ and 0.70 for the 3a′ orbital to match the experimental intensity. This is further evidence of the extensive pole strength splitting that occurs for ionization from these orbitals.

The high sensitivity of the energy-dispersive multichannel EMS spectrometer (approximately a factor of ten times that of a single channel instrument) was crucial for the measurements reported in this thesis. However, further improvements in sensitivity and energy resolution are highly desirable so that even larger molecules as well as low density targets such as excited molecules, free radicals and ions may be studied. A new high performance EMS spectrometer is currently being constructed in this laboratory which is multichannel in both energy and angle [269]. This spectrometer is designed to detect all outgoing electrons around the entire 360° azimuth (i.e. electrons will be detected at all ϕ angles simultaneously) while also using the energy-dispersive capabilities of the present EMS spectrometer in the radial direction. This new instrument will complete the progression of symmetric non-coplanar EMS spectrometers developed over the past 25 years. Earlier single-channel spectrometers measured coincidence data at only a single azimuthal angle and at a given binding energy [20,21] while current multichannel spectrometers measure either over a small range of binding energy [42,45] or over a small range of angles [47]. The increase in sensitivity from the high performance instrument currently under construction is predicted to be at least four orders of magnitude greater than that of the multichannel instrument used in the present work. The greatly increased sensitivity will also allow monochromation of the incident electron beam and much higher energy resolution. These increases in energy resolution and sensitivity will permit

the study of closely spaced orbitals of larger molecules as well as species of low ionization cross-section and/or low target number density.

Bibliography

[1] Fukui, *Accounts Chem. Res.* **4** (1971) 57.

[2] R.B. Woodward and R. Hoffman, *The Conservation of Orbital Symmetry* (Verlag Chemie, Weinheim, 1970).

[3] B. Williams, *Phys. Scr.* **15** (1977) 92.

[4] P. Lindner, *Phys. Scr.* **15** (1977) 112.

[5] M.J. Cooper, *Rep. Prog. Phys.* **48** (1985) 415.

[6] P. Coppens and E.D. Stevens, *Adv. Quantum Chem.* **10** (1977) 1.

[7] R.A. Bonham and H.F. Wellenstein, in *Compton Scattering*, ed. B.G. Williams (Mcgraw-Hill, New York, 1977) p. 234.

[8] D.A. Kohl and L.S. Bartell, *J. Chem. Phys.* **51** (1969) 2891.

[9] R.N. West, *Adv. Phys.* **22** (1973) 263.

[10] S. Berko, in *Compton Scattering*, ed. B.G. Williams (Mcgraw-Hill, New York, 1977) p. 273.

[11] C.E. Brion, *Int. J. Quantum Chem.* **29** (1986) 1397, and references therein.

[12] I.E. McCarthy and E. Weigold, *Rep. Prog. Phys.* **91** (1991) 789, and references therein.

[13] J.G.A. Baker, I.E. McCarthy and C.E. Porter, *Phys. Rev.* **120** (1960) 254.

[14] Yu. F. Smirnov and V.G. Neudatchin, *Soviet Phys. JETP Letters.* **3** (1966) 192.

[15] V.G. Neudatchin, G.A. Novoskol'tseva and Yu. F. Smirnov, *Soviet Phys. JETP.* **28** (1969) 540.

[16] A.E. Glassgold and G. Ialongo, *Phys. Rev.* **175** (1968) 151.

[17] H. Ehrhardt, M. Schulz, T. Tekaat and K. Willmann, *Phys. Rev. Lett.* **22** (1969) 89.

[18] J.U. Amaldi, A. Egidi, R. Marconero and G. Pizella, *Rev. Sci. Instrum.* **40** (1969) 1001.

[19] R. Camilloni, A. Giardini-Guidoni, R. Tiribelli and G. Stefani, *Phys. Rev. Letters.* **29** (1972) 618.

[20] E. Weigold, S.T. Hood and P.J.O. Teubner, *Phys. Rev. Letters.* **30** (1973) 475.

[21] J.B. Furness and I.E. McCarthy, *J. Phys. B.* **6** (1973) L204.

[22] S.T. Hood, E. Weigold, I.E. McCarthy and P.J.O. Teubner, *Nature Phys. Sci.* **245** (1973) 65.

[23] S.T. Hood, A. Hamnett and C.E. Brion, *Chem. Phys. Lett.* **39** (1976) 252.

[24] A. Hamnett, S.T. Hood and C.E. Brion, *J. Electron Spectry. Relat. Phenom.* **11** (1977) 263.

[25] I.E. McCarthy, *J. Phys. B.* **6** (1973) 2358.

[26] I.E. McCarthy, *J. Phys. B.* **8** (1975) 2133.

[27] V.G. Levin, V.G. Neudatchin, A.V. Pavlitchenkov and Yu.F. Smirnov, *J. Chem. Phys.* **63** (1975) 1541.

[28] J.H. Moore, M.A. Coplan, T.L. Skillman Jr. and E.D. Brooks, *Rev. Sci. Instrum.* **49** (1978) 463.

[29] M.P. Banjavcic, B.H. Watt, T.D. Pope, T.A. Daniels, R.P. Hammond and K.T. Leung, *Chem. Phys. Lett.* **160** (1989) 371.

[30] L.A. Graham, S.J. Desjardins and A.D.O. Bawagan, *Can. J. Phys.* **71** (1993) 216.

[31] S. Zhou, X. Fan, X. Chen, Y. Zheng, C.E. Brion, G. Frey and E.R. Davidson, "Orbital Imaging for CO by Electron Momentum Spectroscopy - Comparison with High-Level MRSD-CI and DFT Calculations", Abstract in *The Twentieth International Conference on the Physics of Electronic and Atomic Collisions*, ed. G. Betz, 1997.

[32] M. Takahashi, H. Nagasaka and Y. Udagawa, *J. Phys. Chem. A.* **101** (1997) 528.

[33] I.E. McCarthy and E. Weigold, *Phys. Rept.* **27** *C* (1976) 275.

[34] E. Weigold and I.E. McCarthy, *Advan. At. and Mol. Phys.* **14** (1978) 127.

[35] I.E. McCarthy and E. Weigold, *Rep. Prog. Phys.* **51** (1988) 299.

[36] A. Giardini-Guidoni, R. Fantoni, R. Camilloni and G. Stefani, *Comments Atom. Mol. Phys.* **10** (1981) 107.

[37] C.E. Brion, in *Correlations and Polarization in Electronic and Atomic Collisions and (e, 2e) Reactions*. Inst. Phys. Conf. Series **122** (1992) 171, Institute of Physics (Bristol).

[38] K.T. Leung, in *Theoretical Models of Chemical Bonding, Part 3. Molecular Spectroscopy, Electronic Structure and Intramolecular Interactions*, ed. Z.B. Maksic (Springer-Verlag, 1991).

[39] C.E. Brion, in *The Physics of Electronic and Atomic Collisions*, Eds. T. Andersen et al., American Institute of Physics Press, New York (1993), 350.

[40] M.A. Coplan, J.H. Moore and J.P. Doering, *Rev. Mod. Phys.* **66** (1994) 985.

[41] K.T. Leung and C.E. Brion, *J. Electron Spectry Relat. Phenom.* **35** (1985) 327.

[42] E. Weigold, Y. Zheng and W. von Niessen, *Chem. Phys.* **150** (1991) 405.

[43] Y. Zheng, *Electron Momentum Spectroscopy of Laser-Excited Atoms and Molecules.* Ph.D. thesis, The Flinders University of South Australia, 1989.

[44] J.P.D. Cook, I.E. McCarthy, A.T. Stelbovics and E. Weigold, *J. Phys. B.* **17** (1984) 2339.

[45] Y. Zheng, J.J. Neville, C.E. Brion, Y. Wang and E.R. Davidson, *Chem. Phys.* **188** (1994) 109.

[46] J.J. Neville, *Studies of Valence Electron Densities Using Electron Momentum Spectroscopy and Computational Quantum Chemistry,* Ph.D. thesis, University of British Columbia, 1997.

[47] B.R. Todd, N. Lermer and C.E. Brion, *Rev. Sci. Instrum.* **65** (1994) 349.

[48] Y. Zheng, I.E. McCarthy, E. Weigold and D. Zhang, *Phys. Rev. Lett.* **64** (1990) 1358.

[49] N. Lermer, *Development and Application of a Momentum dispersive Multichannel Electron Momentum Spectrometer.* Ph.D. thesis, The University of British Columbia, 1995.

[50] N. Lermer, B.R. Todd, N.M. Cann, C.E. Brion, Y. Zheng, S.J. Chakravorty and E.R. Davidson, *Can. J. Phys.* **74** (1996) 748.

[51] N. Lermer, B.R. Todd, N.M. Cann, Y. Zheng, C.E. Brion, Z. Yang and E.R. Davidson, *Phys. Rev. A.* (1997) submitted.

[52] P. Storer, R.S. Caprari, S.A.C. Clark, M. Vos and E. Weigold, *Rev. Sci. Instrum.* **65** (1994) 2214.

[53] Y. Zheng, J.J. Neville and C.E. Brion, *Science* **270** (1995) 5237.

[54] J.J. Neville, Y. Zheng and C.E. Brion, *J. Am. Chem. Soc.* **118** (1996) 10533.

[55] J.J. Neville, Y. Zheng, B.P. Hollebone, N.M. Cann, C.E. Brion, C.K. Kim and S. Wolfe, *Can. J. Phys.* **74** (1996) 773.

[56] D. Feller, C.H. Boyle and E.R. Davidson, *J. Chem. Phys.* **86** (1987) 3424.

[57] I.N. Levine, *Quantum Chemistry* (Prentice-Hall, Englewood Cliffs, 1991).

[58] A.O. Bawagan and C.E. Brion, *Chem. Phys.* **144** (1990) 167.

[59] P. Duffy, M.E. Casida, C.E. Brion and D.P. Chong, *Chem. Phys.* **159** (1992) 347.

[60] P. Duffy, D.P. Chong, M.E. Casida and D.R. Salahub, *Phys. Rev. A.* **50** (1994) 4704.

[61] B.P. Hollebone, J.J. Neville, Y. Zheng, C.E. Brion, Y. Wang and E.R. Davidson, *Chem. Phys.* **196** (1995) 13.

[62] Y. Zheng, C.E. Brion, M.J. Brunger, K. Zhao, A.M. Grisogono, S. Braidwood, E. Weigold, S.J. Chakravorty, E.R. Davidson, A. Sgamellotti, W. von Niessen, *Chem. Phys.* **212** (1996) 269.

[63] J. W. Rabalais, *Principles of Ultraviolet Photoelectron Spectroscopy* (Wiley, New York, 1977).

[64] J.H.D. Eland, *Photoelectron Spectroscopy* (Butterworths, London 1984).

[65] L.S. Cederbaum and W. Domcke, in *Advances in Chemical Physics*, Vol. 36, edited by I. Prigogine and S.A. Rice (Wiley, New York, 1977) p. 205.

[66] I.E. McCarthy, *J. Electron Spectry. Relat. Phenom.* **36** (1985) 37.

[67] S.T. Hood, A. Hamnett and C.E. Brion, *Chem. Phys. Lett.* **41** (1976) 428.

[68] A.O. Bawagan, C.E. Brion, E.R. Davidson, C. Boyle and R.F. Frey, *Chem. Phys.* **128** (1988) 439.

[69] A.O. Bawagan, C.E. Brion, E.R. Davidson and D. Feller, *Chem. Phys.* **113** (1987) 19.

[70] A.O. Bawagan, R. Müller-Fielder, C.E. Brion, E.R. Davidson and C. Boyle, *Chem. Phys.* **120** (1988) 335.

[71] E.R. Davidson, *Can. J. Phys.* **74** (1996) 757.

[72] B.P. Hollebone, Y. Zheng, C.E. Brion, E.R. Davidson and D. Feller, *Chem. Phys.* **171** (1993) 303.

[73] S.A.C. Clark, E. Weigold, C.E. Brion, E.R. Davidson, R.F. Frey, C.M. Boyle, W. von Niessen and J. Schirmer, *Chem. Phys.* **134** (1989) 229.

[74] S.A.C. Clark, C.E. Brion, E.R. Davidson and C.M. Boyle, *Chem. Phys.* **136** (1989) 55.

[75] C.L. French, C.E. Brion and E.R. Davidson, *Chem. Phys.* **122** (1988) 247.

[76] B.P. Hollebone, C.E. Brion, E.R. Davidson and C. Boyle, *Chem. Phys.* **173** (1993) 193.

[77] S.A.C. Clark, T.J. Reddish, C.E. Brion, E.R. Davidson and R.F. Frey, *Chem. Phys.* **143** (1990) 1.

[78] K.T. Leung and C.E. Brion, *Chem. Phys.* **82** (1983) 113.

[79] K.T. Leung and C.E. Brion, *J. Am. Chem. Soc.* **106** (1984) 5859.

[80] J.A. Tossell, S.M. Lederman, J.H. Moore, M.A. Coplan and D.J. Chornay, *J. Am. Chem. Soc.* **106** (1984) 976.

[81] A.O. Bawagan and C.E. Brion, *Chem. Phys. Lett.* **137** (1987) 573.

[82] A.O. Bawagan and C.E. Brion, *Chem. Phys.* **123** (1988) 51.

[83] B.P. Hollebone, P. Duffy, C.E. Brion, Y. Wang and E.R. Davidson, *Chem. Phys.* **178** (1993) 25.

[84] A. Minchinton, C.E. Brion and E. Weigold, *Chem. Phys.* **62** (1981) 369.

[85] S.A.C. Clark, A.O. Bawagan and C.E. Brion, *Chem. Phys.* **137** (1989) 407.

[86] Y. Zheng, E. Weigold and C.E. Brion, *J. Electron Spectry. Relat. Phenom.* **53** (1990) 153.

[87] C.A. Coulson and W.E. Duncanson, *Proc. Camb. Phios. Soc.* **37** (1941) 55, 67, 74, 397, 406.

[88] C.A. Coulson and W.E. Duncanson, *Proc. Camb. Phios. Soc.* **38** (1942) 100.

[89] W.E. Duncanson, *Proc. Camb. Phios. Soc.* **39** (1943) 180.

[90] P.T. Measures, K.A. Mort, N.L. Allen and D.L. Cooper, *J. Comput. Aided Mol. Design.* **9** (1995) 331.

[91] N.L. Allan and D.L. Cooper, *Topics in Current Chemistry.* **173** (1995) 85.

[92] D.L. Cooper, K.A. Mort, N.L. Allan, D. Kinchington and C. McGuigan, *J. Am. Chem. Soc.* **115** (1993) 12615.

[93] K.T. Leung, *Sci. Progress Oxford.* **75** (1991) 157.

[94] J. Rolke, N. Cann, Y. Zheng, B.P. Hollebone, C.E. Brion, Y.A. Wang and E.R. Davidson, *Chem. Phys.* **201** (1995) 1.

[95] J. Rolke and C.E. Brion, *Chem. Phys.* **207** (1996) 173.

[96] J. Rolke, Y. Zheng, C.E. Brion, S.J. Chakravorty, E.R. Davidson and I.E. McCarthy, *Chem. Phys.* **215** (1997) 191.

[97] A. Szabo and N.S. Ostlund, *Modern Quantum Chemistry* (McGraw-Hill, Toronto, 1982).

[98] W. Hehre, L. Radom, P.v.R. Schleyer, and J.A. Pople, *Ab Initio Molecular Orbital Theory,* Wiley Interscience, New York, 1986.

[99] C.C.J. Roothaan, *Rev. Mod. Phys.* **23** (1951) 69.

[100] E.R. Davidson and D. Feller, *Chem. Rev.* **86** (1986) 681.

[101] W.J. Hehre, R.F. Stewart, and J.A. Pople, *J. Chem. Phys.* **51** (1969) 2657.

[102] R. Ditchfield, W.J. Hehre and J.A. Pople, *J. Chem. Phys.* **54** (1971) 724.

[103] R. Krishnan, M.J. Frisch and J.A. Pople, *J. Chem. Phys.* **72** (1980) 4244.

[104] M.J. Frisch, J.A. Pople, and J.S. Binkley, *J. Chem. Phys.* **80** (1984) 3265.

[105] T. Clark, J. Chandrasekhar, G.W. Spitznagel, and P.v.R. Schleyer, *J. Comp. Chem.* **4** (1983) 294.

[106] C.C.J. Roothaan, *Rev. Mod. Phys.* **23** (1960) 179.

[107] J.S. Binkley, J.A. Pople and P.A. Dobosh, *Mol. Phys.* **28** (1974) 1423.

[108] J.A. Pople and R.K. Nesbet, *J. Chem. Phys.* **22** (1954) 571.

[109] P. Hohenberg and W. Kohn, *Phys. Rev. B.* **136** (1964) 864.

[110] W. Kohn and L.J. Sham, *Phys. Rev. A.* **140** (1965) 1133.

[111] R.G. Parr and W. Yang, *Density Functional Theory of Atoms and Molecules.* Oxford University Press, New York, 1989.

[112] S.H. Vosko, L. Wilk and M. Nusair, *Can. J. Phys.* **58** (1980) 1200.

[113] D.M. Ceperly and B.J. Alder, *Phys. Rev. Lett.* **45** (1980) 566.

[114] P.A.M. Dirac, *Proc. Cambridge Phil. Soc.* **26** (1930).

[115] J.P. Perdew, *Phys. Rev. B.* **33** (1986) 8822.

[116] A.D. Becke, *Phys. Rev. A.* **38** (1988) 3098.

[117] J.P. Perdew and Y. Wang, *Phys. Rev. B.* **33** (1986) 8800.

[118] J.P. Perdew and Y. Wang, *Phys. Rev B.* **45** (1992) 13244.

[119] C. Lee, W. Yang and R.G. Parr, *Phys. Rev. B.* **37** (1988) 785.

[120] A.D. Becke, *J. Chem. Phys.* **98** (1993) 5648.

[121] P. Duffy, *The Electron Structure of Molecules.* Ph.D. thesis, The University of British Columbia, 1995.

[122] A. St.-Amant and D.R. Salahub, *Chem. Phys. Lett.* **169** (1990) 387.

[123] D.R. Salahub, R. Fournier, P. Mlanarski, I. Papai, A. St.-Amant, and J. Ushio, in *Density Functional Methods in Chemistry*, J. Labanowski and J. Andzelm (eds.), New York:, Springer-Verlag, 1991, p. 77.

[124] *Gaussian 92, Revision A*, M.J. Frisch, G.W. Trucks, M. Head-Gordon, P.M.W. Gill, M.W. Wong, J.B. Foresman, B.G. Johnson, H.B. Schlegel, M.A. Robb, E.S. Replogle, R. Gomperts, J.L. Andres, K. Raghavachari, J.S. Binkly, C. Gonzalez, R.L. Martin, D.J. Fox, D.J. Defrees, J. Baker, J.J.P. Stewart and J.A. Pople, Gaussian, Inc., Pittsburgh PA, 1992.

[125] *Gaussian 94, Revision A.1*, M.J. Frisch, G.W. Trucks, H.B. Schlegel, P.M.W. Gill, B.G. Johnson, M.A. Robb, J.R. Cheeseman, T.A. Keith, G.A. Petersson, J.A. Montgomerey, K. Raghavachari, M.A. Al-Laham, V.G. Zakrewski, J.V. Ortiz, J.,B. Foresman, J. Cioslowski, B.B. Stefanov, A. Nanayakkara, M. Challacombe, C.Y. Peng, P.Y. Ayala, W. Chen, M.W. Wong, J.L. Andres, E.S. Replogle, R. Gomperts, R.L. Martin, D.J. Fox, J.S. Binkley, D.J. Defrees, J. Baker, J.P. Stewart, M. Head-Gordon, C. Gonzalez and J.A. Pople, Gaussian, Inc. Pittsburgh PA, 1995.

[126] L. Vriens, in *Case Studies in Atomic Collision Physics.* Vol. 1, eds. E.W. McDaniel and M.R.C. McDowell (North-Holland, Amsterdam, 1969) ch. 6, p. 335.

[127] J.P. Coleman, in *Case Studies in Atomic Collision Physics.* Vol. 1, eds. E.W. McDaniel and M.R.C. McDowell (North-Holland, Amsterdam, 1969) ch. 3, p. 101.

[128] K.T. Leung, J.A. Sheehy and P.W. Langhoff, *Chem. Phys. Lett.* **157** (1989) 135.

[129] K.T. Leung and C.E. Brion, *Chem. Phys.* **82** (1983) 87.

[130] M.J. Brunger, S.W. Braidwood, I.E. McCarthy and E. Weigold, *J. Phys. B: At. Mol. Opt. Phys.* **27** (1994) L597.

[131] Y. Zheng and C.E. Brion, unpublished work.

[132] L. Frost, J. Mitroy and E. Weigold, *J. Phys. B: At. Mol. Phys.* **16** (1983) 223.

[133] J.K. Labanowski and J.W. Andzelm, eds. *Density Functional Methods in Chemistry.* Springer-Verlag, New York, 1991.

[134] W. Kohn, A.D. Becke and R.G. Parr, *J. Phys. Chem.* **100** (1996) 12974.

[135] M.E. Casida, *Phys. Rev. A.* **51** (1995) 2005.

[136] J.P. Perdew and M. Levy, *Phys. Rev. Lett.* **51** (1983) 1884.

[137] P. Kaijser and V.H. Smith, Jr., in *Advances in Quantum Chemistry,* Vol. 10, edited by Per-Olov Löwdin (Academic Press, New York, 1977) p. 37.

[138] J.L. Wiza, *Nucl. Instr. and Meth.* **162** (1979) 587.

[139] J.P.D. Cook, J. Mitroy and E. Weigold, *Phys. Rev. Lett.* **52** (1984) 1116.

[140] L.J. Richter and W. Ho, *Rev. Sci. Instrum.* **57** (1986) 1469.

[141] C.W. Gear, in *Proceedings of the Skytop Conference on Computer Systems in Experimental Nuclear Physics*, page 552, USAEC, 1969.

[142] S.J. Chakravorty and E.R. Davidson, private communication.

[143] D.F. Shriver, P.W. Atkins, and C.H. Langford, *Inorganic Chemistry*, W.H. Freeman, New York, 1990.

[144] P. Feldman, O. Griffith, and D. Stuehr, *Chemical and Engineering News.* **71** (50) (1993) 26.

[145] C.E. Brion, J.P.D. Cook, I.G. Fuss, and E. Weigold, *Chem. Phys.* **64** (1982) 287.

[146] R. Fantoni, A. Giardini-Guidoni, and R. Tiribelli, *J. Electron Spectry. Relat. Phenom.* **26** (1982) 99.

[147] J.A. Tossell, J.H. Moore, M.A. Coplan, G. Stefani, and R. Camilloni, *J. Am. Chem. Soc.* **104** (1982) 7416.

[148] J.E. Kouba and Y. Ohrn, *Int. J. Quantum Chem.* **5** (1971) 539.

[149] J. Gdanitz and R. Ahlrichs, *Chem. Phys. Lett.* **143** (1988) 413.

[150] R.J. Cave and E.R. Davidson, *J. Chem. Phys.* **89** (1988) 6798.

[151] C.W. Murray, S.C. Racine and E.R. Davidson, *Int. J. Quantum Chem.* **42** (1992) 273.

[152] P.E. Cade and A.C. Wahl, *At. Data Nucl. Data Tables.* **13** (1974) 339.

[153] W.F. Chan, G. Cooper and C.E. Brion, *Chem. Phys.* **170** (1993) 111.

[154] J.H. Shaw, *J. Chem. Phys.* **24** (1956) 399.

[155] Y. Morino and M. Tanimoto, *Can. J. Phys.* **62** (1984) 1315.

[156] F.P. Billingsley, *J. Chem. Phys.* **62** (1975) 864.

[157] S. Green, *Chem. Phys. Lett.* **13** (1972) 552.

[158] S. Green, *Chem. Phys. Lett.* **23** (1973) 115.

[159] K. Huber and G. Herzberg, *Constants of Diatomic Molecules* (Van Nostrand Reinhold, New York, 1979) p. 209.

[160] R.M. Neumann, *Astrophys. J.* **161** (1970) 779.

[161] J.A. Gray, R.L. Farrow, J.L. Durant, and L.R. Thorne, *J. Chem. Phys.* **99** (1993) 4327.

[162] S.J. Chakravorty, S.R. Gwaltney and E.R. Davidson, *Phys. Rev. A.* **47** (1993) 3649.

[163] D. Feller, E.D. Glendening, E.A. McCullough, Jr. and R.J. Miller, *J. Chem. Phys.* **99** (1993) 2829.

[164] G. Herzberg, *Molecular Spectra and Molecular Structure.* Vol. 3, Van Nostrand, New York, 1966.

[165] S. Heitz, R. Lampka, D. Weidauer, and A. Hese. *J. Chem. Phys.* **94** (1991) 2532.

[166] T.H. Dunning, Jr., *J. Chem. Phys.* **90** (1989) 1007.

[167] R.A. Kendall, T.H. Dunning, Jr., and R.J. Harrison, *J. Chem. Phys.* **96** (1992) 6796.

[168] D.E. Woon and T.H. Dunning, Jr., *J. Chem. Phys.* **98** (1993) 1358.

[169] D.E. Woon and T.H. Dunning, Jr., *J. Chem. Phys.* **99** (1993) 1914.

[170] H. Partridge, *Near Hartree-Fock Quality GTO Basis Sets for the First- and Third-Row Atoms.* NASA Technical Memorandum. **101044** (1989) pp 73, 79, 85.

[171] D. Feller and E.R. Davidson, *J. Chem. Phys.* **74** (1981) 3977.

[172] I.L. Cooper and C.N.M. Pounder, *J. Chem. Phys.* **77** (1982) 5045.

[173] P. Fantucci, V. Bonacic-Koutecky and J. Koutecky, *J. Comput. Chem.* **6** (1985) 462.

[174] K. Kimura, S. Katsumata, Y. Achiba, T. Yamazaki, and S. Iwata, *Handbook of HeI Photoelectron Spectra of Fundamental Organic Molecules* (Halsted Press, New York, 1981).

[175] T. Yamazaki and K. Kimura, *Chem. Phys. Lett.* **43** (1976) 502.

[176] D.W. Turner, C. Baker, A.D. Baker and C.R. Brundle, *Molecular Photoelectron Spectroscopy* (Wiley, New York, 1970).

[177] O. Edqvist, E. Lindholm, L.E. Selin and L. Åsbrink, *Phys. Scr.* **1** (1970) 25.

[178] J.A.R. Samson and J.L. Gardner, *J. Chem. Phys.* **67** (1977) 755.

[179] P. Baltzer, B. Wannberg, L. Karlsson and M. Carlsson Göthe, *Phys. Rev. A.* **45** (1992) 4374.

[180] J.L. Gardner and J.A.R. Samson, *J. Chem. Phys.* **62** (1975) 4460.

[181] K. Ellis, R.I. Hall, L. Avaldi, G. Dawber, A. McConkey and G.C. King, *J. Phys. B: At. Mol. Opt. Phys.* **27** (1994) 3415.

[182] M.S. Banna and D.A. Shirley, *J. Electron Spectry. Relat. Phenom.* **8** (1976) 255.

[183] K. Siegbahn, C. Nordling, G. Johansson, J. Hedman, P.F. Heden, K. Hamrin, U. Gelius, T. Bergmark, L.O. Werme, R. Manne and Y. Baer, *ESCA Applied to Free Molecules* (North-Holland, Amsterdam, 1969).

[184] C.E. Brion, K.H. Tan, M.J. van der Wiel and Ph. E. van der Leeuw, *J. Electron Spectry. Relat. Phenom.* **17** (1979) 101.

[185] I.H. Suzuki, E. Weigold, and C.E. Brion, *J. Electron Spectry. Relat. Phenom.* **20** (1980) 289.

[186] R.N. Dixon and S.E. Hull, *Chem. Phys. Lett.* **3** (1969) 367.

[187] N. Honjou, K. Tanaka, K. Ohno and H. Taketa, *Mol. Phys.* **35** (1978) 1569.

[188] N. Honjou, K. Tanaka, K. Ohno and H. Taketa, *Chem. Phys.* **57** (1981) 475.

[189] J.A. Nichols, D.L. Yeager and P. Jørgenson, *J. Chem. Phys.* **80** (1984) 293.

[190] P. Swanstrom, J.T. Golab, D.L. Yeager and J.A. Nichols, *Chem. Phys.* **110** (1986) 339.

[191] G.D. Purvis and Y. Öhrn, *J. Chem. Phys.* **62** (1975) 2045.

[192] A. Gerwer, C. Asaro, B.V. McKoy and P.W. Langhoff, *J. Chem. Phys.* **72** (1980) 713.

[193] J.A.R. Samson, J.L. Gardner and G.N. Haddad, *J. Electron Spectry. Relat. Phenom.* **12** (1977) 281.

[194] E. Tiemann, *J. Mol. Spectros.* **91** (1982) 60.

[195] D.E. Stogryn and Alex P. Stogryn, *Mol. Phys.* **4** (1966) 371.

[196] Y. Zhang, A.W. Ross, and M. Fink, *Z. Phys. D.* **18** (1991) 163

[197] E.R. Davidson, private communication.

[198] P.A. Cox and F.A. Orchard, *Chem. Phys. Lett.* **7** (1970) 273.

[199] A.O. Bawagan, C.E. Brion, M.A. Coplan, J.A. Tossell and J.H. Moore, *Chem. Phys.* **110** (1986) 153.

[200] J.P.D. Cook and C.E. Brion, *J. Electron Spectry. Relat. Phenom.* **15** (1979) 233.

[201] J.R. Epstein and A.C. Tanner, in: *Compton Scattering,* ed. B.G. Williams (McGraw-Hill, New York, 1977) p. 209.

[202] C.J. Maxwell, F.B.C. Machado and E.R. Davidson, *J. Am. Chem. Soc.* **114** (1992) 6496.

[203] R.T. Morrison and R.N. Boyd, *Organic Chemistry*, 5th ed. Allyn and Bacon, New York, 1991.

[204] M. Witanowski and H. Januszewski, *Can. J. Chem.* **47** (1969) 1321.

[205] M. Alei, Jr., A.E. Florin, W.M. Litchman and J.F. O'Brien, *J. Phys. Chem.* **75** (1971) 932.

[206] W. Hehre and J.A. Pople, *J. Am. Chem. Soc.* **92** (1970) 2191.

[207] J.H. Callomon, E. Hirota, K. Kuchitsu, W.J. Lafferty, A.G. Maki and C.S. Pote, in: *Numerical Data and Functional Relationships in Science and Technology, New Series, Group II: Atomic and Molecular Physics, Vol. 7. Structure Data of Free Polyatomic Molecules,* eds. K.-H. Hellwege and A.M. Hellwege, Springer, Berlin, 1976.

[208] E. Hirota and Y. Morino, *J. Mol. Spectry.* **33** (1970) 460.

[209] L.S. Bartell and L.O. Brockway, *J. Chem. Phys.* **32** (1960) 512.

[210] R. Moccia, *J. Chem. Phys.* **40** (1964) 2176.

[211] G.R. Branton, D.C. Frost, C.A. McDowell and I.A. Stenhouse, *Chem. Phys. Lett.* **5** (1970) 1.

[212] P.J. Bassett and D.R. Lloyd, *J. Chem. Soc., Dalton Trans.* (1972) 248.

[213] R.J. Puddephatt, G.M. Bancroft and T. Chan, *Inorganica Chimica Acta.* **73** (1983) 83.

[214] R.O. Jones and O. Gunnarson, *Rev. Mod. Phys.* **61** (1989) 689.

[215] K.T. Leung and C.E. Brion, *Chem. Phys.* **93** (1985) 319.

[216] B.P. Hollebone and C.E. Brion, unpublished work.

[217] R.K. Harris and B.E. Mann, *NMR and the Periodic Table*, Academic Press, New York, 1978.

[218] K. Takagi and T. Kojima, *J. Phys. Soc. Japan.*, **30** (1971) 1145.

[219] J.E. Wollrab and V.N. Laurie, *J. Chem. Phys.*, **48** (1968) 5058.

[220] J.E. Wollrab and V.N. Laurie, *J. Chem. Phys.*, **51** (1969) 1580.

[221] M.D. Marshall and J.S. Muenter, *J. Mol. Spect.* **85** (1981) 322.

[222] P. Kisliuk, *J. Chem. Phys.* **22** (1954) 86.

[223] D.R. Lide and D.E. Mann, *J. Chem. Phys.* **29** (1958) 914.

[224] C.A. Burrus, *J. Chem. Phys.* **28** (1958) 427.

[225] D.G. Gorenstein, *Prog. NMR Spectros.* **16** (1983) 1.

[226] V. Mark, C.H. Dungan, M.M. Crutchfield and J.R. Van Wazer, *Top. Phosphorus Chem.* **5** (1967).

[227] D.B. Chesnut, in *Phosphorus-31 NMR Spectroscopy in Stereochemical Analysis*, VCH, Deerfield Beach, 1987.

[228] P. Bernard-Moulin and G. Pouzard, *J. Chim. Phys.* **76** (1979) 708.

[229] M. Rajzmann and J.-C. Simon, *Org. Magn. Reson.* **7** (1975) 334.

[230] W.G. Henderson, M. Taagepera, D. Holtz, R.T. McIver, Jr., J.L. Beauchamp and R.W. Taft, *J. Am. Chem. Soc.* **94** (1972) 4728.

[231] R.H. Staley and J.L. Beauchamp, *J. Am. Chem. Soc.* **96** (1974) 6252.

[232] J.J. Brauman, J.M. Riveros and L.K. Blair, *J. Am. Chem. Soc.* **93** (1971) 3914.

[233] M.S.B. Munson, *J. Am. Chem. Soc.* **87** (1965) 2332.

[234] J.J. Brauman and L.K. Blair, *J. Am. Chem. Soc.* **90** (1968) 6561.

[235] J.J. Brauman and L.K. Blair, *J. Am. Chem. Soc.* **93** (1971) 3911.

[236] S.G. Lias, J.E. Bartmess, J.F. Liebman, J.L. Holmes, R.D. Levine and W.G. Mallard, *J. Chem. Phys. Ref. Data.* **17** (1988) Suppl. 1.

[237] S. Berger and J.I. Brauman, *J. Am. Chem. Soc.* **114** (1992) 4737.

[238] S. Ingemann and N.M.M. Nibbering, *J. Chem. Soc., Perkin Trans. 2.* (1985) 837.

[239] J.J. Grabowski, R.D. Roy and R. Leone, *J. Chem. Soc., Perkin Trans. 2.* (1988) 1627.

[240] G.I. Mackay, R.S. Hemsworth and D.K. Bohme, *Can. J. Chem.*, **54** (1976) 1624.

[241] C.K. Ingold, *Structure and Mechanism in Organic Chemistry*, 2nd ed., Cornell University Press, New York, 1969, pp 70-87.

[242] F.A. Cotton and G. Wilkinson, *Advanced Inorganic Chemistry*, 5th ed., Wiley Interscience, New York, 1988.

[243] D.M.P. Mingos, *Comprehensive Organometallic Chemistry*, G. Wilkinson (ed.), Pergamon Press, New York, 1982, Vol. 3, p 1.

[244] E. Muetterties, *Science*, **194** (1976) 1150.

[245] E. Muetterties, *Science*, **196** (1977) 839.

[246] D.J. Chornay, M.A. Coplan, J.A. Tossell, J.H. Moore, E.J. Baerends and A. Rozendaal, *Inorg. Chem.* **24** (1985) 877.

[247] B.R. Higginson, D.R. Lloyd, P. Burroughs. D.M. Gibson and A.F. Orchard, *J. Chem. Soc., Faraday Trans. 2.* **69** (1973) 1659.

[248] A. Jost, B. Rees and W.B. Yelon, *Acta. Crystallogr.* **23** (1975) B31 2658.

[249] S.P. Arnesen and H.M. Seip, *Acta. Chem. Scand.* **20** (1966) 2711.

[250] P.J. Hay and W.R. Wadt, *J. Chem. Phys.* **82** (1985) 270.

[251] W.R. Wadt and P.J. Hay, *J. Chem. Phys.* **82** (1985) 284.

[252] P.J. Hay and W.R. Wadt, *J. Chem. Phys.* **82** (1985) 299.

[253] T.H. Dunning and P.J. Hay, *Modern Theoretical Chemistry*, Plenum, New York, 1976, pp 1-28.

[254] N. Godbout, D.R. Salahub, J. Andzelm and E. Wimmer, *Can. J. Chem.* **70** (1992) 560.

[255] C.L. French, C.E. Brion, A.O. Bawagan, P.S. Bagus, E.R. Davidson, *Chem. Phys.* **121** (1988) 315.

[256] M. Ohno, W. von Niessen and F. Tarantelli, *Phys. Rev. B.* **45** (1992) 1851.

[257] L.H. Jones, R.S. McDowell and M. Goldblatt, *Inorg. Chem.* **8** (1969) 2349.

[258] I.E. McCarthy, Flinders University of South Australia, (e, 2e) computer program.

[259] C.F. Bunge, J.V. Barrientos and A.V. Bunge, *At. Data Nucl. Data Tables.* **53** (1993) 113.

[260] W. von Niessen, G. Bieri and L. Åsbrink, *J. Electron Spectry. Relat. Phenom.* **21** (1980) 175.

[261] M.C.L. Gerry, R.M. Lees and G. Winnewisser, *J. Molec. Spectry.* **61** (1976) 231.

[262] E.C. Weast ed., Handbook of chemistry and physics (Chemical rubber Company, Cleveland).

[263] H. Partridge, *Near-Hartree-Fock quality GTO basis sets for the second-row atoms.* NASA Technical Memorandum **89449** (1987).

[264] K.A.G. MacNeil and N.R. Dixon, *J. Electron Spec. Relat. Phenom.* **11** (1977) 315.

[265] P.Duffy, *Can. J. Chem.* **74** (1996) 763.

[266] L.C. Snyder and H. Basch, *Molecular wavefunctions and properties*, Wiley, New York, 1972.

[267] W.L. Jørgensen and L. Salem, *The organic chemist's book of orbitals*. (Acedemic Press, New York, 1973).

[268] K.T. Leung and C.E. Brion, *Chem. Phys.* **96** (1985) 241.

[269] C.E. Brion, Private communication.